Side-coupled Fabry-Pérot devices for integrated hybrid lasers

Ph.D. Candidate:
Davide **Monopoli**

Side-coupled Fabry-Pérot devices for integrated hybrid lasers

Thesis submitted for the degree of Philosophiae Doctor

Interuniversity Ph.D. Program in **Industry 4.0**
Polytechnic University of Bari

Ph.D. Tutors:

Prof. Giovanna **Calò**

Dr. William **Whelan-Curtin**
(a.k.a. Liam O'Faolain)

Prof. Antonella **D'Orazio**

Dr. Ganga Rao Chinna **Devarapu**

2026

A doctoral thesis submitted in fulfillment of the requirements for a double doctoral degree between Polytechnic University of Bari and Munster Technological University of Cork

Dissertation submitted for the degree of *Philosophiae Doctor*
Interuniversity Ph.D. Program in Industry 4.0

Ph. D. Cycle:
38th (2022, November 1 – 2026, April 30)

Administrative Headquarters:
Polytechnic University of Bari – Department of Electrical and Information Engineering

Hosting University:
Recruiting Host: Polytechnic University of Bari – Department of Electrical and Information Engineering
Co-Host: Munster Technological University of Cork (MTU) - Department of Physical Science Centre for Advanced Photonics & Process Analysis (CAPPA)

Title of the Ph.D. dissertation:
Side-coupled Fabry-Pérot devices for integrated hybrid lasers

Ph.D. Candidate:
Davide Monopoli Email: d.monopoli3@phd.poliba.it / monopolidavide97@gmail.com

Academic Discipline:
Electromagnetic Fields (SSD: IINF-02/A)

Ph.D. tutors:
Prof. Giovanna Calò, Polytechnic University of Bari (Bari, Italy),

Email: giovanna.calo@poliba.it

Dr. William Whelan-Curtin, Munster Technological University of Cork (Cork, Ireland)

Email: william.whelan-curtin@mtu.ie

Prof. Antonella D'Orazio, Polytechnic University of Bari (Bari, Italy)

Email: antonella.dorazio@poliba.it

Dr. Ganga Rao Chinna Devarapu, Munster Technological University of Cork (Cork, Ireland)

_________ __________ Email: Chinna.Devarapu@mtu.ie

Coordinator of the Ph.D. Program:

Prof. Engr. Salvatore Digiesi, Polytechnic University of Bari (Bari, Italy)

____

External Reviewers:

Prof. Bart Kuyken, Ghent University and IMEC (Ghent, Belgium)
Email: Bart.Kuyken@UGent.be

Prof. Béatrice Dagens, CNRS research director at C2N (Palaiseau, France)
Email: beatrice.dagens@c2n.upsaclay.fr

Last version:
May 07, 2026

Politecnico di Bari

LIBERATORIA PER L'ARCHIVIAZIONE DELLA TESI DI DOTTORATO

Al Magnifico Rettore
del Politecnico di Bari

Il sottoscritto Davide Monopoli nato a Molfetta (BA) il 25/07/1997, residente a Bisceglie in via Largo Monsignor Giannattasio n.3, Bisceglie (BT), 76011, Italy, e-mail: monopolidavide97@gmail.com, iscritto al 3° anno di Corso di Dottorato di Ricerca in Industria 4.0 (Industry 4.0), ciclo XXXVIII ed essendo stato ammesso a sostenere l'esame finale con la prevista discussione della tesi dal titolo: Side-coupled Fabry-Pérot devices for integrated hybrid lasers.

DICHIARA

1) di essere consapevole che, ai sensi del D.P.R. n. 445 del 28.12.2000, le dichiarazioni mendaci, la falsità negli atti e l'uso di atti falsi sono puniti ai sensi del codice penale e delle Leggi speciali in materia, e che nel caso ricorressero dette ipotesi, decade fin dall'inizio e senza necessità di nessuna formalità dai benefici conseguenti al provvedimento emanato sulla base di tali dichiarazioni;
2) di essere iscritto al Corso di Dottorato di ricerca in Industria 4.0 (Industry 4.0), ciclo XXXVIII, corso attivato ai sensi del "*Regolamento dei Corsi di Dottorato di ricerca del Politecnico di Bari*", emanato con D.R. n.286 del 01.07.2013;
3) di essere pienamente a conoscenza delle disposizioni contenute nel predetto Regolamento in merito alla procedura di deposito, pubblicazione e autoarchiviazione della tesi di dottorato nell'Archivio Istituzionale ad accesso aperto alla letteratura scientifica;
4) di essere consapevole che attraverso l'autoarchiviazione delle tesi nell'Archivio Istituzionale ad accesso aperto alla letteratura scientifica del Politecnico di Bari (IRIS-POLIBA), l'Ateneo archivierà e renderà consultabile in rete (nel rispetto della Policy di Ateneo di cui al D.R. 642 del 13.11.2015) il testo completo della tesi di dottorato, fatta salva la possibilità di sottoscrizione di apposite licenze per le relative condizioni di utilizzo (di cui al sito http://www.creativecommons.it/Licenze), e fatte salve, altresì, le eventuali esigenze di "embargo", legate a strette considerazioni sulla tutelabilità e sfruttamento industriale/commerciale dei contenuti della tesi, da rappresentarsi mediante compilazione e sottoscrizione del modulo in calce (Richiesta di embargo);
5) che la tesi da depositare in IRIS-POLIBA, in formato digitale (PDF/A) sarà del tutto identica a quelle **consegnate**/inviate/da inviarsi ai componenti della commissione per l'esame finale e a qualsiasi altra copia depositata presso gli Uffici del Politecnico di Bari in forma cartacea o digitale, ovvero a quella da discutere in sede di esame finale, a quella da depositare, a cura dell'Ateneo, presso le Biblioteche Nazionali Centrali di Roma e Firenze e presso tutti gli Uffici competenti per legge al momento del deposito stesso, e che di conseguenza va esclusa qualsiasi responsabilità del Politecnico di Bari per quanto riguarda eventuali errori, imprecisioni o omissioni nei contenuti della tesi;
6) che il contenuto e l'organizzazione della tesi è opera originale realizzata dal sottoscritto e non compromette in alcun modo i diritti di terzi, ivi compresi quelli relativi alla sicurezza dei dati personali; che pertanto il Politecnico di Bari ed i suoi funzionari sono in ogni caso esenti da responsabilità di qualsivoglia natura: civile, amministrativa e penale e saranno dal sottoscritto tenuti indenni da qualsiasi richiesta o rivendicazione da parte di terzi;
7) che il contenuto della tesi non infrange in alcun modo il diritto d'Autore né gli obblighi connessi alla salvaguardia di diritti morali od economici di altri autori o di altri aventi diritto, sia per testi, immagini, foto, tabelle, o altre parti di cui la tesi è composta.

Luogo e data: Cork, Irlanda, 21/06/2026 Firma Davide Monopoli ______________________

Il/La sottoscritto, con l'autoarchiviazione della propria tesi di dottorato nell'Archivio Istituzionale ad accesso aperto del Politecnico di Bari (POLIBA-IRIS), pur mantenendo su di essa tutti i diritti d'autore, morali ed economici, ai sensi della normativa vigente (Legge 633/1941 e ss.mm.ii.),

CONCEDE

- al Politecnico di Bari il permesso di trasferire l'opera su qualsiasi supporto e di convertirla in qualsiasi formato al fine di una corretta conservazione nel tempo. Il Politecnico di Bari garantisce che non verrà effettuata alcuna modifica al contenuto e alla struttura dell'opera.
- al Politecnico di Bari la possibilità di riprodurre l'opera in più di una copia per fini di sicurezza, back-up e conservazione.

Luogo e data: Cork, Irlanda, 21/06/2026 Firma Davide Monopoli ______________________

Politecnico di Bari

MTU
Ollscoil Teicneolaíochta na Mumhan
Munster Technological University

DECLARATION

This thesis is entirely the candidate's own work, except where otherwise accredited.

This thesis has not been submitted for an award in any other institution.

Author’s signature: ______________________
Davide Monopoli

Supervisor’s signature: ______________________
Prof. Giovanna Calò

Supervisor’s signature: ______________________
Dr. William Whelan-Curtin (Liam O’Faolain)

Supervisor’s signature: ______________________
Prof. Antonella D’Orazio

Supervisor’s signature: ______________________
Dr. Ganga Rao Chinna Devarapu

I hope I've been "smart enough",
just like you always encouraged me to be.
This thesis is dedicated to Prof. Marco Grande, who gave me the opportunity to start a new challenge four years ago.
He was a generous and warm soul.
In a scientific world that is not always empathetic, he will be always remembered first for his passion and humanity,
as well as for the remarkable scientist he was.

Table of Contents

Acknowledgements

I would like to begin by expressing my deepest gratitude to my supervisors, Prof. Marco Grande and Dr. William Whelan-Curtin, who believed in me from the very beginning of my journey, starting from my master's thesis and continuing throughout my PhD. Marco, I still vividly remember the day of my master's graduation. While everyone else was ready to celebrate the end of that chapter, we found ourselves immersed in a conversation about a potential PhD proposal, even keeping others waiting. That moment, in hindsight, marked the true beginning of this path. I chose to pursue a PhD because I trusted you completely. Your enthusiasm and passion for research were genuinely contagious and resonated deeply with my own growing interest in photonics. That shared passion became the foundation of this entire journey. I also cherish the many moments we shared exchanging ideas, not only in the lab, but especially during the drives back home. Those conversations often went beyond research; we spoke about life. I remember asking you more than once how you managed to balance everything, projects, responsibilities, life itself. Most of the time, your answer was simply a smile. Over time, I came to understand that when you truly care about something, when you put passion and love into it, you do not look back, you simply do your best, every day. I am grateful that, even now, there is still a way to stay connected, also through Daniele. It gives me the feeling that this journey has not truly ended but continues in a different shape but still deep one.

I would also like to thank you, Dr. Willliam Whelan-Curtin. From the very first months, I remember how you would often describe me as "expert" in design or in specific tasks. I never truly felt like an expert but hearing that from you meant a great deal and gave me confidence along the way. Thank you for your guidance throughout these years, both in person and remotely. I always felt your mentorship and support, even in the early stages when results were still far away. What I value even more is the personal relationship and trust we built over time, which goes beyond a purely scientific collaboration. There were times when my passion for photonics completely took over, pushing me to face high expectations, uncertainties about the future, and my own tendency to be a bit pessimistic, often focusing on potential drawbacks before the positives. At times, this pressure weighed on me, but you were always there with a positive attitude, offering support and encouragement. P.S.: Will, sounds good now that the thesis has ended eh!

Thank you very much, Prof. Calò. Joining this path midway, during such a demanding and chaotic period, was not easy, but from the very first day I felt a good connection, something I truly valued. I appreciated your directness and clarity in guiding me when I needed a more structured approach, as well as your ability to see things from my perspective and believe in our work even before results came. I'm genuinely glad you were part of what we achieved, and I will always value exchanging ideas with you.

In conclusion, I would like to thank all my supervisors for their support during the revision of this thesis, and especially for navigating the countless documents we had to handle—quite a challenge, but we made it.

In particular, I am grateful to Dr. G.C.R. Devarapu for his essential support, often acting as a bridge between me and the larger collaborative projects. I did my best to keep you updated on the progress, and I am glad that what started as preliminary individual results grew into something more significant. Thank you also for your thoughtful messages when they were most needed, they meant a lot to me.

The experience in the Netherlands gave me a lot, especially on a personal level. My time at ESTEC and at Leiden (Anton, you were right about the place and the beer) was truly important: I met many people, and after two years, I still keep strong connections. The Shed cannot really be described, but it was the best environment I could have found during that period of my life. I was working for three countries at the time, so the stress was intense, but I still carry with me many important memories from those years. Of course, I feel nostalgic after leaving, but I am sure we will meet again somewhere. Martin, Riccardo, and Simone, we shared wonderful times together, and I promise this will continue, because our friendship means a lot to me. A big thanks to the TEC-ESC section at ESA–ESTEC for giving me the chance to spend a year in such a motivating environment. A special thank-you to Alberto Mengali and Angelo Altamura: even though you were always busy, you were more present and supportive than many others. And of course I'll never forget the non-stop "farewell" celebrations when I was leaving ESA, everyone so happy I was finally going away, ahah. Un abbraccio, e ci sentiamo eh, per scherzare un po' come sempre. Porto io il Limoncellow.

I want to thank my family, including my dog Kali, the cutest of them all, for their incredible patience with me. It is not easy to deal with me during the stressful period of writing a thesis, and I know it has not been easy to miss many events and birthdays in Italy over these years while I was mostly abroad. But for you, the important thing was that I could achieve my ambitions, and that is the best support I could have received. I still remember how you celebrated my two published papers even more than I did, with a surprise, even though I was, as usual, underestimating them. And now I have finally started to understand how to maintain a strong bond with family and friends even from far away, something that was very difficult for me before.

To my friends from Bisceglie, Antonio, Fulvio, and Giovanna: although I was physically in Bisceglie, we did not spend much time together in these last six months, but even from abroad you remained an important support for me. You also came to Ireland, and we shared wonderful, windy days in Cork, almost getting lost in Kinsale and even hopping into random cars to reach the city center. It is, and will always be, a long-lasting and important friendship.

A special message is dedicated to my grandfather Mauro, we were scared a lot over the last months for what it happened, we couldn't stay without the big stone of the family, and I couldn't think of stopping our deep conversations, especially in this period. I am happy that you will be able to celebrate with me this graduation now, mai abbattersi… come dici tu.

This final long paragraph is now because I would like to thank the nPEG and CAPPA groups, at Polytechnic University of Bari and MTU, not only as research entities but for the people I met, and I spent time in these years.
Carlitas, from the very first moment, even before you had officially started your PhD, I already saw you as a colleague. And when you finally began, we could at last complain together, which was honestly very important, ahah. Jokes aside, what I value most is not just the work we did together, but the conversations and the time we shared. I think we understood each other from the beginning, we could joke about our flaws, but at the same time we were always there to support each other in difficult moments. I'm sure this friendship will continue, even if I disappear sometimes.
Gionni and Fransisca, thank you for sharing so many light and enjoyable moments during our breaks in Bari—between coffees at Monocle and video calls while each of us was somewhere around the world. I know I haven't been very present, especially recently, but the trips we did together, also with Carla, were amazing (even if I "lost a leg" in Paris), and we will definitely do them again! Fransisca, you were right, we should have had more "fit" lunches at Poliba, but I skipped them way too often; you should be really proud of what you did in France, I think they want you back, eh… Gionni, keep going like this in Cork; you've become an important part of the group, and it was really nice, during my time there, to share those moments together.
Ajmal, I remember the first days in Bari when we could talk, have coffee, and just run a few simulations and be satisfied with that ahah. Then we took on more and more responsibilities, and I was happy that we could share that process also in Cork. You were always worried not to forget the happy moments: having lunch together in your castle in Cork (or home, it's the same eh) and the caterpillar cakes. Ubitha, thanks for your kindness as well; wherever you are, you never complain and you always push yourself to take on new challenges, and that is great.
Artem, I don't remember how many times I complained to you about my problems ahah. You generally replied in a very Russian way, but deep down I know that you cared about me and I could see it from small but important gestures. Over these years I've got to know you a little bit, and I hope you will have more and more chill periods; you really deserve them after these hard years.
Ehi Nico, I think it really takes some patience to deal with me, especially when I'm working, as you've probably noticed. I was happy to share hours in the lab with someone, which in previous years was rare for me, and it definitely made the time a bit less hard and stressful. We have different rhythms in our lives, but it was nice to share so many personal moments over this year as well. P.S., please there is the need to update your music playlist eh.
Hallo Gio, I hope your "exotic" American life will give you many happy moments, because I've rarely seen someone who deserves a bit of quietness as much as you do. Usually, the first impression I give people is not the best, but when I spent time with you in Cork (the *frasche* dream), for the first time I felt truly understood, and the friendship we've built over these years was, and still is, very important to me. In some ways we are very similar, including our Beamish addiction.
Gabri, leave the postdoc and become an artist travelling around the world… you'll get more money, but mostly more bracelets for your collection! Thank you for the important moments we shared in Cork, especially in the last period; even the usual ugly Sundays were a lot less ugly with you around.
Then there is Hadi, my adopted father, haha. From the very beginning, I felt comfortable working with you, exchanging ideas, and even giving you assistance to score amazing goals when playing football. I never saw a difference between PhD and postdoc, because you are so humble and genuine, and that is a truly great quality.
Ciao Cian, you can become the first successful scientist who is also a successful powerlifter: remember to use that strength when facing two or three reviewers who don't want to accept the paper, haha. By now, you're basically Italian, aren't you? Diego, daje eh…your craziness alternating with your super-quiet life is shaking all of Cork. Just be careful when you dance, eh… otherwise you'll have to escape to Mexico!
Salam, Fratello, Mexican with the Mexican, Italian with the Italian, Salam with everyone. Thank you for all the funny moments we shared, for all the nonsense we said together, and for the good laughs that always made everything lighter. Your mix of deep, poetic side and joking spirit is something truly rare and hard to find.
Ashik, you are the only student I have tried to support because, when I met you, I saw in you some of the same qualities I had when I started my first experience more than four years ago. You are genuine, but you need to trust yourself more: everyone makes mistakes, and what matters most is how you react and explain your effort. In this environment, it is important to claim what you deserve… you have already done great, trust me.
Finally, I would like to acknowledge all my colleagues from MTU for their wonderful collaboration, for their advice and kindness (sorry but especially the panda-based kindness of Ailbhe (Alva/Alfa/Arva)), and the colleagues and friends in Tyndall where I spent countless hours over the past year. I met many great experts and kind people who helped me take a break from the harsh and busy times. To the Italian group at Tyndall, thank you for letting me show my playful (per non dire alter parole eh) side during coffees, lunches, and social events.
And… Sorry but the thesis is super long I cannot overcome the two pages…!

List of abbreviations

Abbreviations	*Description*
AlN	Aluminum nitride
AlInGaAs	aluminum indium gallium arsenide
AR	anti-reflection
ASE	amplified spontaneous emission
AWB	Adhesive wafer bonding
BCB	benzocyclobutene
BOX	dioxide buried oxide
BSL	balanced Sagnac loop
BW	bandwidth
CAPPA	Centre for Advanced Photonics & Process Analysis
CCW	counterclockwise
CIP	Centre for Integrated Photonics
CMOS	Complementary Metal–Oxide–Semiconductor
CMP	chemical mechanical polishing
CMT	coupled mode theory
COC	chip on carrier
CRR	coupled ring resonator
CW	clockwise
CWML	continuous wave mode locking
DBR	distributed Bragg reflector
DC	duty cycle
DCS	dual comb spectroscopy
DFB	distributed-feedback
DFWM	dissipative four wave mixing
DI	de-ionized
DUV	deep ultraviolet
DWDM	dense wavelength division multiplexing
EBL	electron beam lithography
ECL	external-cavity lasers
EDWA	erbium doped waveguide amplifier
EO	electro-optic
ER	extinction ratio
ERI	effective refractive index
ESA	electrical spectrum analyzer
FC	fiber coupler
FCA	free carrier absorption
FCD	free carrier dispersion
FDE	finite difference eigenmode
FDTD	finite-difference time domain
FFT	fast Fourier transform
FIA	flow injection analysis
FL	fiber laser
FP	Fabry-Pérot
FSO	Free space optical
FSR	free spectral range
FWHM	full width at half maximum

FWM	Four-wave mixing
GaAs	Gallium arsenide
GDD	group delay dispersion
GDS	Graphic Design System
GNSS	Global Navigation Satellite Systems
GVD	group velocity dispersion
HARPS	High Accuracy Radial velocity Planet Searcher
HECL	hybrid external-cavity laser
HPF	Habitable-zone Planet Finder
HPLC	high performance liquid chromatography
HR	high-reflectivity
HSQ	hydrogen silsesquioxane
ICP	inductively coupled plasma
InP	Indium Phosphide
IPA	isopropyl alcohol
LEO	low Earth orbit
LiDAR	light detection and ranging
LN	lithium niobate
LO	local oscillator
LOD	limit of detection
MI	modulation instability
MIR	multimode interference reflector
MLL	mode-locked laser
MMI	based multimode interferometer
MPW	multi project wafer
MQW	multiple quantum well
MWL	multi-wavelength laser
MZM	Mach Zehnder modulator
NIR	near infrared
NPEG	NanoPhotonics and Electromagnetics Group
NPR	nonlinear polarization rotation
OFC	Optical frequency comb
OSA	optical spectrum analyzer
PAT	pointing, acquisition, and tracking
PC	polarization controller
PDL	polarization dependent loss
PDMS	polydimethylsiloxane
PECVD	plasma enhanced chemical vapor deposition
PIC	photonic integrated circuit
PM	photonic molecule
PSA	pressure sensitive adhesive
PSD	power spectral density
PWB	photonic wire bonding
PZT	piezoelectric
QD	quantum dot
QW	quantum well
QSML	Q-switched mode locking
RF	radiofrequency
RI	refractive index
RMS	root mean square
RSOA	reflective semiconductor optical amplifier

RV	radial velocity
SA	saturable absorber
SC	side coupled
SC-FP	side-coupled FP
SEM	scanning electron microscopy
Si	silicon
SiN	silicon nitride
SMF	single mode fiber
SMSR	side mode suppression ratio
SOA	semiconductor optical amplifier
SOI	silicon on insulator
SOTA	state-of-the-art
SPM	self-phase modulation
SWG	subwavelength grating
SWL	single-wavelength laser
TBIRD	TeraByte InfraRed Delivery
TCMT	Temporal coupled mode theory
TE	transverse electric
TEC	thermoelectric cooler
TFLN	thin film lithium niobate
THG	Third harmonic generation
TM	transverse magnetic
TMM	Transfer Matrix Method
TOC	thermo-optic coefficient
TOD	third order dispersion
TP	transfer printing
TPA	two photon absorption
UBSL	unbalanced Sagnac type loop
VarFDTD	variational finite-difference time-domain
WDM	wavelength division multiplexing
XGM	cross gain modulation
XPM	cross phase modulation

Abstract

The growing demand for advanced photonic integrated circuits (PICs) and technological platforms that ensure high performance in telecommunications, sensing, metrology, and space applications has driven the development of laser sources with improved coherence, spectral purity, compactness, and integration density. Conventional monolithic semiconductor lasers, while a mature technology, face fundamental limitations in linewidth, tunability, and phase noise that prevent them from meeting the requirements of next-generation systems. These requirements have motivated a major shift toward hybrid external-cavity laser (HECL) architectures, in which an active gain element, typically a semiconductor optical amplifier (SOA), reflective SOA (RSOA), or erbium-doped waveguide amplifier (EDWA), is coupled to a passive PIC integrating reflectors and other optical components. By combining the high optical gain of III–V semiconductor materials with the ultra-low propagation losses and mature fabrication techniques of silicon on insulator (SOI) or silicon nitride (SiN) waveguide platforms, hybrid lasers can achieve narrow linewidths, low phase noise, broad wavelength tunability, and chip-scale footprints.

This thesis, entitled "Side-coupled Fabry–Pérot devices for integrated hybrid lasers", aims to develop and experimentally validate a new class of wavelength-selective resonant reflectors based on SiN integrated side-coupled Fabry–Pérot (SC-FP) architectures and to integrate them with active gain elements to realize high-performance HECLs.

The SC-FP device, consisting of a DBR-bounded (Distributed Bragg Reflector – bounded) cavity evanescently coupled to a bus waveguide, is designed, fabricated, and characterized as a tunable high-Q resonant reflector supporting both single- and multi-wavelength operation in the C-band. By systematically engineering mirror reflectivity, coupling strength, cavity geometry, and grating design, this work shows that SC-FP resonators can be tailored for distinct functionalities, ranging from broad stopband operation to highly selective filters and reflectors, as well as dispersive cavities suitable for nonlinear applications. Building on this versatile platform, SC-FP structures are implemented in HECL configurations that evolve from fiber-coupled external-cavity assemblies to fully integrated heterogeneous platforms on a single PIC.

A first laser configuration combines a SiN PIC hosting the SC-FP reflector with fiber-based balanced and unbalanced Sagnac loop reflectors, together with a commercial fiber-coupled SOA. This architecture demonstrates a hybrid laser with multi-wavelength emission aligned to the SC-FP resonances, using a fiber-assisted HECL scheme with an external-cavity extending over tens of meters.

Despite longitudinal-mode competition within each lasing peak, isolating a single resonance enables coherent pulse-train generation with RF linewidths of a few kilohertz, around 3 kHz, and clear signatures of partially harmonic mode locking. Further evolution towards a more integrated hybrid laser configuration has been achieved by assessing butt-coupling between the RSOA gain and SIN passive circuit chips, in a fiber-free external-cavity and reducing the external-cavity length from meters to the millimeter scale, which enhances mechanical robustness and polarization stability while preserving spectral control. This two-chip butt-coupled HECL exhibits single-wavelength operation with side-mode suppression ratios (SMSRs) above 45 dB, and preliminary heterodyne measurements indicating sub-100 kHz optical linewidths, when a systematic analysis of different RSOAs and SC-FPs has been conducted.

The constraints of the latter configuration, particularly in terms of mechanical robustness, polarization control, and alignment stability during multi-chip handling, led to the realization of a highly compact HECL architecture by transfer printing the RSOA directly onto the SiN PIC silicon substrate. While posing a more challenging single-chip integration route in terms of thermal and alignment control, it offers the most stable performance and potentially higher output power, with sub-50 kHz laser linewidths, single-wavelength operation with side-mode suppression exceeding 40 dB, and preliminary on-chip output powers up to 0.6 mW.

These results consolidate SC-FP-based HECLs as scalable building blocks for compact, high-performance single- and multi-wavelength integrated laser sources for potential application as refractive-index sensors and compact optical frequency comb (OFC) for space applications.

In this framework, ultra-narrow HECL emission reports the reduction of the detection limit by about two orders of magnitude (10^{-5} RIU) compared with passive resonator-based refractive index sensors, while heterodyne-based sensing further improves it to around 10^{-7} RIU by exploiting the MHz-level beat note, well beyond the capabilities of standard spectrometric techniques and direct lasing measurements.

Multi-wavelength HECL-based OFC sources are promising for space, leveraging comb technologies already demonstrated in free-space links, atomic clocks, spectroscopy, atmospheric sensing, and astronomy. Hybrid laser platforms are well suited to space photonics because they combine high performance with reliability and size, weight, and power (SWaP) constraints, while also meeting the high-power, low-phase-noise, and frequency-stability requirements of FSO links.

Outline

The thesis is structured as step-by-step workflow for the experimental realization of a compact, fully integrated hybrid external-cavity laser (HECL) platform based on SC-FP reflectors, specifically engineered to support both single- and multi-wavelength operation for refractive-index sensing and future space applications. It is organized as follows.

Chapter 1: Introduces hybrid external-cavity laser architectures based on the combination of high-gain III-V amplifiers and low-loss passive photonic integrated circuits, starting from low-integration configurations such as fiber-assisted HECLs and butt-coupled two-chip assemblies, and progressing to fully integrated platforms enabled by micro-transfer printing and heterogeneous bonding techniques, all supported by representative state-of-the-art applications. It reviews the main gain media, passive photonic platforms, and feedback elements, spanning from broadband to wavelength-selective reflectors, as well as the widely established optical coupling mechanisms. The chapter also defines the key laser performance metrics with emphasis on noise mechanisms and intrinsic versus effective linewidth and concludes by highlighting representative state-of-the-art multi-wavelength HECL demonstrations, from mode-locked lasers to optical frequency comb sources.

Chapter 2: Develops the theoretical framework employed throughout the thesis to describe the underlying physical mechanisms and key parameters of DBR structures and FP resonators. It presents a modified transfer-matrix method to model the DBR response for uniform and apodized gratings, enabling extraction of its phase response.
Thus, accurate prediction of the free spectral range of DBR-based FP cavities is enabled, providing design formulas used in the following chapters.
The final part of the chapter presents a rate-equation description and the lasing conditions of a three-mirror external-cavity lasers, extending the analysis to the SC-FP reflector configuration, models its response using temporal coupled-mode theory, and outlines the main Kerr-driven nonlinear effects relevant to this resonator platform.

Chapter 3: Demonstrates through design, fabrication, and characterization, a novel SiN side-coupled Fabry–Pérot reflector with DBR mirrors (Fig. O1), featuring dispersion-engineered apodized gratings and systematic studies of cavity and coupling geometry that yield practical guidelines for tailoring resonance spacing, Q-factor, and reflectivity.

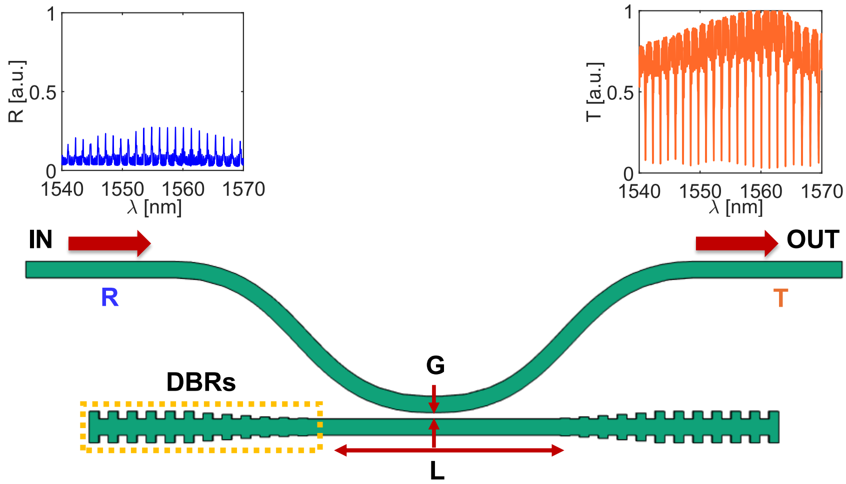

Fig. O1: Schematic of the side-coupled FP resonator: details on the main design parameters, the reflection and transmission response of the structure.

Chapter 4: Implements the fiber-assisted HECL platform, in which the proposed SC-FP reflector and a Sagnac-based loop reflector form a long external-cavity using a commercial SOA and fiber-coupled connections (Fig. O2). It produces SC-FP mode-aligned multi-wavelength emission and partially harmonic mode-locked pulse trains among the external-cavity longitudinal modes, suitable for low-phase-noise microwave generation and other advanced applications.

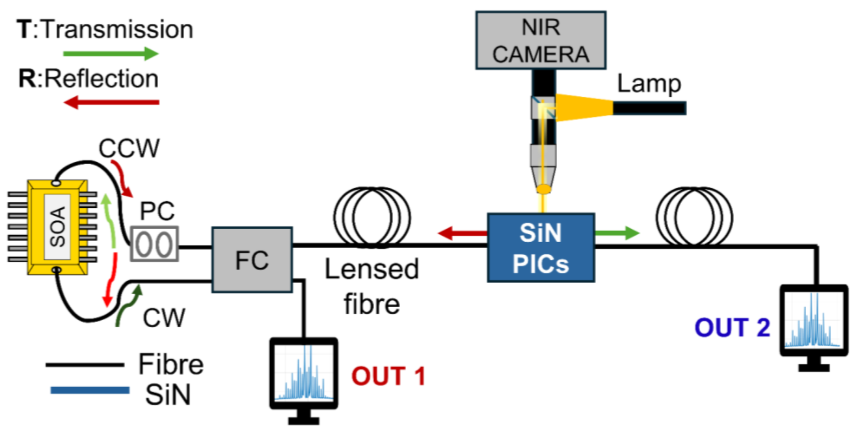

Fig. O2: Fiber-assisted HECL architecture: schematic of the experimental setup.

Chapter 5: Advances toward compact, fiber-free HECLs by implementing butt-coupling between two chips: the RSOA gain and the SiN PIC (Fig. O3(top)). For different gain chips and SC-FPs design are experimentally retrieved the performance of the HECLs in terms of output power, spectral response, and linewidth. It then shows the realized transfer printed HECLs in which RSOAs and SiN SC-FP reflectors (Fig. O3(bottom)) are co-integrated on a common substrate via polymer-based spot-size converters and optimized alignment. The laser exhibits sub-50 kHz linewidths with high SMSR and paving the way for fully reconfigurable single and multi-wavelength sources for WDM and sensing.

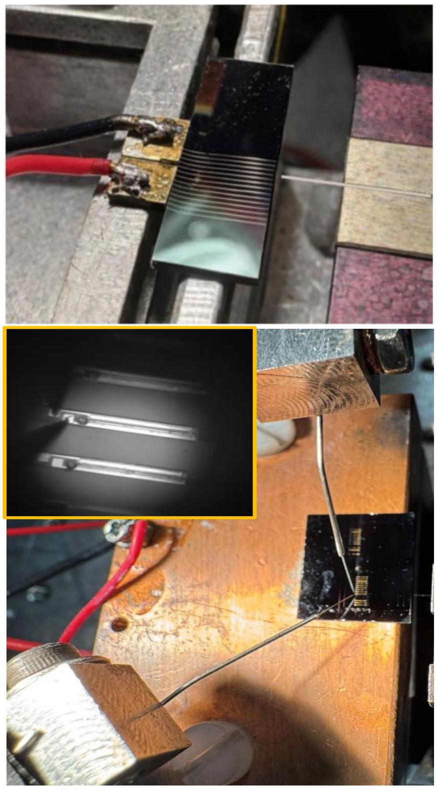

Fig. O3: Fiber-free HECL based on butt-coupling between gain chip and SiN PIC. (top) Two-chips HECL, (bottom) transfer printed HECL.

Chapter 6: Explores SC-FP-based refractive index sensing applications. It reports the sensor performance in terms of sensitivity and limit of detection extracted from simple passive resonators, SC-FP based photonic molecule configurations, and discusses the prospects of single-wavelength SC-FP-based HECLs for liquid and gas sensing and multi-wavelength sources for high-resolution sensing and space-borne photonic systems.

Chapter 1: Hybrid external-cavity lasers

Silicon photonic integrated circuits (PICs) exploit the high refractive index contrast between silicon (Si) and silicon dioxide (SiO_2) to achieve strong optical confinement and compact waveguide geometries. Over the past two decades, this has positioned the silicon-on-insulator (SOI) platform as the flagship technology for large-scale silicon photonics, reaching a high-level of maturity with a broad ecosystem of standalone, off-the-shelf optical and optoelectronic components. These capabilities support applications ranging from short-reach interconnects to high-capacity coherent communication systems [1-3]. However, silicon’s indirect bandgap prohibits efficient optical gain, so an electrically pumped continuous-wave laser cannot be realized monolithically in silicon alone. This fundamental limitation has driven the development of a spectrum of hybrid laser strategies that bring III–V gain media into the low-loss silicon photonics platform. Among the *hybrid laser* architectures developed in this thesis, the classification adopted here is based on the degree of integration, following the reviews in [1], and [2].

The most straightforward solutions historically have relied on external-cavity lasers (ECLs) that incorporate gain section fiber-coupled to a PIC, as shown in Fig. 1.1(a), often in combination with free-space optic components and an optical isolator to mitigate back-reflections. While robust, such schemes are inherently bulky, costly, and difficult to scale to complex or high-volume (long external cavities) systems. In addition, they can exhibit significant polarization-dependent loss (PDL), arising from the mismatch between the generally unknown and unstable state of polarization in the single-mode fiber and the fundamental mode supported by the PIC waveguide [4]. This necessitates the implementation of polarization management strategies to ensure stable and efficient fiber-to-PIC coupling.

More advanced hybrid external-cavity laser (HECL) integration approaches co-package separate III–V and silicon photonic chips in so-called two-chip butt-coupled HECL (or hybrid 2.5D in [1]) architectures. As depicted in Fig. 1.1(b), the two chips are separated by an air gap. In this framework, fully or partially fabricated III–V gain chips, are assembled alongside a silicon photonic die and coupled via in-plane butt-coupling (also named edge-coupling) and photonic wire bonding (PWB) techniques. This route allows independent optimization of each technology on its native substrate and can offer good thermal management, it requires high-precision assembly, remains constrained by tight package-level alignment tolerances, and demands careful mode matching to optimize optical coupling between the two chips.

Pushing integration one step further leads to 3D hybrid schemes [1], such as flip-chip bonding or micro-transfer printing (μ-TP), in which compact III–V gain elements are integrated directly onto the silicon photonic die (Fig. 1(c)). In μ-TP, pre-fabricated III–V coupons containing the active gain region are released from the donor wafer and precisely placed onto the target photonic circuit, enabling localized integration only where optical gain is required. This integration process will be discussed in more detail later. In this regard, μ-TP can be treated as bridging technology between classical hybrid assembly and full wafer-scale *heterogeneous* integration, as defined in [1],[2]. Specifically, although transfer printing shares many process-integration advantages with heterogeneous III–V on Si technologies, avoiding handling of multi-chips, they still employ etched and pre-defined gain elements (micro-scale devices that are "picked and placed" onto the target wafer, preserving some of the flexibility of hybrid approaches in terms of device selection and pre-testing) rather than unprocessed dies.

As a result, μ-TP preserves part of the flexibility of hybrid approaches in terms of device selection, pre-testing, and cavity architecture, while remaining within the broader heterogeneous integration family from a fabrication perspective; for this reason, it is included in the thesis under this broader classification. In these architectures, the III–V gain medium is placed in close proximity to the underlying silicon or silicon nitride waveguides, enabling strong optical coupling through either butt coupling or evanescent coupling, supporting realization of high-Q external cavities that can reduce laser linewidth to the hertz regime.

These hybrid techniques naturally support multi-wavelength operation and flexible lasing wavelength selection, but as the number of wavelengths and on-chip lasers grows, questions remain about their ultimate scalability in terms of assembly throughput, yield, and cost for very large wavelength division multiplexing (WDM) photonic systems.

By contrast, *heterogeneous laser integration,* refers to the transfer of an unprocessed thin film of a III–V heterostructure onto PIC core platform through wafer- or die-level bonding [2],[3],[5]. According to the bonding mechanism, and excluding metallic bonding from this discussion, such processes can be broadly classified as either covalent/molecular bonding or adhesive bonding.

In this approach, unpatterned III–V dies or wafers are bonded directly onto pre-patterned passive photonic wafers, as shown in Fig. 1.1 (d), and subsequently processed lithographically in situ, following standard planar PIC fabrication workflows to define the active devices. According to the fabrication process considered in the bonding technique, can be distinguished (i) covalent wafer bonding and (ii) adhesive wafer bonding. The last case is schematically drawn with a planar benzocyclobutene (BCB) layer for simplicity; in practice, however, the spin-coated or spray-coated BCB will not be perfectly planar over the patterned regions.

This sequence means that all III–V device patterning is performed directly on large-diameter silicon wafers, leveraging mature CMOS (Complementary Metal–Oxide–Semiconductor) toolsets, fine lithographic resolution, and wafer-scale process control. Compared to approaches where III–V devices are first fabricated on smaller native substrates and then assembled onto silicon; the heterogeneous route avoids a separate chip-by-chip assembly step, supports wafer-scale integration, and relaxes alignment constraints because the optical interfaces are defined lithographically rather than by submicron placement.

In the resulting heterogeneous III–V-on-silicon structures, the optical mode in the active region is shared between the III–V and the underlying silicon waveguide, and the confinement can be engineered by tailoring the silicon waveguide geometry. This enables precise modal control for efficient gain, low-loss coupling between active and passive sections, and broadband, low-reflection transitions. In particular, coupling is achieved through evanescent, adiabatic mode transfer between the bonded III–V gain region and the underlying waveguide core, making the coupling section an integral part of the on-chip cavity design, while any residual butt-coupling interfaces (e.g. fiber I/O) play only a complementary packaging role.

The III–V stack supplies the direct-bandgap gain necessary for efficient electrically pumped lasing, while the silicon (or silicon nitride (SiN)) waveguide layer provides low-loss routing, compact passive functionality, and access to industrial CMOS infrastructure with high yield and small feature sizes. Heterogeneous integration does not merely represent a packaging solution but a device-level co-fabrication strategy that supports volume scaling and complex photonic integration, and it underpins the current generation of Si/III–V hybrid lasers that are now entering commercial deployment.

In this framework, the common thread throughout the thesis is the implementation of wavelength-selective resonant mirrors based on engineered side-coupled Fabry–Pérot resonators, incorporating Bragg-grating reflectors, into hybrid external-cavity lasers (HECLs). The external-cavity concept refers to a laser configuration in which the resonator cavity extends beyond the semiconductor gain section and incorporates all passive optical elements along the optical propagation path, as well as the cavity reflector.

Depending on the specific implementation, these architectures can take several forms. In this thesis, the experimental realization of hybrid lasers will be demonstrated across a progressive evolution of integration levels: from a lower-integration level **"***fiber-assisted HECL***"**, in which fiber coupling provides the connection between the gain element and the PIC resonator used as a reflector; to the **"***two-chip butt-coupled HECL***"**, corresponding to the hybrid 2.5D approach detailed above; and finally to the **"***μ-TP heterogeneous butt-coupled HECL***"**, based on a hybrid 3D architecture enabled by micro-transfer printing. This latter approach relies on advanced heterogeneous integration techniques to transfer the patterned gain element onto the same substrate as the passive resonator die. For simplicity, from this point onward in the text, we will refer to bonding-based lasers as *heterogeneous ECLs*, to keep consistency with the external-cavity architecture and the fabrication process. The following subsections decompose the external-cavity laser structure into its constituent components, examining the III–V gain solutions, the photonic platforms used to implement the resonator and other passive optical components in the PIC, and the distinct types of photonic reflector architectures.

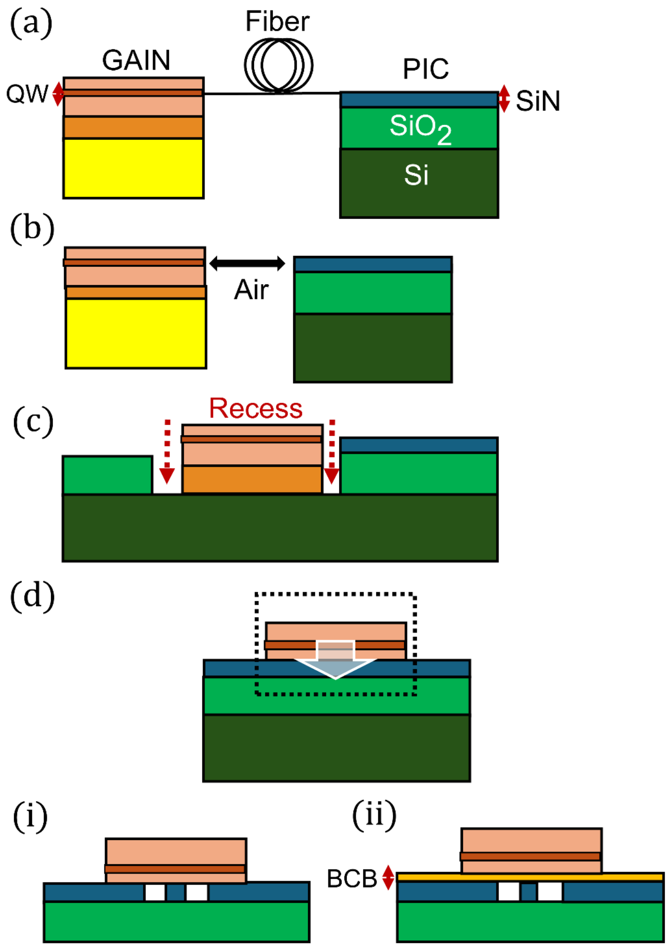

Figure 1.1: Classification of external-cavity lasers based on the coupling between gain section (in this picture the active region of the laser is indicated as a quantum well (QW)) and passive PIC: (a) fiber-assisted HECL, (b) two-chip butt-coupled HECL, (c) transfer printed HECL, and (d) bonding-based heterogeneous ECL. Among the bonding integration is distinguished: (i) covalent wafer bonding and (ii) adhesive wafer bonding.

A detailed overview of the state-of-the-art (SOTA) in the different classes of hybrid lasers and heterogeneous integrated lasers, together with the corresponding optical coupling techniques employed, is provided. This chapter further discusses the main laser performance metrics, with a specific analysis on the noise processes and the intrinsic and effective linewidth and concludes by reporting selected SOTA recent demonstrations of multi-wavelength HECLs, spanning from mode-locked lasers to optical frequency comb sources.

1.1 Gain chip materials and platforms

Gain media in hybrid and heterogeneous ECLs are primarily based on III–V compound semiconductors, whose direct bandgap enables efficient radiative recombination and stimulated emission. Optical gain is achieved when carrier injection raises the population inversion above the transparency condition, allowing stimulated emission to dominate over absorption processes [6].

Indium phosphide (InP)-based heterostructures represent the most widely adopted platform for operation in the telecom wavelength range (1.3–1.6 µm), owing to their capability to support a full set of active photonic components, including lasers, semiconductor optical amplifiers (SOAs) [7], and modulators. These materials enable large-scale photonic integration, with demonstrated circuits exceeding (10^5) components, highlighting their scalability and maturity for complex PICs [7]. In practical devices, InP-based gain sections are typically implemented using strained quantum well structures, which provide strong carrier confinement and efficient gain generation.

For hybrid-integrated gain chips, internal optical losses in III–V waveguides are a critical parameter governing laser performance. Reported values for indium arsenide (InAs) quantum dot (QD) waveguide materials lie in the range of 1–5 cm^{-1}, directly impacting the threshold gain required for lasing [8]. The threshold gain of a composite cavity is determined not only by internal loss but also by mirror reflectivity and coupling efficiency between the III–V gain region and the passive silicon waveguide. High reflectivity mirrors (up to ~90%) and efficient coupling are therefore essential to minimize threshold conditions [8].

Quantum dot gain media, particularly in Gallium arsenide- (GaAs) based systems, offer several advantages compared to quantum well structures. These include reduced transparency current density, improved temperature stability, and enhanced tolerance to optical feedback, making them well-suited for O-band operation and energy-efficient integrated lasers [6-8]. Additionally, QD-based devices exhibit lower linewidth enhancement factors and broader gain bandwidth, which are beneficial for stable single-mode operation and wavelength tunability.

From an architectural standpoint, gain elements in HECLs are commonly realized as semiconductor optical amplifiers integrated within external or extended cavities. These cavities incorporate wavelength-selective feedback elements, such as diffraction gratings or Bragg reflectors, to enforce single-frequency operation and reduce spectral linewidth compared to solitary diode lasers. The external-cavity configuration enables narrow linewidth emission, improved spectral purity, and wide tunability, while maintaining the high efficiency characteristic of semiconductor gain media.

Finally, heterogeneous integration of III–V gain materials onto silicon has emerged as a key enabling technology for scalable photonic systems. Silicon, being an indirect bandgap material, cannot efficiently generate light and therefore relies on integrated III–V gain sections to provide optical amplification and lasing functionality [2]. This approach combines the superior gain properties of III–V materials with the scalability and manufacturability of silicon photonics, forming the foundation of next-generation integrated laser platforms.

Regardless of material system, gain chips intended for HECL integration are typically structured as reflective semiconductor optical amplifiers (RSOAs), incorporating a high-reflectivity (HR) back facet and an anti-reflection (AR) coated output facet, or as mirrorless SOAs with integrated on-chip reflectors, defining the cavity reflectivity on both sides. This design flexibility enables precise engineering of lasing threshold, suppression of higher-order spatial modes and parasitic back-reflections, and optimized coupling efficiency at the III-V/passive waveguide interface for seamless hybrid or heterogeneous bonding to CMOS-compatible photonic platforms.

1.2 Passive Photonic Platforms

Passive photonic platforms constitute the foundational technological layer of PICs, enabling the guiding, routing, and spectral shaping of optical signals. Their performance is primarily governed by intrinsic material properties, including refractive index contrast, propagation loss, transparency window, nonlinear optical response, and thermal stability.

Silicon-on-insulator, silicon nitride (SiN), and silica-based technologies are among the most established CMOS-compatible photonic platforms, benefiting from mature microelectronic fabrication processes including lithography, deposition, and plasma etching, thereby enabling wafer-scale fabrication, high reproducibility, and scalable manufacturing [9-12].

Historically, SOI has been the dominant platform for integrated photonics because of the very high refractive index contrast between silicon, with $n \approx 3.48$ at wavelength 1550 nm, and silicon dioxide, with $n \approx 1.44$, which enables strong optical confinement and very compact devices with bending radii of only a few micrometers. However, silicon is limited by its bandgap, leading to strong absorption at wavelengths below approximately 1.1 μm, and is therefore mainly used in the near-infrared, especially around the 1.3 μm and 1.55 μm telecom windows. In addition, silicon exhibits two-photon absorption (TPA) at telecom wavelengths, which generates free carriers and introduces excess loss and phase perturbations, while typical SOI propagation losses are on the order of 1–2 dB/cm in standard foundry processes [9-12].

Silicon nitride has emerged as a highly attractive passive platform because it combines broad transparency, low loss, and improved thermal stability. Its transparency window extends approximately from 400 nm in the visible to about 4–4.6 μm in the mid-infrared, making it suitable not only for telecommunications but also for spectroscopy, biosensing, optical coherence tomography, ranging, and quantum photonics. Moreover, because of its large bandgap, SiN does not exhibit TPA at telecom wavelengths, allowing significantly higher optical powers to propagate without the nonlinear loss mechanisms that affect silicon waveguides.

A major advantage of SiN is its extremely low propagation loss. With optimized fabrication processes deposition, high-temperature annealing, chemical-mechanical polishing, and improved sidewall control, state-of-the-art waveguides can reach losses below 0.1 dB/m, enabling ultra-high quality factor resonators with quality factors exceeding 10^7. These losses are orders of magnitude lower than those of standard silicon waveguides and are mainly limited by surface-scattering at core-cladding interfaces and residual material absorption, for example from hydrogen-related impurities in the film [13-15]. SiN also offers superior thermal stability compared with Si. The thermo-optic coefficient of silicon is approximately $1.86 \times 10^{-4}\ \mathrm{K}^{-1}$ whereas that of SiN is about 2.45×10^{-5} [16], nearly one order of magnitude smaller, which results in reduced temperature-induced resonance shifts in filters and microring resonators (MRRs).

The refractive index is typically around $n \approx 1.98/2.0$ in the C-band wavelength range, which leads to a relatively low index contrast and weak optical mode confinement. As a consequence, larger bend radius and device footprints are required; however, the reduced index contrast also lowers sensitivity to sidewall roughness and fabrication imperfections, thereby mitigating scattering losses [14]. For these reasons, modern PICs increasingly exploit the complementary advantages of both platforms. Silicon remains highly attractive for compact active devices and electronic co-integration, whereas silicon nitride is often preferred for low-loss passive routing, high-Q resonators, broadband operation, and high-power nonlinear photonics.

1.3 Feedback elements

A convenient distinction for the passive integrated-feedback section is between broadband reflectors and wavelength-selective reflectors [17]. Broadband reflectors, such as Sagnac loop mirrors [18-20] and retroreflectors [21], are primarily designed to return a large fraction of the optical power to the gain section over a wide wavelength range. Their role is therefore mainly to provide strong cavity feedback, while the spectral selectivity of the external-cavity laser is determined by the gain medium. A second class comprises distributed wavelength-selective reflectors, including DBR-based and photonic-crystal-based structures [22]-[25]. In these devices, reflection originates from a distributed periodic perturbation rather than from a purely geometric return path. As a result, the reflection is intrinsically wavelength dependent, and both amplitude and phase of the reflected field contribute to the external-cavity behavior. In particular, the phase response of grating-based reflectors introduces a finite penetration length, which becomes an important parameter in the cavity design and will be discussed later.

A further category is that of wavelength-selective resonant reflectors, in which the reflection spectrum is defined by discrete resonances. This group includes Fabry–Pérot filters, add-drop ring resonators [26], and coupled-cavity or Vernier filters [27-30]. In these architectures, the resonant condition directly determines the feedback spectrum, so that the reflector acts simultaneously as a cavity mirror and as a spectral filter. Such devices are therefore especially attractive when narrow-linewidth emission, single-mode operation, or wavelength tunability must be implemented directly within the passive cavity. Among these solutions, ring resonators are particularly well suited to integrated platforms because of their compact footprint, high spectral selectivity, and straightforward thermal tunability. Add-drop rings can provide narrowband reflective filtering, while coupled or slightly detuned ring cavities can exploit the Vernier effect to suppress unwanted longitudinal modes and enlarge the effective free spectral range.

Fabry–Pérot-based reflectors provide an alternative resonant solution: depending on the configuration, reflection may be obtained from the output of in-line FP cavities by means of optical circulator or from the input side of side-coupled resonators [31],[32] enabling not only wavelength-selective feedback but also enhanced dispersive control of the cavity response in a compact design. These specific resonant reflector architectures will be examined in detail throughout the thesis.

1.4 SOTA of HECLs

The hybrid external-cavity laser architectures introduced at the beginning of the chapter are examined here, together with recent demonstrations and their operating principles. In accordance with the prior classification, the discussion is organized as a progression toward increasingly integrated hybrid and heterogeneous laser architectures: from conventional fiber-assisted HECL, through two-chip butt-coupled HECL, to fully integrated solutions enabled by transfer printing (hybrid 3D) and bonding (heterogeneous) configurations.

1.4.1 Fiber-assisted HECL

A first, and still highly relevant, integration approach comprises architectures in which the active gain element remains physically separate from the passive resonator chip, with the connection established through a macroscopic external-cavity interface.

In the conventional implementation, the silicon photonic integrated circuit is linked to an external laser source by an optical fiber, typically together with an optical isolator and, where needed, additional free-space beam-shaping optics [1],[4].

This configuration preserves a clear separation between the active and passive sections and offers important practical advantages: the source and PIC can be designed, tested, and optimized independently, while mature and relatively low-cost commercial solutions, such as butterfly-packaged fiber-coupled gain devices, can be readily employed. Its main limitations arise from the fiber interface itself, which can increase sensitivity to mechanical perturbations, alignment drift, and polarization fluctuations, all of which are particularly critical in narrow-linewidth or environmentally sensitive external-cavity systems.

A further step toward tighter integration is obtained when the optical path is only partially fiber-based and the final connection between the gain chip and the resonator chip is made through a short free-space section. In this case, coupling can be implemented using lensed fibers, micro-optical elements, or dedicated alignment structures. Relative to a fully fiber-coupled arrangement, this solution reduces both footprint and cavity length, while retaining the flexibility associated with the use of a discrete, pre-characterized gain element.

Among the well-established in this framework, *Jyu et al.* in [33] demonstrated a 250-GHz passive harmonic mode-locked Er-doped fiber laser based on dissipative four-wave mixing in a cavity incorporating a silicon microring resonator as an intracavity comb filter. The setup included an EDFA, a 250-m high-nonlinearity fiber section, grating-coupled fiber-to-chip interfaces, and polarization control elements to ensure stable operation. The passive mode-locked laser achieved pulse trains with sub-picosecond pulse durations, reaching 1.48 ps for a 2-nm optical bandwidth and 875 fs for a 6-nm bandwidth.

Liles et al. [34] demonstrated a fiber-based external-cavity laser in which a fiber-pigtailed SOA was coupled by free space into a silicon photonic crystal resonator acting as a wavelength-selective mirror. The cavity was dominated by fiber patch cords, and the lasing wavelength was lithographically controlled by tuning the photonic crystal geometry with sub-nanometer precision. The device lased at 1547.32 nm, with milliwatt-level output power, a 23.6 mA threshold, and side-mode suppression above 25 dB.

Raja et al. [35] demonstrated a 99-GHz soliton microcomb driven by a compact hybrid semiconductor laser, in which a gain chip is combined with a fiber Bragg grating and coupled through optical fibers to a high-Q SiN microresonator chip. The architecture remains fiber-based because both the external-cavity wavelength selection and the chip-to-laser connection rely on fiber components, while the SiN device provides the nonlinear soliton-generating stage. The semiconductor laser itself is butterfly-packaged and consists of a gain chip, an FBG, and an external fiber cavity. The system produced a single-soliton state with 131 fs pulses, 19 nm bandwidth, and Lorentzian/Gaussian beat note linewidths of 9 kHz and 61 kHz, respectively, and the soliton state could be maintained for more than one hour without active temperature stabilization.

1.4.2 Two-chip butt-coupled HECL

According to the specific PIC platform, the passive structures implemented, and the type of gain chip employed, different configurations of two-chip butt-coupled HECLs can be distinguished. In this section, the discussion focuses primarily on the works carried out by CHILAS [36] and LIONIX [37], together with the demonstrations from the Kippenberg group, which represent an exemplary reference for this hybrid laser approach.

CHILAS has commercialized a hybrid external-cavity laser based on a reflective InP gain chip butt-coupled to a low-loss SiN feedback circuit fabricated on LioniX's TriPleX platform. The SiN photonic integrated circuit incorporates a phase section and a Vernier filter formed by coupled MRRs with slightly mismatched free spectral ranges, enabling wide C-band tuning over more than 100 nm, sub-kHz linewidth operation, and output powers exceeding 30 mW, with 100 mW under development, all within a 14-pin butterfly package. The schematic of the HECL architecture and its packaged integration is reported in Fig. 1.2(a). Two product families are built on this same SiN module: ATLAS, designed for quasi-static narrow-linewidth operation across multiple bands, and COMET, intended for rapidly swept-source applications such as optical coherence tomography and spectroscopy. LioniX provides the ultra-low-loss SiN PIC technology underlying this architecture, including high-Q ring resonators, dispersion engineering, and thermal phase tuning, thereby enabling both high coherence and fast wavelength sweeping. In particular, Ref. [28] describes the basic operating principle of the hybrid butt-coupled laser architecture. In this configuration, a single InP gain chip, operated as an RSOA, is butt-coupled to a low-loss SiN/Si feedback circuit on the TriPleX platform, thereby forming an external-cavity characterized by long photon lifetime, low propagation loss, and high spectral selectivity. The SiN PIC integrates thermally tunable phase sections, a Mach–Zehnder output coupler, and a two-ring Vernier filter for wavelength selection and linewidth narrowing. The wide bandgap of the TriPleX platform suppresses nonlinear absorption effects that limit silicon-based feedback circuits, while the integrated heaters provide more than 2π phase tuning, enabling continuous, mode-hop-free tuning across the gain bandwidth. Experimentally, this architecture has achieved fiber-coupled output powers up to 24 mW, a tuning range of approximately 120 nm around 1.55 μm, side-mode suppression ratios up to 63 dB, and an intrinsic linewidth on the order of 2.2 kHz. The same configuration has been further extended through design optimization, operational variants, and more complex feedback circuits, targeting specific laser requirements such as mode-hop-free operation and reduced intrinsic linewidth, while preserving a compact hybrid laser architecture.

The first limitation arises because the continuous tuning span in the phase-variable section is FSR-limited by the long external-cavity, leading to mode hops after wavelength shifts of only a few hundredths of a nanometer. To achieve mode-hop-free operation, [38] extends the same InP–SiN cavity architecture by adding coordinated thermal tuning of both microrings together with the phase section, so that the Vernier passband continuously follows the lasing mode. This increases the mode-hop-free tuning range from approximately 0.034 nm to 0.22 nm, corresponding to about 28 GHz, without compromising the intrinsic linewidth or output power reported previously.

A second operational mode employs the same architecture as in Fig. 1(a) but incorporates dual-loop electronic stabilization [39]: short-term locking to an optical frequency discriminator and long-term locking to an acetylene absorption line. This reduces the Allan deviation by up to two orders of magnitude and suppresses long-term frequency drift from hundreds of MHz to below ~10 MHz over several days, while preserving the kilohertz-level intrinsic linewidth.

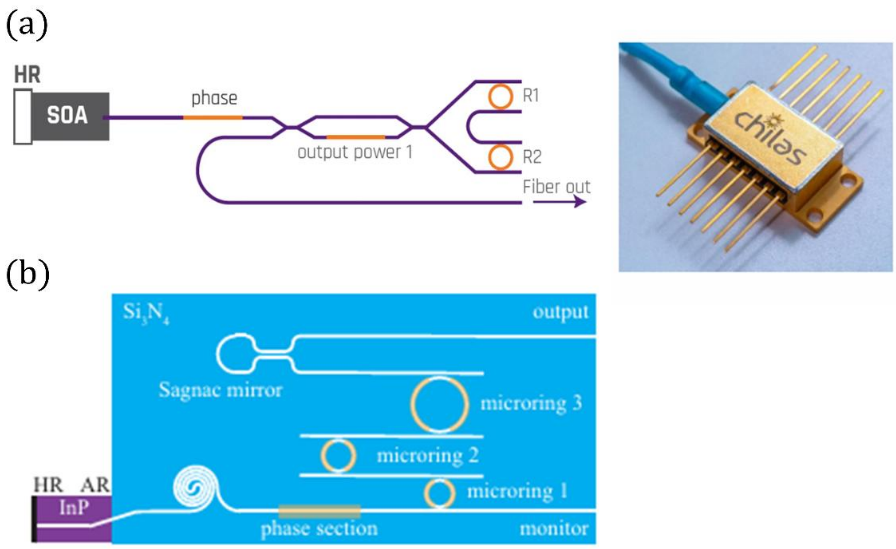

Figure 1.2: (a) Chilas-based butt-coupled hybrid laser module schematic with corresponding butterfly packaged device [28]. (b) LioniX HECL based on Sagnac loop reflector and three cascaded microrings as high spectral filters for narrower laser intrinsic linewidth [40].

Fig. 1.2(b) illustrates the schematic of a hybrid laser variant proposed by LioniX in [40] that targets narrower intrinsic linewidth. A single InP gain section is coupled to a SiN external-cavity that extends the round-trip length to about 0.5 m using a 33 mm spiral waveguide and three cascaded microrings: two small rings (99/102 µm, $Q \approx 2\times10^4$) provide coarse Vernier filtering, while a larger high-Q ring (1485 µm, $Q \approx 2.9\times10^5$) performs fine spectral selection, with a Sagnac loop mirror at the end of the cavity doubling the pass through the resonators. This architecture achieves an intrinsic linewidth of about 40 Hz together with a wavelength tuning range exceeding 70 nm and up to 23 mW of fiber-coupled output power.

The dual-gain configuration shown in Fig. 1.3(a) incorporates two 700-μm InP gain sections symmetrically surrounding an external-cavity with a Vernier filter formed by two microrings (FSRs 208 and 215 GHz). The bidirectional cavity doubles the optical field pass through the filter per round trip to enhance selectivity, while counter-propagating fields are coherently combined into a single output via two tunable couplers. The laser achieves up to 105 mW fiber-coupled power (117 mW on-chip), maintains >70 mW over a 100 nm tuning range (1470–1570 nm), and demonstrates a 320 Hz intrinsic linewidth, SMSR >50 dB, and RIN ≈ −170 dBc/Hz [41].

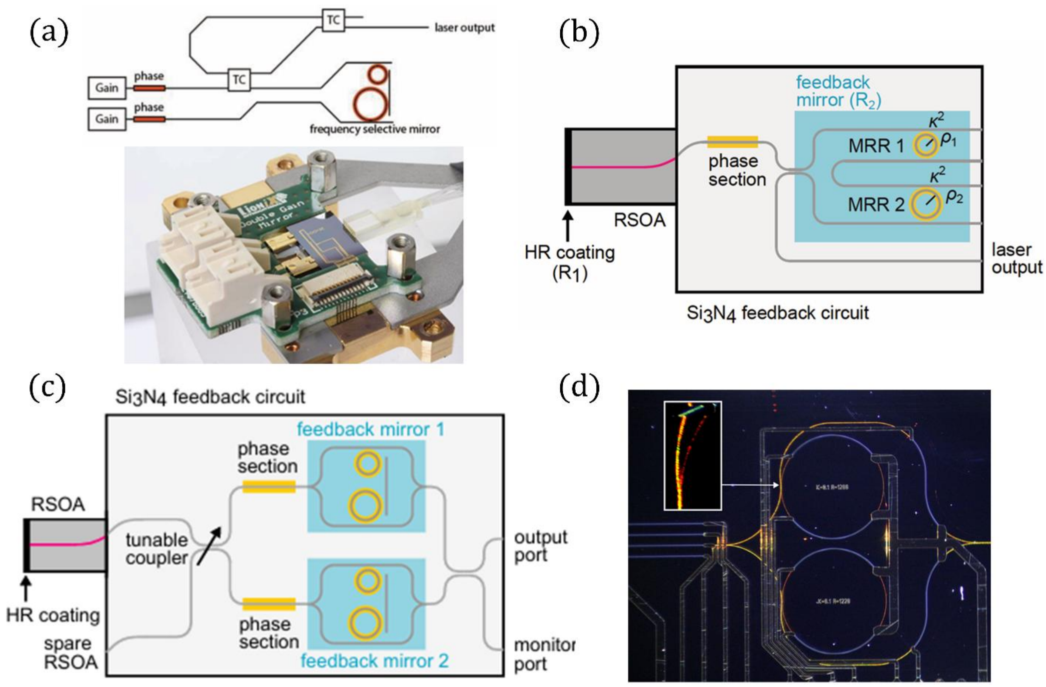

Figure 1.3: (a) Dual-gain HECL architecture for enhanced intra-cavity field [41]. (b) Dual-wavelength HECL with two parallel Vernier feedback branches and a tunable MZI coupler. (c) Multi-frequency HECL using dual SiN Vernier mirrors for stable comb generation. (d) Visible-wavelength SiN Vernier feedback circuit for high-Q hybrid laser operation [28]

For multi-frequency operation, biasing the hybrid cavity so that two adjacent modes experience equal Vernier transmission yields a 17-line comb with 5.5 GHz spacing and approximately 2 mW total power; RF beat notes reveal a single narrow tone with an ∼18 kHz linewidth, while heterodyne measurements indicate individual comb linewidths down to ~34 kHz [28]. A dual-wavelength HECL version [28] splits the TriPleX feedback into two parallel Vernier branches sharing a common InP RSOA via a tunable MZI coupler, enabling stable dual-line emission with up to 12 nm separation and an ∼11 GHz microwave beat note at near-degenerate operation. In parallel, the same hybrid cavity concept was extended to the visible (690 nm) using TE-polarized SiN Vernier rings (radii 1200/1205 μm, FSR ∼10 nm), yielding passive reflection peaks of ∼1.5 pm (∼1 GHz) and demonstrating high-Q feedback for future visible hybrid lasers [28].

In collaboration with LioniX and CHILAS, the Kippenberg group developed a hybrid external-cavity laser based on a two-chip assembly interconnected by 3D-printed optical interconnects. In this architecture, an InP reflective semiconductor optical amplifier (RSOA) is co-packaged with a low-loss SiN photonic integrated circuit on the TriPleX platform, which provides the wavelength-selective external-cavity. In Ref. [42], the two chips are optically linked by a PWB (loss ≈1.6 dB), which bridges a gap of ≈306 μm and relaxes alignment tolerances compared to direct butt-coupling (Fig. 1.4). The SiN cavity integrates a Vernier filter of two thermally tunable racetrack resonators (FSRs 195.7 GHz and 202.0 GHz) inside a Sagnac loop, plus a cavity phase tuner and a tunable Mach–Zehnder output coupler. Output coupling to a fiber array is achieved via 3D-printed facet-attached microlenses (FaML). Experimentally, this design achieves a 90 nm tuning range (1480–1570 nm), on-chip output power >12 dBm, side-mode suppression up to 59 dB, and an intrinsic linewidth of 979 Hz – among the narrowest for two-ring feedback. The laser also served as a pump to generate a single-soliton Kerr frequency comb in a separate high-Q SiN resonator.

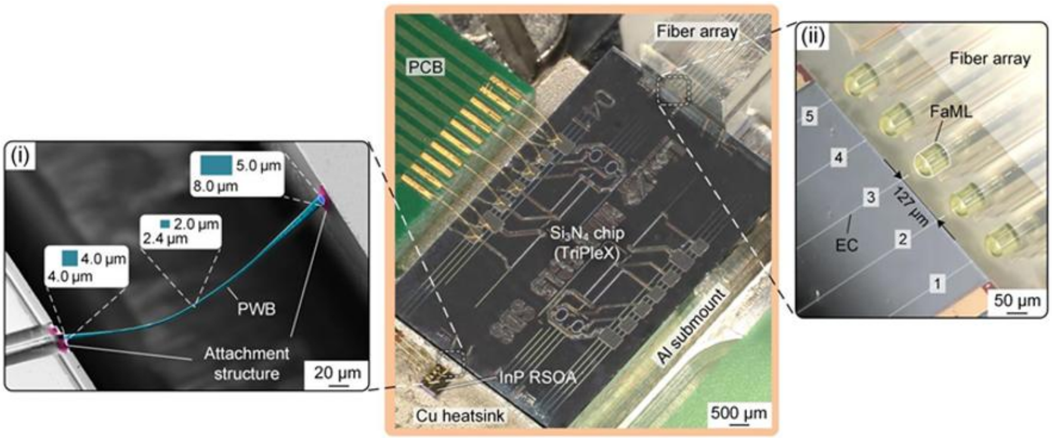

Figure 1.4: PWB-based two-chip butt-coupled hybrid laser assembly with a SiN TriPleX external-cavity and InP RSOA. Focus on the 3D-printed photonic wire (i) and output fiber coupling via facet-attached microlenses (ii) [42].

In the frequency-agile external-cavity laser developed in [43], the laser architecture is the same as that reported in [42], but the butt-coupling is not supported by PWB and on-chip phase shifter is replaced by varying the RSOA injection current, which simplifies the overall design. A key distinguishing feature of this platform is the monolithic integration of both microheaters and piezoelectric (PZT) actuators on the same chip. The microheaters, positioned 15 μm from the ring waveguides, provide coarse thermal tuning for Vernier alignment, whereas the PZT actuators enable fast, low-power, and highly linear frequency actuation with MHz-bandwidth response and nanowatt-level power consumption. The entire laser (whose schematic is illustrated in Fig. 1.5(a)) is assembled in a temperature-stabilized butterfly package with a fiber output as reported in Fig. 1.5(b).

Experimentally, the laser delivers 6 mW fiber-coupled power, a side-mode suppression ratio of 50 dB, and an intrinsic Lorentzian linewidth of 400 Hz. Exploiting the PZT actuators, the device achieves wavelength switching at a 100 kHz repetition rate, with a 7 ns rise time and an energy cost of only 75 nW per switching event. This provides significantly faster tuning and lower power consumption than would be possible with thermal tuning alone, thanks to the integrated piezoelectric actuation.

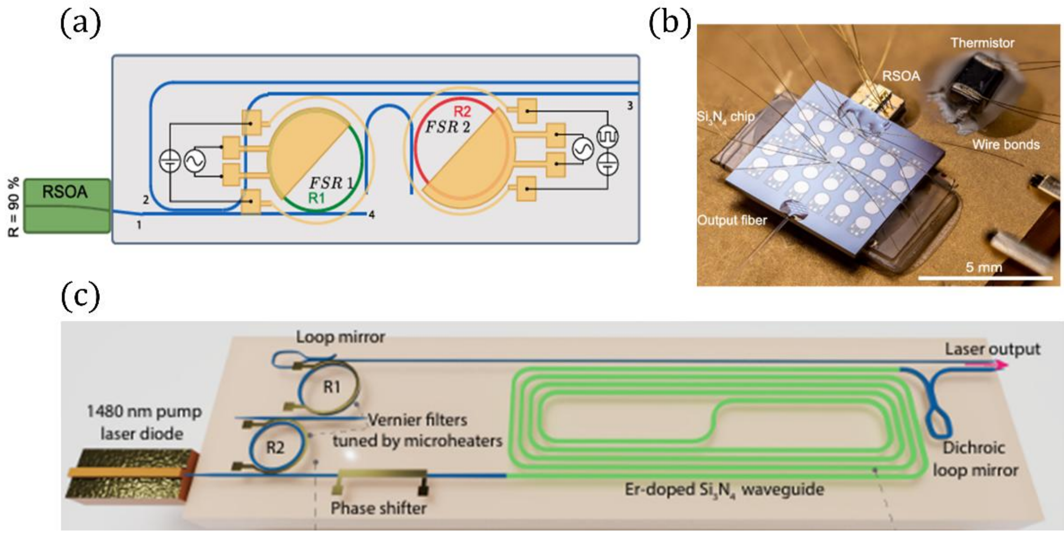

Figure 1.5: (a) Schematic and (b) assembled butt-coupled HECL with monolithic integration of both microheaters and piezoelectric actuators [43]. (c) Schematic of an erbium-doped waveguide in a hybrid gain–PIC laser architecture [44].

A compact two-chip erbium-doped waveguide laser is realized by butt-coupling a 1480 nm InP Fabry–Pérot pump laser diode to an Er-implanted ultralow-loss SiN photonic integrated circuit that serves as both gain medium and cavity [44]. The cavity comprises a 0.2 m densely packed spiral Er:SiN gain waveguide terminated by two Sagnac loop mirrors, together with a narrow-band Vernier filter formed by two cascaded add-drop MRRs, while integrated microheaters align the Vernier peak to a longitudinal cavity mode. The entire laser circuit occupies only 2×3 mm^2 and is packaged in a 14-pin butterfly module.

Experimentally, the laser operates in single mode with SMSR >70 dB, >4 mW output power, 6.7% on-chip slope efficiency, and >40 nm tuning across the C- and L-bands. It exhibits an intrinsic Lorentzian linewidth as low as 50 Hz, RIN below −150 dBc/Hz above 10 MHz offset, and frequency drift below 20 MHz over 4 h and 140 MHz over 24 h, in absence of mode hopping.

1.4.3 Micro-transfer printing

Micro-transfer printing (μ-TP) [45-47] is an emerging wafer-scale integration technology for selectively transferring prefabricated epitaxial semiconductor devices, often called coupons, from their native growth substrate onto non-native target substrates such as silicon or silicon nitride for photonic integrated circuits. In contrast to heterogeneously bonding full dies or wafers, μ-TP works with many small devices in parallel and is particularly attractive for integrating III–V gain sections on low-loss passive waveguide platforms for hybrid and heterogeneous lasers.

In the μ-TP process [47],[48], the III–V devices are first grown and prefabricated on their native substrate, incorporating a sacrificial release layer (for example a high-Al-content AlGaAs layer in a GaAs-based stack) beneath the device layer. Selective under-etching of the sacrificial layer releases the devices, whereas dielectric or photoresist tethers maintain mechanical attachment of each coupon to the source wafer, allowing dense packing at pitches of a few hundred micrometers. A microfabricated elastomeric stamp, typically made of polydimethylsiloxane (PDMS) and patterned with posts corresponding to the coupon layout, is then aligned to the array of released coupons and brought into contact. A fast retraction of the stamp exploits the rate-dependent adhesion between PDMS and the coupon surfaces: the tethers break and the coupons remain attached to the stamp. The same stamp is subsequently aligned to the target wafer, often a silicon or SiN PIC with locally opened recesses in the cladding, and the coupons are brought into contact with the target surface. A slow retraction, sometimes with a controlled shear, leaves the coupons bonded onto the target via van der Waals forces or an ultrathin adhesive such as divinylsiloxane-bis-benzocyclobutene (DVS-BCB), after which the stamp is fully released. A key strength of μ-TP is that it is a massively parallel process: hundreds to thousands of coupons can be picked up and printed in a single cycle of tens of seconds, allowing high-throughput population of a target wafer.

State-of-the-art tools achieve placement accuracies of about ±0.5 μm (3σ) for reticle-sized stamps [48], which is sufficient for alignment-tolerant adiabatic tapers that couple light efficiently between III–V waveguides and underlying Si or SiN waveguides. Because the III–V devices are prefabricated and can be electrically/optically tested on their native substrate before release, μ-TP enables pre-screening and only transfers known-good devices, which is particularly valuable for laser arrays where defective emitters cannot be repaired after integration. The technique is back-end compatible with CMOS processing, since only local recesses or openings in the dielectric cladding are required to host the printed III–V coupons, making it attractive for integrating gain sections, modulators, or detectors on mature silicon photonic platforms.

μ-TP also uses III–V material efficiently because coupons can be tightly packed on the source wafer but printed sparsely across a larger target wafer, effectively multiplying the usable area of expensive epitaxial material. Wafer-to-wafer and die-to-wafer bonding provide excellent alignment because devices are patterned after bonding, but they are sensitive to particles at the bond interface, offer limited per-device pre-testing, and require complex process development. Flip-chip bonding of fully processed III–V dies enable accurate alignment and full pre-testing but is inherently serial, low throughput, and introduces significant topography from the die and solder bumps. In contrast, transfer printing combines wafer-like parallelism, flip-chip-like pre-testing, planar integration with thin coupons, and efficient use of III–V material, at the cost of lower technology maturity and specific mechanical and thermal design constraints. The main limitations of μ-TP arise from the mechanics and the interface. Thin, suspended coupons must be carefully tethered and sometimes encapsulated to avoid fracture, and the need for a sacrificial release layer complicates the epitaxial design and front-end processing. The bonding interface, whether van der Waals or a thin polymer, introduces thermal resistance and may therefore limit heat dissipation; consequently, transferred devices do not necessarily replicate the thermal behavior of devices on their native III–V substrate [49]. More details on the fabrication process and the optical characterization of micro-transfer printed based laser will be explored in Section 5.3.

1.4.3.1 μ-TP ECLs

The work in [50] presents a wafer-scale heterogeneous integration platform that combines GaAs-based III–V gain elements with low-loss SiN waveguides to realize extended-cavity lasers and passively mode-locked frequency combs at 800 nm. As illustrated in Fig. 1.6(a), the approach relies on micro-transfer printing to place a fully pre-processed III–V coupon into a locally etched recess of the SiN photonic circuit, enabling direct butt coupling between the III–V and SiN waveguides.

The passive chip is built on a SiN waveguide platform with a 300 nm thick SiN core buried in silicon oxide. A recess is dry etched through the top cladding and the buried oxide down to the silicon substrate, exposing a clean vertical facet of the SiN waveguide. The III-V coupon is then printed into this recess so that its own waveguide facet faces the SiN facet with a separation below 500 nm, limited mainly by the slope of the recess sidewall. Vertical alignment between the III-V and SiN waveguide modes is engineered by carefully matching the total epitaxial layer thickness of the coupon to the depth of the recess; the simulated modal overlap reaches 96 %. The small gap is later filled with BCB during post-processing, which planarizes the structure and provides a stable optical interface.

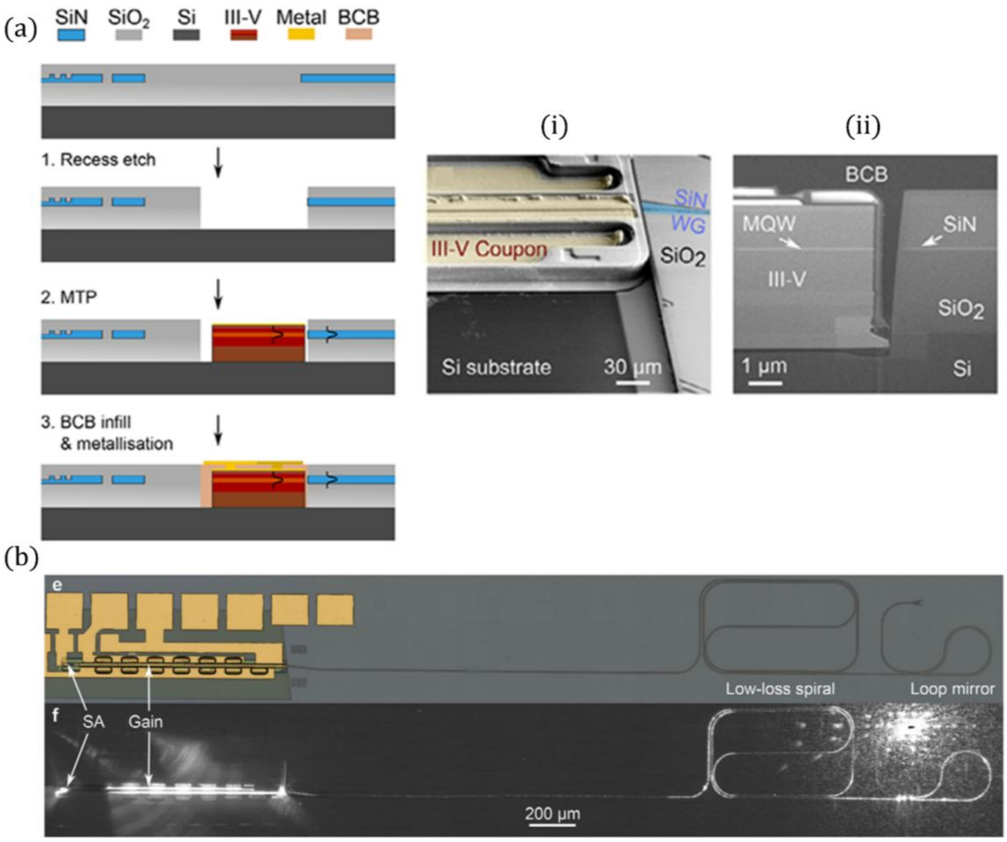

Figure 1.6: (a) Key steps of the micro-transfer printing of III-V gain into SiN PIC (on the silicon substrate after SiO_2 recess): (i) view of the butt-coupling between printed coupon and SiN waveguide, (ii) cross-section analysis of the printed coupon, showing small separation due to the recess-etch angle. (b) Microscope image of the external-cavity laser architecture [50].

Regarding the III-V coupons, two variants are produced: RSOAs with a 7° angled front facet and a gold high-reflectivity coating on the rear facet, and Fabry–Pérot coupons with a 0° front facet that provides an 8% Fresnel reflection to sustain lasing. The angled facet of the RSOA suppresses back-reflections into the III-V waveguide (from –11 dB to –70 dB in simulation), which is critical when the coupon is used inside an extended cavity. The saturable absorber is formed by electrically isolating a short segment, assessed to around 3–5 % of the total coupon length, that can be reverse-biased independently from the gain section.

The extended laser cavity is completed by the SiN circuit, which consists of a low-loss waveguide spiral terminated by a Sagnac loop mirror. The spiral sets the cavity length and thus the fundamental repetition rate (3.2, 7.5, or 9.2 GHz), while the Sagnac mirror, implemented as an asymmetric multimode interferometer, provides a broadband 75 % reflectivity that serves as the output coupler. Optically, the cavity is linear: the gold-coated rear facet of the RSOA coupon forms one end mirror, and the Sagnac loop forms the other. Light generated in the gain section passes through the butt-coupled interface, propagates in the SiN spiral, and is partially reflected into the

III-V waveguide, while the transmitted portion is collected via a grating coupler. The long photon lifetime afforded by the low-loss SiN cavity, improves the phase coherence and substantially reduces the fundamental RF linewidth of the mode-locked comb. Design choices are deliberately balanced between power and noise performance. The high 75 % reflectivity maximizes the cavity quality factor and yields a record passive-stability RF linewidth of 519 Hz (timing jitter as low as 51 fs), but it limits the waveguide-coupled output power to a few milliwatts. The authors report that by lowering the Sagnac mirror reflectivity to 10 % and reducing the coupling losses, output powers exceeding 60 mW and pulse energies of several pico-joules are achievable.

A narrow-linewidth frequency comb source operating in the L-band (around 1580 nm) was demonstrated in [51] by injection-locking a heterogeneously integrated III-V-on-silicon mode-locked laser to a continuous-wave seed laser with 50 kHz linewidth. The device features a linear-cavity colliding-pulse mode-locked laser (MLL) fabricated on a silicon photonics platform, where the III-V active region is bonded to the silicon waveguide layer.

It includes two 430 µm gain sections and a central 100 µm saturable absorber, with 150 µm tapered spot-size converters for ensure coupling between the III-V and silicon waveguides. The cavity incorporates two 0.7 cm silicon spiral waveguides, setting the repetition rate to 4.71 GHz.

First-order distributed Bragg reflectors, providing ~50% reflectivity, serve as cavity mirrors and enable emission in the L-band. The entire laser schematic is illustrated in Fig. 1.7(a). This configuration reduces the MHz-range linewidth of the MLL's longitudinal modes to match the 50 kHz seed linewidth, with over 50 coherent laser lines achieved.

In free-running operation, the laser's individual longitudinal modes show optical linewidths of several MHz, with a fundamental RF linewidth of 55 kHz. Two injection-locking schemes were explored to narrow the optical linewidths and stabilize the repetition rate.

In the first scheme, the laser was hybrid mode-locked by applying a 4.71 GHz RF signal (5 dBm) to the saturable absorber, combined with injection of the 50 kHz-linewidth continuous wave seed at 0.6 mW on-chip power. This achieved coherence across 30 comb lines and sub-hertz RF beat notes for the six modes nearest the seed. The second configuration avoided the need for hybrid mode-locking by injecting a modulated seed (11 dB depth at the 4.71 GHz repetition rate) into the passively mode-locked laser at 0.1 mW on-chip power. This reduced the RF linewidth to sub-hertz levels and confirmed coherence over >55 modes spanning ~2.1 nm. Excessive injection (~1 mW) caused collapse to single-mode operation.

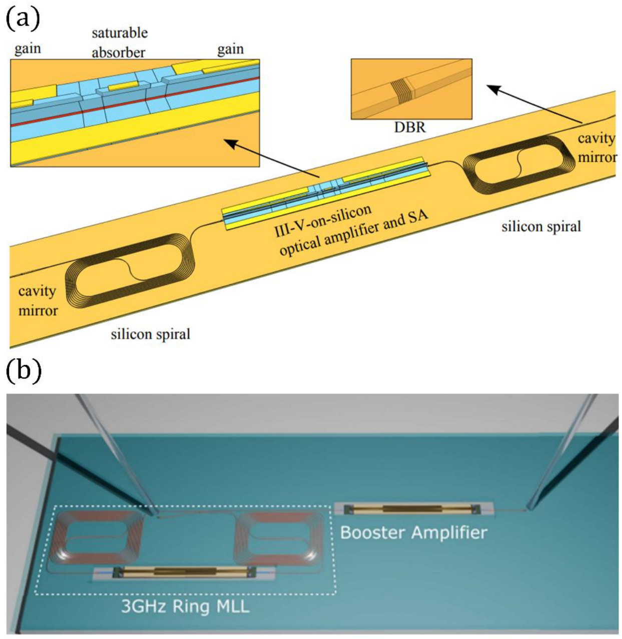

Figure 1.7: (a) Schematic of the linear cavity colliding pulse mode-locked laser structure: two μ-TP SOAs and a SA are placed in the middle of the cavity, while on the left and right side are defined DBRs and spiral waveguides [51]. (b) MLL architecture with view of the printed booster amplifier and III/V SOA gain [52].

The work in [52], presents a heterogeneously integrated III-V on SiN mode-locked laser operating at a 3 GHz repetition rate, combined with a co-integrated booster amplifier for significant output power enhancement. The laser is built on a low-loss SiN waveguide platform and uses a symmetric ring topology to form a colliding-pulse mode-locked laser. To overcome the large refractive index mismatch between the low-index SiN waveguides and the high-index III-V gain material, a thin silicon interposer coupon is micro-transfer printed directly above the SiN waveguide inside a locally etched recess. After printing, the silicon layer is patterned into adiabatic tapers (tip width 120 nm) that transfer the optical mode evanescently from the SiN waveguide up into the silicon, and subsequently into the III-V amplifier mesa. This tapered silicon intermediate layer enables efficient, broadband coupling with simulated transmission above 95% even for lateral misalignments up to 500 nm (a more detailed analysis on these taper structures will be detailed in Section 1.5).

The laser cavity includes two 2 cm long SiN spirals, a 2.5 mm multi-quantum-well semiconductor optical amplifier, and a 100 μm reverse-biased saturable absorber. An additional identical III-V SOA is micro-transfer printed on one output arm as a booster amplifier, which amplifies the comb output by up to 10.5 dB, as depicted in Fig. 1.7(b).

The on-chip average power reaches 11 dBm (4.2 pJ pulse energy), and the optical 10 dB bandwidth is nearly 10 nm. The fundamental RF linewidth is 1.4 kHz in passive mode locking, and hybrid mode locking reduces the integrated timing jitter to 3.5 ps (10 kHz–1 MHz). The laser operates stably for 48 continuous hours.

1.4.4 Heterogeneous integration: bonding

The primary distinction in III–V on silicon integration lies between die-level and wafer-level bonding. In die-level bonding, individual III–V dies are attached to a silicon photonic wafer, preserving flexibility in placement and enabling the use of pre-selected known good dies. In contrast, wafer-level bonding involves attaching an entire III–V wafer to a silicon wafer early in the fabrication process, enabling lithographically aligned co-fabrication of active and passive components and supporting higher integration density and scalability.

Within heterogeneous integration [1],[2],[4],[53], three main assembly schemes are typically identified: wafer-to-wafer, die-to-wafer, and die-to-die bonding. Wafer-to-wafer bonding offers the highest throughput and alignment accuracy due to parallel processing, but suffers from yield limitations, as defective regions on either wafer cannot be avoided. This issue is exacerbated by the size mismatch between III–V and silicon wafers, which increases material waste and cost.

Die-to-wafer bonding provides a balance between scalability and yield, as it allows the selection of known good dies prior to bonding, reducing the impact of defects and avoiding unnecessary consumption of expensive III–V material. Die-to-die bonding shares the same yield advantage but has the lowest throughput, making it suitable mainly for low-volume or highly customized applications. Cost–yield analyses [53] indicate that wafer-to-wafer bonding is only advantageous under conditions of very low defect density and small die size, while die-to-wafer bonding becomes more favorable as defectivity or die size increases. In all cases, defect density remains the dominant cost factor, with throughput playing a secondary role.

To address throughput limitations of die-based approaches, collective die-to-wafer (CoD2W) bonding has been introduced [54],[55].

This method enables the simultaneous transfer and bonding of multiple dies, combining the yield benefits of known good die selection with improved manufacturing efficiency. Additionally, it allows selective placement of III–V material only where active functionality is required, reducing material consumption and supporting cost-effective large-scale integration. For these reasons, the following section focuses on die-to-wafer bonding approaches based on covalent and adhesive mechanisms, which are more compatible with photonic device requirements and front-end integration. Metallic bonding is not treated further, as its associated optical losses, interdiffusion effects, and more restrictive processing conditions make it less suitable for the realization of low-loss, high-performance photonic integrated circuits.

1.4.4.1 Covalent wafer bonding

Among heterogeneous integration strategies for III–V/Si photonic platforms, covalent wafer bonding [3],[56],[57] (CWB), also known as direct or hydrophilic wafer bonding, has become the benchmark technique due to its ultrathin inorganic interface, high bond strength, and excellent optical and mechanical reliability. This process relies on the reactivity of hydroxyl-terminated surfaces: both the III–V and silicon wafers are prepared with oxide-covered, OH-passivated surfaces, either native or intentionally deposited (e.g., SiO_2 or, in some cases, Al_2O_3). When brought into contact at room temperature, these surfaces form a dense network of hydrogen bonds mediated by –OH groups and adsorbed water molecules.

A subsequent low-temperature annealing step, typically performed at 250–400 °C under an applied pressure of approximately 1–2 MPa, drives dehydration and condensation reactions that convert hydrogen bonds into covalent Si–O–Si or M–O–Si linkages. This process densifies the interfacial oxide and yields a hermetic, mechanically robust interface with sub-nanometer roughness tolerance and negligible additional optical loss. Compared to earlier hydrophobic wafer fusion approaches, which require annealing temperatures above 600 °C and can degrade III–V material quality, hydrophilic bonding achieves comparable bond strength at CMOS-compatible temperatures while better accommodating the thermal expansion mismatch between InP (2.6×10^{-6} K^{-1}) and silicon ($4.5\text{–}5.0\times10^{-6}$ K^{-1}), provided that film thickness and stress are properly engineered.

In a typical process flow for InP-on-SOI integration, the native oxides on both wafers are first removed to produce smooth hydrophobic surfaces. An ultrathin oxide layer (∼1–15 nm), rich in reactive Si–OH or M–OH groups, is then formed via O_2 plasma oxidation or chemical vapour deposition of SiO_2. When thicker oxides are used, chemical–mechanical polishing (CMP) ensures that the root mean square (RMS) roughness is reduced below approximately 1 nm, enabling high-yield spontaneous bonding.

A wet chemical activation step generates hydrophilic OH-terminated surfaces. Upon contact, spontaneous bonding occurs at room temperature through hydrogen bonding and van der Waals interactions. During subsequent annealing (∼300 °C for 1–10 hours), gaseous by-products such as H_2 and H_2O are released as the interface densifies. If not properly managed, these species can accumulate and form interfacial voids, particularly when using ultrathin (<20 nm) oxide layers required to maintain strong optical and thermal coupling between the III–V gain region and the silicon waveguide.

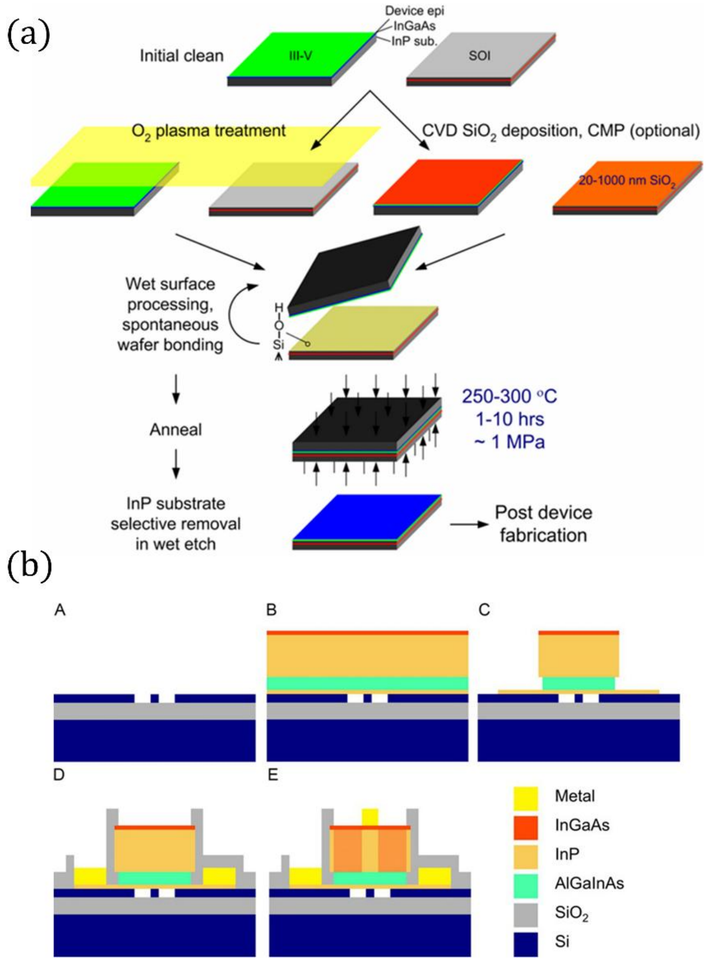

Figure 1.8: Schematic of the main CWB processes [56]. Cross-section-based fabrication flow of a heterogeneous silicon/InP laser: (A) processed SOI waveguide, (B) after bonding and InP substrate removal, (C) after III–V mesa etch, (D) after bottom n-metal and via-oxide formation, and (E) final device with top p-metal and isolation implant [57].

To mitigate void formation, vertical outgassing channels (VOCs) are typically etched through the silicon device layer down to the buried oxide prior to bonding [56]. These micrometer-scale vias provide diffusion pathways and local sinks for trapped gases, enabling void-free bonding over more than 98% of the wafer area even under low-temperature annealing conditions.

After bonding, the InP substrate is selectively removed via wet etching, leaving a thin (~2 µm) InP-based epitaxial stack bonded to the SOI wafer.

1.4.4.2 CWB ECLs

The work in [58] has demonstrated a widely tunable C-band laser using a coupled-ring-resonator (CRR) mirror architecture. In this design, the cavity is formed by two pairs of coupled ring resonators placed on either side of a III–V SOA, with slightly different ring circumferences (471 μm and 513 μm) exploited to realize Vernier-effect tuning. Thermal control of the ring pairs enables a coarse tuning range of 29 nm, while the omission of a drop-port bus waveguide concentrates the output power into two ports. The schematic of the proposed HECL is illustrated In Fig. 1.9(a). The CRR mirror simultaneously provides an effective cavity-length enhancement and an optical negative-feedback mechanism when lasing occurs on the long-wavelength side of the ring resonance, leading to a significantly reduced linewidth of 160 kHz and a side-mode suppression ratio (SMSR) exceeding 40 dB across the full tuning range. The device delivers more than 15 mW of output power with a threshold current of 56 mA.

Moreover, high-coherence distributed-feedback (DFB) lasers have been realized on this heterogeneous platform by fundamentally decoupling the photon resonator from the lossy active medium. This is achieved through a tailored design strategy, as detailed by *Santis et al.* [59], in which a low-refractive-index spacer layer is introduced between the III–V gain material and the underlying high-Q silicon resonator based on a one-dimensional photonic crystal design (Fig. 1.9(b)).

This configuration serves two key functions. First, it significantly reduces the modal overlap with the lossy III–V region, increasing the loaded cavity quality factor Q. Second, it suppresses spontaneous emission into the lasing mode by reducing the normalized modal energy intensity within the active region. Experimentally, increasing the spacer thickness leads to a progressive reduction in the quantum noise-limited linewidth. In the optimized device, most of the optical mode is confined in the low-loss silicon waveguide (95%), with only a small fraction residing in the III–V material and an even smaller portion in the quantum wells (0.2%). As a result, this design achieves a record-low intrinsic Lorentzian linewidth (< 1 kHz) for a free-running semiconductor laser, nearly three orders of magnitude lower than that of a conventional DFB laser operating at the same pump offset. CWB has also enabled the generation of optical frequency combs characterized by 900 fs pulses with a peak power of 98 mW and a narrow RF linewidth of 1.1 kHz at a 20 GHz repetition rate, demonstrating simultaneous high peak power, short pulse duration, and excellent spectral purity [20].

Fig. 1.9(c) shows the architecture of an optimized colliding-pulse design, integrating a 2 mm long III–V gain section with a centrally located saturable absorber, passive silicon waveguides, and on-chip Sagnac loop mirrors. The structure incorporates a three-section adiabatic taper to enable a low-loss transition between active and passive regions, along with a spline-shaped Sagnac loop mirror featuring a minimum bend radius of 3 μm to reduce propagation loss and suppress parasitic modes.

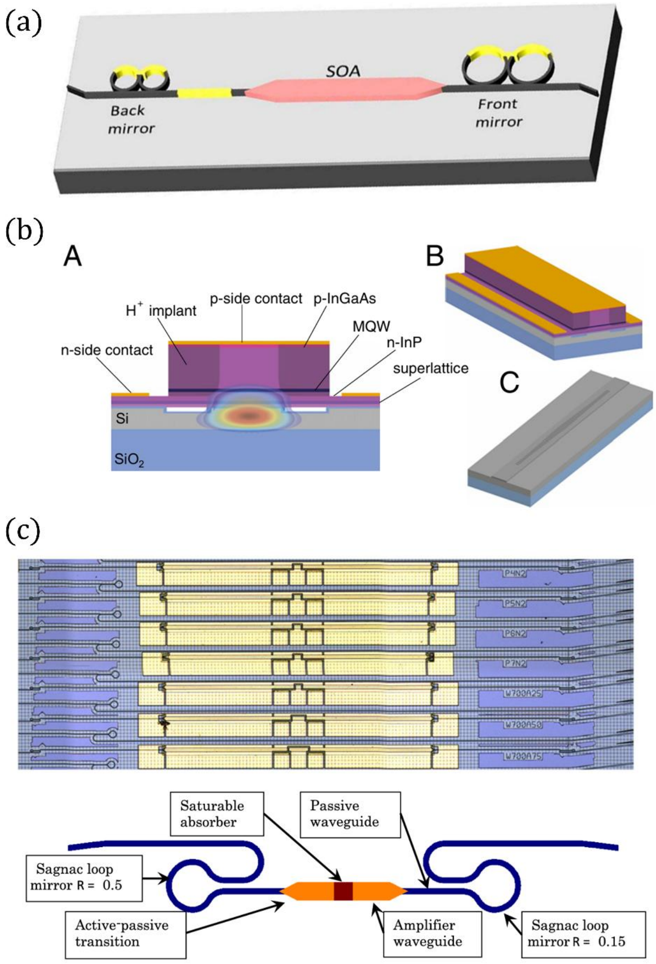

Figure 1.9: (a) Widely tunable C-band laser using coupled-ring-resonator (CRR) mirrors around a III–V SOA, exploiting Vernier-effect thermal tuning [58]. (b) Heterogeneous DFB laser based on III–V gain and high-Q silicon PCR: (A), (B) cross-section of the III–V/Si waveguide, (C) view of the 1D PCR [59]. (c) Colliding-pulse MLL combining a III–V gain section with a central SA, passive Si waveguides, and on-chip Sagnac loop mirrors: (top) fabricated device view, (bottom) schematic of the HECL [20].

1.4.4.3 Adhesive wafer bonding

Adhesive wafer bonding (AWB) [3], [60-62] is widely used to transfer compound semiconductors onto silicon photonic platforms because the adhesive layer naturally planarizes the surface, relaxing both cleanliness and surface-roughness requirements and thus significantly simplifying bonding preparation and defect sensitivity compared with covalent bonding. Most work relies on DVS-BCB (divinylsiloxane-bis-benzocyclobutene), a thermosetting polymer.

The silicon surface is first encapsulated in silica and CMP-planarized, an adhesion promoter is spin-coated, followed by spin-coating of the BCB layer, which is then baked at low temperature to remove solvents before bonding under uniform pressure in nitrogen at temperatures below about 250 °C for roughly an hour to complete polymerization. This polymer bonding approach can effectively planarize wafer topography, protect patterned features, and has demonstrated interfacial polymer layers thinner than 50 nm, but large-scale deployment must consider polymer thickness uniformity, compatibility with subsequent processing, and long-term stability, since BCB can degrade over time and is generally less durable than direct molecular bonds.

In addition, in all bonding methods, including adhesive bonding, a thermal anneal at elevated temperature is required to achieve a strong bond, which makes careful management of thermomechanical stress essential due to the mismatch in coefficients of thermal expansion between materials such as Si (2.6×10^{-6}/°C), InP (4.8×10^{-6}/°C), and GaAs (5.7×10^{-6}/°C).

The DVS-BCB adhesive bonding process is defined in the schematic in Figure 1.10.

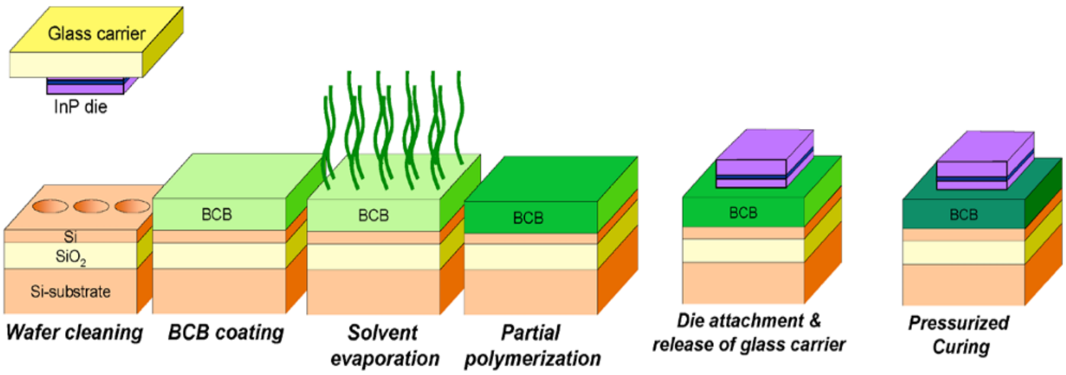

Figure 1.10: III-V/Silicon AWB integration: steps of heterogeneous DVS-BCB bonding fabrication [60].

Prior to bonding, the SOI surface is cleaned, while the III-V dies (InP/InGaAsP, previously cleaved and mounted epi-side up on a glass carrier) are cleaned and sacrificial layers are selectively etched to remove organics and particles and to expose a fresh surface. Next, an adhesion promoter is spin coated on the SOI, and a diluted DVS-BCB solution diluted is spin coated either on the III-V dies or the SOI wafer to obtain an ultra-thin bonding layer (typically <100 nm), thin enough to give good optical and thermal coupling despite the SOI topography.

The solvent evaporation and partial polymerization steps in Figure 1.10 correspond to a pre-bake around 150 °C, which evaporates the solvents and partially polymerizes the DVS-BCB, making it more solid-like and improving thickness uniformity while avoiding void formation in the final bond.

While in the die attachment and release of glass carrier step in Figure 1.10, the cleaned III-V die is aligned and brought epi-side down onto the SOI wafer, typically in a wafer bonder. After pumping to vacuum and heating to about 150 °C, pressure (~300 kPa) is applied while the glass carrier is released, leaving the III-V die bonded on top of the partially cured BCB layer. In the final step, the stack is heated to around 280 °C for about one hour under pressure, fully curing the

DVS-BCB, the III-V substrate can then be removed by grinding and wet etching, leaving a thin III-V membrane on the SOI platform.

1.4.4.4 AWB ECLs

Adhesive bonding of III–V gain materials onto silicon photonic integrated circuits using DVS-BCB has enabled high-performance mode-locked lasers, demonstrating short pulses, stable repetition rates, and efficient frequency-comb generation.
Keyvaninia et al. in [63] demonstrated III–V-on-silicon mode-locked lasers by bonding an InGaAsP multiple-quantum-well (MQW) stack onto a 400 nm silicon-on-insulator waveguide circuit using a ~40 nm DVS-BCB adhesive layer, as schematically illustrated in Fig. 1.11(a).

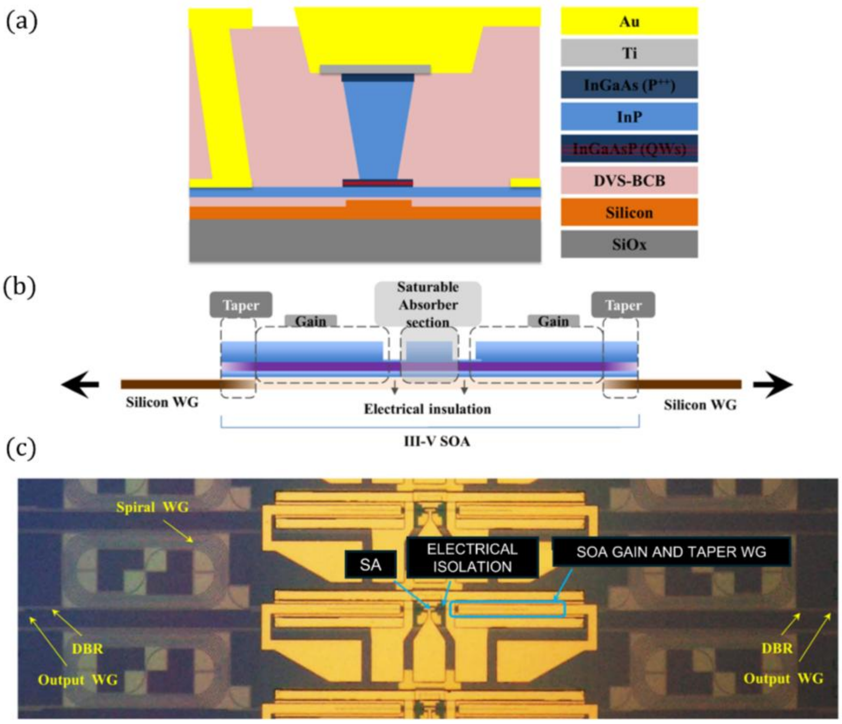

Figure 1.11: (a) Cross-section view of the AWB-based fabricated waveguide. (b) Schematic of the linear cavity colliding pulse MLL architecture. (c) Microscope image of the fabricated device [63].

The low-loss silicon waveguides (~0.7 dB/cm at 1550 nm) enable long on-chip cavities, while efficient III–V/Si coupling is achieved through a spot-size converter composed of a 150-µm-long III–V mesa taper (from 3 µm to a 500-nm tip) and a complementary inverse silicon taper. In the linear colliding-pulse configuration (Fig. 1.12(a)), a 100 µm saturable absorber is positioned symmetrically between two 430 µm SOAs, with first-order DBR mirrors defining the cavity, and the remaining path length implemented in centimeter-scale silicon waveguides to obtain a repetition rate of ~4.7 GHz. The schematic depicting the optical components constituting the external-cavity is represented in Fig. 1.11 (b), while the camera view of the implemented heterogeneous HECL is shown in Fig. 1.11(c). This device generates pulses as short as 1.5 ps with a 3 dB optical bandwidth of ~9 nm and exhibits an RF linewidth of about 12 kHz.

Conversely, a ring-cavity geometry, whose schematic is reported inn Fig. 1.12(b), has enabled suppression of the spurious RF tones at half the repetition rate by routing the cavity through a ~1.3 cm silicon loop, combined with longer SOAs (~790 µm) and a 180 µm saturable absorber. In this case, the optical bandwidth is reduced to ~2.5 nm, but the RF linewidth remains low (≈16 kHz). Both the linear and ring configurations can also operate in a hybrid mode-locking regime by RF modulating the saturable absorber section, in this condition, the timing jitter in the linear colliding-pulse cavity is reduced to approximately 353 fs.

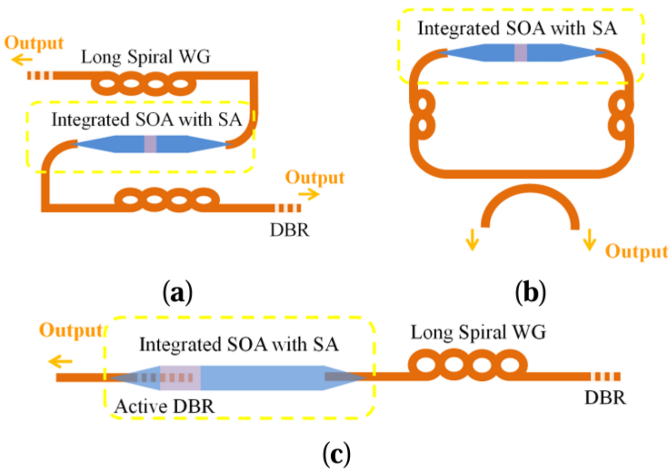

Figure 1.12: Layouts of III–V-on-silicon mode-locked laser cavities: (a) linear colliding-pulse configuration, (b) ring-cavity configuration, and (c) linear anti-colliding-pulse configuration [61].

Wang et al. [64] extended the adhesive-bonding approach to realize a III–V-on-silicon mode-locked laser operating at a record-low fundamental repetition rate of 1 GHz, for high-resolution dual-comb spectroscopy applications. The overall external-cavity laser layout is illustrated in Figure 1.13(c). The implemented mode-locking system follows the anti-colliding-pulse configuration depicted in Fig. 1.12(c). The cavity incorporates a long low-loss silicon spiral waveguide integrated with the bonded III–V gain and saturable absorber sections, while the reflectors are based on a full-feedback DBR mirror, defined at one end of the cavity, and a partial-feedback DBR mirror integrated directly beneath the saturable absorber, as shown schematically in Fig. 1.13(a),(b). Placing the saturable absorber directly above the output coupler, as indicated in both figures, enhances the extraction efficiency and leads to higher output power, reduced timing jitter, and improved RF spectral purity compared with a conventional colliding-pulse design. A 37.4 mm-long low-loss silicon spiral waveguide provides the dominant cavity length and enables the 1 GHz repetition rate.

The active section comprises an 800 µm-long semiconductor optical amplifier and a 40 µm-long saturable absorber, with adiabatic spot-size converters coupling the hybrid III-V/Si waveguide to the passive silicon spiral. At the optimal bias point (injection current 91 mA, saturable absorber reverse bias −2.6 V), the passively mode-locked laser generated an optical frequency comb with a 10-dB optical bandwidth of approximately 12 nm and a fundamental RF linewidth below 900 Hz (10-dB) at 1.009 GHz. The combination of the broad spectrum and the narrow mode spacing produced a dense comb containing over 1400 equally spaced optical lines. The longitudinal mode linewidth was measured to be below 400 kHz across the entire comb span. The laser was further stabilized via hybrid mode-locking by applying an RF signal to the saturable absorber; under these conditions the fundamental RF tone narrowed to sub-Hz linewidth while preserving the broad comb spectrum, demonstrating the viability of this adhesive-bonded III-V-on-silicon platform as a compact, chip-scale frequency comb source for precision spectroscopy and metrology.

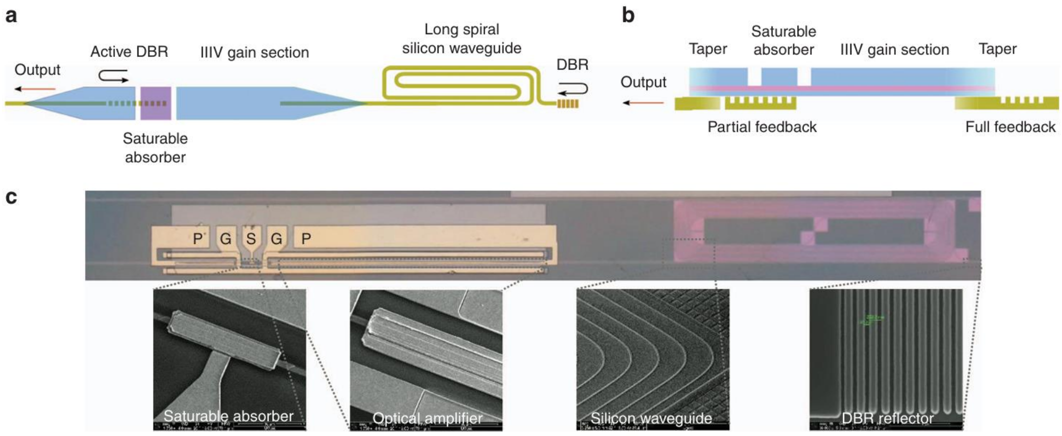

Figure 1.13: Top- and side-view renderings of the anti-colliding mode-locked laser are shown in (a) and (b), while (c) presents a microscope image of the III–V-on-silicon device with insets highlighting microscope images of key cavity components [64].

1.5 Optical coupling

This section introduces the various approaches used to realize optical coupling in hybrid laser systems, that is, the mechanisms by which the optical field generated in the active gain section is transferred into the passive resonator or routing circuitry on the photonic integrated circuit. The focus of this discussion is intentionally placed on coupling physics and geometrical design, rather than on the specific integration technology. This distinction is motivated by the fact that a given material platform (e.g., silicon, silicon nitride, or III–V-on-silicon) can, in principle, be realized through different integration approaches while still supporting similar coupling schemes, or conversely, may not be restricted to a single coupling strategy.

Separating these two aspects highlights that the fabrication and assembly methodology is conceptually distinct from the mechanism by which the optical mode is transferred between the gain and passive sections. In line with the overall goal of this thesis, namely, to chart the pathway toward fiber-free hybrid external-cavity laser integration, as will be demonstrated in Chapter 5, the discussion concentrates on three main coupling families: butt-coupling, vertical coupling, and evanescent coupling. Butt-coupling refers to direct, facet-to-facet transfer of the optical mode between adjacent waveguides; vertical coupling encompasses grating-based and surface-normal schemes where light is coupled out of plane into an overlying or underlying device; evanescent coupling relies on distributed power transfer between overlapping guided modes in closely spaced waveguides. The coupling method is also important for the optimization of the output collection in the laser, but this is generally implemented as butt-coupled and vertically coupled PIC-to fiber techniques.

Specifically in heterogeneous III–V-on-silicon devices, the optical mode in the active region extends over both the III–V stack and the underlying silicon waveguide, and its confinement can be engineered primarily via the silicon waveguide width and height.

The transition between the two active and passive cores is a critical part of the laser: it must provide low insertion loss, low parasitic reflections, minimal excitation of higher-order modes, and sufficiently broad optical bandwidth for the targeted application.

Different interface concepts have been explored, including lateral and vertical directional couplers, grating-assisted couplers, and adiabatic tapers, with taper-based schemes being widely adopted in state-of-the-art heterogeneous lasers because they can be designed essentially reflection-free and very broadband.

1.5.1 Vertical coupling

Vertical coupling refers to out-of-plane optical transfer between the active gain section and the passive photonic circuit. In this case, the optical field is transferred between vertically separated photonic layers rather than through an in-plane facet interface.

This coupling scheme is particularly relevant in compact 3D hybrid assemblies, including flip-chip implementations, and is commonly realized through grating couplers, vertically resonant structures, or more specialized solutions such as cantilever couplers. In these architectures, coupling efficiency is governed by the overlap between the vertically emitted or redirected field and the receiving guided mode, and is therefore affected by vertical spacing, layer geometry, diffraction strength, and alignment tolerance. Specifically, vertical coupling is attractive for multilayer integration because it removes the need for edge access and is compatible with compact, vertically stacked integration of light sources and photonic waveguides [65-69].

Grating couplers are widely used to vertically interface silicon waveguides with bonded III–V devices such as photodetectors and VCSELs. A subwavelength grating etched into the silicon layer diffracts the guided mode upward into the III–V stack. The key metric is directionality, defined as the fraction of diffracted power emitted upward, which depends on grating parameters (period, etch depth, duty cycle) and on interference effects caused by reflections at the bonding interface and substrate [61]. In bonded III–V photodetectors, the silicon grating, the bonding layer, the III–V stack, and the buried oxide form a vertical cavity; thus, the precise position of the grating within this cavity and the thicknesses of the intermediate layers strongly influence directionality and hence coupling efficiency.

By optimizing the bonding and oxide thicknesses, or by introducing an anti-reflection coating between the III–V and the bonding polymer, unwanted cavity effects can be mitigated, yielding a more robust grating response over wavelength and process variations. Compared with edge or evanescent tapers, such vertical grating interfaces typically offer relaxed in-plane alignment tolerances (on the order of several micrometers for a 1 dB penalty) and the freedom to place the III–V device almost anywhere on the PIC surface, at the cost of somewhat higher minimum insertion loss in many implementations [70].

1.5.2 Butt coupling

Butt coupling is an in-plane, facet-to-facet coupling scheme in which the optical mode emitted by one waveguide is launched directly into another waveguide that is aligned edge-to-edge. In the context of hybrid external-cavity lasers, this is one of the most widely adopted mechanisms: a discrete III–V gain chip is positioned at the edge of a silicon or silicon-nitride PIC, and the laser output is injected straight into the passive core of the resonator or routing circuit. The coupling efficiency is set primarily by the overlap between the mode profiles on the two sides of the interface and by parasitic Fresnel reflections at the chip facet; consequently, it is strongly affected by mode-field mismatch, facet quality and roughness, any residual air gap between the chips, and sub-micrometer lateral and vertical misalignment.

To alleviate these constraints, butt-coupled interfaces are almost always paired with dedicated mode-conversion structures on the passive side. Typical examples include inverse tapers, trident tapers, SiN-assisted spot-size converters, multilayer taper sections, and graded-index or MMI-based converters that expand and reshape the on-chip mode to better match the larger, more weakly confined mode emitted by the III–V ridge waveguide [71-76]. In silicon photonics, such edge-coupled mode converters are designed to transform the small, high-index contrast mode of a silicon or SiN wire into a broader mode with an effective index and mode-field diameter closer to that of the III–V gain facet, thereby improving overlap and reducing coupling loss. This often requires taper lengths of order 100–300 µm and carefully cleaved or polished facets, and the resulting performance remains highly sensitive to the alignment and stability of the assembled chips. For this reason, butt-coupled schemes place stringent demands not only on the optical design of the mode converters but also on the mechanical packaging, thermal-expansion management, and long-term reliability of the hybrid laser assembly. The coupling mechanism is dominated by the direct overlap of the fundamental modes at the facet, so efficient operation requires sub-micrometer lateral and vertical alignment, excellent facet quality, and stable control of any residual gap between chips. In practice, this often necessitates dedicated packaging solutions, such as Kovar butterfly packages and carefully engineered mounts, to ensure that thermal cycling and long-term drift do not degrade the alignment or increase insertion loss over the device lifetime.

In this framework, demonstrations of engineered mode-converters for butt-coupling are described below. In [77], the hybrid mode-locked laser consists of an active InP chip butt-coupled to a passive SiN photonic circuit, forming an external-cavity. The InP chip provides gain and pulse formation through a self-colliding configuration that includes a multimode interference reflector (MIR) acting as one cavity mirror, followed by a 50 µm saturable absorber, an 850 µm gain section, a 1×1 MMI filter to enforce single-mode operation, and a 7° angled output facet to suppress back-reflections. Light from the InP waveguide is coupled into the SiN chip via an intermediate SU-8 polymer edge coupler, which compensates for mode mismatch and provides high coupling efficiency and alignment tolerance. Within the passive chip, light is transferred from the SiN waveguide to the SU-8 waveguide through an inverse taper, allowing adiabatic mode expansion and efficient coupling. The SiN circuit includes a spiral waveguide (with length ranging from 1.2 mm to 3 cm) that forms the external-cavity and provides optical delay. At the end of this cavity, a Sagnac reflector with approximately 70% reflectivity feedback toward the InP chip to sustain lasing, while the remaining portion is routed to the output via a second SU-8 mode converter and collected with a lensed fiber.

The passive SiN chip is fabricated on a 300 nm SiN layer over 3.3 µm SiO_2 on a silicon substrate, with air-clad waveguides defined by e-beam lithography and reactive ion etching. Efficient and alignment-tolerant coupling to the InP chip (mode size ≈ 2.8 µm × 0.96 µm) is achieved through a polymer-based SU-8 edge coupler, which serves as an intermediate mode adapter. A ~875 nm-thick SU-8 layer is spin-coated and patterned into a 3.8 µm-wide waveguide featuring an angled facet (15.2°) that matches the emission angle of the InP facet, thereby minimizing reflection and improving coupling efficiency.

Critically, light transfer from the SiN waveguide to the SU-8 coupler is enabled by an inverse taper in the SiN layer: as the SiN waveguide width is gradually reduced, the optical mode expands and shifts into the overlaid SU-8 waveguide through evanescent coupling. This adiabatic transition allows the initially tightly confined SiN mode to evolve into a larger, more symmetric mode supported by the SU-8, which is better matched to the InP waveguide. The resulting overlap between the InP and SU-8 fundamental TE modes reaches ~90%, with alignment tolerances of ±500 nm horizontally and ±250 nm vertically for maintaining high coupling efficiency (85–90%). The SU-8 thickness is relatively non-critical, provided it remains within the 0.8–1.5 µm range to ensure proper mode confinement and avoid cutoff.

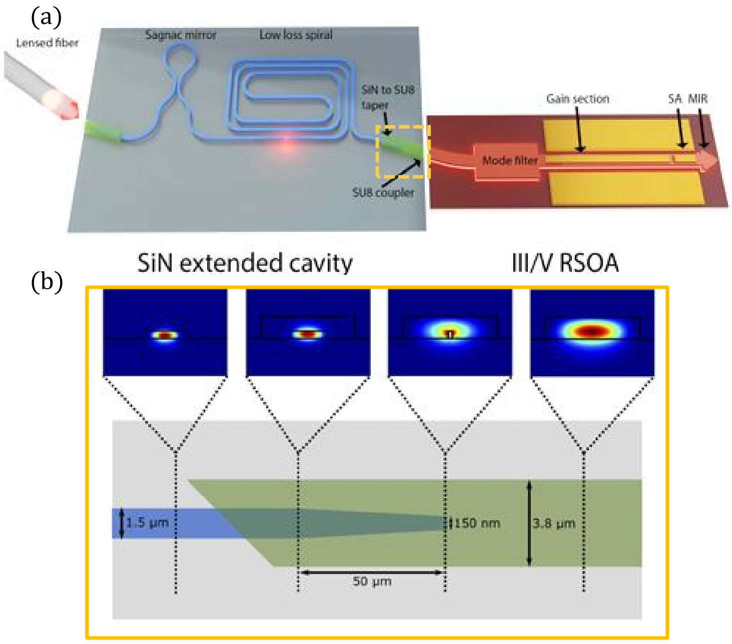

Figure 1.14: (a) Schematic of the hybrid external-cavity laser architecture. (b) Schematic of the taper in the SiN layer to match the SU-8 waveguide mode [77].

Within the butt-coupling approach, photonic wire bonding (PWB) can be viewed as an evolution of the conventional two-chip butt-coupled HECL architecture [78]. Rather than allowing the optical field to propagate across a short unguided air gap, a three-dimensional polymer waveguide is directly written between the gain-chip facet and the passive waveguide input, effectively replacing the free-space section with a tailored guided interconnect.

This approach preserves the modularity and flexibility of chip-to-chip hybrid integration while significantly improving the robustness of the optical interface. From a device engineering standpoint, it mitigates key limitations such as sensitivity to placement accuracy, beam divergence, and modal mismatch between the III–V output and the passive waveguide. Moreover, because the wire bond can be shaped to accommodate actual chip positions and engineered for mode-size adaptation, it relaxes alignment tolerances and enhances coupling efficiency between the two sections [79],[80]. The work [42], previously reported in Fig. 1.4, demonstrates an InP RSOA and a low-loss SiN PIC co-packaged and interconnected via a 3D photonic wire bond bridging a few hundred micrometers, reducing alignment sensitivity compared to butt-coupling while maintaining low insertion loss (≈1.6 dB).

(a)

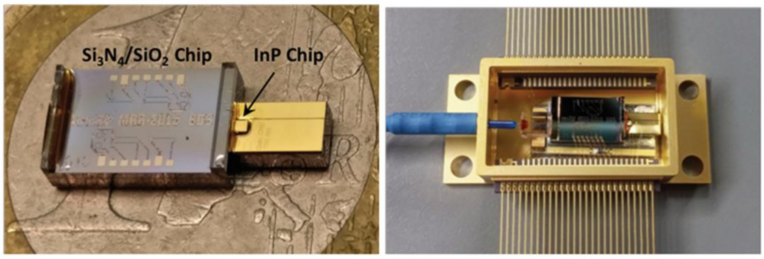

(b)

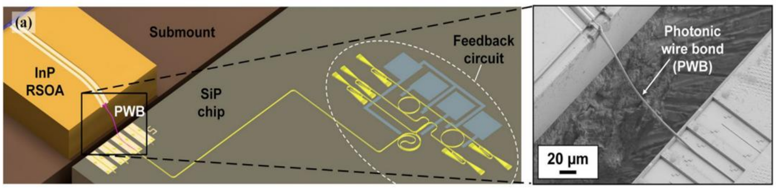

Figure 1.15: (a) Two-chip butt-coupled HECL and it is compact integration in a Kovar butterfly package [28]. PWB-based coupling between RSOA gain and external-cavity: zoom-in of the PWB component by means of a microscope image [42].

1.5.3 Evanescent coupling

Evanescent coupling [81],[82], relies on the overlap of the evanescent tails of adjacent active and passive optical modes over a finite interaction length, rather than on transmission across a discrete facet interface. When the III–V active region is brought sufficiently close to the silicon photonic waveguide, optical power is transferred through the evanescent field of the guided mode, which extends into and overlaps with the neighboring waveguide. This approach is particularly well suited to bonded III–V-on-silicon platforms [55], [83-86], where coupling is defined by the multilayer stack geometry instead of post-assembly facet alignment.

Within this framework, adiabatic taper interfaces represent the most widely adopted and effective implementation of III–V/Si evanescent coupling. In heterogeneous III–V-on-Si devices, the optical mode is initially strongly confined within the III–V ridge to ensure efficient gain, resulting in a substantial wavevector mismatch with the tightly confined silicon waveguide mode. By gradually tapering the width, and in some designs, also the thickness of the III–V waveguide and/or the silicon core, the effective index of the hybrid supermode is smoothly transitioned from III–V-like to silicon-like. This enables a progressive transfer of the optical field into the passive silicon waveguide.

If the structural variation along the propagation direction is sufficiently gradual, the taper operates in the adiabatic regime, where the fundamental mode evolves continuously without significant coupling to higher-order or radiation modes, thereby minimizing reflections and radiation losses.

In practice, double- or multi-section adiabatic tapers are often employed. An initial section typically reduces the III–V ridge width from several micrometers to approximately one micrometer, enhancing mode confinement and reducing the effective index mismatch with the silicon waveguide.

A subsequent section then tapers both waveguides to complete the mode transfer into the silicon core. When properly optimized, such mode converters can achieve sub-dB insertion loss over broad wavelength ranges, with negligible parasitic feedback, an essential requirement for heterogeneous external-cavity or DFB/DBR lasers, which are highly sensitive to spurious reflections. The coupling efficiency in these evanescent and adiabatic schemes is primarily governed by the vertical separation between layers, the interaction length, and the taper geometry. Consequently, the most critical fabrication tolerances relate to bonding thickness, waveguide dimensions, and overall stack uniformity, all of which can be effectively controlled within CMOS-compatible processes.

Compared with butt coupling, evanescent coupling thus provides a more intrinsic and scalable route to active–passive co-integration, at the cost of tighter requirements on bonding quality and vertical stack control rather than on post-packaging mechanical alignment.

Figure 1.16(a) shows the cross-section of the heterogeneously integrated III/V-on-silicon-nitride structure implemented in [52]. A SiN waveguide (300 nm thick) is embedded in a thick SiO_2 cladding on a Si substrate. Locally, the oxide cladding is removed to create a recess. Inside this recess, a 400-nm-thick silicon coupon is first micro-transfer-printed onto a 70-nm BCB adhesive layer. On top of this silicon interposer, the III/V amplifier (containing the multi-quantum well (MQW)) is printed. BCB enables a strong bond after curing. Light couples evanescently from the low-index SiN waveguide ($n \approx 1.95$) into the silicon layer ($n \approx 3.4$) and then vertically into the III/V material.

(a)

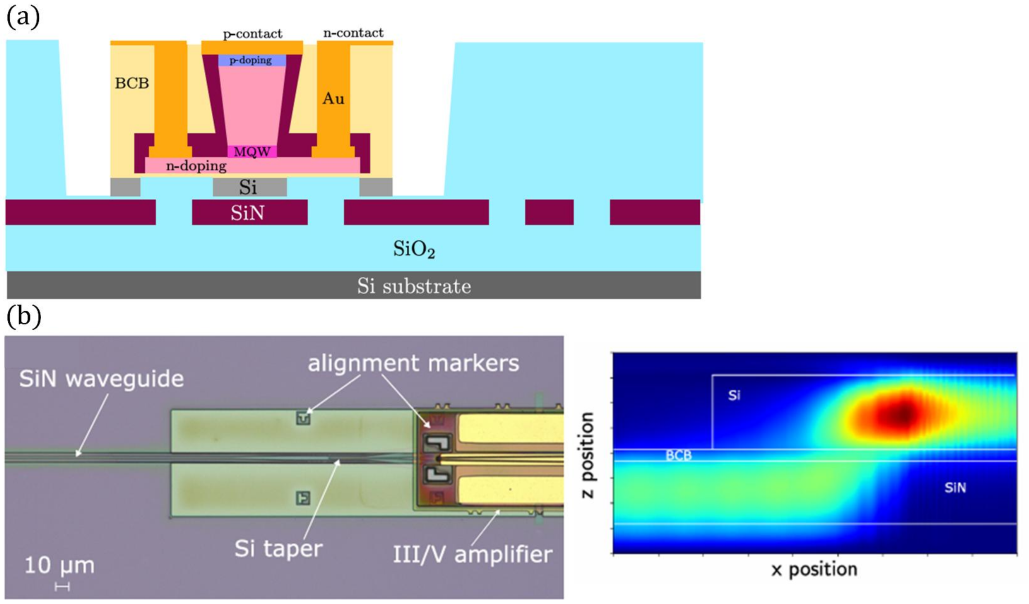

Figure 1.16: (a) Cross-section of the III–V amplifier integrated above the SiN waveguide; a silicon taper acts as adiabatic taper for the evanescent coupling between SiN and the III-V gain. (b) SEM image and simulated mode profile showing evanescent coupling from the SiN to the Si taper [52].

Figure 1.16(b) provides a top-view scanning electron microscopy (SEM) image. A SiN waveguide (visible at the bottom left) approaches the printed silicon coupon. On top of the silicon coupon lies the III/V amplifier. The key element for efficient mode transfer is the silicon taper, which is defined by electron-beam lithography after the transfer-printing step. The taper starts at the edge of the silicon coupon where it first overlaps with the SiN waveguide; its width there is approximately 2–3 µm, matching the mode size of the SiN waveguide. Over a length of 81 µm, the taper adiabatically narrows down to a 120 nm tip at the opposite end, just before the III/V active region. This long, shallow taper ensures that the optical mode is gradually transformed from the SiN waveguide into the silicon layer with minimal loss. Simulations show a transmission > 95% and negligible reflections, with tolerance to lateral misalignments up to 500 nm. Defining the taper after printing (rather than pre-patterning it) exploits the 100-nm alignment accuracy of electron-beam lithography, relaxing the constraints on the micro-transfer-printing step.

A final example of evanescent coupling between the gain section of the heterogeneously integrated III-V-on-silicon is reported in [86]. In this work, a three-part adiabatic coupling structure is implemented to enable high-efficiency, broadband light transfer between the active III-V membrane and the passive silicon waveguide. At the center, a III-V waveguide 2 µm (or 3 µm wide) confines the optical mode within the quantum-well stack and is etched through the active layer to facilitate n-type contact access. On both sides of this central region, an inverted taper

coupler is implemented in two sequential stages. Taper I reduces the III-V mesa width more abruptly, from 2 µm (or 3 µm) to 900 nm over 30 µm (or 50 µm).
Subsequently, Taper II gradually narrows the III-V mesa from 900 nm down to 300 nm over a length of 150 µm. Critically, during this same Taper II section, the underlying SOI rib waveguide is also tapered, but in the opposite direction: its width increases from 300 nm to 1 µm over the identical 150 µm length. This concurrent, inverse tapering of the III-V and SOI waveguides ensures adiabatic mode transfer with minimal loss. After the coupling region, light propagates in a 400-nm-thick silicon rib waveguide, which is then converted to a 220-nm-thick silicon device layer via a low-loss waveguide transition (30 µm length, 100 nm tip width).

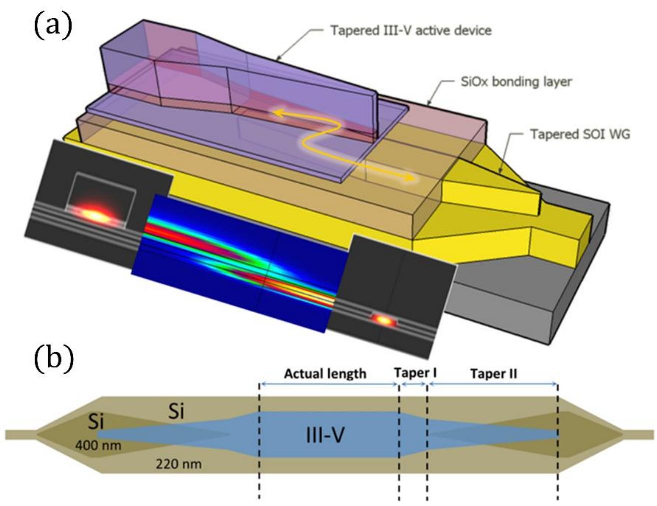

Figure 1.17: (a) Three-dimensional view of the three-levels taper coupling structure. (b) Top view of the adiabatic coupler: detailed sections of the tapers and layers [86].

1.6 SOTA of multi-wavelength lasers

This section reviews the state of the art in multi-wavelength laser sources, with particular focus on mode-locked lasers and optical frequency combs, which represent key approaches for generating stable and coherent multi-line spectra.

1.6.1 Mode-locked lasers

Mode-locking is the process through which the longitudinal modes of a laser cavity are forced to oscillate with a fixed phase relation. As a result, the laser output is no longer determined by independently oscillating cavity resonances, but by their coherent superposition.
In the time domain, this produces a stable train of ultrashort optical pulses, typically in the picosecond or femtosecond regime; in the frequency domain, it gives rise to a set of equally spaced

spectral lines [87]. For this reason, mode-locked lasers (MLLs) can be regarded at the same time as short-pulse sources and coherent multi-line optical emitters.

The most common classification distinguishes active and passive MLLs. In active mode-locking, an external electrical signal drives an intracavity modulator that periodically changes the cavity loss or phase at the round-trip frequency, or at one of its harmonics.

This approach is particularly effective for achieving high repetition rates, although the generated pulses whose widths are often longer than those obtained in passive schemes. A recent example [88] has been performed by considering lithium-niobate (LN) platform, where electrical phase modulation enabled 10 GHz operation with pulse widths around 4.8 ps and pulse energies above 2.6 pJ, showing the potential of electro-optic integrated platforms for highly controllable active mode-locking. Graphene-assisted silicon-photonic devices [89] have also recently demonstrated active mode-locking at 4 and 10 GHz, motivated in particular by applications such as low-jitter clock generation for high-speed analog-to-digital conversion.

In passive mode-locking, pulse formation occurs without an external electronic clock signal and instead relies on an intensity-dependent intracavity element, most commonly a saturable absorber (SA). SA introduces lower loss for intense light than for weak background fluctuations, thereby favoring the buildup of short pulses while suppressing low-intensity noise.

In this sense, the saturable absorber is the key physical element of passive mode-locking: as the optical intensity increases, its absorption decreases, so high-peak-power fluctuations experience less loss and are preferentially amplified over successive cavity round trips, whereas weak noise-like components remain strongly attenuated. Through this mechanism, the absorber promotes pulsed operation and enables the phase-locking of the longitudinal modes.

A wide range of saturable absorber platforms has been investigated for this purpose, including semiconductor saturable absorber mirrors (SESAMs) [90], carbon nanotubes [91],[92], two-dimensional materials such as graphene [92], and even charcoal nanoparticles [93].

In integrated semiconductor lasers, the absorber is often implemented as an electrically isolated section operated in reverse bias. Among the various material platforms, graphene has attracted particular interest because of its broadband response, ultrafast recovery time, and compatibility with scalable silicon-photonics fabrication.

Recent hybrid integrated extended-cavity lasers have demonstrated hybrid mode-locking and absorber-free passive mode-locking. Hybrid mode-locking combines active and passive pulse-shaping mechanisms within the same laser cavity and is often regarded as a particularly robust approach to pulse generation. In this configuration, a passive element, typically a saturable absorber, promotes pulse shortening, while an active modulator or external RF injection synchronizes the pulses and stabilizes the repetition rate. As a result, hybrid mode-locking brings together some of the main advantages of both schemes, namely the high stability and controllability of active mode-locking and the shorter pulse widths typically associated with passive operation [94].

A notable example is the hybrid integrated MLL diode architecture in [77], that combines a III–V active section with a low-loss SiN external-cavity reporting RF linewidths as low as 31 Hz at 2.18 GHz. At the same time, passive mode-locking does not always require a discrete saturable absorber. Absorber-free passive mode-locking can arise from nonlinear intracavity processes such as four-wave mixing (FWM), injection locking, or nonlinear polarization rotation (NPR), all of which can induce phase correlation among the cavity modes and support short-pulse formation. In these cases, phase locking originates from frequency-selective feedback and nonlinear cavity dynamics rather than from a dedicated absorber section. NPR, for example, relies on the Kerr nonlinearity of a fiber combined with a polarizer to create an effective intensity-dependent loss that favors pulse narrowing, whereas dissipative four-wave mixing (DFWM) exploits FWM together with an intracavity optical resonator filter, such as MRRs, to generate high-repetition-rate pulse trains. These approaches broaden the concept of passive mode-locking beyond conventional saturable-absorber-based implementations, show that stable pulsed operation can also be achieved through carefully engineered nonlinear dynamic and paves the way for heterogeneous platform-based external cavities systems [20].

Recent InP–SiN extended-cavity laser based on Vernier filtering demonstrated absorber-free operation around 500 MHz and, under hybrid stabilization, a detection-limited RF linewidth of about 300 mHz [95]. These results are especially significant because they show that sub-GHz mode-locking and very strong repetition-rate stabilization can be achieved even without a dedicated saturable absorber, provided that the cavity filtering and feedback are sufficiently selective.

The state of the art in passive integrated mode-locking increasingly relies on combining III–V gain with low-loss passive waveguide technologies in order to extend the cavity, reduce the repetition rate, and improve phase noise. III–V-on-silicon devices have already demonstrated very narrow RF linewidths and dense comb spectra [96], including 1 GHz line spacing with more than 1000 optical modes and RF linewidths down to 150 Hz, which made these sources attractive for dual-comb interferometry and spectroscopy. Earlier narrow-linewidth III–V-on-silicon extended-cavity lasers also reported 1.5 ps pulses at repetition rates around 4.7 GHz, confirming the benefit of low-loss passive feedback sections for noise reduction [63].

A second important classification concerns the operating regime, namely continuous-wave mode-locking (CWML) and Q-switched mode-locking (QSML). In CWML, the laser emits a regular and nearly stationary pulse train, which is generally the desired regime for stable ultrafast operation. In QSML, by contrast, short mode-locked pulses are modulated by a slower Q-switched envelope. This regime typically appears when the intracavity pulse energy is insufficient to sustain stable CWML, or when the balance among gain dynamics, absorber recovery, and cavity losses is not yet optimized. QSML is therefore usually regarded as an intermediate or less stable regime, whereas CWML corresponds to the fully developed mode-locked state. In this context, graphene-based integrated absorbers have recently shown electrically tunable passive mode-locking, offering useful control over insertion loss and absorber saturation to help reach stable CWML operation.

Another standard classification distinguishes fundamentals from harmonic mode-locking. In fundamental mode-locking, a single pulse circulates in the cavity during each round trip, so the repetition rate is equal to the cavity free spectral range, (f_{REP}). In harmonic mode-locking, multiple pulses coexist within the cavity, causing the repetition rate to become an integer multiple of the fundamental value. This regime is particularly important when very high repetition rates are required without reducing the cavity length to impractically small dimensions.

The integrated hybrid III–V/SiN long-cavity laser in [97], demonstrated passive mode-locking at a low fundamental repetition rate of f_{REP}≈364 MHz, with more than 470 optical tones, and harmonic mode-locking at 3.64 GHz with 8 ps pulses width. This low free spectral range (FSR) architecture was explicitly proposed for optically assisted radar systems, where the laser can operate as an optical RF frequency bank. At much higher repetition rates, passive harmonic mode-locking based on dissipative four-wave mixing in a microring-assisted erbium-doped fiber laser has reached 250 GHz with pulse widths as short as 875 fs [33], further highlighting the relevance of harmonic mode-locking for sub-THz pulse generation.

1.6.2 Optical frequency combs

Mode-locked lasers constitute the earliest practical realization of optical frequency combs, since they generate phase-locked pulse trains whose spectra consist of equally spaced and mutually coherent lines [98]. The defining signature of mode locking is therefore the formation of a periodic pulsed waveform in the time domain, produced by a fixed phase relationship among the longitudinal modes of an active laser cavity. By contrast, the term optical frequency comb (OFC) refers more generally to the spectral output, not implying time pulsed operation.

Whereas early comb generation relied on intracavity mode-locking mechanisms, many contemporary chip-scale comb platforms are instead driven by a continuous-wave pump laser and generate comb lines through modulation or nonlinear frequency conversion. Within the broader class of pump-conversion combs, electro-optic (EO) combs are associated primarily with $\chi^{(2)}$-mediated processes, including the Pockels effect and, in advanced platforms, second-harmonic and sum-frequency generation.

In these sources, a continuous-wave seed laser is transformed into a set of equally spaced and mutually coherent spectral lines by externally driven electro-optic modulation, rather than by pulse formation inside an active laser cavity. Accordingly, unlike mode-locked lasers, EO combs rely on the nonlinear conversion of the seed field under an applied radiofrequency or microwave drive, with the comb spacing directly determined by the electrical modulation frequency.

The underlying physical mechanism is the second-order nonlinearity $\chi^{(2)}$, most notably through the Pockels effect, whereby the refractive index of a non-centrosymmetric material varies linearly with an applied electric field.

For this reason, thin-film lithium niobate (TFLN) and related electro-optic materials have emerged as especially attractive platforms, owing to their strong Pockels response, high-speed operation, and compatibility with resonant enhancement and integrated photonics [99-101].

A key advantage of EO combs is their tunable line spacing, since the comb repetition rate can be selected and adjusted electronically via the external RF drive, rather than being fixed by the laser cavity length or by the free spectral range of a passive resonator. Although conventional integrated EO combs have often been limited by relatively modest pump-to-comb conversion efficiency, recent resonant and coupled-resonator implementations in TFLN have shown substantial progress toward broader bandwidth, higher efficiency, and shorter pulse generation.

Particularly, single-resonator EO combs in TFLN have enabled record-high comb bandwidths well beyond earlier integrated demonstrations [102], while coupled-resonator EO-comb architectures have achieved roughly two orders of magnitude improvement in conversion efficiency together with a 2.2-fold increase in bandwidth and the generation of on-chip femtosecond pulses with durations down to 336 fs [103]. More recently, hybrid Kerr–electro-optic comb generation on TFLN has further extended the functionality of this platform by combining electro-optic control with Kerr nonlinear dynamics in a single integrated device [104].

By contrast, micro-combs are governed predominantly by $\chi^{(3)}$nonlinearities, most notably the Kerr effect. In this case, a high-Q passive resonator is pumped by a continuous-wave laser, and the strong intracavity field drives parametric four-wave mixing and cascaded frequency conversion, progressively redistributing the pump into a broadband set of mutually coherent comb lines separated by the resonator free spectral range. Thus, in analogy with EO combs, microcombs are also fundamentally pump-conversion devices; however, the conversion mechanism is not electro-optic modulation, but Kerr-mediated parametric interaction enhanced by cavity buildup and strongly shaped by the resonator dispersion. The nonlinear dynamics of micro-resonator comb formation, which depend critically on dispersion engineering and cavity detuning, are addressed in the following section.

1.6.2.1 Microcomb generation in externally pumped resonators

In Kerr micro-resonators, optical frequency comb generation originates from the interaction between a continuous-wave pump laser and a high-Q resonant cavity exhibiting third-order optical nonlinearity. Under resonant field enhancement, the intracavity intensity can become sufficiently large for the Kerr effect to induce parametric frequency conversion, transforming the monochromatic pump into a series of equally spaced and mutually coherent spectral components, as shown in Fig. 1.18. The spacing between adjacent comb lines is primarily set by the resonator free spectral range.

The initial stage of this process is governed by degenerate four-wave mixing, in which two pump photons are annihilated to generate a signal-idler pair while satisfying the condition $2\omega_p = \omega_s + \omega_i$. For this process to become efficient, the cavity must simultaneously satisfy energy conservation and phase matching, with the Kerr nonlinear phase shift compensating for the dispersive phase mismatch. Comb initiation occurs when the resulting parametric gain overcomes the total cavity losses, leading to the appearance of the first symmetric sidebands around the pump resonance [103],[105]. Following the emergence of the primary parametric sidebands, further nonlinear interactions take place through non-degenerate four-wave mixing between the pump, the newly generated sidebands, and the additional frequency components that they seed. This cascading process progressively broadens the optical spectrum, showing that microcomb generation is not a single-step event but a multistage nonlinear evolution. In general, comb formation begins with the appearance of primary sidebands, continues through the development of secondary lines and sub-combs, and can ultimately evolve into a dense and coherent optical frequency comb. The final spectral bandwidth and coherence are strongly influenced by cavity dispersion, the pump conditions, and the pump-resonator detuning. The onset of this process is commonly interpreted in terms of modulation instability (MI).

In Kerr micro-resonators, MI describes the breakup of the intracavity continuous-wave field into discrete sidebands as a result of the interplay between Kerr nonlinearity and group-velocity dispersion. From this perspective, modulation instability provides the dynamical route by which the first comb lines emerge from the pumped continuous-wave state, and it may be regarded as the cavity-enhanced manifestation of degenerate four-wave mixing at the initial stage of comb formation.

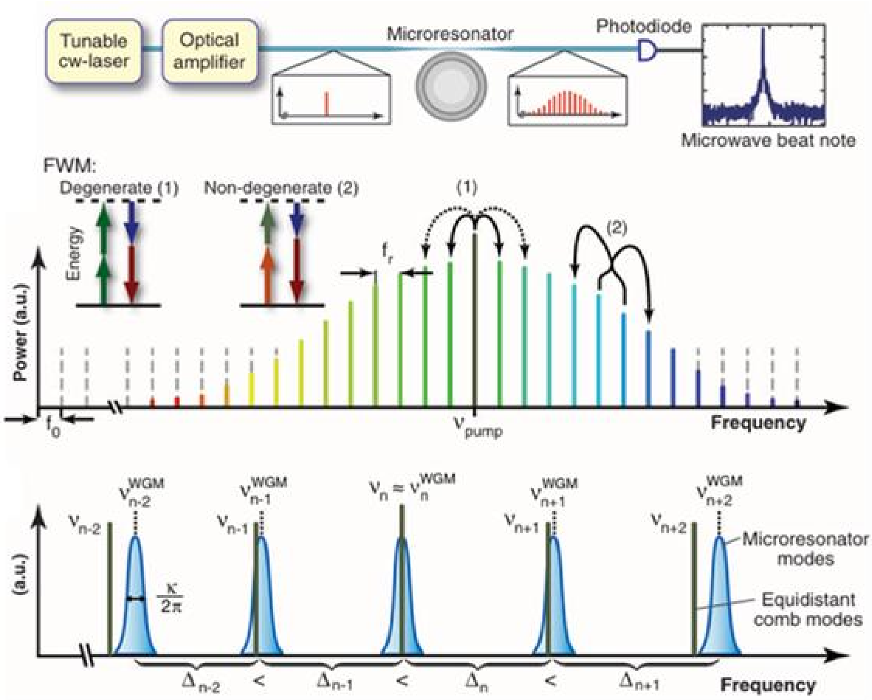

Fig. 1.18: Schematic of optical frequency-comb generation in a micro-resonator. A continuous wave pump excites a cavity resonance, initiating degenerate and then cascaded non-degenerate four-wave mixing, which generates equally spaced comb lines with repetition rate f_r and offset f_0. In the bottom panel, the blue peaks correspond to the discrete resonant modes of the microresonator, whereas the green lines represent the ideally equidistant comb modes. The degree of overlap between these two sets of modes determines the efficiency of comb generation and is progressively affected by cavity dispersion, which modifies the resonator mode spacing across the spectrum. The picture is extracted from Ref. [103].

Several physical parameters determine the efficiency, threshold, and stability of microcomb generation. Among these parameters, the resonator quality factor Q governs the degree of intracavity field enhancement and thus has a strong influence on the thresholds for parametric oscillation and modulation instability. High-Q resonators are particularly advantageous, as they significantly lower the pump power required to initiate comb generation.

The pump power is also a critical parameter, as the nonlinear gain must exceed the total cavity loss for parametric sidebands to grow. The free spectral range sets the comb line spacing, while the cavity linewidth and overall optical losses determine the resonance sharpness and the threshold for parametric oscillation. The effective modal volume and the Kerr nonlinear coefficient further control the strength of the nonlinear interaction, with smaller volume and stronger nonlinearity generally favoring more efficient comb formation [105].

A key control parameter is the laser-cavity detuning, defined as the frequency offset between the pump laser and the cavity resonance, which determines the intra-cavity power buildup and, consequently, strongly influences which nonlinear operating state can be accessed.

It is important to distinguish between the cold-cavity detuning, defined with respect to the unperturbed resonance of the passive cavity, and the hot-cavity detuning, which includes resonance shifts induced during operation by Kerr and thermal effects. In strongly driven micro-resonators, these shifts can significantly displace the actual resonance from their cold-cavity value, so that the true operating point differs markedly from the nominal detuning. [106-108].

Within this detuning-dependent landscape, the nonlinear dynamics of a Kerr micro-resonator generally unfold through a sequence of intermediate states rather than through a direct transition from continuous-wave pumping to a fully coherent comb state. When multiple sub-combs coexist with slightly different offset frequencies or repetition rates, the system may enter a chaotic modulation-instability regime characterized by enhanced radio-frequency noise, reduced temporal coherence, and pronounced amplitude fluctuations. Upon further variation of the pump-resonator detuning, this high-noise state can collapse abruptly into a coherent pulsed regime, a transition that is frequently identified experimentally through discrete steps in the transmitted or intracavity power and is widely associated with the formation of dissipative soliton states as shown in Fig. 1.19. [102],[105],[106].

The accessibility and nature of these nonlinear states are governed by the dispersion landscape of the resonator, since dispersion determines both the existence of modulation-instability gain and the efficiency of phase matching for four-wave mixing [104],[105].

In the anomalous-dispersion regime, where $\beta_2 < 0$, MI is naturally supported because the Kerr-induced nonlinear phase shift can be balanced by negative group-velocity dispersion. This regime therefore constitutes the conventional domain for bright Kerr combs and bright dissipative Kerr solitons, including multi-soliton and single-soliton states. In the time domain, such states correspond to localized high-intensity pulses circulating on top of a weak continuous background within the resonator. Bright solitons produce flat and broad spectra, with a conversion efficiency limited to around 1%, decreasing as the number of comb lines increases [109].

By contrast, in the normal-dispersion regime, where $\beta_2 > 0$, conventional modulation instability is generally suppressed because the phase-matching condition is not intrinsically satisfied and often require auxiliary phase-matching mechanisms for comb initiation.

In this regard, comb formation may still occur when local effective anomalous dispersion is introduced through mode coupling, avoided mode crossings, or other forms of dispersion engineering. Under these conditions, the coherent operating state is more commonly a dark-pulse or dark-soliton-like structure rather than a bright soliton.

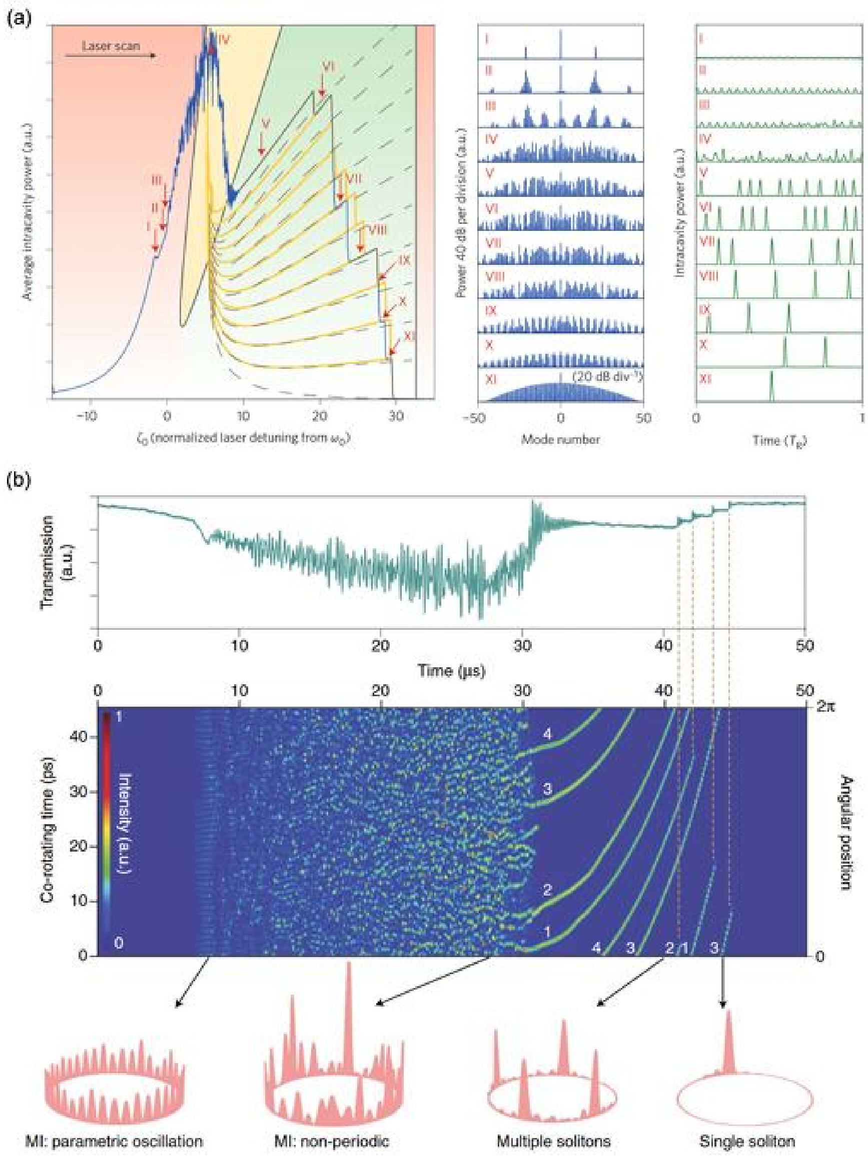

Fig. 1.19: Dynamic evolution of mode-locked soliton formation in a micro-resonator: (a) Simulated intracavity power trace showing soliton (green), breather (yellow), and no-soliton (red) states. (b) Experimental soliton steps—pump transmission, spatiotemporal imaging, and cavity-frame intensity patterns. Picture is extracted from Ref. [102].

Such states theoretically offer a high conversion efficiency of over 50% [110], while their spectra are narrow and irregular. Near-zero-dispersion devices represent a dispersion-engineered subset of Kerr microcombs rather than a distinct nonlinear mechanism, since comb generation still relies on Kerr-mediated parametric frequency conversion. In such devices, the small magnitude of the second-order dispersion enhances the relative impact of higher-order dispersion terms, which strongly influence phase matching, dispersive-wave emission, spectral shaping, and the accessible nonlinear states [111-113].

Hybrid-assisted configurations, in which Kerr dynamics are modified by mode hybridization, coupled resonators, Raman or Brillouin interactions, or the coexistence of Kerr and thermo-optic effects, provide additional degrees of freedom for tailoring comb formation and coherent-state accessibility [114].

1.6.2.2 Advanced microcombs generation

Representative recent studies show that Kerr microcomb platforms have expanded well beyond the canonical single microring, encompassing Fabry–Pérot resonators with mirror-defined dispersion, normal-dispersion coupled-ring architectures, photonic-molecule soliton systems, and efficiency-optimized coupled anomalous-dispersion micro-resonators. Each mechanism modifies the accessible comb states and performance characteristics in a distinct manner.

An early demonstration of dispersion-engineered Kerr microcombs in the normal-dispersion regime was reported using a dual-coupled SiN microring platform, where comb initiation was not driven by the natural anomalous-dispersion modulation-instability pathway but instead by thermally controlled mode interactions between a main ring and an auxiliary ring [115]. In this device, the main ring operated in a clearly normal-dispersion regime, while the auxiliary ring was equipped with an integrated microheater that tuned its resonances to selectively split individual modes of the coupled system, creating avoided crossings that locally restore the phase-matching conditions required for four-wave-mixing-based comb initiation. Figure 1.20(a) illustrates this concept: a microscope image of the dual-ring structure and the heater, together with a measured comb spectrum and a zoom-in of the avoided-crossing region in the resonance map, highlight how a single engineered mode interaction can seed broadband comb generation in an otherwise normal-dispersive cavity. By adjusting the heater power, the authors could program which sideband mode experiences the strongest splitting, thereby controlling the effective local dispersion and enabling repetition-rate-selectable combs with spacings from approximately one to six free spectral ranges, corresponding to repetition rates from about 378 GHz up to 2.27 THz at an on-chip pump power of 0.5 W. Fine tuning of the heater allowed additional repetition-rate adjustment on the order of 390 MHz for a 20 mW heater change, while at higher pump powers the system underwent a transition from a noisy comb to a low-noise, phase-locked state with a 10-dB optical bandwidth of about 120 nm and compressed pulses of roughly 130 fs after line-by-line phase compensation, confirming the high coherence of the normal-dispersion microcomb.

This concept was subsequently extended in an analogous photonic-molecule approach, in which two linearly coupled micro-resonators were used not only to initiate comb formation but also to introduce an additional synthetic degree of freedom for the generation and control of dissipative Kerr solitons [116]. The main cavity again operated in the normal-dispersion regime, while the auxiliary cavity, equipped with an integrated platinum microheater, was used to tune the frequency of a targeted resonance into degeneracy with a mode of the main ring, thereby creating a controllable split resonance. Figure 1.20(b) illustrates the vertically coupled main and auxiliary rings with the heater patterned above the auxiliary cavity, and the accompanying spectra compare two soliton microcombs obtained when the pump is aligned to a shorter-wavelength (blue-shifted) split resonance and to a longer-wavelength (red-shifted) split resonance, highlighting how the same device can generate blue- and red-shifted soliton spectra with conversion efficiencies of $\eta = 0.32$ and $\eta = 0.49$, respectively.

The fabricated photonic molecules exhibited mean intrinsic quality factors around 5.7×10^6, with FSRs of 104.84 GHz and 106.9 GHz for the main and auxiliary rings and supported broadly tunable DKS microcombs over roughly 40 nm within the C-band (1530–1570 nm) at nearly constant on-chip pump power between about 13 and 18 mW. As the pump was tuned from the shorter-wavelength (blue) doublet to the longer-wavelength (red) doublet, the measured conversion efficiency increased from 32% to 49%, reflecting the wavelength-dependent coupling and effective critical-coupling condition of the photonic molecule.

Moreover, by exploiting the enlarged DKS existence region at lower pump power, stable, spectrally flat soliton combs could still be generated with only 2.5 mW of on-chip pump power, yielding a conversion efficiency of 36% and more than 12 μW per comb line with a comparatively uniform spectral envelope.

These results demonstrate that coupled-cavity Kerr-comb platforms can simultaneously improve the accessibility of DKS states in pump–detuning space and deliver a practically attractive combination of high conversion efficiency, spectral flatness, low-power operation, and wavelength-tunable soliton spectra that can be shifted between blue- and red-detuned configurations by reconfiguring the split resonance of the photonic molecule.

Continuous-wave-driven dissipative Kerr solitons have also been realized in integrated Fabry–Pérot cavity with nanostructured photonic-crystal mirrors [117].

In this platform, comb generation still follows the standard sequence of modulation instability and subsequent soliton formation under blue-to-red pump tuning; however, the dispersion is dominated by the engineered mirror response rather than by the waveguide geometry.

(a)
(b)
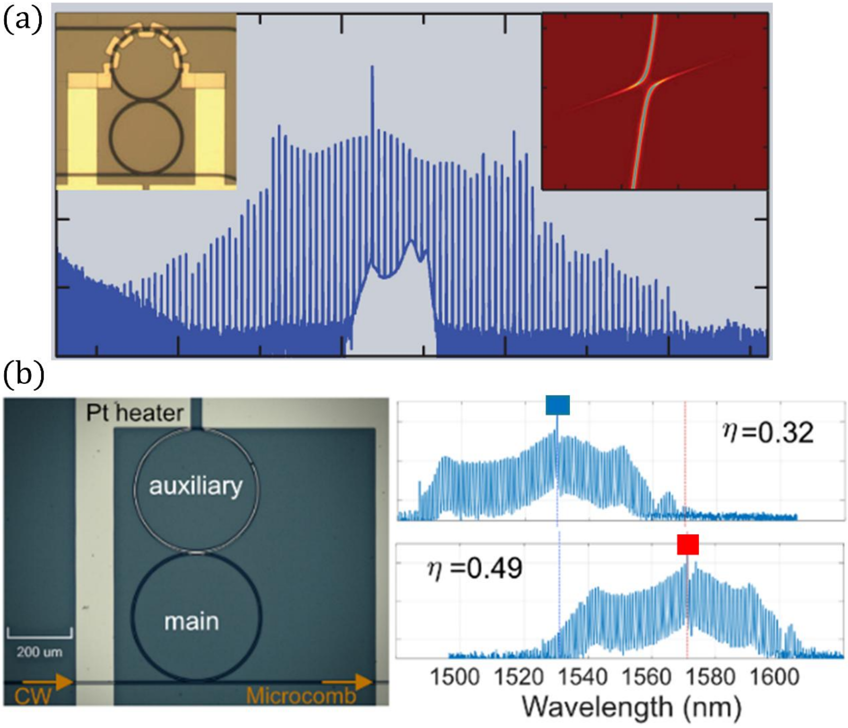

Fig. 1.20: Photonic molecules for tunable microcombs: (a) Comb envelope and resonance splitting overview obtained in [115], and (b) Heater tuning shifts crossing points, enabling pump-tuned wavelength-selectable microcombs with varying pump-to-comb efficiencies ($\eta = 0.32{,}0.49$) [116].

This mirror-mediated dispersion control allows the Fabry–Pérot cavity to access both normal- and anomalous-dispersion regimes and, in contrast to ring resonators, eliminates counter-propagating modes associated unintentional mode splitting that can perturb soliton formation.

The devices achieved average intrinsic linewidths of about 47 MHz, with FSR ≈ 18.55 GHz, and more strongly coupled soliton devices exhibited total linewidths on the order of 56 MHz.

Figure 1.21(a) shows the experimental setup used to excite solitons: a TM-polarized pump laser is amplified and injected into the FP cavity via a circulator that collects the reflection dips from the resonator. An auxiliary TE-polarized laser is co-propagated to thermally stabilize the resonance during the pump scan.

Soliton states are accessed by tuning the laser pump from the blue to the red side of a cavity resonance in the anomalous-dispersion regime (at 1587 nm), so that the intracavity field first undergoes modulation instability and then transitions to quantized power steps corresponding to single- and multi-soliton states, as illustrated in the laser transmission response of Fig. 1.21(b) and the associated RF spectra as function of the time scans in Fig. 1.21(c).

The final single-soliton spectrum corresponded to a transform-limited pulse duration of about 300 fs. This work established that coherent Kerr-comb generation is not limited to travelling-wave topologies and can be implemented in standing-wave architectures with engineered dispersion.

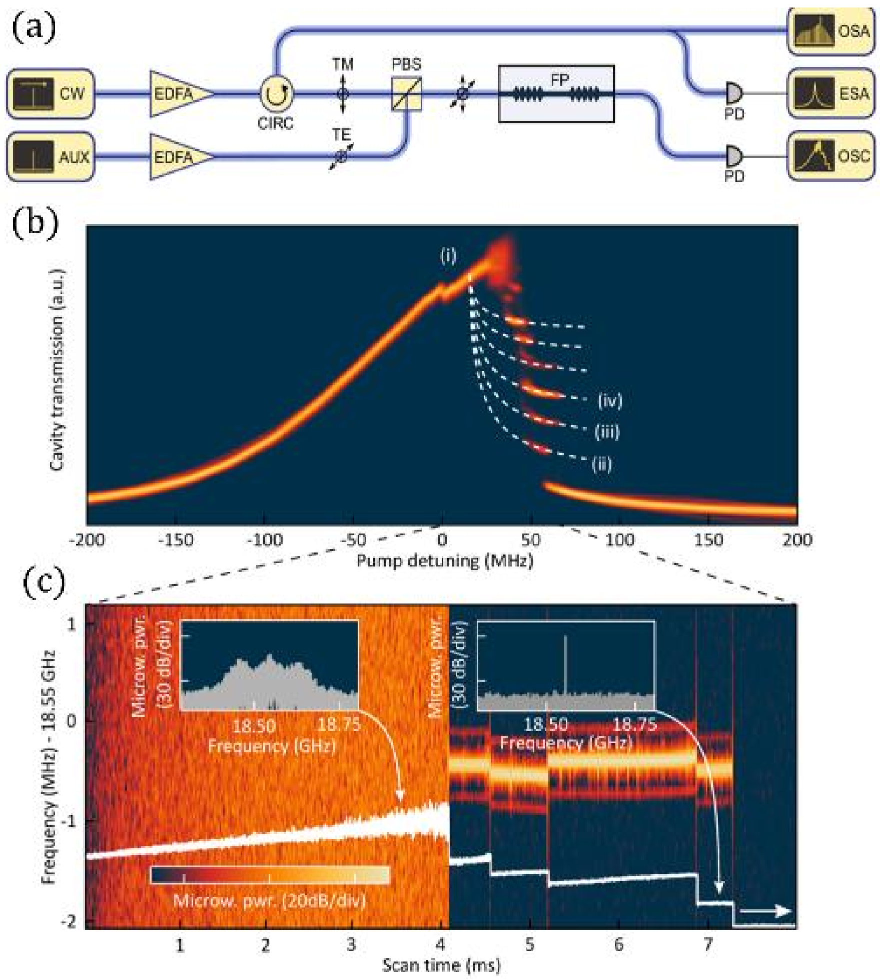

Fig. 1.21: Soliton generation in chip-integrated photonic crystal Fabry-Pérot cavities: (a) schematic setup, (b)-(c) cavity transmission as function of pump detuning, and corresponding RF power spectra during soliton formation scans (i–iv) [117].

Coupled-cavity engineering has further been used to address one of the main practical limitations of bright anomalous-dispersion soliton combs, namely their typically low pump-to-comb conversion efficiency under single-cavity continuous-wave pumping.

In a high-efficiency coupled-resonator architecture [118], two linearly coupled anomalous-dispersion SiN MRRs are employed to impose a controllable frequency shift on the pumped resonance of the main cavity, thereby decoupling the usual link between pump detuning and intracavity coupling that limits bright-soliton efficiency in single resonators.

The pump laser is coupled into the bus waveguide and amplified before exciting the main ring, while an auxiliary, smaller-FSR ring is side-coupled to the main cavity to create a controlled modes hybridization that selectively shifts only the pumped longitudinal mode, leaving the rest of the comb modes essentially unperturbed.

Figure 1.22 illustrates the schematic of the proposed microcomb laser: a continuous wave fiber laser, filtered and amplified, is edge-coupled to the chip hosting the photonic-molecule device, and the generated soliton comb is monitored via an optical spectrum analyzer and a high-speed photodiode connected to RF diagnostics, while the inset in the bottom part of the figure highlights the main and auxiliary cavities and their coupling region on the chip.

This engineered pump-mode shift allows the laser to remain close to the center of the shifted resonance, so that the pump is efficiently coupled into the cavity while the comb lines experience the large effective red detuning needed to sustain a single dissipative Kerr soliton.

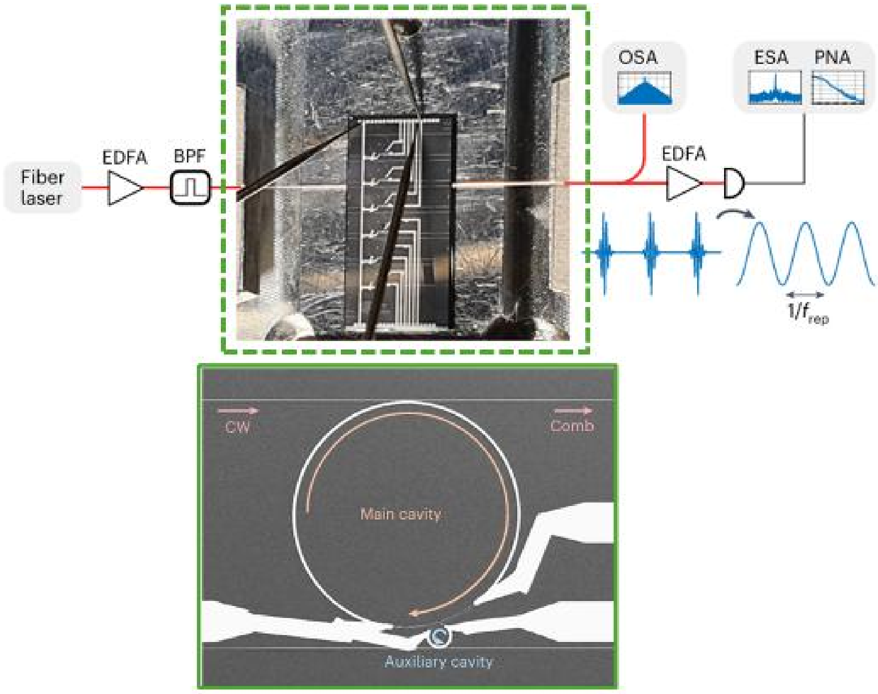

Fig. 1.22: Schematic of the photonic-molecule microcomb setup implemented in [118], showing a zoom-in of the main and auxiliary cavities with integrated heater pads powered via electrical probes.

The resulting DKS microcombs exhibit conversion efficiencies exceeding 50%, with a remarkably flat spectrum (35 consecutive lines above −13 dBm and 73 lines above a slightly lower power level). The same concept, implemented in a larger-radius photonic molecule, yields a 49.85 GHz repetition-rate soliton comb with about 35% conversion efficiency and a narrow, low-phase-noise RF beat note directly suitable for microwave-photonics applications.

Finally, soliton Kerr microcombs have been demonstrated in a compact, electrically driven architecture that dispenses with external pump lasers, feedback electronics, and active temperature control while remaining compatible with CMOS-oriented integration [119].

In this reference, an ultra-low-loss SiN microresonator is combined with an electrically pumped RSOA to form a dual-cavity system, in which the high-Q microresonator is embedded directly inside the external-cavity laser so that lasing and comb generation are co-designed on chip.
As schematized in Fig. 1.23(a), the RSOA is edge-coupled to the SiN chip, Vernier microring filters and an adjustable cavity-phase section select and tune the lasing wavelength, and the main microresonator provides both a narrowband back-reflection (due to frequency degenerate counter-propagating modes originated by backscattering) that closes the laser cavity and the nonlinear four-wave-mixing interaction responsible for Kerr-comb formation.By eliminating the bulky, power-hungry external lasers used in earlier demonstrations, this self-contained dual-cavity design offers a practical route toward portable precision-comb systems, including battery-operated operation.

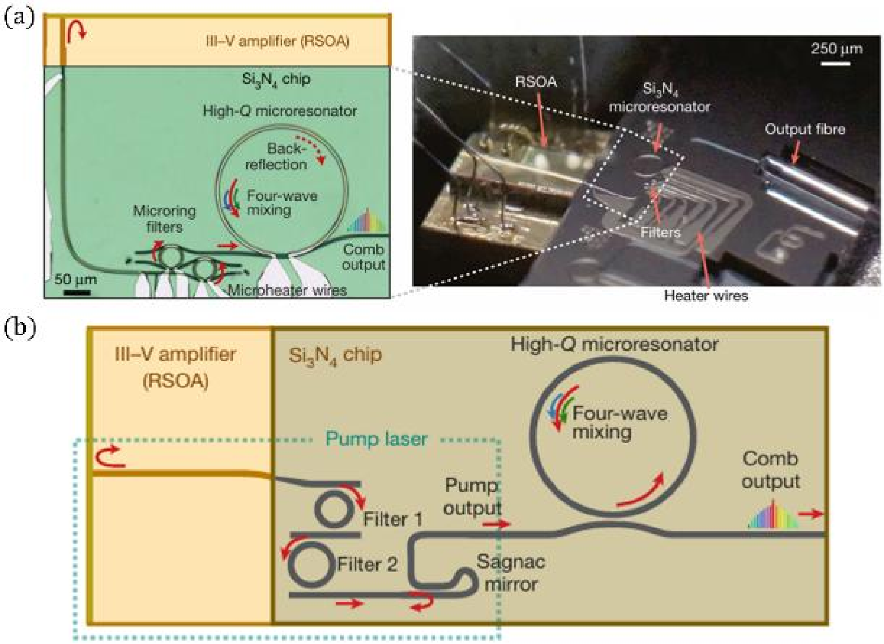

Fig. 1.23: Two different microcomb sources implemented in [119]: (a) RSOA gain chip coupled to SiN tunable microring filters and high-Q nonlinear micro-resonator acting as second cavity reflector in the generated external-cavity laser. (b) Integrated pump laser (RSOA with Sagnac loop mirror and microring filters) injected into high-Q resonator for comb generation.

In the primary integrated configuration, as the microresonator is thermally tuned into resonance with the on-chip laser, the device evolves from single-frequency lasing to a noisy, chaotic comb and finally to a mode-locked single-soliton state with the characteristic sech^2 spectrum and strong RF-noise suppression. The latter, yields a 194-GHz-repetition-rate comb near 1550 nm that spans more than 8 THz and exhibits an optical linewidth of about 40 kHz, all using only 98 mW of electrical pump power, sufficient for operation from a standard AAA battery. A more modular variant, schematically illustrated in Fig. 1.23(b), separates the laser cavity from the nonlinear resonator by inserting a broadband Sagnac loop mirror as the laser output coupler.

In this case, the integrated laser first operates independently, and tuning the second resonator into resonance generates a multiple-soliton comb spanning 13.4 THz (105 nm) with a measured conversion efficiency of 1.6%, demonstrating the flexibility of the platform in trading efficiency, bandwidth, and control over the pump and comb sections.

1-References

[1] Shekhar, Sudip, et al. "Roadmapping the next generation of silicon photonics." *Nature Communications* 15.1 (2024): 751.

[2] Liang, Di, and John E. Bowers. "Recent progress in heterogeneous III-V-on-silicon photonic integration." *Light: Advanced Manufacturing* 2.1 (2021): 59-83.

[3] J. M. Ramirez *et al*., "III-V-on-Silicon Integration: From Hybrid Devices to Heterogeneous Photonic Integrated Circuits," in *IEEE Journal of Selected Topics in Quantum Electronics*, vol. 26, no. 2, pp. 1-13, March-April 2020.

[4] Carroll, Lee, et al. "Photonic packaging: transforming silicon photonic integrated circuits into photonic devices." *Applied Sciences* 6.12 (2016): 426.

[5] Komljenovic, Tin, et al. "Photonic integrated circuits using heterogeneous integration on silicon." *Proceedings of the IEEE* 106.12 (2018): 2246-2257.

[6] Coldren, Larry A., Scott W. Corzine, and Milan L. Mashanovitch. *Diode lasers and photonic integrated circuits*. John Wiley & Sons, 2012.

[7] Wang, Yi, Yuqing Jiao, and Kevin Williams. "Scaling photonic integrated circuits with InP technology: A perspective." *APL Photonics* 9.5 (2024).

[8] Albeladi, F. T., et al. "On-chip gain elements for integrated photonics." *Optics Express* 33.25 (2025): 52356-52372.

[9] Siew, Shawn Yohanes, et al. "Review of silicon photonics technology and platform development." *Journal of Lightwave Technology* 39.13 (2021): 4374-4389.

[10] Baets, Roel, et al. "Silicon photonics: Silicon nitride versus silicon-on-insulator." *Optical fiber communication conference*. Optica Publishing Group, 2016.

[11] Xiang, Chao, Warren Jin, and John E. Bowers. "Silicon nitride passive and active photonic integrated circuits: trends and prospects." *Photonics research* 10.6 (2022): A82-A96.

[12] Ricchiuti, Giovanna. Novel approaches in mid-IR photothermal spectroscopy (PTS): from the benchtop to the chip. Ph.D. Diss. TU Wien, 2024.

[13] Liu, Junqiu. Silicon nitride integrated nonlinear photonics. Ph.D. Diss. EPFL, 2020.

[14] Dai, Daoxin, Jared Bauters, and John E. Bowers. "Passive technologies for future large-scale photonic integrated circuits on silicon: polarization handling, light non-reciprocity and loss reduction." Light: Science & Applications 1.3 (2012): e1-e1

[15] Stutius, W., and W. Streifer. "Silicon nitride films on silicon for optical waveguides." *Applied Optics* 16.12 (1977): 3218-3222.

[16] Nejadriahi, Hani, et al. "Thermo-optic properties of silicon-rich silicon nitride for on-chip applications." *Optics Express* 28.17 (2020): 24951-24960.

[17] Mroziewicz, B. "External cavity wavelength tunable semiconductor lasers-a review." *Opto-Electronics Review* 16.4 (2008): 347-366.

[18] Moss, David. "Review of Sagnac interference based integrated photonic devices." (2023).

[19] Zhao, Ruiling, et al. "Hybrid dual-gain tunable integrated InP-Si3N4 external cavity laser." *Optics Express* 29.7 (2021): 10958-10966.

[20] Davenport, Michael L., Songtao Liu, and John E. Bowers. "Integrated heterogeneous silicon/III–V mode-locked lasers." *Photonics Research* 6.5 (2018): 468-478.

[21] Xu, Hongnan, et al. "Million-Q integrated Fabry-Perot cavity using ultralow-loss multimode retroreflectors." *Photonics Research* 10.11 (2022): 2549-2559.
[22] Han, Liangshun. "1D photonic crystals: principles and applications in silicon photonics." *Theoretical foundations and application of photonic crystals*. IntechOpen, 2017.
[23] Ortega-Moñux, Alejandro, et al. "Silicon photonic Bragg grating structures for spectral filtering." *Integrated Optics: Devices, Materials, and Technologies XXVIII*. SPIE, 2024.
[24] Iadanza, Simone, et al. "Thermally stable hybrid cavity laser based on silicon nitride gratings." *Applied optics* 57.22 (2018): E218-E223.
[25] Siddharth, Anat, et al. "Piezoelectrically tunable, narrow linewidth photonic integrated extended-DBR lasers." *Optica* 11.8 (2024): 1062-1069.
[26] Pan, Shilong, et al. "Reflective-type microring resonator for on-chip reconfigurable microwave photonic systems." *IEEE Journal of Selected Topics in Quantum Electronics* 26.5 (2020): 1-12.
[27] Wu, Yilin, et al. "Ultra-low-noise hybrid III–V/Si3N4 laser achieving wide-range wavelength switching." *APL Photonics* 10.4 (2025).
[28] Boller, Klaus-J., et al. "Hybrid integrated semiconductor lasers with silicon nitride feedback circuits." *Photonics*. Vol. 7. No. 1. Multidisciplinary Digital Publishing Institute, 2020.
[29] Lin, Yi, et al. "Characterization of hybrid InP-TriPleX photonic integrated tunable lasers based on silicon nitride (Si3N4/SiO 2) microring resonators for optical coherent system." *IEEE photonics journal* 10.3 (2018): 1-8.
[30] Fan, Youwen, et al. "Optically Integrated InP–Si3N4 Hybrid Laser." *IEEE photonics journal* 8.6 (2016): 1-11.
[31] Monopoli, Davide, et al. "Fabry-Pérot cavity in SiN for non-linear applications." *British and Irish Conference on Optics and Photonics*. Optica Publishing Group, 2024.
[32] Ulanov, Alexander E., et al. "Laser diode self-injection locking to an integrated high-Q Fabry–Perot microresonator." *Optics Letters* 49.21 (2024): 6261-6264.
[33] Jyu, Siao-Shan, et al. "250-GHz passive harmonic mode-locked Er-doped fiber laser by dissipative four-wave mixing with silicon-based micro-ring." *IEEE Photonics Journal* 5.5 (2013): 1502107-1502107.
[34] Liles, Alexandros A., Kapil Debnath, and Liam O'Faolain. "Lithographic wavelength control of an external cavity laser with a silicon photonic crystal cavity-based resonant reflector." *Optics Letters* 41.5 (2016): 894-897.
[35] Raja, Arslan S., et al. "Chip-based soliton microcomb module using a hybrid semiconductor laser." *Optics Express* 28.3 (2020): 2714-2721.
[36] https://chilasbv.com/technology/
[37] https://www.lionix-international.com/
[38] Van Rees, Albert, et al. "Ring resonator enhanced mode-hop-free wavelength tuning of an integrated extended-cavity laser." *Optics express* 28.4 (2020): 5669-5683.
[39] van Rees, Albert, et al. "Long-Term Absolute Frequency Stabilization of a Hybrid-Integrated InP-Si 3 N 4 Diode Laser." *IEEE Photonics Journal* 15.5 (2023): 1-8.
[40] Fan, Youwen, et al. "Hybrid integrated InP-Si3N4 diode laser with a 40-Hz intrinsic linewidth." *Optics express* 28.15 (2020): 21713-21728.
[41] Epping, Jörn P., et al. "High power, tunable, narrow linewidth dual gain hybrid laser." *Advanced Solid State Lasers*. Optica Publishing Group, 2019.
[42] Maier, Pascal, et al. "Sub-kHz-Linewidth External-Cavity Laser (ECL) With Si3N4 Resonator Used as a Tunable Pump for a Kerr Frequency Comb." *Journal of Lightwave Technology* 41.11 (2023): 3479-3490.
[43] Lihachev, Grigory, et al. "Frequency agile photonic integrated external cavity laser." *APL Photonics* 9.12 (2024).
[44] Liu, Yang, et al. "A fully hybrid integrated erbium-based laser." *Nature Photonics* 18.8 (2024): 829-835.
[45] Katsumi, R. et al. Micro-transfer printing for heterogeneous integration of III–V devices on silicon photonics. *Optica* 7, 121–127 (2020).
[46] Justice, J. et al. Transfer printing for heterogeneous integration of semiconductor photonic

devices. *IEEE Photonics Technology Letters* 24, 1371–1374 (2012).
[47] Roelkens, G. et al. III–V/Si photonics by heterogeneous integration. *Laser & Photonics Reviews* 4, 751–779 (2010).
[48] Roelkens, Gunther, et al. "Micro-transfer printing for heterogeneous Si photonic integrated circuits." *IEEE Journal of selected topics in quantum electronics* 29.3: Photon. Elec. Co-Inte. and Adv. Trans. Print. (2022): 1-14.
[49] Loi, Ruggero, et al. "Thermal analysis of InP lasers transfer printed to silicon photonics substrates." Journal of lightwave technology 36.24 (2018): 5935-5941.
[50] Kiewiet, Max, et al. "Micro-Transfer Printed Continuous-Wave and Mode-Locked Laser Integration at 800 nm on a Silicon Nitride Platform." *Laser & Photonics Reviews* 20.7 (2026): e00956.
[51] Uvin, Sarah, et al. "Narrow line width frequency comb source based on an injection-locked III–V-on-silicon mode-locked laser." *Optics Express* 24.5 (2016): 5277-5286.
[52] Poelman, Stijn, et al. "High-power heterogeneously integrated mode-locked laser enabled by a booster amplifier." *Optics Express* 33.26 (2025): 54747-54756.
[53] Palesko, Amy, and Chet Palesko. "Cost and Yield Comparison of Wafer-to-Wafer, Die-to-Wafer, and Die-to-Die Bonding." *International Symposium on Microelectronics*. Vol. 2014. No. 1. International Microelectronics Assembly and Packaging Society, 2014.
[54] Sanchez, Loic, et al. "Collective die direct bonding for photonic on silicon." *Electrochemical Society Transactions aimes2018* 86.5 (2018): 223-231.
[55] Xu, Pengfei, et al. "Collective die-to-wafer bonding enabling low-loss evanescent coupling for optically interconnected System-on-Wafer." *IEEE Transactions on Components, Packaging and Manufacturing Technology* 16.1 (2025): 186-197.
[56] Liang, Di, et al. "Hybrid integrated platforms for silicon photonics." *Materials* 3.3 (2010): 1782-1802.
[57] Davenport, Michael L., et al. "Heterogeneous integration of III–V lasers on Si by bonding." *Semiconductors and Semimetals*. Vol. 99. Elsevier, 2018. 139-188.
[58] Srinivasan, S., et al. "Coupled-ring-resonator-mirror-based heterogeneous III–V silicon tunable laser." *IEEE Photonics Journal* 7.3 (2015): 1-8.
[59] Santis, Christos T., et al. "Sub-kHz quantum linewidth semiconductor laser on silicon chip." *2015 Conference on Lasers and Electro-Optics (CLEO)*. IEEE, 2015.
[60] Roelkens, Gunther, et al. "Wafer bonding and heterogeneous integration: III-V/silicon photonics." *14th European Conference on Integrated Optics*. Vol. 191. 2008.
[61] Roelkens, Gunther, et al. "III-V-on-silicon photonic devices for optical communication and sensing." *Photonics*. Vol. 2. No. 3. MDPI, 2015.
[62] Niklaus, Frank, et al. "Adhesive wafer bonding." *Journal of applied physics* 99.3 (2006).
[63] Keyvaninia, Shahram, et al. "Narrow-linewidth short-pulse III-V-on-silicon mode-locked lasers based on a linear and ring cavity geometry." *Optics express* 23.3 (2015): 3221-3229.
[64] Wang, Z., Van Gasse, K., Moskalenko, V. *et al.* A III-V-on-Si ultra-dense comb laser. *Light Sci Appl* **6**, e16260 (2017).
[65] Sodagar, Majid, et al. "High-efficiency and wideband interlayer grating couplers in multilayer Si/SiO2/SiN platform for 3D integration of optical functionalities." *Optics express* 22.14 (2014): 16767-16777.
[66] Singaravelu, P. K. J. et al. Low-loss, compact, spot-size-converter based vertical couplers for photonic integrated circuits. J. Phys.D: Appl. Phys. 52, 214001 (2019).
[67] Sun, P. & Reano, R. M. Vertical chip-to-chip coupling between silicon pho tonic integrated circuits using cantilever couplers. Opt. Express 19,4722–4727 (2011). 165.
[68] Atsumi, Yuki, et al. "Vertically-curved Si surface optical coupler for coupling with standard single-mode optical fibers." *Optical Fiber Communication Conference*. Optica Publishing Group, 2020.
[69] Qvotrup, C. et al. Curved GaAs cantilever waveguides for the vertical coupling to photonic integrated circuits. Opt. Express 32,3723–3734 (2024).
[70] Van Thourhout, Dries, et al. "Coupling mechanisms for a heterogeneous silicon nanowire platform." *Semiconductor Science and Technology* 23.6 (2008): 064004.

[71] Ahmed, T. Optical Quilt Packaging: A New Chip to Chip Optical Coupling and Alignment Technique. Ph.D. thesis, University of Notre Dame (2017).
[72] Zhu, Yiran, et al. "Integrated Electro-Optically Tunable Narrow-Linewidth III–V Laser." *Advanced Photonics Research* 5.11 (2024): 2400018.
[73] He, An, et al. "Ultra-Low Loss SiN Edge Coupler for III-V/SiN Hybrid Integration." *Laser & Photonics Reviews* 17.10 (2023): 2300100.
[74] Matsumoto, T. et al. Hybrid-integration of SOA on silicon photonics platform based on flip-chip bonding. J. Lightwave Technol. 37,307–313 (2019).
[75] Weninger, Drew, et al. "Graded index couplers for next generation chip-to-chip and fiber-to-chip photonic packaging." *Journal of Physics: Photonics* 8.1 (2026): 015005.
[76] Weninger, Drew, et al. "Advances in waveguide-to-waveguide couplers for 3D integrated photonic packaging." *Light: Science & Applications* 15.1 (2026): 17.
[77] Vissers, Ewoud, et al. "Hybrid integrated mode-locked laser diodes with a silicon nitride extended cavity." *Optics Express* 29.10 (2021): 15013-15022.
[78] Xu, Yilin, et al. "Hybrid external-cavity lasers (ECL) using photonic wire bonds as coupling elements." *Scientific Reports* 11.1 (2021): 16426.
[79] Thomson, David, et al. "Roadmap on silicon photonics." *Journal of Optics* 18.7 (2016): 073003.
[80] Zhang, Yu, et al. "High-density wafer-scale 3-D silicon-photonic integrated circuits." *IEEE Journal of Selected Topics in Quantum Electronics* 24.6 (2018): 1-10.
[81]Zhang, Yichi, et al. "Low-loss and broadband wafer-scale optical interposers for large-scale heterogeneous integration." *Optics Express* 32.1 (2023): 40-51.
[82] Lamponi, M., et al. "Low-threshold heterogeneously integrated InP/SOI lasers with a double adiabatic taper coupler." *IEEE photonics technology letters* 24.1 (2011): 76-78.
[83] Huang, Qiangsheng, et al. "Ultracompact tapered coupler for the Si/III–V heterogeneous integration." *Applied optics* 54.14 (2015): 4327-4332.
[84] He, An, et al. "Ultra-compact coupling structures for heterogeneously integrated silicon lasers." *Journal of Lightwave Technology* 38.15 (2020): 3974-3982.
[85] Stanković, Stevan, et al. "Die-to-die adhesive bonding for evanescently-coupled photonic devices." *Electrochemical Society Transactions 218* 33.4 (2010): 411-420.
[86] Keyvaninia, Shahram, et al. "Demonstration of a heterogeneously integrated III-V/SOI single wavelength tunable laser." *Optics express* 21.3 (2013): 3784-3792.
[87] Garside, B. K., and T. K. Lim. "Laser mode locking using saturable absorbers." *Journal of Applied Physics* 44.5 (1973): 2335-2342.
[88] Guo, Qiushi, et al. "Ultrafast mode-locked laser in nanophotonic lithium niobate." *Science* 382.6671 (2023): 708-713.
[89] Reep, Tom, et al. "Graphene absorber on an SOI chip for active and passive mode locking of lasers." *Scientific Reports* 15.1 (2025): 9399.
[90] Dohms, Alexander, et al. "Strain-free SESAMs with iron doped absorber for femtosecond fiber laser mode locking at 1560 nm." *Optics Express* 30.12 (2022): 21609-21620.
[91] Set, Sze Y., et al. "Laser mode locking using a saturable absorber incorporating carbon nanotubes." *Journal of lightwave Technology* 22.1 (2004): 51.
[92] Hu, Hongyu, et al. "Hybrid mode-locked fiber ring laser using graphene and charcoal nanoparticles as saturable absorbers." *Micro-and Nanotechnology Sensors, Systems, and Applications VIII*. Vol. 9836. SPIE, 2016.
[93] Li, Wenbo, et al. "High-speed ultrashort pulse fiber ring laser using charcoal nanoparticles." *Applied Optics* 55.9 (2016): 2149-2154.
[94] Li, Wenbo. "Different methods to achieve hybrid mode locking." *Cogent Physics* 6.1 (2019): 1707624.
[95] Memon, Anzal, et al. "Absorber-free mode-locking of a hybrid integrated diode laser at sub-GHz repetition rate." *Photonics*. Vol. 11. No. 11. MDPI, 2024.
[96] Van Gasse, Kasper, et al. "Recent advances in the photonic integration of mode-locked laser diodes." *IEEE Photonics Technology Letters* 31.23 (2019): 1870-1873.
[97] Ibrahimi, Yasmine, et al. "Packaged Long Cavity Hybrid III-V/Si 3 N 4 Mode-Locked Laser With

Improved Modulation Efficiency." *IEEE Journal of Quantum Electronics* 59.3 (2023): 1-8.

[98] Li, Nanxi, et al. "Fully integrated electrically driven optical frequency comb at communication wavelength." *Nanophotonics* 11.13 (2022): 2989-3006.

[99] Zhang, Mian, et al. "Broadband electro-optic frequency comb generation in a lithium niobate microring resonator." *Nature* 568.7752 (2019): 373-377.

[100] Hu, Yaowen, et al. "High-efficiency and broadband on-chip electro-optic frequency comb generators." *Nature photonics* 16.10 (2022): 679-685.

[101] Song, Yunxiang, et al. "Hybrid Kerr-electro-optic frequency combs on thin-film lithium niobate." *Light: Science & Applications* 14.1 (2025): 270.

[102] Shu, Haowen, et al. "Microcomb technology: from principles to applications." Photonics Insights 3.4 (2024): R09-R09.

[103] Kippenberg, Tobias J., Ronald Holzwarth, and Scott A. Diddams. "Microresonator-based optical frequency combs." *science* 332.6029 (2011): 555-559.

[104] Del'Haye, Pascal, et al. "Phase steps and resonator detuning measurements in microresonator frequency combs." *Nature communications* 6.1 (2015): 5668.

[105] Gaeta, Alexander L., Michal Lipson, and Tobias J. Kippenberg. "Photonic-chip-based frequency combs." *nature photonics* 13.3 (2019): 158-169.

[106] Herr, Tobias, Michael L. Gorodetsky, and Tobias J. Kippenberg. "Dissipative Kerr solitons in optical microresonators." Nonlinear optical cavity dynamics: from microresonators to fiber lasers (2016): 129-162.

[107] Stone, Jordan R., et al. "Thermal and nonlinear dissipative-soliton dynamics in Kerr-microresonator frequency combs." Physical review letters 121.6 (2018): 063902.

[108] Lucas, Erwan, et al. "Detuning-dependent properties and dispersion-induced instabilities of temporal dissipative Kerr solitons in optical microresonators." Physical Review A 95.4 (2017): 043822.

[109] Bao, Changjing, et al. "Nonlinear conversion efficiency in Kerr frequency comb generation." Optics letters 39.21 (2014): 6126-6129.

[110] Xue, Xiaoxiao, et al. "Microresonator Kerr frequency combs with high conversion efficiency." Laser & Photonics Reviews 11.1 (2017): 1600276.

[111] Anderson, Miles H., et al. "Dissipative solitons and switching waves in dispersion-modulated Kerr cavities." Physical Review X 13.1 (2023): 011040.

[112] Xu, Chaoyu, et al. "Near-Zero-Dispersion Kerr Soliton Molecules with Coexisting Dark and Bright States." Laser & Photonics Reviews 19.14 (2025): 2402153.

[113] Anderson, Miles H., et al. "Zero dispersion Kerr solitons in optical microresonators." Nature communications 13.1 (2022): 4764.

[114] Li, Zongda, et al. "Ultrashort dissipative Raman solitons in Kerr resonators driven with phase-coherent optical pulses." Nature Photonics 18.1 (2024): 46-53.

[115] Helgason, Óskar B., et al. "Dissipative solitons in photonic molecules." Nature Photonics 15.4 (2021): 305-310.

[116] Xue, Xiaoxiao, et al. "Normal-dispersion microcombs enabled by controllable mode interactions." *Laser & Photonics Reviews* 9.4 (2015): L23-L28.

[117] Wildi, Thibault, et al. "Dissipative Kerr solitons in integrated Fabry–Perot microresonators." Optica 10.6 (2023): 650-656.

[118] Helgason, Óskar B., et al. "Surpassing the nonlinear conversion efficiency of soliton microcombs." Nature Photonics 17.11 (2023): 992-999.

[119] Stern, Brian, et al. "Battery-operated integrated frequency comb generator." Nature 562.7727 (2018): 401-405.

Chapter 2: Theoretical framework

In this chapter, the theory of distributed Bragg grating reflectors and Fabry–Pérot cavities are detailed, extracting the key figures of merit such as stopband, reflection and transmission response, quality factor, free spectral range, finesse, linewidth, and penetration length that will be investigated along the thesis framework. The conventional theoretical approach based on coupled-mode theory and Fabry–Pérot multiple-reflection interference derivation is extended to modified transfer-matrix method consisting of effective refractive index numerical simulations extraction. The employed methodologies ensure precise design and modelling of integrated FP optical micro-resonators, based on DBR reflectors, which form the core devices of this thesis. Specifically, the full derivation of the FP dispersion is detailed, enabling tailored engineering of resonator performance for targeted applications such as single- and multi-wavelength hybrid lasers, as explored in subsequent chapters.

The final sections develop the fundamental theory of a three-mirror external-cavity lasers, that integrates a side-coupled Fabry–Pérot resonator acting as a frequency-selective reflector, deriving the laser threshold and output power expressions. The resonant reflector is modelled using a temporal coupled-mode theory (TCMT) to retrieve its reflection and transmission responses. In addition, this chapter provides a description of the main laser noise contributions, a derivation of the intrinsic and effective laser linewidths, and an overview of the main $\chi^{(3)}$-related nonlinear effects that can be exploited for laser emission, discussing their impact on the optical field.

2.1 Uniform distributed Bragg reflectors

A distributed Bragg reflector (DBR) [1],[2] is a wavelength-selective reflector formed by a one-dimensional periodic modulation of the refractive index along the direction of propagation, realized in multilayer stacks of alternating refractive indices or in periodically corrugated guiding structures. In integrated photonics, DBRs are commonly implemented directly in a waveguide by periodically modulating its geometry, which induces a small perturbation of the effective refractive index experienced by the guided mode [3],[4]. The periodic structure is composed of N identical grating elements, each with length Λ, referred to as the grating periodicity, which generates a weak reflection from the propagating optical field.

While individual reflections are negligible, their cumulative effect yields strong overall reflection when the phase alignment satisfies the Bragg condition. This distributed feedback distinguishes DBRs from discrete reflectors, such as end facets or mirrors. Constructive interference among backward-propagating fields occurs only near the Bragg wavelength λ_B, defined as:

$$\lambda_B = 2\,\bar{n}_{\text{eff}}\,\Lambda, \tag{2.1}$$

where $\bar{n}_{\text{eff}}$ is the average effective index.

Specifically, in waveguide-based integrated DBRs employing geometric modulation (e.g., width corrugation), the perturbation yields an alternating effective index profile $n_{\text{eff}}(z)$ between high-index sections (n_{eff2}) and low-index sections (n_{eff1}). The average refractive index in general is a duty-cycle-weighted value $\bar{n}_{\text{eff}} = DC \cdot n_{\text{eff2}} + (1 - DC)n_{\text{eff1}}$, where DC is the duty cycle (defined as high-index region length divided by the period). In case of *DC*=50%, this reduces to $\bar{n}_{\text{eff}} = (n_{\text{eff1}} + n_{\text{eff2}})/2$.

At wavelengths near λ_B, the distributed reflections combine coherently, producing strong reflection. For wavelengths detuned from this condition, the reflections interfere destructively and the grating becomes largely transparent. As a result, a DBR operates as a wavelength-dependent reflector with a well-defined stopband centered at λ_B.

According to the coupled-mode theory (CMT), inside the grating region, the optical field can be expressed as the superposition of forward- and backward-propagating waves [1]. Under the slowly varying envelope approximation, the total electric field is written as:

$$E(z) = E_f(z)e^{-j\beta_0 z} + E_b(z)e^{j\beta_0 z}, \tag{2.2}$$

where $E_b(z)$and $E_f(z)$represent the complex amplitudes of the backward- and forward-propagating waves, respectively, while $\beta_0 = \frac{2\pi n_{\text{eff}}}{\lambda_B}$ is the propagation constant at the Bragg wavelength. The envelopes $E_b(z)$ and $E_f(z)$ vary slowly along the propagation direction, owing to the weak and distributed nature of the index perturbation. Assuming weak coupling and uniform grating parameters, the interaction between the forward and backward waves is described by the coupled-mode equations as:

$$\begin{cases} \dfrac{dE_b(z)}{dz} + j\Delta\beta E_b(z) = -j\kappa E_f(z), \\ \dfrac{dE_f(z)}{dz} - j\Delta\beta E_f(z) = j\kappa E_b(z) \end{cases} \tag{2.3}$$

where $\Delta\beta = \beta - \beta_0$ denotes the detuning from the Bragg condition, and κ is the coupling coefficient, representing the distributed reflection strength per unit length. These equations show that periodic modulation facilitates continuous energy exchange between the two counter-propagating waves. Solving the coupled-mode equations for a uniform grating of length L yields the complex reflection coefficient:

$$r = \frac{-j\kappa \sinh(\gamma L)}{\gamma \cosh(\gamma L) + j\Delta\beta \sinh(\gamma L)}, \tag{2.4}$$

where $\gamma^2 = \kappa^2 - \Delta\beta^2$.

This result fully describes the spectral response of an ideal, uniform DBR within the coupled-mode approximation. At the exact Bragg resonance ($\Delta\beta = 0$), the expression simplifies to:

$$r = -j\tanh(\kappa L), \tag{2.5}$$

and the corresponding peak power reflectivity is $R_{\text{peak}} = \tanh^2(\kappa L)$. The reflectivity is governed by the product κL, representing the cumulative coupling strength over the grating length. High reflectivity can therefore be achieved either by increasing the grating length or by enhancing the coupling coefficient. The spectral bandwidth of a uniform DBR can be estimated from the condition corresponding to the first zero of the reflection spectrum, given by:

$$\Delta\beta^2 - \kappa^2 = \left(\frac{M\pi}{L}\right)^2, M = 1,2, \dots \tag{2.6}$$

For the first-order null ($M = 1$), the null-to-null bandwidth becomes [5]:

$$\Delta\lambda = \frac{\lambda_B^2}{\pi n_g}\sqrt{\kappa^2 + \left(\frac{\pi}{L}\right)^2}, \tag{2.7}$$

where the group index $n_g = n_{\text{eff}} - \lambda \frac{dn_{\text{eff}}}{d\lambda}$ accounts for waveguide dispersion.

The analytical results above rely on the assumption of a uniform coupling coefficient κ and constant Bragg condition across the grating. Moreover, the model approximates well only weak-coupling regimes (shallow corrugations); for strong coupling (high index contrast), standard CMT deviates from real measurements. In order to have additional degrees of freedom for spectral tailoring, particularly aiming for high-Q and dispersive resonators, DBRs beyond the uniform case are employed. These demand predictive models extending classic CMT. The following sections will introduce grating variants and a modified transfer-matrix method (TMM).

2.1.1 Apodization and chirping

In an apodized Bragg grating, the coupling coefficient, is deliberately varied along the longitudinal coordinate to suppress unwanted sidelobes and tailor the spectral response [1],[6]. Within the coupled-mode formalism, this is modelled by replacing the constant coupling coefficient κ to a real, slowly varying function $\kappa(z)$, while retaining the same detuning parameter $\Delta\beta$. In the coupled-mode theory, Eq. (2.3) becomes [1],[7]:

$$\begin{cases} \dfrac{dE_b(z)}{dz} + j\Delta\beta E_b(z) = -j\kappa(z)E_f(z), \\ \dfrac{dE_f(z)}{dz} - j\Delta\beta E_f(z) = j\kappa(z)E_b(z) \end{cases} \tag{2.8}$$

In practice, $\kappa(z)$ may be implemented through a controlled variation of the corrugation depth (high-index region), duty cycle, or low-index waveguide width [4],[6],[8]. The longitudinal profile

$\kappa(z)$ effectively acts as an envelope on the local reflectivity, so that smooth tapering of $\kappa(z)$towards the grating ends reduces the abrupt index discontinuities responsible for spectral sidelobes. Analytical solutions are generally not available for arbitrary $\kappa(z)$, and the spectral response is computed either via transfer-matrix or piecewise-uniform approximations, in which the apodized grating is discretized into short segments with locally constant coupling.

Chirped Bragg gratings are characterized by a longitudinally varying Bragg period, such that the local Bragg wavelength $\lambda_B(z)$changes along the structure. In the simplest case of a linearly chirped grating [9],[10], the period can be written as:

$$\Lambda(z) = \Lambda_0 + Cz, \tag{2.9}$$

where C is the chirp parameter, leading to a position-dependent Bragg condition $\lambda_B(z) = 2n_{\text{eff}}\Lambda(z)$. In the coupled-mode description, chirp is introduced as a longitudinal variation of the phase mismatch:

$$\Delta\beta(z) = \beta - \beta_0(z), \tag{2.10}$$

where $\beta_0(z) = 2\pi n_{\text{eff}}/\lambda_B(z)$ is varying along the z-axis. The governing Eq. (2.3) can be written as:

$$\begin{cases} \dfrac{dE_b(z)}{dz} + j\Delta\beta(z)E_b(z) = -j\kappa E_f(z), \\ \dfrac{dE_f(z)}{dz} - j\Delta\beta(z)E_f(z) = j\kappa E_b(z) \end{cases} \tag{2.11}$$

Since distinct wavelengths Bragg-match at different positions, chirped gratings inherently broaden the reflection spectrum and impart strong wavelength dependence to group delay [11]. These attributes render chirped gratings potential candidates for dispersion compensation and engineered-delay applications.

2.2 Fabry Pérot etalon

Fabry–Pérot resonators form the foundation of many optical cavities, ranging from simple mirror pairs to advanced integrated devices. They represent the most elementary realization of a dielectric segment bounded by two partially reflecting interfaces and therefore provide a basic building block for more complex mirror and resonator structures in semiconductor and integrated photonics. In this section, the Fabry–Pérot cavity is modeled as a two-port optical network and described in terms of its scattering coefficients and the associated round-trip phase.

Furthermore, the principal characteristics of the resonator, namely the resonance condition, free spectral range, finesse, linewidth, and quality factor Q, are derived within this framework.

2.2.1 Scattering matrix analysis

Fabry–Pérot (FP) resonators can be modeled as a dielectric block of physical length L and refractive index n_2, bounded on the left and right by semi-infinite regions of refractive index n_1 and n_3, respectively. The interfaces at $z = 0$ and $z = L$ are characterized by the complex amplitude reflection and transmission coefficients (r_1, t_1) and (r_2, t_2) defined at reference planes coincident with the physical boundaries. Wave propagation inside the section is governed by the (in general complex) propagation constant β, which for a monochromatic wave of angular frequency ω in a medium of refractive index n_2 is defined as $\beta = \frac{n_2\omega}{c}$, with c that is light speed in vacuum.

A single pass across the cavity corresponds to a phase shift βL, and the associated round-trip phase is $\delta = 2\beta L$. In this chapter, material absorption and gain are neglected, so β is taken to be real and the magnitude of the propagation factor is unity. Under these assumptions, the propagation relations for a lossless, uniform segment are [12]:

$$\begin{cases} a_2' = b_1' e^{-j\beta L}, \\ a_1' = b_2' e^{-j\beta L} \end{cases} \tag{2.12}$$

where a_1' and b_1' (respectively a_2' and b_2') denote the forward- and backward-propagating field amplitudes at the left (right) interface. At the left interface, relating external fields (a_1, b_1) to internal fields (a_1', b_1'), yields:

$$\begin{cases} b_1 = -r_1 a_1 + t_1 a_1', \\ b_1' = t_1 a_1 + r_1 a_1' \end{cases} \tag{2.13}$$

On the contrary, at the right interface, the internal fields (a_2', b_2') are related to external fields (a_2, b_2) through:

$$\begin{cases} b_2 = -r_2 a_2 + t_2 a_2', \\ b_2' = t_2 a_2 + r_2 a_2' \end{cases} \tag{2.14}$$

Equations (2.12)– (2.14) fully describe the fields in the FP cavity, while the schematic in Fig. 1.1 illustrates the geometrical parameters and the forward and backward propagating field inside and outside the dielectric block under analysis. The Fabry–Pérot etalon can then be viewed as a two-port network with normalized forward and backward fields (a_1, b_1)at the left port and (a_2, b_2) at the right port. Its scattering description, results:

$$\begin{bmatrix} b_1 \\ b_2 \end{bmatrix} = \begin{bmatrix} S_{11} & S_{12} \\ S_{21} & S_{22} \end{bmatrix} \begin{bmatrix} a_1 \\ a_2 \end{bmatrix}, \tag{2.15}$$

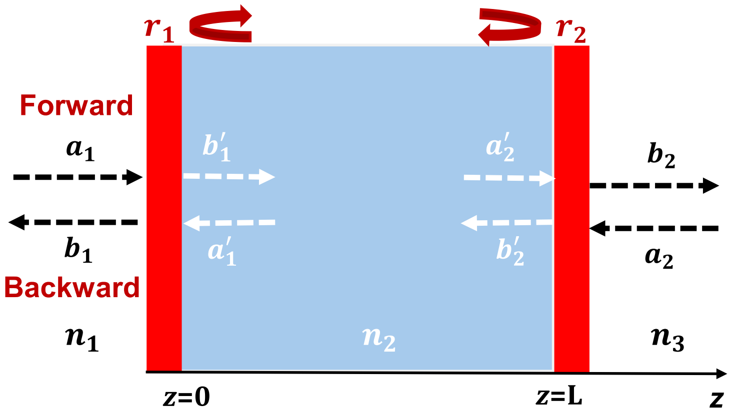

Fig. 2.1: Schematic of the Fabry-Pérot etalon: transmission and reflection amplitude fields at the three interfaces are reported.

where $S_{11}$and S_{22} are the complex amplitude reflection coefficients as seen from the left and right, respectively, while $S_{21}$and S_{12} are the corresponding transmission coefficients. For the symmetric, lossless Fabry–Perot considered here, the network is reciprocal and passive, and therefore $S_{12} = S_{21}$. By solving the interface and propagation relations for the internal fields and eliminating the intermediate amplitudes, the scattering coefficients of the Fabry–Pérot etalon are obtained as:

$$\begin{cases} S_{11} = \dfrac{-r_1 + t_1^2 r_2 e^{-j2\beta L}}{1 - r_1 r_2 e^{-j2\beta L}} \\ S_{21} = S_{21} = \dfrac{t_1 t_2 e^{-j\beta L}}{1 - r_1 r_2 e^{-j2\beta L}} \\ S_{22} = \dfrac{-r_2 + t_2^2 r_1 e^{-j2\beta L}}{1 - r_1 r_2 e^{-j2\beta L}} \end{cases} \quad (2.16)$$

These expressions are the standard FP etalon formulas in scattering-matrix form, and the full derivation has been reported in Appendix A.1.

2.2.2 Fabry-Pérot resonator intensity transmission

The standard Fabry-Pérot resonator configuration considers just excitation driven from a single side. Assuming excitation from the left side, such that the incident and outgoing fields at the left port satisfy $a_1 = E_{\text{in}}$ and $a_2 = 0$, respectively. Under this condition, the transmitted field at the right facet is obtained directly from the scattering coefficient S_{21}, which yields:

$$E_{\text{t}} = b_2 = S_{21} a_1 = \frac{t_1 t_2 e^{-j\beta L}}{1 - r_1 r_2 e^{-j2\beta L}} E_{\text{in}}, \quad (2.17)$$

The associated intensity (power) transmission coefficient is defined as the ratio between the transmitted and incident powers. Using Eq. (2.17), this ratio can be written as:

$$T(\nu) = \left|\frac{E_{\mathrm{t}}}{E_{\mathrm{in}}}\right|^2 = |S_{21}|^2 = \frac{|\, t_1 t_2 \,|^2}{|\, 1 - r_1 r_2 e^{-j2\beta L} \,|^2}. \tag{2.18}$$

Where the dependence on optical frequency ν enters through the propagation constant $\beta(\nu) = 2\pi n_2 \nu / c$. Further analytical simplification is possible in the common case of identical, lossless mirrors. If $|\, r_1 \,| = |\, r_2 \,| = r$, $|\, t_1 \,|^2 = |\, t_2 \,|^2 = 1 - r^2 = 1 - R$, and the round-trip phase $\delta = 2\beta L$ is replaced in the denominator in (2.18), it can be rewritten as:

$$|\, 1 - Re^{-j\delta} \,|^2 = (1 - R)^2 + 4R\sin^2(\delta/2). \tag{2.19}$$

Substitution of this expression into (2.18) leads directly to the standard Airy form for the Fabry–Pérot intensity transmission (see full derivation in Appendix A.2):

$$T(\delta) = \frac{(1-R)^2}{(1 - R)^2 + 4R\sin^2(\delta/2)} = \frac{1}{1 + F\sin^2(\delta/2)}). \tag{2.20}$$

where the coefficient of finesse is defined as $F = 4R/(1-R)^2$. Equations (2.17)– (2.20) provide a complete description of the Fabry–Pérot resonator in terms of its scattering parameters and round-trip phase, and they form the basis for the analysis of more complex resonant cavities in the next chapters.

2.2.3 Resonator quality factor

The quality factor (Q) is a central parameter for characterizing optical resonators, as it quantifies how efficiently electromagnetic energy is stored relative to the rate at which it is dissipated. In general, it is defined as [13]:

$$Q = 2\pi \times \frac{\text{energy stored}}{\text{energy lost per cycle}} = \frac{\nu_0}{\Delta\nu}, \tag{2.21}$$

where ν_0 is the resonance frequency and $\Delta\nu$ is the FWHM of the resonance peak. This form highlights that high-Q cavities exhibit narrow spectral linewidths and therefore enhanced energy storage. Since the linewidth is directly related to the total energy decay rate κ, the quality factor can equivalently be written as:

$$Q = \frac{\omega_0}{\kappa} = \frac{\omega_0}{\kappa_0 + \kappa_{\mathrm{ext}}}, \tag{2.22}$$

with $\omega_0 = 2\pi\nu_0$. The total decay rate κ generally contains multiple contributions, which are commonly separated into internal losses κ_0 and coupling losses κ_{ext}.

Internal losses (κ_0) arise from mechanisms such as absorption, scattering, or imperfect mirror reflectivity, while external losses (κ_{ext}) describe energy coupling between the cavity and the external optical field.

Following this decomposition, it can be defined three related quality factors [14]:

(i) Intrinsic quality factor (Q_i) that describes the cavity in the absence of external coupling and therefore reflects only internal dissipation mechanisms, defined as $Q_i = \frac{\omega_0}{\kappa_0}$;

(ii) The coupling quality factor (Q_c) characterizes how strongly the cavity exchanges energy with the external optical field. This parameter is determined primarily by mirror transmissivity or coupling geometry: $Q_\mathrm{c} = \frac{\omega_0}{\kappa_\mathrm{ext}}$.

(iii) The loaded quality factor (Q_L) experimentally observed, including both intrinsic and coupling losses obtained as: $\frac{1}{Q_L} = \frac{1}{Q_0} + \frac{1}{Q_\mathrm{ext}}$.

By considering the finesse parameter ($\mathcal{F}$), defined as the ratio between the free spectral range and the full width at half maximum of a resonance, this is linked to the coefficient of finesse F as:

$$\mathcal{F} = \frac{\mathrm{FSR}}{\Delta\nu} = \frac{\pi\sqrt{F}}{2}, \tag{2.23}$$

This definition allows to express the photon lifetime as: $\tau_p = \mathcal{F}/2\pi \cdot \mathrm{FSR}$, and the Q-factor as follows:

$$Q = \frac{\omega_0}{\kappa} = \frac{\omega_0}{2\pi\,\Delta\nu} = \frac{\omega_0}{2\pi}\frac{\mathcal{F}}{\mathrm{FSR}}, \tag{2.24}$$

$$\mathcal{F} = \frac{2\pi\,\mathrm{FSR}}{\omega_0}Q. \tag{2.25}$$

While the ideal Fresnel mirror is characterized by constant reflectivity and a flat phase response across frequency, integrated or dielectric resonators that use DBRs as cavity mirrors exhibit several important deviations from this behavior. Firstly, the reflectivity and phase of a DBR are inherently frequency dependent.

Reflectivity amplitude reaches its maximum at the Bragg wavelength within the stopband, while its phase varies strongly across this spectral region due to the dispersive nature of the corrugated waveguides. This frequency-dependent behavior also affects the cavity geometry, as effective reflection does not occur at the physical interface but rather at a finite penetration depth inside the mirror, effectively shifting the position of the optical reflection plane and thereby altering the cavity's free spectral range. The achievable finesse is constrained not only by the finite reflectivity of the DBRs but also by additional losses arising from scattering and absorption within the mirror layers and the spacer regions. Moreover, the cavity mode structure can be influenced by polarization effects: birefringent or polarization-dependent DBRs may introduce a small splitting between transverse electric (TE) and transverse magnetic (TM) resonances, leading to a more complex modal response.

2.3 Modelling of Bragg gratings-based FP resonators

The numerical model that is able to simulate and predict the features of integrated Bragg grating mirrors, and the consequent dispersion effects in the Fabry–Pérot cavities, is a modified Transfer Matrix Method based on effective refractive index (ERI) calculation for each grating period, defined as TMM-ERI [15].

In this approach, the physical grating geometry is mapped into a sampled, wavelength-dependent effective index profile $n_{\text{eff}}(z, \lambda)$ along the optical path z, and the overall optical response is obtained by cascading interface and propagation matrices across the discretized structure.

This method is particularly suited for analyzing gratings combining different apodization profiles along the optical path (yielding spatially varying n_{eff}) and extends beyond the limitations of classical TMM [2] and weak-coupling DBR theory.

The modelled structure accommodates rectangular-shaped integrated Bragg grating, implemented by alternating layers every half-period $\Lambda/2$ (in case of duty cycle equals to 50 %) with effective indices $n_{\text{eff},1}$ and $n_{\text{eff},2}$ corresponding to the low-index grating region and the high-index perturbed region, respectively. It allows to consider both uniform DBR periods N, and apodized grating periods N_T, whose combination fixes the physical mirror length $L_{\text{mirror}} = N_{tot}\,\Lambda$. The main outputs are the single-mirror reflectivity and transmissive spectra, the reflection phase and group delay, combined with the penetration depth L_{eff}, that consequently is used to define the side-coupled FP resonator free spectral range.

2.3.1 ERI-TMM model

In the ERI-TMM [15] approach, the grating geometry is translated into a longitudinal effective index profile $n_{\text{eff}}(z)$ via the waveguide's width-dependent dispersion. In the implemented model, the waveguide effective index $n_{\text{eff}}(\lambda, w)$ is extracted using Lumerical MODE solver running a nested sweep, that incorporates an outer sweep over a dense wavelength grid λ in the C-band regime and an inner sweep over the corrugation width W (from $W_1$to final corrugation depth in uniform section W_2).

For each wavelength step, the effective indices are loaded, and represented by a 5th-order polynomial fit as function of the corrugation grating width W as:

$$n_{\text{eff}}(\lambda, W) = C_0(\lambda) + C_1(\lambda)W + C_2(\lambda)W^2 + C_3(\lambda)W^3 + C_4(\lambda)W^4 + C_5(\lambda)W^5, \quad (2.26)$$

with each $C_k(\lambda)$, that are the coefficients extracted fitting as a quadratic polynomial in λ:

$$C_k(\lambda) = P_{0,k} + P_{1,k}\lambda + P_{2,k}\lambda^2, k = 0 \dots 5, \quad (2.27)$$

where $P_{0,k}$, $P_{1,k}$, and $P_{2,k}$ are the coefficients of the quadratic polynomial defined for each k.

This approach is consistent with the ERI-TMM methodology, where the waveguide is first characterized to obtain $n_{\text{eff}}(\lambda, W)$, then the integrated Bragg grating geometry $W(z)$ is mapped onto $n_{\text{eff}}(\lambda, z) = n_{\text{eff}}(\lambda, W(z))$. Once the effective index values $n_{\text{eff}}(z, \lambda)$ are calculated from the grating geometry, the structure is sampled into discrete layers, each with constant effective index $n_{\text{eff},i}$ and thickness d_i(typically half period in case of duty cycle equals to 50 %).

The ERI-TMM core then proceeds calculating the Interface matrix I_i at the boundary between layers $i-1$ characterized by $n_{eff,i-1}$ and the i-th layer possessing $n_{eff,i}$: this matrix enforces continuity of tangential electric and magnetic fields for TE polarization and results:

$$I_i = \frac{1}{2n_{i-1}} \begin{pmatrix} n_{i-1} + n_i & n_{i-1} - n_i \\ n_{i-1} - n_i & n_{i-1} + n_i \end{pmatrix}. \tag{2.28}$$

where the off-diagonal terms capture local reflection/transmission at index steps. Then is defined the propagation matrix $C_i$through layer i of thickness d_i. This describes phase accumulation for forward and backward waves:

$$C_i = \begin{pmatrix} e^{ik_0 n_i d_i} & 0 \\ 0 & e^{-ik_0 n_i d_i} \end{pmatrix}. \tag{2.29}$$

with $k_0 = \frac{2\pi}{\lambda}$ and the diagonal exponential terms tracking the phase delay over distance d_i. For each layer, the combined step matrix is $M_i = I_i C_i$. The total transfer matrix M_T for the entire grating sections is then matrix product from input to output:

$$M_T = M_M M_{M-1} \cdots M_2 M_1 = \begin{pmatrix} m_{11} & m_{12} \\ m_{21} & m_{22} \end{pmatrix}. \tag{2.30}$$

From M_T elements, complex reflection and transmission coefficients are directly extracted:

$$r(\lambda) = \frac{m_{21}}{m_{11}}, t(\lambda) = \frac{1}{m_{11}}. \tag{2.31}$$

With corresponding reflection power $R(\lambda) = | r |^2$, and transmission spectrum $T(\lambda) = | t |^2$. Once estimated the reflection coefficients, the phase term $\phi_r(\lambda) = \arg(r(\lambda))$ allows to define the reflection group delay $\tau(\lambda)$[16]:

$$\tau(\lambda) = \frac{\lambda^2}{2\pi c} \frac{d\phi_r}{d\lambda}, \tag{2.32}$$

The penetration depth, interpreted as the effective length of a single Bragg reflector, is computed from the group delay as:

$$L_{\text{eff}}(\lambda) = \frac{c\,\tau(\lambda)}{2\,n_g(\lambda)}. \tag{2.33}$$

The accurate modelling of this term allows to estimate and predict the FP resonator free spectral range as will be detailed in the next paragraph.

2.3.2 FSR modelling in the FP cavity

The guided mode forward propagation in z-direction inside a uniform waveguide can be written as:

$$E(x,y,z) = E_0(x,y)e^{-i\beta(\lambda)z}. \tag{2.34}$$

where $E_0(x,y)$ is the transverse mode profile and $\beta(\lambda) = \frac{2\pi}{\lambda} n_{\text{eff}}(\lambda)$ is the propagation constant. Considering a Fabry–Pérot cavity of physical length L_{phys}, an optical wave completing one full round trip travels a distance $2L_{\text{phys}}$ and thus accumulates a propagation phase of:

$$\Phi_{\text{prop}}(\lambda) = 2\beta(\lambda)L_{\text{phys}}, \tag{2.35}$$

This is the phase gained purely from traveling through the waveguide, excluding mirror effects. At the resonance, a wave returning after one round trip must interfere constructively with the newly emitted wave. This requires that the total round-trip phase be an integer multiple of 2π:

$$\Phi_{\text{RT}}(\lambda_m) = 2\beta(\lambda_m)L_{\text{phys}} + \phi_{r,1}(\lambda_m) + \phi_{r,2}(\lambda_m) = 2\pi m, \tag{2.36}$$

where $\phi_{r,1}$ and $\phi_{r,2}$ are the phase shifts upon reflection at the left and right mirrors, and $m \in \mathbb{Z}$ is the longitudinal mode order. This is the fundamental resonance condition. Considering two consecutive longitudinal modes with orders m and $m+1$, occurring at wavelengths λ_m and λ_{m+1}, their resonance conditions are, respectively:

$$\begin{cases} 2\beta(\lambda_m)L_{\text{phys}} + \phi_r(\lambda_m) = 2\pi m, \\ 2\beta(\lambda_{m+1})L_{\text{phys}} + \phi_r(\lambda_{m+1}) = 2\pi(m+1), \end{cases} \tag{2.37}$$

Subtracting the first equation from the second eliminates the mode order m and gives:

$$2L_{\text{phys}}[\beta(\lambda_{m+1}) - \beta(\lambda_m)] + [\phi_r(\lambda_{m+1}) - \phi_r(\lambda_m)] = 2\pi. \tag{2.38}$$

The wavelength spacing $\Delta\lambda = \lambda_{m+1} - \lambda_m$ represents the free spectral range in wavelength domain. Since $\Delta\lambda$ is typically smaller compared to λ, the difference can be approximated using first-order Taylor expansions:

$$\begin{cases} \beta(\lambda_{m+1}) - \beta(\lambda_m) \approx \dfrac{d\beta}{d\lambda}\Delta\lambda, \\ \phi_r(\lambda_{m+1}) - \phi_r(\lambda_m) \approx \dfrac{d\phi_r}{d\lambda}\Delta\lambda, \end{cases} \tag{2.39}$$

Substituting these into the subtracted equation yields:

$$\beta\left(2L_{\text{phys}}\frac{d\beta}{d\lambda} + \frac{d\phi_r}{d\lambda}\right)\Delta\lambda = 2\pi. \tag{2.40}$$

This relates the FSR to the derivatives of both the propagation constant and the mirror reflection phase. The derivative of β with respect to wavelength is not simply constant; it depends on waveguide dispersion. Using the standard identity:

$$\frac{d\beta}{d\lambda} = -\frac{2\pi}{\lambda^2} n_g(\lambda), \tag{2.41}$$

where the group index $n_g(\lambda)$ is defined as: $n_g(\lambda) = n_{\text{eff}}(\lambda) - \lambda \frac{dn_{\text{eff}}}{d\lambda}$. Substituting Eq. (2.41) into Eq. (2.40), and solving for $\Delta\lambda$ (i.e. FSR_λ), it gives:

$$\text{FSR}_\lambda(\lambda) \approx \frac{\lambda^2}{2n_g(\lambda)L_{\text{phys}} + \frac{\lambda^2}{2\pi}\frac{d\phi_r}{d\lambda}}. \tag{2.42}$$

In conclusion, the resonator FSR (that can refer to both the in-plane or side-coupled FP cavity) depends not only on the length and group index of the resonant cavity, but also on the wavelength derivative of the mirror reflection phase.

For simple Fresnel facets, $d\phi_r/d\lambda \approx 0$, and the expression reduces to the familiar ideal Fabry–Pérot FSR. However, for DBR mirrors, $\phi_r(\lambda)$ is strongly dispersive and this term cannot be neglected. A DBR mirror is characterized by its complex reflection coefficient: $r(\lambda) = |r(\lambda)|e^{i\phi_r(\lambda)}$, where $|r(\lambda)|$ determines the reflectivity magnitude and $\phi_r(\lambda) = \arg(r(\lambda))$ is the reflection phase.

The reflection phase encodes a phase penetration depth: light effectively reflects from a virtual plane inside the DBR rather than at its physical front facet. This phase shift modifies the cavity round-trip phase and consequently the FSR. The group delay associated with the DBR reflection is:

$$\tau(\lambda) \triangleq \frac{d\phi}{d\omega}|_{\omega=\omega_B} = -\frac{\lambda_B^2}{2\pi c}\frac{d\phi_r(\lambda)}{d\lambda}, \tag{2.43}$$

where $\omega_B = 2\pi c/\lambda_B$ is the Bragg angular frequency. The penetration depth of the DBR is then defined as:

$$L_{\text{eff}}(\lambda) = \frac{c}{2n_g(\lambda)}\tau(\lambda). \tag{2.44}$$

Substituting Eq. (2.43) into Eq. (2.44):

$$L_{\text{eff}}(\lambda) = -\frac{\lambda^2}{4\pi n_g(\lambda)}\frac{d\phi_r(\lambda)}{d\lambda}. \tag{2.45}$$

When both cavity mirrors are DBRs, the total effective cavity length becomes $L_{\text{tot}}(\lambda) = L_{\text{phys}} + 2L_{\text{eff}}(\lambda)$, and the FSR expression Eq. (2.42) can be re-written as:

$$\text{FSR}_\lambda(\lambda) \approx \frac{\lambda^2}{2n_g(\lambda)L_{\text{tot}}(\lambda)}. \tag{2.46}$$

2.4 Microresonators dispersion

Chromatic dispersion is the fundamental wave-propagation phenomenon where the phase velocity, and consequently the group velocity, varies with optical frequency (or wavelength).

This occurs because the propagation constant $\beta(\omega)$ is not perfectly linear with angular frequency ω, causing different spectral components to travel at different speeds through a medium or waveguide. In integrated photonics, chromatic dispersion stems from two primary sources: material dispersion, due to the intrinsic frequency dependence of the refractive index $n(\omega)$ in the core and cladding materials; and waveguide (geometrical) dispersion, arising from frequency-dependent modal confinement and evanescent field penetration into the cladding.

The latter alters both the effective index $n_{eff}(\omega)$ and the fraction of optical energy distributed between core and cladding regions.

Micro resonator dispersion represents the manifestation of chromatic dispersion at the level of cavity eigenfrequencies in integrated micro resonators. It appears directly as deviations from perfectly uniform spacing between discrete resonance frequencies in the measured spectrum. These deviations arise because the resonator's round-trip phase accumulation, which determines the resonance condition, itself depends on frequency through the underlying chromatic dispersion of the guided modes. Together, these effects create the anomalous or normal dispersion profiles essential for applications like Kerr frequency comb generation and broadband micro resonator lasers. For a single spatial mode of Fabry–Pérot resonator of physical length L, a resonance occurs when the roundtrip phase accumulation is an integer multiple of 2π, which leads to the resonance condition:

$$\beta(\omega_m)\, L = 2\pi m, \tag{2.47}$$

where m is the longitudinal mode number and $\beta(\omega)$ is the propagation constant of the guided mode. Only the discrete frequencies ω_m that satisfy this equation can resonate. Choosing a reference resonance at $\omega_0 = \omega|_{m=0}$ and defining the relative mode index as $\mu = m - m_0$, the same condition can be rewritten as:

$$[\beta(\omega_\mu) - \beta(\omega_0)]\, L = 2\pi\mu, \tag{2.48}$$

The resonance condition provides an exact link between the discrete spectrum ω_μ and the continuous propagation function $\beta(\omega)$. Longitudinal modes are labeled by the integer index μ, with resonance frequencies f_μ (in Hz) or corresponding angular frequencies $\omega_\mu = 2\pi f_\mu$ (in rad/s). The central resonance ω_0 is typically chosen at the center of the grating stopband, and it serves as reference to express the spectrum in the local basis ω_μ (μ) as a function of mode number μ. Deviations of ω_μ from a perfectly linear dependence on μ provide a direct, experimentally accessible measure of the underlying chromatic dispersion of the guided mode. Chromatic dispersion [17], in this framework, is quantified by expanding the propagation constant around ω_0:

$$\beta(\omega) = \beta_0 + \beta_{1,\omega}(\omega - \omega_0) + \frac{1}{2}\beta_{2,\omega}(\omega - \omega_0)^2 + \frac{1}{6}\beta_{3,\omega}(\omega - \omega_0)^3 + \cdots. \tag{2.49}$$

where $\beta_{n,\omega} = \frac{\partial^n \beta}{\partial \omega^n}|_{\omega_0}$ are the n-th order dispersion coefficients in the angular frequency domain. In detail, $\beta_{1,\omega}$is the group delay per unit length defined in s/m, $\beta_{2,\omega}$is the group-velocity dispersion (GVD) in s^2/m, and $\beta_{3,\omega}$is the third-order dispersion (TOD) expressed in s^3/m.

The total micro-resonator dispersion can be measured as the deviation $\Delta\omega_\mu = (\omega - \omega_0)$ of the resonance frequencies from equidistance, which encodes the frequency dependence of $\beta(\omega)$experienced by the guided mode.

$$[\beta_{1,\omega}\Delta\omega_\mu + \frac{1}{2}\beta_{2,\omega}\Delta\omega_\mu^2 + \frac{1}{6}\beta_{3,\omega}\Delta\omega_\mu^3 + \cdots]\, L = 2\pi\mu \tag{2.50}$$

Considering the chromatic dispersion contribution for each resonance ω_μ, the latter varies smoothly with μ, and expanding the modal spectrum in a Taylor series about $\mu = 0$, can be obtained [18],[19]:

$$\omega_\mu = \omega_0 + D_{1,\omega}\mu + \frac{1}{2}D_{2,\omega}\mu^2 + \frac{1}{6}D_{3,\omega}\mu^3 + \ldots \tag{2.51}$$

with dispersion coefficients $D_{n,\omega} = \frac{\partial^n \omega_\mu}{\partial \mu^n}|_{\mu=0}$. Equivalently, in optical frequency f_μ:

$$f_\mu = f_0 + D_{1,f}\mu + \frac{1}{2}D_{2,f}\mu^2 + \frac{1}{6}D_{3,f}\mu^3 + \cdots \tag{2.52}$$

and since $\omega_\mu = 2\pi f_\mu$, the expansion coefficients satisfy:$D_{n,\omega} = 2\pi D_{n,f}$.

To isolate the dispersion from the trivial offset and linear FSR, the most commonly used figure of merit is the integrated dispersion, that is indicated in the angular-frequency domain as:

$$D_{\text{int},\omega}(\mu) = \omega_\mu - (\omega_0 + D_{1,\omega}\mu), \tag{2.53}$$

or equivalently in the frequency domain: $D_{\text{int},f}(\mu) = f_\mu - (f_0 + D_{1,f}\mu)$.

In the following chapters, the integrated dispersion $D_{int,f}(\mu)$ is retrieved by fitting the experimentally measured resonant frequencies f_μ with a cubic polynomial as:

$$f(\mu) \approx p_1\mu^3 + p_2\mu^2 + p_3\mu + p_4, \tag{2.54}$$

where $p_i|\, i = 0,4$ corresponds to the coefficients described in Eq. (2.52). From this fit, the frequency-domain dispersion coefficients in THz units are obtained analytically as:

$$\begin{cases} D_{1,f}^{(\mathrm{fit})}(\mu) = \dfrac{\partial f}{\partial \mu} = 3p_1\mu^2 + 2p_2\mu + p_3, \\ D_{2,f}^{(\mathrm{fit})}(\mu) = \dfrac{\partial^2 f}{\partial \mu^2} = 6p_1\mu + 2p_2, \\ D_{3,f}^{(\mathrm{fit})}(\mu) = \dfrac{\partial^3 f}{\partial \mu^3} = 6p_1. \end{cases} \tag{2.55}$$

While higher orders dispersion terms ($D_{n,\omega}$) provide a complete description of the resonator dispersion in mode space, many physical processes, in particular the formation and dynamics of intracavity pulses, are more naturally discussed in terms of the propagation constant $\beta(\omega)$of the underlying guided mode.

The link between the discrete coefficients $D_{n,\omega}$ and the coefficients $\beta_{n,\omega}$ follows from the resonance condition of the cavity and are reported in Eq. (2.56) (see Appendix B for a complete derivation).

$$\begin{cases} \beta_{1,\omega}(\mu) = \dfrac{2\pi}{L\, D_{1,\omega}(\mu)}, \\ \beta_{2,\omega}(\mu) = -\dfrac{D_{2,\omega}(\mu)\, \beta_{1,\omega}(\mu)}{D_{1,\omega}(\mu)^2}, \\ \beta_{3,\omega}(\mu) = -\dfrac{1}{D_{1,\omega}(\mu)^3}\left[\beta_{1,\omega}(\mu)\, D_{3,\omega}(\mu) + 3\, \beta_{2,\omega}(\mu)\, D_{1,\omega}(\mu)\, D_{2,\omega}(\mu)\right]. \end{cases} \tag{2.56}$$

The dispersion can be defined in terms of figures of merit directly linked to pulse propagation effects, such as group delay $\tau_g(\omega)$and group-delay dispersion (GDD). The total round-trip phase of the resonator is $\phi(\omega) = \beta(\omega)L$. The group delay per round trip is the first derivative:

$$\tau_g(\omega) = \frac{\partial \phi}{\partial \omega} = L\beta_{1,\omega}, \tag{2.57}$$

representing the round-trip time for the mode at frequency ω. The group-delay dispersion (Eq. (2.58)) directly measures the curvature of the round-trip phase, and thus the temporal broadening experienced by an intracavity pulse. Positive GDD (positive $\beta_{2,\omega}$) means that higher-frequency components take longer per round trip than lower-frequency ones, stretching the pulse; negative GDD implies pulse compression.

$$\mathrm{GDD} = \frac{\partial^2 \phi}{\partial \omega^2} = L\beta_{2,\omega}, \tag{2.58}$$

To align with straight waveguides and fibers, the group-velocity dispersion can be expressed as the chromatic dispersion parameter: $D_\lambda = -\frac{2\pi c}{\lambda^2}\beta_{2,\omega}$, expressed in ps/(nm·km). Here, $D_\lambda < 0$ signals anomalous dispersion at wavelength λ, while $D_\lambda > 0$ indicates normal dispersion, as referred in Kerr soliton microcomb context.

2.5 Laser theory

A single-mode semiconductor laser featuring an active region volume V_a, carrier density N(carriers/cm^3) in the active region, and photon density S in the lasing mode (defined as photons per unit volume), is characterized by the following coupled rate equations [12]:

$$\frac{dN}{dt} = \eta_i \frac{I}{qV_a} - R_{\mathrm{sp}}(N) - R_{\mathrm{nr}}(N) - v_g\, \Gamma\, g(N)\, S, \tag{2.59}$$

$$\frac{dS}{dt} = v_g\, \Gamma\, g(N)\, S - \frac{S}{\tau_p} + \beta_{\mathrm{sp}} R_{\mathrm{sp}}(N). \tag{2.60}$$

In the rate-equation model several physical quantities appear. The drive current Iinjects carriers into an active region of volume V, with q elementary charge and consequently $\frac{I}{qV}$ sets the carrier injection rate. Only a fraction η_{int} of these carriers contributes to stimulated emission, which is described by the material gain coefficient g (defined in cm^{-1}), that refers to the amplification per unit length as a function of carrier density.

The optical field propagates with group velocity $v_g = c/n_g$, where n_g is the group index of the guided mode, and only the fraction $\Gamma$of the modal energy that overlaps with the gain region experiences this amplification. Carriers are removed from the active region by spontaneous radiative recombination at rate R_{sp} and by non-radiative processes at rate R_{nr}, both expressed in [carriers$\cdot$cm$^{-3}\cdot$ s^{-1}]. A small fraction β of the spontaneous emission couples into the lasing mode; this parameter links the carrier dynamics to the build-up of photons in the cavity. Finally, τ_p is the photon lifetime in the cavity (expressed in seconds), and accounts for all optical losses, including internal absorption and mirror output coupling and is defined as:

$$\frac{1}{\tau_p} = v_g(\langle\alpha_i\rangle + \alpha_m), \tag{2.61}$$

where $\langle\alpha_i\rangle$ is the average internal loss and α_m indicates the equivalent distributed mirror loss. At threshold, in steady state, the photon density is only just beginning to increase, so $dS/dt = 0$, while S remains finite. Neglecting the spontaneous-emission term in Eq. (2.60) and substituting Eq. (2.61) into it then yields:

$$v_g\, \Gamma\, g_{\mathrm{th}} = \frac{1}{\tau_p} = v_g(\langle\alpha_i\rangle + \alpha_m), \tag{2.62}$$

Re-arranging, Eq. (2.62) becomes:

$$\Gamma\, g_{\mathrm{th}} = \langle\alpha_i\rangle + \alpha_m. \tag{2.63}$$

Thus, at threshold the net modal gain exactly balances the sum of the internal loss and the mirror loss per unit length. For the specific laser cavity under consideration, explicit expressions for g_{th}, α_i and α_m are obtained from the round-trip amplitude condition.

2.5.1 Two-mirror laser cavity

A generic two-mirror semiconductor laser [12] characterized by an active section of length L_g, a passive section of length L_p, and facets amplitude reflectivity $r_1$and r_2, can be represented as in Fig. 2.2. For this laser structure the steady state threshold condition is equivalent to Eq. (2.63), while the average internal loss and the equivalent distributed mirror loss parameters are defined as:

$$\langle\alpha_i\rangle = \frac{\alpha_{i,a}L_g + \alpha_{i,p}L_p}{L}, \qquad L = L_g + L_p, \tag{2.64}$$

$$\alpha_m = \frac{1}{L}\ln\left(\frac{1}{R_m}\right), \qquad R_m = r_1 r_2. \tag{2.65}$$

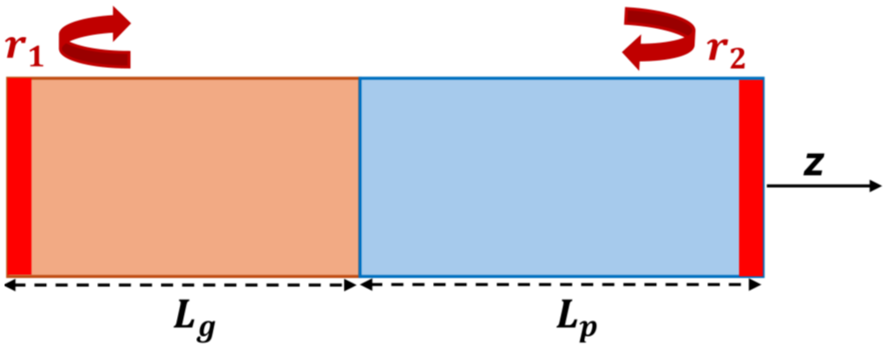

Fig. 2.2: Schematic of a conventional two-mirror laser system: L_g denotes the gain section length, L_p the passive device section, with emission extracted from the second mirror characterized by lower amplitude reflectivity r_2.

These quantities are retrieved by carrying out mathematical calculation based on the round-trip amplitude condition for the specific two-mirror laser architecture as detailed in Appendix C.1. Moreover, it can be defined the threshold current (I_{th}), and the output power (P_{out}) extracted from a mirror facet, which increase linearly with the driving current as follows:

$$P_{\text{out}} = \eta_d \frac{h\nu}{q}(I - I_{\text{th}}), \tag{2.66}$$

with the differential quantum efficiency η_d, given by the ratio between the output-facet mirror loss $\alpha_{m,\text{out}}$ and the total loss multiplied by the internal quantum efficiency η_i:

$$\eta_d = \eta_i \frac{\alpha_{m,\text{out}}}{\langle\alpha_i\rangle + \alpha_m}, \tag{2.67}$$

2.5.2 Three-mirror external-cavity laser: SC-FP reflector

The laser architectures implemented in this thesis, that will be treated in Chapters 4,5, are based on a three-mirror external-cavity configuration, which requires extending the cavity equations introduced in the previous section to include an additional wavelength-selective reflector in the laser dynamic. The ECL implemented in Chapter 4 incorporates a SOA as gain section combined with a fiber-based reflector, while in Chapters 5, the laser cavity comprises a reflective amplifier (RSOA) with HR back mirror with amplitude reflectivity r_1, an active section of length L_g, and an AR-coated front facet with amplitude reflectivity $r_2 \approx 0$.

Both the systems are butt-coupled to a photonic PIC that include an integrated passive resonator that ensure a wavelength-dependent reflection contribution r_3. The ideal schematic of the three-mirror laser system is illustrated in Fig. 2.3(a) while Fig. 2.3(b) depicts its practical implementation. In the following, the analysis focuses on the configuration in which the generic gain section in Fig. 2.3(a) is replaced by an RSOA; however, the same considerations apply directly to the corresponding SOA-based architecture.

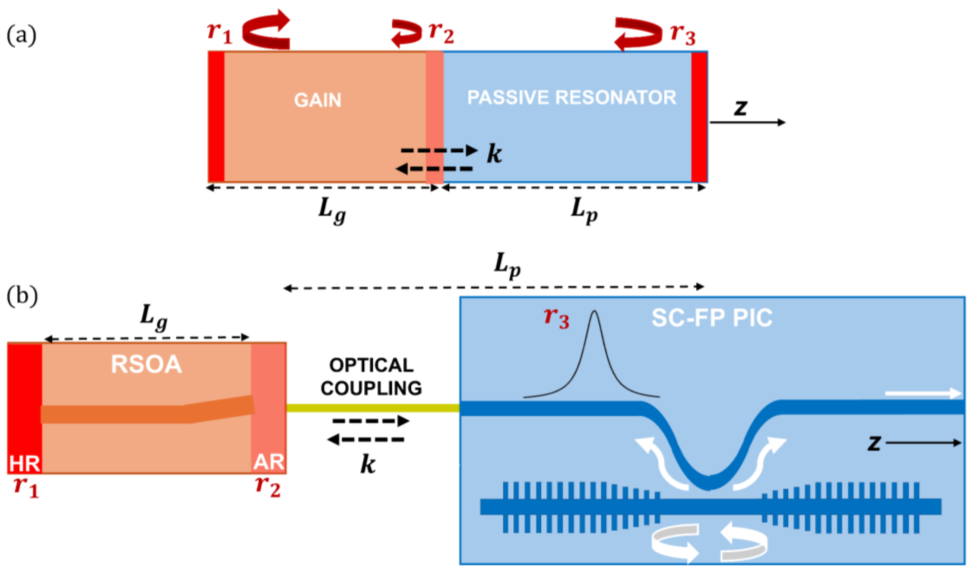

Fig. 2.3: (a) Ideal schematic of the implemented three-mirror laser system: longitudinal cavity representation highlighting the gain section, passive resonator, mirror reflectivities r_1, r_2, r_3, and the coupling coefficient κ. (b) Chip-level implementation showing the RSOA with HR/AR facets butt-coupled to the SC-FP PIC, where the side-coupled FP section provides the wavelength-selective third mirror.

The passive resonator in the schematic is implemented as a Fabry–Pérot cavity formed by DBRs, side-coupled to the waveguide optically coupled to the gain section. This side-coupled FP (SC-FP), that is described in detail in the next chapter, acts as a wavelength-selective reflector in the cavity providing resonance peaks, whose amplitude reflectivity is referred as $r_3(\lambda)$, in the input section and corresponding dips in transmission at the output of the passive chip. The AR-coated front facet of the RSOA couples light into a passive PIC that contains the SC-FP resonator. Together with the HR back facet of the RSOA and the effective reflection of the SC-FP, this creates a three-mirror cavity: the HR RSOA facet provides the first mirror, the AR-coated RSOA facet combined with the coupling interface acts as the second mirror, and the wavelength-dependent SC-FP reflectivity $r_3(\lambda)$ forms the third mirror in the external section. The RSOA–PIC interface is characterized by a power-coupling efficiency κ $(0 < \kappa \leq 1)$[22], while the passive section length L_p is defined as the distance from the AR-coated RSOA facet to the effective reflection plane of the SC-FP along the longitudinal z-axis.

By appropriately designing the SC-FP resonance condition and linewidth, the structure acts as a spectrally selective mirror that stabilizes the lasing wavelength and can be used to tailor the longitudinal mode spectrum of the three-mirror cavity. Under a steady-state assumption, the effect of the external mirror can be described by replacing the entire passive section L_p with a single effective mirror of amplitude reflectivity r_{eff}. Assuming all the reflectivity terms y are real and positive, the corresponding effective amplitude reflectivity at the gain–passive interface can be written as:

$$r_{\text{eff}}(\lambda) = \kappa^2\, r_3(\lambda), \tag{2.68}$$

In this configuration, κ that is the field coupling coefficient between active and passive region, accounts for all coupling-related losses between the RSOA and the external reflector (mode mismatch, alignment, Fresnel reflection), so that only a fraction κ^2 of the forward field reaches the resonant reflector and the same fraction of the reflected field is coupled back into the gain section. Under these considerations, the three-mirror external-cavity scheme can be treated as an equivalent two-mirror cavity with amplitude reflectivities $r_1$and r_{eff}, with the laser output collected at the mirror of reflectivity r_{eff}. The corresponding threshold expression becomes [21]:

$$\Gamma g_{\text{th}} L_g = \alpha_{i,a} L_g + \alpha_{i,p} L_p + \ln\left(\frac{1}{r_1 r_{\text{eff}}}\right) = \alpha_{i,a} L_g + \alpha_{i,p} L_p + \ln\left(\frac{1}{r_1 \kappa^2 r_3}\right), \tag{2.69}$$

which shows that the round-trip modal gain in the active section (left-hand side) balances all internal losses in the active and passive regions and the effective output coupling provided by the HR mirror and the side-coupled FP-based mirror (right-hand side).The corresponding mirror-loss term is obtained by dividing the logarithmic term by the total cavity length L, yielding [21]:

$$\alpha_m(\lambda) = \frac{1}{L}\ln\left(\frac{1}{r_1 \kappa^2 r_3(\lambda)}\right), \tag{2.70}$$

with $L = L_g + L_{\text{p}}$.

For the long-passive section considered here, it is more accurate to write $L = L_g + L_{\text{eff}}(\lambda)$, where $L_{\text{eff}}(\lambda)$ includes both the physical passive section L_p and the wavelength-dependent penetration depth associated with the phase of the Bragg grating section that affects the FP resonant modes spacing (as defined in Section 2.3.) and the laser emission. Using the mean mirror intensity reflection:

$$R_m(\lambda) = r_1 r_{\text{eff}}(\lambda) = r_1 \kappa^2 r_3(\lambda), \tag{2.71}$$

Finally, the threshold condition can be written in a compact form as:

$$\Gamma g_{\text{th}}(\lambda) = \langle \alpha_i \rangle + \alpha_m(\lambda), \tag{2.72}$$

where $\langle \alpha_i \rangle$ is the length-weighted average internal loss and the wavelength-dependent term $\alpha_m(\lambda)$ is given by Eq. (2.65). In this scenario, the DBR-based resonant reflector and its coupling to the gain chip affect the laser threshold current. Consequently, also the output power and the slope-efficiency parameters result wavelength dependent as follows:

$$P_{\text{out}}(\lambda) = \eta_d(\lambda) \frac{h\nu}{q} \left(I - I_{\text{th}}(\lambda)\right), \tag{2.73}$$

$$\eta_d(\lambda) = \eta_i \frac{\alpha_{m,1}}{\langle \alpha_i \rangle + \alpha_m(\lambda)} \tag{2.74}$$

where $\alpha_{m,1}$ is the mirror-loss contribution of the HR back facet.

Increasing either k or r_{eff} reduces the overall mirror loss α_m and therefore lowers the lasing threshold, but this comes at the expense of a smaller fraction of the total loss being extracted at the laser output and thus a reduced differential efficiency. Additional laser figures of merit are extracted in Appendix C.2. In particular, the reflectivity provided by the side-coupled FP device $r_3(\lambda)$, can be modelled using temporal coupled-mode theory (TCMT), as will be discussed in the next section, which allows precise tuning of the laser operating conditions by adjusting the geometrical design parameters of the passive resonator.

2.5.3 TCMT: side-coupling between waveguide and resonator

Temporal coupled-mode theory (TCMT) provides a general framework for modelling resonant photonic systems under the weak-coupling approximation [22]. Specifically, this approach can be applied to describe the dynamics of a side-coupled cavity–waveguide configuration, in which a single cavity mode exchanges energy with a guided mode through a localized coupling region. Figure 2.4(a) depicts the generic side-coupled geometry, where a single-mode resonator is placed in close proximity (side-coupled) to a straight bus waveguide, while Fig. 2.4(b) illustrates the specific implementation used in this work, namely a standing-wave Fabry–Pérot cavity based on DBR mirrors, comprising a combination of uniform and apodized sections, side-coupled through bent-waveguide coupler. The cavity is treated as an oscillator with complex amplitude $a(t)$ and resonance frequency ω_0, while the waveguide is modelled as a transmission line carrying travelling power waves $s_{+,in}$ and backward wave $s_{-,in}$. The TCMT equation is:

$$\frac{da}{dt} = (j\omega_0 - \Gamma_0 - \Gamma_C)a + \kappa_C s_{+,in}, \tag{2.75}$$

where Γ_C denotes the energy decay rate from the cavity into the waveguide, in both the directions, Γ_0 is the intrinsic energy decay rate of the cavity, accounting for the radiation, absorption and scattering losses of the waveguide cavity, while $\Gamma_0 + \Gamma_C$ consider the total decay rate (also referred to as loaded decay rate).

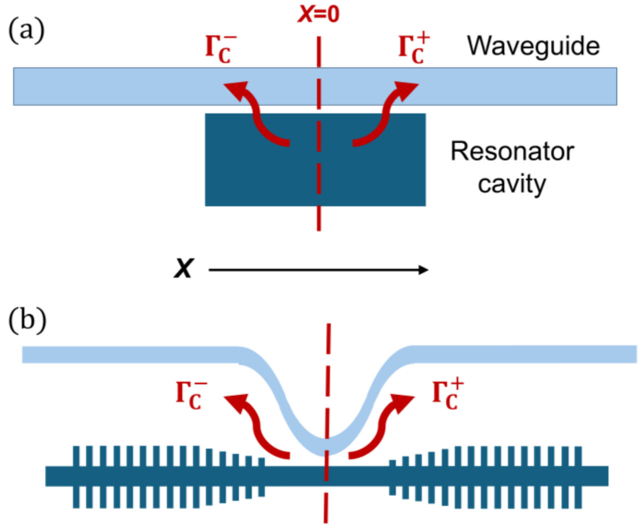

Fig. 2.4: Schematic of waveguide side-coupling to a resonant cavity: (a) generic representation, and (b) implemented side-coupled Fabry-Pérot architecture modeled using TCMT approach.

Energy conservation and time-reversal symmetry require $|\ \kappa_c\ |^2 = 2\Gamma_c$, so that the power flowing from the cavity into the waveguide is equal to the power extracted from the cavity mode. For a single-mode resonator cavity in the side-coupling geometry, the standing-wave cavity mode has no preferred propagation direction along the waveguide. As a result, the coupling to the forward and backward waveguide modes is identical, i.e. $\Gamma_c^+ = \Gamma_c^- = \Gamma_c/2$.

The forward output field is given by the coherent sum of the incident wave and the field re-radiated by the cavity, whereas the backward-reflected field originates solely from the cavity:

$$\begin{cases} s_{+,out} = s_{+,in} + \kappa_c a, \\ s_{-,out} = \kappa_c a \end{cases} \tag{2.76}$$

Solving the steady state cavity equation for a monochromatic excitation at angular frequency ω, with input field $a(t) = Ae^{j\omega t}$, and defining the detuning parameter as $\Delta\omega = \omega - \omega_0$, i.e., the frequency offset between the incident light and the cavity resonance at ω_0, yields:

$$A = \frac{\kappa_c\, s_{+,in}}{j\Delta\omega + \Gamma_0 + \Gamma_c}, \tag{2.77}$$

which is fully demonstrated in Appendix C.3, and it directly links the stored energy to the input amplitude and the total decay rate. Using these relations, the power transmission and reflection coefficients are:

$$\begin{cases} T(\omega) = \left|\frac{s_{+,out}}{s_{+,in}}\right|^2 = \frac{\Delta\omega^2 + \Gamma_0^2}{\Delta\omega^2 + (\Gamma_0 + \Gamma_c)^2}, \\ R(\omega) = \left|\frac{s_{-,out}}{s_{+,in}}\right|^2 = \frac{\Gamma_c^2}{\Delta\omega^2 + (\Gamma_0 + \Gamma_c)^2} \end{cases} \tag{2.78}$$

At the exact resonance ($\Delta\omega = 0$), the expressions simplify to:

$$\begin{cases} T_{\text{res}} = \frac{\Gamma_0^2}{(\Gamma_0+\Gamma_c)^2}, \\ R_{\text{res}} = \frac{\Gamma_c^2}{(\Gamma_0+\Gamma_c)^2} \end{cases} \tag{2.79}$$

Relating the decay rates to quality factors via $Q_0 = \omega_0/2\Gamma_0$ and $Q_c = \omega_0/2\Gamma_c$, it results $Q_L = \frac{\omega_0}{2(\Gamma_0+\Gamma_c)}$ and $\frac{1}{Q_L} = \frac{1}{Q_0} + \frac{1}{Q_c}$, which highlights how intrinsic and coupling losses jointly determine the transmitted and reflected powers. Considering the relationship between the decay rates and quality factors, the intensity reflection and transmission terms at the resonance wavelength result:

$$\begin{cases} T_{\text{res}} = \frac{Q_L^2}{Q_O^2}, \\ R_{\text{res}} = \frac{Q_L^2}{Q_C^2} \end{cases} \tag{2.80}$$

Equation (2.78) can be recast as functions of wavelength by expressing the detuning in terms of λ and replacing the decay rates with the corresponding quality-factor definitions.

Near resonance, considering $\omega = 2\pi c/\lambda$ and $\omega_0 = 2\pi c/\lambda_0$, the detuning term becomes: $\Delta\omega = 2\pi c\left(\frac{1}{\lambda} - \frac{1}{\lambda_0}\right)$. Under small detuning condition, $|\lambda - \lambda_0| \ll \lambda_0$, a first-order expansion of $1/\lambda$ around λ_0 gives $\Delta\omega \approx -\frac{2\pi c}{\lambda_0^2}(\lambda - \lambda_0)$. Defining the intrinsic and coupling decay rates in terms of the Q-factors in the wavelength domain, the transmitted ($T(\lambda)$) and reflected powers ($R(\lambda)$) are defined as:

$$\begin{cases} T(\lambda) = \dfrac{\left(\frac{\lambda_0 - \lambda}{\lambda}\right)^2 + \frac{1}{(2Q_i)^2}}{\left(\frac{\lambda_0 - \lambda}{\lambda}\right)^2 + \frac{1}{(2Q_L)^2}} \\ R(\lambda) = \dfrac{\frac{1}{(2Q_c)^2}}{\left(\frac{\lambda - \lambda_0}{\lambda_0}\right)^2 + \frac{1}{(2Q_L)^2}} \end{cases} \tag{2.81}$$

The expressions in Eq. (2.81) take the form of Lorentzian functions whose linewidths are determined by the loaded quality factor Q_L. These analytical formulas will be used in this thesis to fit the experimental spectra of the SC-FP resonators and thereby extract the relevant quality factors and resonator figures of merit. Using the side-coupled resonant reflector reflectivity defined from the TCMT derivation at the resonance λ_0, the term $r_3(\lambda_0)$ in the three-mirror laser architecture results:

$$r_3(\lambda_0) = \frac{\Gamma_C}{\Gamma_0 + \Gamma_C} = \frac{1/Q_C}{1/Q_0 + 1/Q_C} = \frac{Q_L}{Q_C}, \tag{2.82}$$

And the effective mirror reflectivity at resonance is:

$$r_{eff}(\lambda_0) = \kappa \frac{Q_L}{Q_C} \tag{2.83}$$

In addition, the threshold condition can be re-arranged in terms of the Q-factor terms. The mirror loss term can be retrieved as:

$$\alpha_m = \frac{1}{L} \ln\left(\frac{1}{r_1 r_{eff}}\right) = \frac{1}{L}\left[\ln\left(\frac{1}{r_1}\right) + \ln\left(\frac{1}{\kappa}\right) + \ln\left(\frac{Q_C}{Q_L}\right)\right]. \tag{2.84}$$

2.6 Laser noise

A single-frequency laser can be described as an optical oscillator whose amplitude and phase undergo small fluctuations due to intrinsic processes in the laser cavity as well as external environmental perturbations [23]. The electric field emitted by the laser can therefore be expressed as:

$$E(t) = E_0[1 + \alpha(t)]\cos(2\pi\nu_0 t + \phi(t)). \tag{2.85}$$

where E_0 denotes the nominal electric-field amplitude, t is the time, ν_0 is the optical carrier frequency, $\alpha(t)$represents relative amplitude fluctuations, and $\phi(t)$ represents phase fluctuations. These stochastic variations determine the spectral purity of the laser emission. In narrow-linewidth lasers, spectral broadening is primarily governed by phase fluctuations rather than amplitude fluctuations, since variations of the optical phase directly perturb the instantaneous optical frequency. The instantaneous frequency of the laser can be written as:

$$\nu(t) = \nu_0 + \Delta\nu(t). \tag{2.86}$$

where $\Delta\nu(t)$ represents the frequency fluctuation around the carrier frequency. This fluctuation is directly related to the temporal evolution of the phase through:

$$\Delta\nu(t) = \frac{1}{2\pi}\frac{d\phi(t)}{dt}. \tag{2.87}$$

This relation shows that frequency noise corresponds to the time derivative of the phase noise. Consequently, understanding the spectral properties of $\phi(t)$provides direct information about the frequency stability and linewidth of the laser. Laser noise is commonly characterized, in the frequency domain, using the power spectral density (PSD) of the fluctuations. For a general random process $x(t)$, the statistical properties of the signal can be described through its autocorrelation function:

$$R_x(\tau) = \langle x(t)x(t+\tau)\rangle. \tag{2.88}$$

which measures the degree of correlation between the signal at two different times separated by a delay τ. The PSD is then obtained as the Fourier transform of this autocorrelation function and represents how the noise power is distributed over Fourier frequency as follows:

$$S_x(f) = \int_{-\infty}^{\infty} R_x(\tau)e^{-i2\pi f\tau}d\tau \tag{2.89}$$

This spectral description is especially valuable for laser characterization, since it enables the respective contributions of phase and frequency fluctuations to be distinguished through their power spectral densities and associated with the physical processes that broaden the laser linewidth. Because frequency noise is the time derivative of phase noise, their corresponding power spectral densities are directly related [23]:

$$S_{\Delta\nu}(f) = f^2 S_\phi(f) \tag{2.90}$$

2.6.1 Noise Processes

The phase and frequency-noise spectra of a laser typically contain multiple components with different frequency dependences, reflecting the presence of distinct underlying physical noise processes. Accordingly, the frequency-noise power spectral density can often be expressed as a sum of power-law contributions [24]:

$$S_{\Delta\nu}(f) = h_0 + \frac{h_{-1}}{f} + \frac{h_{-2}}{f^2} \tag{2.91}$$

where h_0 denotes the frequency-independent (white) frequency-noise level, usually dominated by spontaneous-emission noise, h_{-1} is the coefficient of the $1/f$ (flicker) frequency-noise term, often associated with slow electronic or environmental fluctuations, and h_{-2} quantifies the $1/f^2$ random-walk frequency-noise contribution, typically linked to slow thermal and mechanical drifts in the laser or its surroundings. Since phase and frequency noise are related by Eq. (2.90), and re-naming the coefficients, the corresponding phase-noise spectrum becomes:

$$S_\phi(f) = \frac{\delta\nu}{\pi f^2} + \frac{k_{fl}}{\pi f^3} + \frac{k_{rw}}{\pi f^4}, \tag{2.92}$$

where $\delta\nu$ denotes the white frequency-noise term, which is directly associated with the intrinsic Lorentzian linewidth, k_{fl} accounts for flicker frequency noise, and k_{rw} represents random-walk frequency noise.

This expression is commonly employed in the analysis of experimentally measured phase- or frequency-noise power spectral densities to identify and separate the physical noise processes contributing to linewidth broadening.

2.7 Intrinsic and effective laser linewidth

The intrinsic linewidth of a laser is the minimum linewidth determined by quantum noise processes inside the cavity. The fundamental mechanism is spontaneous emission, which randomly perturbs the phase of the optical field. This effect leads to the Schawlow–Townes linewidth, given by [25]:

$$\delta\nu_{ST} = \frac{h\nu L_{tot} T_{oc}}{2\pi\tau_r P_{out}} \tag{2.93}$$

In this expression, h is Planck's constant, ν denotes the lasing optical frequency, L_{tot} accounts for the total round-trip cavity losses, T_{oc} is the output coupler transmission, τ_{rt} is the cavity round-trip time, and P_{out} is the emitted optical output power. The Schawlow–Townes limit corresponds to white frequency noise, producing a Lorentzian spectral line with full width at half maximum (FWHM), $\delta\nu = \pi S_{\Delta\nu}$, as defined above in Eq. (2.92).

However, in semiconductor lasers, a more accurate expression for the intrinsic linewidth must also account for the coupling between optical gain and the complex refractive index of the gain medium, usually written as $n + jn'$. This amplitude-phase coupling is described by the linewidth enhancement factor α_{lin} [26]:

$$\alpha_{lin} = \frac{dn}{dn'} \tag{2.94}$$

Taking this effect into account, it modifies the Schawlow–Townes limit to:

$$\delta'\nu = \frac{h\nu L_{tot} T_{oc}}{4\pi\tau_r P_{out}}(1 + \alpha_{lin}{}^2). \tag{2.95}$$

Whereas, in the presence of a high-finesse external-cavity, the linewidth is reduced approximately as $\Delta\nu = \Delta\nu_0 / \left(1{+}\sqrt{1+\alpha_{lin}{}^2}\sqrt{\kappa}\ \frac{Q_{ext}}{Q_{int}}\right)^2$ [27], where $\Delta\nu_0$ denotes the free-running linewidth, κ the power mode-coupling factor, and Q_{ext} and Q_{int} the quality factors of the external and internal cavities, respectively. An equivalent interpretation is obtained by treating the device as a solitary laser with an effective extended cavity, for which $\Delta\nu = \Delta\nu_0 \left(\frac{n_{int}L_{int}}{n_{int}L_{int}+n_{ext}L_{ext}}\right)^2$.

The parameters n_{int} and L_{int} denote the effective refractive index and physical length of the internal cavity related to the gain section and its own reflective facets, respectively, while n_{ext} and L_{ext} are the corresponding quantities for the external-cavity section based on the passive PIC.

These expressions indicate that a wavelength-selective resonant mirror reduces the intrinsic linewidth of the hybrid laser through the increase of the effective cavity quality factor and photon lifetime, while also enforcing frequency-selective feedback around the resonant wavelength.
Nevertheless, the experimentally measured linewidth is generally larger than the intrinsic linewidth, since it is determined not only by the fundamental quantum limit but also by the presence of technical noise sources, such as thermal fluctuations, mechanical vibrations, acoustic perturbations, optical feedback, and slow frequency drift. Because the instantaneous laser frequency may vary during the acquisition time, the measured spectrum corresponds to the superposition of instantaneous spectra centered at different frequencies. As a result, the effective linewidth depends on the observation time and is particularly sensitive to noise contributions at low Fourier frequencies.
In the presence of low-frequency noise processes, such as flicker frequency noise or random-walk frequency noise, the definition of a unique linewidth becomes less rigorous, since the resulting spectral profile may deviate significantly from an ideal Lorentzian line shape.

2.8 Nonlinear effects

An optical device must be characterized by accounting for both linear and nonlinear phenomena that govern its response to an applied optical field. The dipole moment per unit volume, or polarization vector $\widetilde{\mathbf{P}}(t)$, describes this behavior and can be decomposed into a linear and a nonlinear contribution [28],[29]:

$$\widetilde{\mathbf{P}}(t) = \widetilde{\mathbf{P}}_L(t) + \widetilde{\mathbf{P}}_{NL}(t). \tag{2.96}$$

Each term, indicated with bold text to represent the vector notation, is expressed as:

$$\begin{cases} \widetilde{\mathbf{P}}_L(t) = \varepsilon_0 \int_{-\infty}^{+\infty} \chi^{(1)}\,(t-t')\cdot \tilde{\mathbf{E}}(\mathbf{r},t')\,dt', \\ \widetilde{\mathbf{P}}_{NL}(t) = \varepsilon_0 \iiint_{-\infty}^{+\infty} \chi^{(3)}\,(t-t_1, t-t_2, t-t_3)\,\tilde{\mathbf{E}}(\mathbf{r},t_1)\tilde{\mathbf{E}}(\mathbf{r},t_2)\tilde{\mathbf{E}}(\mathbf{r},t_3)\,dt_1 dt_2 dt_3 \end{cases} \tag{2.97}$$

In these expressions, ε_0 ($8.85\cdot10^{-12}$ F/m) is the permittivity of free space, while the variables t' and t_1, t_2, t_3 are dummy integration variables representing the time-dependent response of the optical field; they account for the non-instantaneous response of the material. The linear response is governed by the first-order susceptibility $\chi^{(1)}$, while the nonlinear response arises from higher-order susceptibilities. For inversion symmetric materials, such as Si and SiN treated in this thesis, the second-order polarization vanishes, so the dominant nonlinear contribution arises from the third-order susceptibility $\chi^{(3)}$. The latter, originates from various physical effects with different characteristic response times. In the context of frequency comb generation, the dominant effect is the electronic polarization of the medium, which can be considered instantaneous, with a response time on the order of 10^{-15} s [29]. On longer time scales, additional mechanisms, such as molecular orientation and electrostriction, may also contribute to the overall $\chi^{(3)}$ nonlinearity. The $\chi^{(3)}$ term provides information both on nonlinear Kerr-related effects and nonlinear loss contribution. In guided structures, the overall strength of the third-order response is conveniently described by the complex nonlinear parameter $\gamma(\omega)$[30]:

$$\gamma(\omega) = \frac{3\omega}{4\varepsilon_0 c^2 A_{\mathrm{eff}} n_{\mathrm{eff}}^2} \chi^{(3)}(\omega) = \frac{\omega n_2}{c A_{\mathrm{eff}}} + j\, \frac{\beta_{\mathrm{TPA}}}{2A_{\mathrm{eff}}}, \tag{2.98}$$

where the real part ($\propto n_2$) accounts for the Kerr effect and the imaginary part ($\propto \beta_{\mathrm{TPA}}$) includes the TPA effect. In semiconductors, TPA is typically the dominant nonlinear loss at telecommunication wavelengths and simultaneously generates free carriers.

These carriers contribute an additional absorption term, free-carrier absorption (FCA), and modify the refractive index via free-carrier dispersion (FCD). The TPA coefficient $\beta_{\mathrm{TPA}}(\omega)$ is strictly linked to the imaginary part of third-order susceptibility $\chi^{(3)}_{(\mathrm{Imag})}$ as:

$$\beta_{\mathrm{TPA}}(\omega) = \frac{3\pi}{c\,\varepsilon_0 \lambda\, n_0^2}\, \chi^{(3)}_{(\mathrm{Imag})} \tag{2.99}$$

In particular, the absorption coefficient contains a linear term α_{lin}, which is independent of intensity, and a nonlinear contribution ($\beta_{\mathrm{TPA}}(\omega)$) that introduces a linear dependence of the absorption coefficient on the optical intensity *I*:

$$\alpha(\omega) = \alpha_{\mathrm{lin}} + \beta_{\mathrm{TPA}}(\omega)\, I, \tag{2.100}$$

At the material level, the Kerr effect corresponds to an intensity-dependent refractive index:

$$n = n_0 + n_2 I_k + 2n_2(I_l + I_m), \tag{2.101}$$

defined for a field E_k co-propagating with other fields $E_l$and E_m, where $I_{k,l,m} = \frac{1}{2} n_0 \varepsilon_0 c \left|E_{k,l,m}\right|^2$.

Regarding the real part of the nonlinear parameter $\gamma(\omega)$, the nonlinear refractive index results:

$$n_2 = \frac{3}{2n_0^2 \varepsilon_0 c}\, \chi^{(3)}_{(\mathrm{real})}. \tag{2.102}$$

The parameter n_2 is also referred to Kerr term and produces two main effects: self-phase modulation (SPM) and cross-phase modulation (XPM). SPM occurs when a wave modifies its own phase through its intensity$|\, E_k \,|^2$, leading to spectral broadening and resonance shifts in cavities. XPM arises when a wave experiences an additional index change $\Delta n_{XPM} = 2n_2(I_l + I_m)$ due to co-propagating fields; for a given intensity, this XPM contribution is twice as strong as the SPM term. Instead, the effect of the nonlinear polarization term in Eq. (2.97) is to act as an adding source component in the nonlinear wave equation [30]:

$$-\nabla^2 \tilde{\mathbf{E}} + \frac{\varepsilon_L}{c^2} \frac{\partial^2 \tilde{\mathbf{E}}}{\partial t^2} = -\mu_0 \frac{\partial^2 (\tilde{\mathbf{P}}_{\mathrm{NL}})}{\partial t^2}. \tag{2.103}$$

This equation describes the propagation of light in a nonlinear medium. In detail, when several frequency components co-propagate, $\widetilde{\mathbf{P}}_{NL} \propto \chi^{(3)}\boldsymbol{E}^3$couples different spectral components and enables a variety of $\chi^{(3)}$parametric processes.

For an input field composed of several tones, $E(t) = \sum_n E_n\, e^{-j\omega_n t} +$ c.c., the expansion of E^3, under the instantaneous scalar model, contains products of three field amplitudes that oscillate at new frequencies. Among these processes, the ones following can be distinguished [31]:

- Third-harmonic generation (THG) at $\omega_n = 3\omega_k$:

$$P_{NL}(\omega_n = 3\omega_k)e^{ik_n z} = \varepsilon_0\chi^{(3)}E_k^3 e^{i3k_k z}, \tag{2.104}$$

- Triple sum-frequency generation at $\omega_n = 2\omega_k + \omega_l$ or $\omega_k + \omega_l + \omega_m$:

$$\begin{cases} P_{NL}(\omega_n = 2\omega_k + \omega_l)e^{ik_n z} = 3\varepsilon_0\chi^{(3)}E_k^2 E_l e^{i(2k_k+k_l)z} \\ P_{NL}(\omega_n = \omega_k + \omega_l + \omega_m)e^{ik_n z} = 6\varepsilon_0\chi^{(3)}E_k E_l E_m e^{i(k_k+k_l+k_m)z} \end{cases} \tag{2.105}$$

- FWM at $\omega_n = \omega_k + \omega_l - \omega_m$ (non-degenerate) or $2\omega_k - \omega_l$(degenerate):

$$\begin{cases} P_{NL}(\omega_n = \omega_k + \omega_l - \omega_m)e^{ik_n z} = 6\varepsilon_0\chi^{(3)}E_k E_l E_m^* e^{i(k_k+k_l-k_m)z} \\ P_{NL}(\omega_n = 2\omega_k - \omega_l)e^{ik_n z} = 3\varepsilon_0\chi^{(3)}E_k^2 E_l^* e^{i(2k_k-k_l)z} \end{cases} \tag{2.106}$$

In these expressions, ω_j denotes the optical angular frequency, E_j with $j = n, k, l, m$ represents the complex amplitude of the electric field at frequency ω_j, and E_j^* the complex conjugate of the electric field component E_j. The FWM process corresponds to the annihilation of two photons and the creation of two new photons such that energy is conserved and it can be distinguished in a non-degenerate case ($\omega_k + \omega_l = \omega_m + \omega_n$) and the degenerate case ($2\omega_k = \omega_l + \omega_n$).

For efficient frequency conversion, the nonlinear polarization P_{NL}must act as a coherent source for the newly generated wave, which requires phase matching. In the case of FWM, this condition can be written as:

$$\begin{cases} \Delta k = k_n - k_k - k_l + k_m \approx 0, \\ \Delta k = k_n - 2k_k + k_l \approx 0 \end{cases} \tag{2.107}$$

where $k_j = n_{\mathrm{eff}}(\omega_j)\,\omega_j|_{j=n,k,l,m}$ are the propagation constants of the interacting waves.

When $\Delta k \approx 0$, the generated field and the driving nonlinear polarization remain in phase and interfere constructively along the propagation direction, allowing the new frequency components to build up efficiently. In guided-wave devices, this phase-matching condition is determined by the dispersion of the effective index $n_{\mathrm{eff}}(\omega)$.By appropriate dispersion engineering and exploiting the Kerr-induced nonlinear phase shift (which modifies the effective k through the intensity-dependent index), can be realized broadband four-wave mixing and Kerr-comb generation, all within the nonlinear-polarization framework described above.

2-References

[1] Erdogan, Turan. "Fiber grating spectra." *Journal of Lightwave Technology* 15.8 (1997): 1277-1294.
[2] Cheng, Rui, and Lukas Chrostowski. "Spectral design of silicon integrated Bragg gratings: A tutorial." *Journal of Lightwave Technology* 39.3 (2020): 712-729.
[3] Jiang, Guomin, et al. "Slab-modulated sidewall Bragg gratings in silicon-on-insulator ridge waveguides." *IEEE Photonics Technology Letters* 23.1 (2010): 6-8.
[4] Wang, Xu, et al. "Uniform and sampled Bragg gratings in SOI strip waveguides with sidewall corrugations." *IEEE Photonics Technology Letters* 23.5 (2010): 290-292.
[5] Wang, Xu. Silicon photonic waveguide Bragg gratings. Ph.D. Diss. University of British Columbia, 2013.
[6] Simard, Alexandre D., et al. "Apodized silicon-on-insulator Bragg gratings." *IEEE Photonics Technology Letters* 24.12 (2012): 1033-1035.
[7] Poladian, L. "Variational technique for nonuniform gratings and distributed-feedback lasers." *Journal of the Optical Society of America A* 11.6 (1994): 1846-1853.
[8] Wang, Xu, et al. "Narrow-band waveguide Bragg gratings on SOI wafers with CMOS-compatible fabrication process." *Optics express* 20.14 (2012): 15547-15558.
[9] Ennser, Karin, N. Zervas, and R. L. Laming. "Optimization of apodized linearly chirped fiber gratings for optical communications." *IEEE journal of quantum electronics* 34.5 (1998): 770-778.
[10] Ouellette, Francois. "Dispersion cancellation using linearly chirped Bragg grating filters in optical waveguides." *Optics letters* 12.10 (1987): 847-849.
[11] Pastor, Daniel, et al. "Design of apodized linearly chirped fiber gratings for dispersion compensation." *Journal of Lightwave Technology* 14.11 (1996): 2581-2588.
[12] Coldren, Larry A. "Diode lasers and photonic integrated circuits." Optical Engineering 36.2 (1997): 616.
[13] Aspelmeyer, Markus, Tobias J. Kippenberg, and Florian Marquardt. "Cavity optomechanics." *Reviews of Modern Physics* 86.4 (2014): 1391-1452.
[14] Vahala, Kerry J. "Optical microcavities." *nature* 424.6950 (2003): 839-846.
[15] Praena, José Ángel, and Alejandro Carballar. "Integrated Bragg Grating Spectra." *Photonics*. Vol. 12. No. 4. MDPI, 2025.
[16] Comis, Farah, et al. "Experimental analysis and modeling of the penetration depth of uniform and apodized integrated Bragg reflectors." *Optics Express* 32.26 (2024): 47447-47457.
[17] Karabchevsky, Alina, and Amol Choudhary, eds. *On-Chip Photonics: Principles, Technology and Applications*. Elsevier, 2024.
[18]Chembo, Yanne K. "Kerr optical frequency combs: theory, applications and perspectives." *Nanophotonics* 5.2 (2016): 214-230.
[19] Herr, Tobias, Michael L. Gorodetsky, and Tobias J. Kippenberg. "Dissipative Kerr solitons in optical microresonators." *Nonlinear optical cavity dynamics: from microresonators to fiber lasers* (2016): 129-162.
[20] Liles, Alexandros Athanasios. Hybrid photonic crystal cavity based lasers. Ph.D. Diss. University of St Andrews, 2017.
[21] Iadanza, Simone. MOS Compatible Deposited Materials for Optical Interconnects. Ph.D. Diss. Munster Technological University of Cork, 2022.
[22] Xu, Yong, et al. "Scattering-theory analysis of waveguide-resonator coupling." *Physical Review E* 62.5 (2000): 7389.
[23] Rubiola, Enrico. "Phase noise and frequency stability in oscillators." *Phase Noise and Frequency Stability in Oscillators*. 2008. 1-203.
[24] Mukherjee, Shambo. Development of a Fabry-Pérot optical interferometer with low thermal and accelerometric sensitivities. Ph.D. Diss. Université Bourgogne Franche-Comté, 2024.
[25] Schawlow, Arthur L., and Charles H. Townes. "Infrared and optical masers." *Physical review* 112.6 (1958): 1940.
[26] Henry, C. "Phase noise in semiconductor lasers." *Journal of Lightwave Technology* 4.3 (2003):

298-311.
[27] Peng, Jiwang, et al. "Principles, measurements and suppressions of semiconductor laser noise—a review." *IEEE Journal of Quantum Electronics* 57.5 (2021): 1-15.
[28] Lin, Q., Oskar J. Painter, and Govind P. Agrawal. "Nonlinear optical phenomena in silicon waveguides: modeling and applications." *Optics express* 15.25 (2007): 16604-16644.
[29] Boyd, Robert W. "Nonlinear optics third edition." (2008).
[30] Monopoli, Davide. *Design and fabrication of silicon-rich silicon nitride based multimode interferometers for comb lasers*. Master Diss. Polytechnic University of Bari, 2022.
[31] Herr, Tobias. *Solitons and dynamics of frequency comb formation in optical microresonators*. Ph.D. Diss. EPFL, 2013.

Chapter 3: Integrated SC-FPs based on engineered Bragg gratings mirrors

Chapter 3 presents the design, fabrication and characterization of the core resonators implemented in this thesis, that are integrated SC-FP resonators on a silicon nitride platform. A comparison with established micro-resonators, such as microring resonators and in-plane FPs, is performed, highlighting key design parameters. The implemented SC-FPs incorporate a combination of uniform and apodized Bragg grating reflectors, investigating different DBR architectures alongside parametric sweeps of FP cavity geometrical parameters.

These structures enable precise tailoring of integrated dispersion and broadening of the optical stopband in the near-infrared (NIR) wavelength range through engineering of grating corrugation width and profile, duty cycle, and taper length in apodized reflectors.

The fabricated SC-FPs can achieve stopbands exceeding 70 nm and offer controlled transitions from strongly anomalous to strongly normal integrated-dispersion regimes. Furthermore, this chapter demonstrates that these devices can operate either as high-Q micro-resonators with resonant modes up to $Q_l \approx 2.3\times10^5$, or as compact resonant reflectors with high peak reflectivity ($ER_{inter\text{-}peak} \approx 6.8$ dB), depending on the specific geometrical parameters and mirror design. These characteristics make SC-FP resonators highly attractive building blocks for hybrid integrated lasers, nonlinear photonic circuits, and high-sensitivity on-chip sensing platforms. The work presented in this chapter has led to a journal publication in *Scientific Reports*, listed as [j1] in the list of publications section.

3.1 Optical resonator: in-line and side-coupled FPs

In the last decades, the rapid expansion of PICs across mature CMOS-compatible platforms, such as SOI, SiN on insulator, and heterogenous photonic integration [1-6], has been facilitated by advancements in fabrication, integration and packaging techniques. This progress, enhancing manufacturability and minimizing performance losses, has driven the development of more complex photonic structures that ensure compactness and efficient photonic performance.

Integrated optical resonators are fundamental building blocks in PICs, enabling scalable deployment of high-performance optical systems on a single chip. Their scalability unlocks the full potential of integrated photonics for next-generation communication, sensing, and lasing applications, such as frequency selection and feedback [7-11].

The cavity's ability to store light over many round trips in a tightly confined mode enhances light–matter interactions, boosting the efficiency of nonlinear processes and the sensitivity of measurements relying on absorption or refractive index changes. Consequently, integrated micro-resonators underpin applications including dense wavelength-division multiplexing (DWDM) filters, cavity-enhanced spectroscopic sensors, optical frequency comb generators, and hybrid on-chip lasers. The continued pursuit of higher performance and stronger miniaturization in optical sensing, laser technology, and telecom systems has therefore intensified the development of compact, high-performance micro-resonators, establishing them as pivotal components of next-generation photonic integrated platforms.

Among the implemented architectures, traveling-wave resonators, such as microring and whispering-gallery-mode cavities, have been extensively investigated [12-14] and adopted thanks to their high-quality factors, compact footprint, and straightforward compatibility with planar waveguide platforms. Nevertheless, the ring-shaped geometry inherently constrains the maximum achievable free spectral range, as increasing the FSR requires reducing the resonator radius, which in turn increases bending-induced losses and introduces additional complexity in the device design required to mitigate the associated propagation losses [15].

Additionally, at ultra-high quality factors, typically beyond about 10^6, random backscattering from sidewall roughness can couple counter-propagating modes, leading to strong and stochastic resonance line splitting, mode crosstalk, and resonance shifts that degrades device reproducibility [16]. These structures offer limited flexibility for dispersion engineering, crucial for nonlinear applications such as Kerr comb generation and soliton formation, and their performance can be highly sensitive to fabrication tolerances. The main design degrees of freedom available to mitigate these limitations are associated with careful waveguide cross-section engineering in the microring layout.

This includes tailoring the ring path geometry, for example driving to long racetrack configurations or different waveguide shapes along the ring circumference, as well as engineering the waveguide cross-section (designed material thickness and/or waveguide width) for reducing sidewall-scattering losses and varying dispersion features. In this regard, a common approach has involved broadening the waveguide width to achieve the desired optical properties; however, this inevitably drives the structure into a multimode regime [17], thereby requiring the implementation of carefully engineered adiabatic taper-based mode converters to suppress inter-modal coupling and minimize crosstalk between guided modes.

To address the drawbacks of traveling-wave resonators, standing-wave resonators, and in particular integrated FP cavities, have emerged as an attractive alternative, providing a complementary route to high-Q operation while maintaining a compact footprint [18],[19].

In FP cavities, light oscillates between two partially reflecting mirrors, forming a standing-wave pattern whose resonances are set by the cavity length and the phase response of the mirrors, rather than by a curved propagation path. The response of these integrated resonators conceptually follows the FP analysis presented in Section 2.2, with the key distinction that the ideal reflectors are replaced by PIC-based structures. Such integrated reflectors leverage CMOS-compatible technologies, including SOI and SiN platforms, which enable low propagation losses and consequently improved resonator performance.

Among the different strategies investigated in the literature, ranging from integrated Sagnac loops, to waveguide retroreflectors [20], on-chip mirrors are typically realized as DBRs implemented by periodically modulating the effective index of a waveguide via cladding modulation [21], waveguide-width corrugation [22],[23], or patterned features in the waveguide and full air-gap gratings [24],[25]. The implementation of DBR gratings as reflectors provide precise control over mirror reflectivity, stopband width, and group-delay dispersion, and their spectral response can be engineered via parameters such as periodicity, duty cycle, and corrugation depth, as well as through chirped or apodized envelopes along the mirror length.

In particular, apodized DBRs allow the optical penetration length into the mirrors to be tailored [21], which directly sets the effective cavity length, free spectral range, and dispersion profile, while simultaneously reducing side-lobe levels.

Compared to MRRs, the linear FP geometry offers more direct and independent control of resonance spacing and dispersion. It allows for implementing shorter cavity lengths, enabling single-resonance operation within the DBR stopband, together with improved robustness against bend-induced loss. Moreover, backscattering in the FP cavity is mainly attributed to random fabrication-induced imperfections in the DBR mirrors and to stochastic mode perturbations, which manifest predominantly as additional scattering loss. In this configuration, the mirrors inherently couple the forward and backward waves into a single standing-wave eigenmode, so there are no separate frequency-degenerate clockwise (CW) and counterclockwise (CCW) modes that random scattering can *hybridize* into mode-splitting, unlike in MRRs (Supplementary material of [16]). FP resonators can employ either in-line or side-coupled (SC) configurations, depending on whether light accesses the cavity through one of the reflectors or via evanescent coupling from an adjacent waveguide.

When light is launched collinearly into the cavity and along the grating mirrors, the structure is referred to as an in-plane FP resonator. Recent demonstrations of high-Q in-line FP resonators have significantly advanced the state of the art, enabling dispersive photonic functionalities [16], non-linear applications [19],[26] and engineered-grating designs [18],[27].

In this work, the FP architecture consists of a waveguide resonant cavity characterized by a geometrical length L, bounded by two integrated symmetric rectangular shaped DBRs. Each DBR is implemented as a corrugated rectangular waveguide featuring alternating high- and low-index regions, whose widths are W_1 and W_2 respectively, defined by a periodicity (Λ), and a duty cycle (DC). These DBRs act as high-reflectivity mirrors that confine light within the cavity. The total grating sections are composed of a total number of gratings N_{TOT}, that can accommodate for combined uniform DBR periods (N) and apodized periods (N_T).

Figure 3.1(a) illustrates a schematic of the in-plane FP cavity, summarizing the main design parameters and reporting the reflection dips (b), in the input section, and the transmission peaks (c), in output, extracted experimentally.

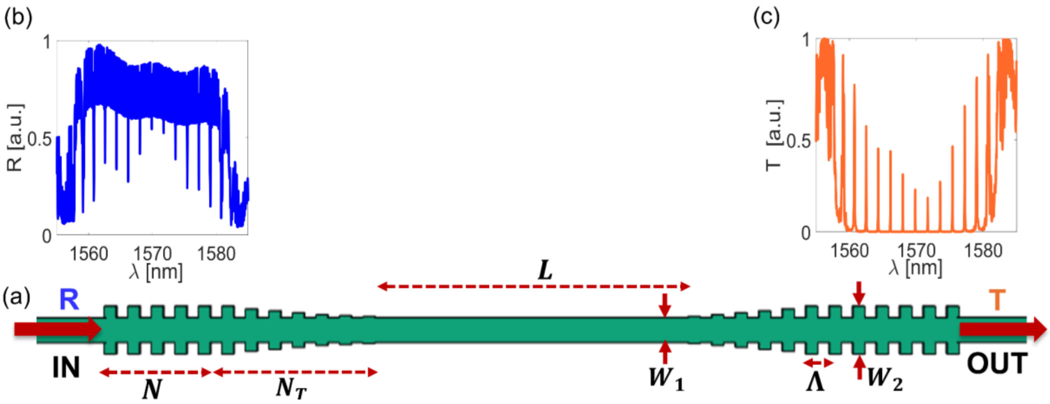

Figure 3.1: In-plane FP resonator: (a) schematic of the implemented architecture with the main design parameters. Example of experimental reflection dips (b) and transmission peaks (c) extracted in input and output, respectively.

In this configuration, the Bragg mirrors are part of the same waveguide that carries light on and off the chip: the corrugated section is directly connected to the input and output waveguides, so the DBR simultaneously acts as the cavity mirror and as coupling interface.

While this approach is conceptually simple and can deliver high reflectivity and strong resonant enhancement, it intrinsically links mirror design to both internal and external coupling conditions, and any imperfections or roughness in the mirror region directly affects the propagating signal, potentially increasing scattering losses into the surrounding circuit. Moreover, as mirror reflectivity improves by increasing the grating periods N, transmission efficiency decreases, resulting in elevated insertion losses.

In the side-coupled configuration [15],[20],[28-30], by contrast, the resonant cavity is formed by a straight waveguide segment terminated by two mirrors (in this work will be still treated DBRs as mirrors), whereas a separate bus waveguide is coupled to the cavity via evanescent interaction over a defined coupling region. In this scheme, the DBRs in the waveguide cavity define the resonator longitudinal modes, spectral selectivity, and dispersion, while the external coupling rate is set independently by the geometry of the side coupler, specifically through the coupling gap, length, implementation of low-loss bends (such as Bézier or Euler bends), and relative alignment between the bus and cavity waveguides.

The SC-FP architecture offers several advantages that are particularly relevant for high-performance PICs. The access waveguide is decoupled from the resonant feedback path. As a result, scattering and radiation loss in the etched DBR sections occur inside the cavity and do not translate directly into additional insertion loss at the input/output ports.

By adjusting the side coupler geometry, the external coupling can be optimized to minimize the impact of mirror losses on the bus waveguide, while the DBR mirror reflectivity can be designed independently. This decoupling between mirror and coupler design allows precise control of the coupling conditions and modal selectivity and enables a drastic increase in the number of grating periods without incurring in additional insertion losses as in the in-plane FP. Accurate engineering of the photonic platform and reflector geometry can further enhance system stability and noise performance.

Implementing the resonators on a low index contrast such as SiN platform and operating at moderate group index renders the cavities intrinsically less susceptible to disorder induced backscattering than devices on high index contrast SOI platforms [31].

In addition, adiabatic cavity–reflector transitions at the DBR interfaces minimize mode mismatch between the uniform waveguide mode and the Bloch mode of the high-contrast grating, thereby reducing radiation losses, enhancing the intrinsic quality factor, and lowering sensitivity to fabrication-induced perturbations. [27], [32]. The bidirectional propagation inside the FP cavity simultaneously produces transmission dips and reflection peaks in the input and output section of the adjacent waveguide, whose extinction ratio is set by the balance between intrinsic losses and external coupling [33].

In contrast to travelling-wave resonators, the standing-wave SC-FP cavity exhibits a different critical-coupling behavior, without a coupling condition for which the reflected power vanishes. Specifically, the coupling regime can be tuned from under-coupled to over-coupled. Increasing the coupling gap reduces insertion losses and enhances the loaded quality factor, whereas tighter coupling leads to broader resonance linewidths with higher peak reflectivity. Fig. 3.2(a) shows a schematic of the SC-FP resonator structure and the relative reflection peaks (b), defined in input, and transmission dips (c) obtained in output.

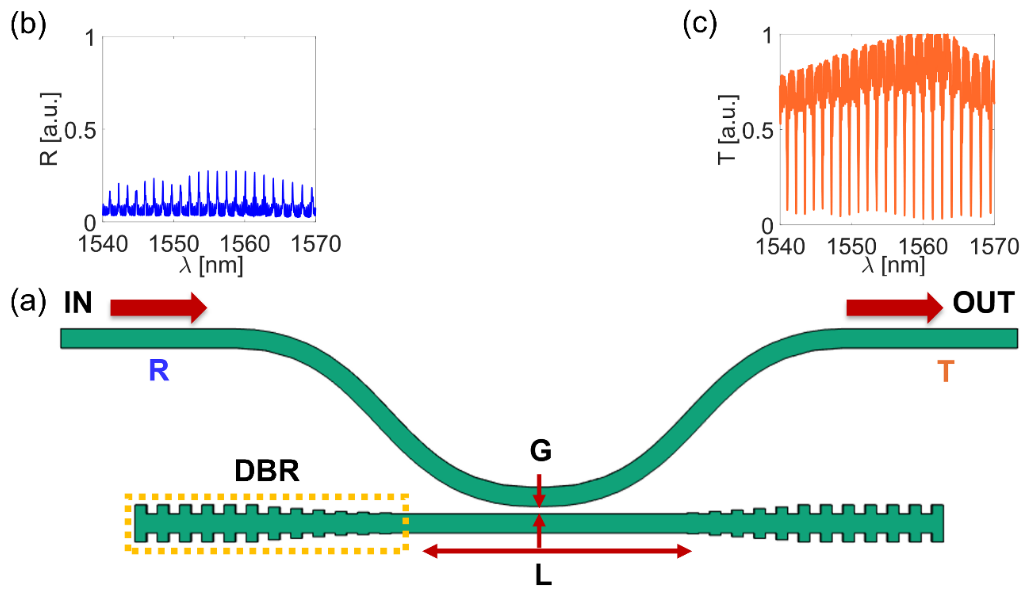

Figure 3.2: Side-coupled FP: schematic of the implemented architecture featuring a Bèzier-based side-coupler spaced *G* from the FP structure detailed in Fig. 3.1. Example of experimental reflection peaks (b) and transmission dips (c) extracted in input and output of the bus waveguide, respectively.

In this work, an experimental study is presented on different SC-FP resonator architectures on a 300 nm SiN platform, realized using DBRs based on waveguide-width modulation and air-gap structures [34]. Particular emphasis is placed on grating-section engineering, with a systematic analysis of how different taper lengths in apodized DBRs affect the resonator dispersion and optical penetration length, while the enhanced effective index contrast provided by accurate DBR designs enables exceptionally broad stopband widths in SiN.

3.2 Resonator design

The proposed integrated SC-FP consists of a straight SiN waveguide forming a Fabry–Pérot cavity, terminated on both sides by identical DBR sections. A third-order Bézier [35] bent waveguide, separated from the cavity by a designed coupling gap G, provides evanescent side-coupling between the waveguide and the FP cavity.

Among the key design parameters, the cavity length L and the gap G are systematically varied, and, in combination with the DBR features (period P, duty cycle, and apodization profile), they determine the coupling coefficient between the coupler waveguide and the FP cavity, the SC-FP reflectivity, the FSR, and the dispersion properties of the resonator.

Figure 3.3(a) presents a schematic of the SC-FP based on integrated Bragg gratings realized by periodically modulating the waveguide width with a rectangular-wave profile of period P. Fig. 3.3(b) highlights the gratings region, showing both uniform and apodized DBR sections, as illustrated in the SEM image, while further details on the fabrication process and inspection of the realized devices are discussed in the next sections.

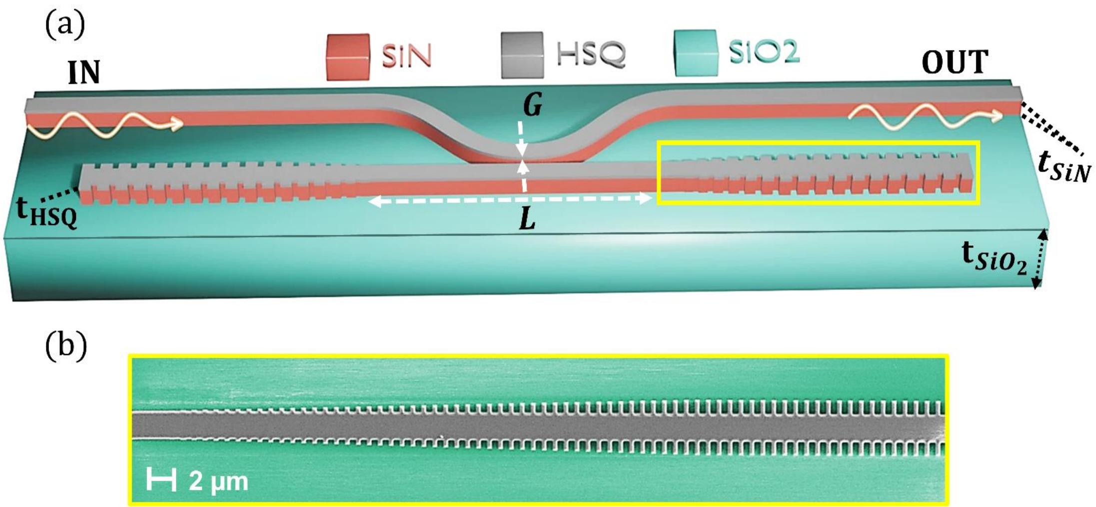

Fig. 3.3: (a) Schematic of the integrated SC-FP resonator with details on the geometrical parameters (coupling gap and cavity length) and thickness of the technological platforms used. (b) SEM image of the fabricated DBR section incorporating a combination of uniform and apodised gratings.

The high tunability offered by the SC-FP structure allow to implement distinct architectures obtained by tailoring the corrugation waveguide width in both the DBR and in the resonant cavity waveguide. In particular, Fig. 3.4(a) summarizes the main geometrical parameters that can be tuned in the DBR section to realize different SC-FP configurations. In the apodized version of the DBRs, the narrower and larger width of the modulation are linearly tapered from W_3 to W_1 and W_2, respectively, over the first N_T periods of the DBR a schematized in Fig. 3.4(a). At both edges of the cavity waveguide the DBR begins with the same width W_3, where $W_1 \leq W_3 < W_2$. Hereafter, if not specified, the nominal duty cycle (DC=l_{HIGH}/P) of the DBR corrugation is assumed to be DC = 50%.

An additional degree of freedom is the variation of the waveguide width in the FP cavity (W_4). This parameter can be increased so that $W_4 \geq W_3$, using a short linear taper to connect the wider central section to the DBRs, to reduce sidewall scattering losses in the resonator cavity. The uniform DBR sections differ from the apodized sections for a constant corrugation profile over N grating periods. Figure 3.4(b) depicts an extreme variation of the corrugation parameters, in which the waveguide width is reduced from W_3 down to a narrow tip W_1, corresponding to the minimum feature size allowed by the fabrication process (approximately ≈50 nm).

Beyond this point, the structure transitions to a sequence of air gaps separating the SiN segments. This particular configuration will be referred to, in the following as air-gap grating [34].

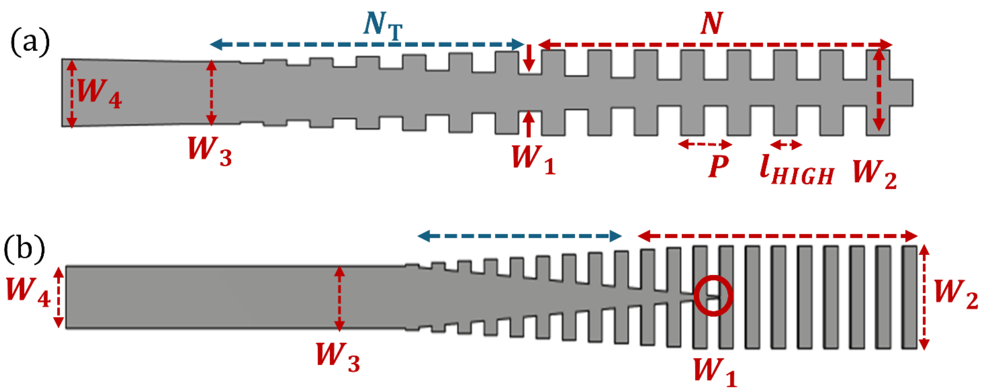

Fig. 3.4: (a) On-chip DBR key design parameters: distinct grating families are achieved by varying these quantities. (b) Air-gap DBR configuration: the high-index gratin region is tapered down from W_2 to W_3, while the low-index region is tapered down from W_3 to a small tip width (W_1=50 nm) and then the structure transitions to a sequence of air gaps separating the SiN layers (W_1=0).

The mask layouts of the DBR architectures and the corresponding side-coupled SC-FP resonators are designed using GDSII file format. GDS (Graphic Design System), widely recognized as the industry standard for PIC layout exchange, represents planar geometries into a hierarchical structure. Within this framework, geometric elements are organized into distinct layers, where each layer groups features distinct fabrication relevance. The information encoded in individual or combined layers is subsequently used to generate photomasks for lithographic fabrication and wafer patterning. In this work, electron beam lithography is employed, and its process will be detailed in the following section. The patterned structures are designed using appropriate layout software. In this work, KLayout CAD [36] is employed for standard designs, while more complex geometries are generated using the Python-based Nazca design framework.

The GDS layout is typically finalized following a preliminary cycle of numerical simulations aimed at assessing device performance and optical behavior. These simulations are used to evaluate light propagation, optimize key design parameters, and, in the case of DBR gratings, determine the grating period, ensure proper mode matching between tapered sections, and analyze transmission and reflection spectra.

ANSYS Lumerical [37] software is primarily employed for this purpose. In particular, the finite-difference eigenmode (FDE) solver is used to extract modal properties such as effective index and group index. Time-domain analysis is initially performed using a simplified variational finite-difference time-domain (varFDTD) approach in a 2.5D environment, enabling rapid parameter exploration. Once the main design parameters are established, high-resolution simulations are carried out using the full 3D finite-difference time-domain (FDTD) solver to achieve more accurate results. MATLAB and Python are used for the post-processing of both simulated and experimental data, enabling the extraction of key figures of merit, data fitting, and the analysis of both passive and active responses of the photonic devices under test.

3.3 Fabrication process

Fabrication was conducted at the University of Glasgow cleanroom using electron beam lithography (EBL) process. EBL offers key advantages over conventional photolithography, including maskless direct-write capability that eliminates costly mask fabrication and enables rapid design iterations. This direct-write EBL technique, leveraging the short de Broglie wavelength of high-energy electrons, enables the precise definition of critical elements such as narrow coupling gaps and photonic structures with features size well below the diffraction limit of optical lithography. The main fabrication steps are illustrated in Figure 3.5.

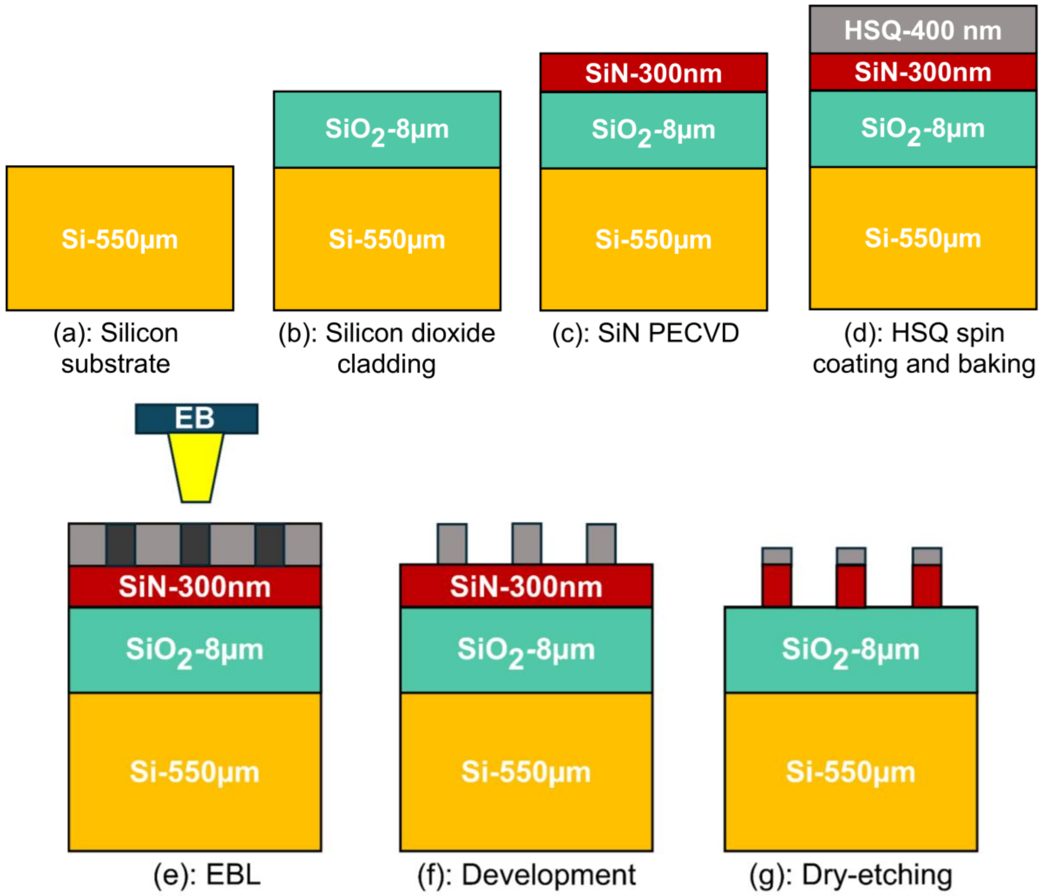

Fig. 3.5: Description of the PIC-fabrication flow for 300 nm thick SiN on 8 µm SiO_2 platform.

The technological platform employed for the SC-FP and DBR devices utilizes commercially supplied wafers from LioniX International BV [38], featuring a 300 nm-thick SiN core deposited via low-temperature plasma-enhanced chemical vapor deposition (PECVD) on an 8 µm-thick thermally grown SiO_2 bottom cladding over a 525 μm-thick bulk silicon substrate, with air as the top cladding (Fig. 3.5(a-c)). Air cladding has been deliberately considered here to support future refractive-index-sensing applications, as demonstrated in Section 6.1.

Wafers were first cleaned with acetone and isopropyl alcohol (IPA) to ensure optimal resist adhesion, followed by spin-coating and soft-baking a ~400 nm-thick layer of negative-tone hydrogen silsesquioxane (HSQ) resist onto the SiN surface (Fig. 3.5(d)).

Device layouts, including DBRs, SC-FP resonators, alignment markers, were digitally designed on an accurate GDS file and directly exposed at 100 kV via raster-scanning of a focused electron beam (Fig. 3.5(e)), delivering superior resolution compared to trench-exposure methods used in case of positive resist spin-coating. After EBL exposure, where the electron beam crosslinks exposed HSQ regions, making them insoluble, development selectively dissolves the unexposed (soluble) areas to reveal the inverted nanoscale pattern (Fig. 3.5(f)). Further details of the EBL fabrication process on passive photonic platforms, are provided in [39].

This patterned HSQ mask is then transferred into the underlying SiN layer via anisotropic inductively coupled plasma (ICP) etching with an O_2:CHF_3 (4:21) gas chemistry (Fig. 3.5(g)), where reactive plasma species chemically attack the nitride while accelerated ions provide directional sputtering to yield vertical sidewalls essential for low-loss waveguide performance.

From the initial HSQ thickness, approximately 70 nm of residual mask material remained after etching. This thin overlayer was deliberately left in place, as an additional HF-based wet-etch step would have exposed the SiO_2 lower cladding to HF, which could result in partial undercutting of the waveguide introducing extra scattering and absorption losses that could degrade device performance. Fig. 3.6(a) shows a schematic cross-section of the single-mode waveguide after fabrication, while Fig. 3.6(b) presents a SEM image of the fabricated structure used to verify dimensional accuracy and process fidelity.

As highlighted in the schematic and SEM cross-section image, the residual HSQ layer and part of the underlying SiN one deviate from an ideal rectangular profile.

This trapezoidal shape was measured to extend for 50 nm in the SiN with non-vertical sidewalls that initially exhibit an average top angle characterized by an average top angle $\theta_1 \approx 66°$, gradually transitioning to a shallower angle $\theta_2 \approx 24°$, before abruptly straightening into a near-ideal vertical sidewall ($\sim 90°$). This non-uniform profile, lacking perfectly vertical sidewalls throughout, arises from a non-optimized ICP dry etching recipe.

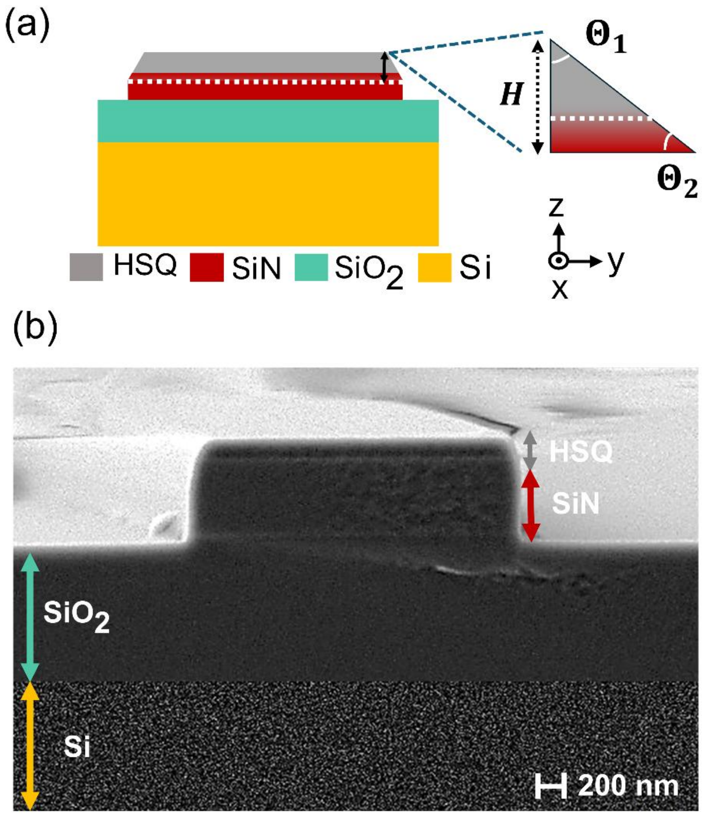

Fig. 3.6: (a) Schematic cross-section of the fabricated single-mode waveguide (*W*=1.3 µm) in the y–z plane. Along the y-axis is defined the lateral waveguide width, while in z-axis are defined the different material thickness layers: t_{HSQ}=70 nm, t_{SiN}=300 nm, t_{SiO_2}=8 µm, and t_{Si}=525 µm. (b) Corresponding SEM picture of the waveguide cross-section.

3.4 Optical characterization setup

The optical characterization of the passive devices was carried out in the CAPPA photonics laboratories in Tyndall National Institute (Cork), specifically using an end-fire (butt-coupling) configuration, in which light is launched directly into the chip waveguide end facets to assess transmission characteristics, propagation losses, and spectral response. While effective for on-chip photonics, this method requires precise alignment to mitigate degradation from misalignment, thermal drifts, or mechanical vibrations that can compromise coupling efficiency. The optical setup is shown in Figure 3.7.

A broadband amplified spontaneous emission (ASE) source that delivers power up to 40 mW across 1520-1620 nm exits a fiber holder and passes through a 10× collimation lens, then encounters a polarizing beam splitter to suppress TM (or TE) polarization and transmit only TE (or TM) mode. A 60× focusing lens on a 3-axis (x-y-z) stage then tightly couples the beam into the chip facet.

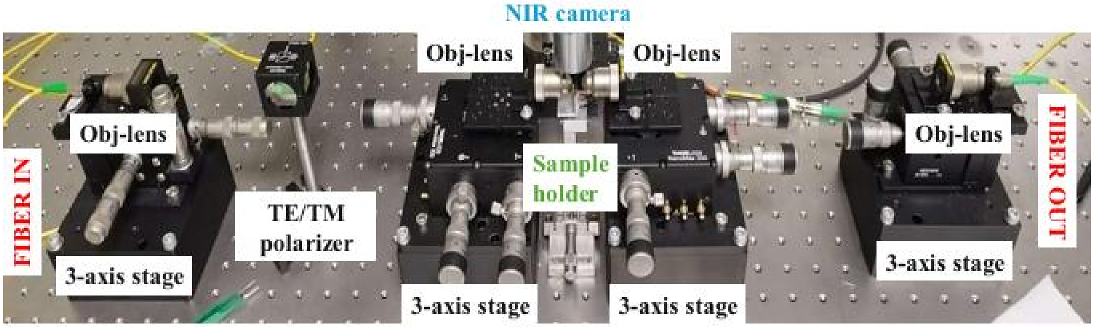

Fig. 3.7: Sketch of the end-fire optical setup.

These collimation and focusing lenses efficiently couple light into the waveguide when properly aligned, using 3-axis translation stages that allow precise positioning of the waveguide relative to the incident beam, alternatively lensed fibers can be also used ensuring 3 dB insertion losses. The photonic chip is mounted on a stable holder using conductive carbon tape (Fig. 3.8), sometimes adding a Peltier cell glued on the sample holder for ensuring thermal stabilization. A NIR camera with 20× objective lens, positioned on top of the waveguide, allows for monitoring the light beam spot at the input, at the output and along the waveguide's length to assess visually the coupling and any scattering that occurs. Transmitted light is symmetrically collected by an opposing 60× lens on another 3-axis stage, recollimated via 10× lens, and fiber-coupled generally to a 90/10 beam splitter: 10% diverts to a power meter for intensity quantification, while 90% routes to an optical spectrum analyzer (OSA) for detailed spectral readout.

Additional optical components like polarizers, fiber optic elements (such as circulators, couplers, reflectors), or mounts can be implemented based on the device under measurement.

OSA traces are streamed to a PC for live monitoring and post-processing analysis carried out in MATLAB. This versatile configuration supports the characterization of distinct photonic structures, including waveguides, DBRs, FP resonators, detailed in following sections.

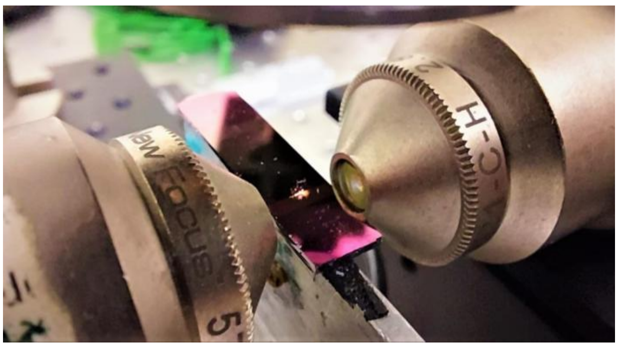

Fig. 3.8: Representation of the PIC mounted in the T-mount stage, illustrating alignment at the input and output facets.

3.5 On-chip DBRs: stopband characterization

Building on the schematics illustrated in Fig. 3.4 in the resonator design section (Section 3.2), the implemented on-chip DBRs in this work are organized into three design families (A, B, and C), distinguished by the specific choice of the design parameters. These three DBR families give rise to three corresponding SC-FP configurations.

The geometric parameters were selected through an optimization workflow aimed at maximizing the stopband width in air upper-cladding operation, increasing the effective index contrast varying the corrugation widths and duty cycle, while preventing the structure from entering a strongly multimode regime. At the same time, the designs were constrained to remain compatible with the available EBL process, accounting for practical limits on minimum feature size, pattern-transfer fidelity, etch robustness, so that the final geometry could be reliably fabricated and characterized. Rectangular-shaped corrugations are a common choice for integrated Bragg gratings and are also adopted in all the families of this work. The use of a rectangular profile for the DBRs maximizes the effective index contrast between high- and low-index segments for a given width variation, thereby providing a relatively large coupling coefficient and a broad stopband. This profile is straightforward to implement with standard EBL and anisotropic etching, since it requires only two well-defined width levels, whereas sinusoidal or multi-level modulations would demand tighter process control and additional patterning steps, increasing sensitivity to lithographic and etch non-uniformities.

Although rectangular features can in principle be smoothed towards a quasi-sinusoidal shape by lithography- and etch-induced rounding [40], SEM inspection of the fabricated devices that will be reported for the fabricated DBRs shows well-defined corrugation edges and a largely preserved rectangular geometry, indicating that the realized DBRs closely follow the intended square-wave profile and that fabrication-induced smoothing does not significantly degrade the performance. Family A DBR is obtained by considering the schematic reported in Fig. 3.4(a) and employing a low-index region of width $W_1 = W_3 = 1.3\ \mu$m, and a high-index region of width $W_2 = 2.5\ \mu$m. This design realizes the largest corrugation width W_2, while maintaining a conservative single-mode waveguide width of 1.3 μm in air cladding. Fig. 3.9 shows SEM images of the uniform rectangular family A gratings, zooming on the etched features in the SiN core and HSQ cladding. The rectangular waveguide corrugation is clearly resolved, and the measured widths W_1 and W_2 in the SiN core slightly deviate from the nominal design values of 1.30 μm and 2.50 μm to approximately 1.26 μm and 2.47 μm, respectively, while the corresponding HSQ features exhibit average widths of about 1.114 μm and 1.33 μm. This inspection, combined with the cross-section SEM shown in Fig. 3.6, confirm the presence of non-vertical sidewalls.

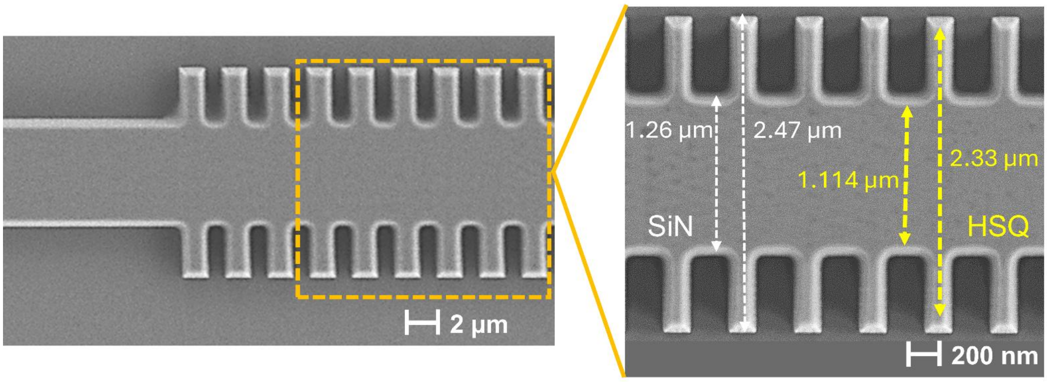

Fig. 3.9: SEM image of the uniform family A DBR, reporting a zoomed view of the average etched features for the SiN (white) and HSQ (yellow) layers, after fabrication.

Moreover, the fabrication process impacts also on the effective duty cycles of the implemented DBRs. Among the same grating family, different nominal duty cycles were designed and experimentally investigated, and their deviations from the target values were analyzed to quantify systematic imperfections in the widths of the individual DBR teeth. Fig. 3.10 reports the average etched dimensions and the corresponding duty cycles extracted from SEM analysis for the family A DBRs nominally designed with DC = 40%, 50%, and 70%, which after fabrication result in effective duty cycles of approximately 33.5%, 44%, and 63%, respectively.

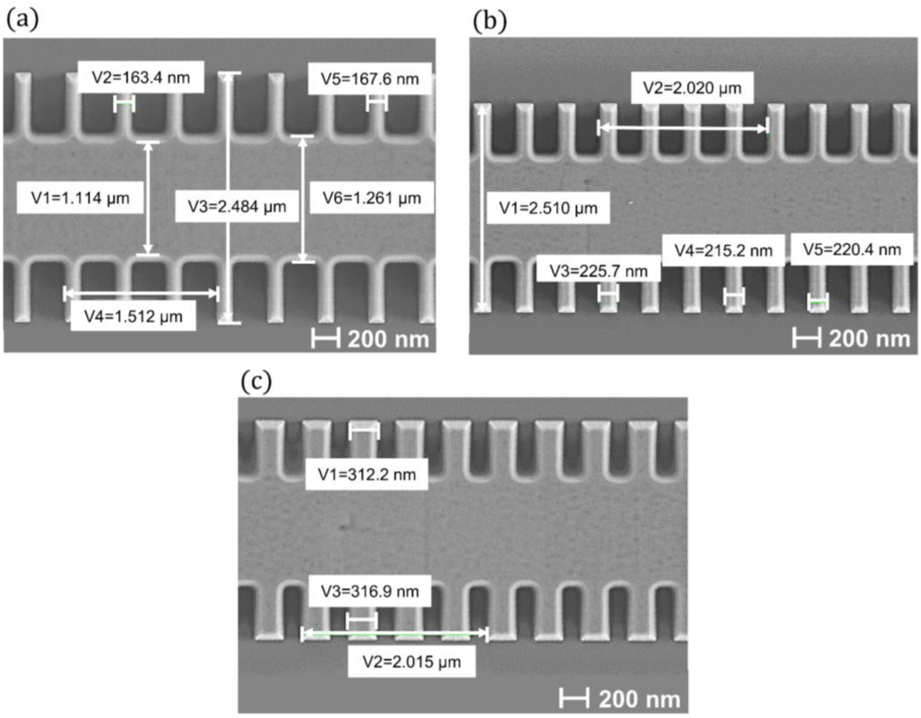

Fig. 3.10: SEM images of Family A-based DBR characterized by a rectangular corrugation shape and designed for duty cycles of (a) 40%, (b) 50%, and (c) 70%. Average corrugation width and etch dimension after fabrication process, are shown. By simple calculations, it can be estimated that the effective duty cycles result 33.5%, 44%, and 63%, respectively.

These measurements provide average indicators of the systematic deviation between the designed and fabricated devices. All such dimensional variations modify the effective index contrast, impacting the DBR stopband width, Bragg wavelength, and coupling strength.

Family B DBRs, in contrast, are based on the same schematic of Fig. 3.4 but start from a single-mode waveguide $W_3 = 1.3\,\mu$m and then transition to a narrower low-index segment $W_1 = 0.8\,\mu$m, while keeping the high-index segment $W_2 = 2.1\,\mu$m fixed. This configuration increases the effective index contrast by reducing W_1, thereby enhancing the stopband, while maintaining W_2 at a width that remains safely away from strongly multimode operation. Fig. 3.11(a) shows a SEM image of a uniform rectangular family B grating, highlighting deviations from the nominal corrugation widths: the SiN features deviate from the design values of 0.80 µm and 2.10 µm to approximately 0.753 µm and 2.07 µm, respectively, while the corresponding HSQ features exhibit average widths of about 0.585 µm and 1.92 µm. In this architecture, apodisation is particularly beneficial, as it ensures a smooth transition and mitigates mode-mismatch losses at both the interface between W_1 and W_2, and the W_3 to W_1 one.

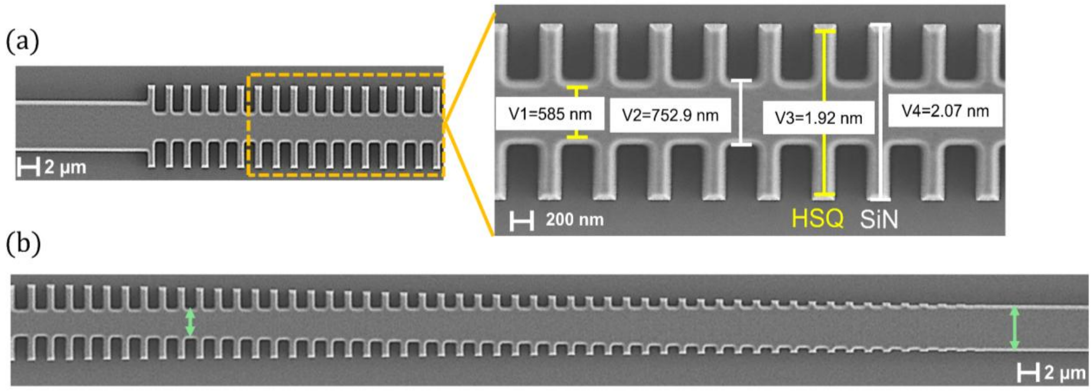

Fig. 3.11: (a) SEM image of the uniform family B DBR, reporting a zoomed view of the average etched features for the SiN (white) and HSQ (yellow) layers, after fabrication. (b) Overview of the double tapering implementation in the family B DBR: smooth transitions occurs both for the single-mode waveguide (W_3 tapered down to W_1), and for the teeth corrugation widths (W_1 tapered up to W_2).

Family C DBRs implement an air-gap DBR architecture, corresponding to the schematic in Fig. 3.4(b), by linearly tapering down the high-index regions from W_2=2.3 µm to W_3=1.3 µm and the low-index ones from W_3=1.3 μm to the minimum feature size related to fabrication constraints that for the implemented EBL process results W_1=50 nm, over N_T=250 periods.

Beyond the taper tip, the grating transitions to a fully air-gap structure, in which air gaps separate adjacent SiN segments, thereby maximizing the effective index contrast. For this configuration, SEM images are not reported in this chapter; a detailed description of the air-gap DBR implementation, including high-resolution SEM inspection and fabrication process information are provided in Chapter 6 (Section 6.2.1) of this thesis.

The stopband characterization of the three grating families was performed using the end-fire setup described in Section 3.4. Families A and B were measured in transmission using DBRs with $N = 1000$ uniform grating periods, because the applied apodisation does not significantly modify the experimentally extracted stopband width, whereas the stopband of family C devices was estimated from the wavelength range over which the SC-FP transmission exhibits resonance dips, as defined in [34]. Figure 3.12 (a) shows the comparison between the achieved stopband width between family A and B Bragg grating reflectors.

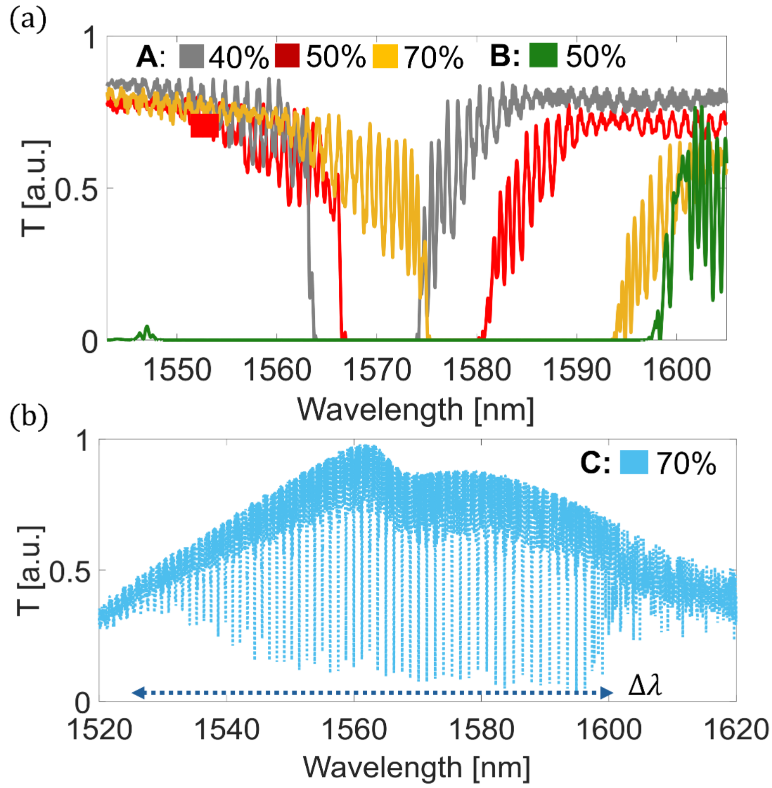

Fig. 3.12: Bragg grating stopband characterization. (a) Measured normalized transmission spectra for family A DBR with duty cycles of DC = 40%, 50%, and 70%, compared with family B architecture designed with DC = 50%. (b) Normalized transmission spectrum of air-gap SC-FP based on family C gratings (DC = 70%): a stopband Δλ ≈ 74 nm can be extracted.

Specifically, by varying the DC from 40% (grey trace) to 70% (yellow trace), the measured 3-dB stopband ($\Delta\lambda$) increases from $\Delta\lambda$ = 10.0 nm to $\Delta\lambda$ = 18.8 nm, with a red-shift of the center of the stopband position from 1569 nm to 1584 nm, for a fixed periodicity P = 506 nm. For a nominal duty cycle value DC=50%, $\Delta\lambda$ results 14 nm, as represented in the red trace in the figure.

Family B gratings further broaden the stopband width: the measured 3-dB stopband extends to $\Delta\lambda \approx 48$ nm (green trace in Fig. 3.12(a)), demonstrating the strong dependence of the mirror bandwidth on the corrugation amplitude modulation, and the consequent effective index contrast. The periodicity is set to P=530 nm to ensure a stopband center around 1574 nm, similar to the family A devices. Regarding the family C DBR, the stopband behavior is extracted from the transmission spectrum of the air-gap SC-FP characterized by N = 1750, N_T =250, L = 370 µm, P = 526 nm, and DC = 70% (Fig. 3.12(b)). This configuration enables the broadest operational bandwidth. The latter is estimated by evaluating the wavelength range over which the SC-FP transmission dips, as defined in [34], are supported and exhibit a value of approximately $\Delta\lambda$≈74 nm. Table 3.1 summarizes the stopbands and the design parameters considered for the three DBR families.

Table 3.1. Experimental bandwidth among different DBR families

DBR family	W_1 [µm]	W_2 [µm]	W_3 [µm]	$\Delta\lambda$ [nm]	
A	1.3	2.5	1.3	DC=40%	10
				DC=50%	14.2
				DC=70%	18.8
B	0.8	2.1	1.3	DC=50%	48
C	0	2.3	1.3	DC=50%	60
				DC=70%	74

*For air-gap DBRs, the stopband is approximately estimated by considering the region in which are supported the SC-FP transmission dips, as carried out in [34].

Furthermore, Table 3.2 provides a comprehensive review of photonic integrated Bragg gratings and DBRs from the literature, highlighting stopband widths, operating bands, core/substrate thicknesses, cladding configuration, and minimum feature sizes in order to compare with the devices presented in this work.

For instance, Ta_2O_5 rib-based DBRs on glass substrates immersed in water achieve $\Delta\lambda$ ≈12 nm, near-UV bands (~850 nm) for label-free biosensing [41].

Triangular corrugation-shaped SiN DBRs (600 nm thick SiN on 1.4 µm silicon dioxide buried oxide (BOX) and 1.5 µm top cladding) exhibit a polarization-independent 15 nm stopband in the O-band, with 40 dB rejection [42].

SOI strip-based gratings from [43], realized on the 220 nm thick SOI platform, implement a single mode waveguide width of W_1=500 nm and report a stopband ranging from 10 nm to 30 nm in the C-band, depending on air or silica cladding and corrugation width.

SiN chirped spiral Bragg gratings demonstrate large group delay dispersion (around 1440 ps) [44] and stopband of around 9.5 nm for 90 nm thick SiN, under SiO_2 cladding, while SOI platform-based [45] delivers $\Delta\lambda$ ≈15 nm with 50 ps group delay dispersion contribution.

In this work, family B DBRs, implemented on a 300 nm SiN core with double tapering of both low- and high-index segments, achieve a broadened stopband of approximately $\Delta\lambda \approx$ 48 nm, enabled by the enhanced effective index contrast engineered through the corrugation widths.

Building on the air-gap between the corrugated DBR waveguides, the proposed family C DBRs further extend the stopband to about $\Delta\lambda \approx$ 74 nm. Notably, this level of bandwidth enhancement is obtained only through DBR-corrugation engineering, without requiring customized layer thicknesses or non-standard cross-sections: all devices are realized on a standard LioniX 300 nm SiN platform using EBL process.

Table 3.2. Comparative overview of stopband performance for various integrated DBRs.

Structure	**Platform**	**Footprint [W×t]**	**Stopband $\Delta\lambda$**	**Ref.**
RIB-based DBR	Dielectric Ta_2O_5 core, Water cladding, Substrate: Schott D263	Rib Core: W=1000 nm Thickness: t=160 nm Min. feature size: 40 nm	≈ 12 nm: UV-band	[41]
Triangular-shaped DBR	SiN core, 1.5 μm SiO_2 cladding Substrate: 1.4 μm BOX	Core: W_1= 600 nm, W_2=1000 nm, Thickness: t=600 nm, Min. feature size: 200 nm	≈ 15 nm, ER=40 dB: O-band	[42]
DBR	Silicon core, air cladding Substrate: 2 μm BOX	Core: W_1: 500 nm, W_2: 820 nm, Thickness: t=220 nm, Min. feature size: P/2≈162 nm	≈ 30 nm, ER>30 dB C-band	[43]: Fig.2.22
DBR	SiN core, air cladding Substrate: 8 μm BOX	Core: W_1: 800 nm, W_2: 2100 nm, Thickness: t=300 nm, Min. feature size: 150 nm	≈ 48 nm, ER=30 dB C-band	This work
		Core: W_1: 1300 nm, W_2: 2300 nm, Thickness: t=300 nm, Min. feature size: tip width≈50 nm	≈ 74 nm: C-band	
Chirped-DBR	SiN on SOI core, SiO_2 cladding	Core: W_1: 2800 nm, W_2: 3000 nm, Thickness: t=90 nm, Min. feature size: 100 nm	≈ 9.5 nm, ER=20/30 dB C-band, 1440 ps group delay	[44]
	SiO_2-on-Si rib core, Air cladding, Substrate: SiO_2	Rib footprint: N.A., 5 mm length Min. feature size: N.A	≈ 15 nm: C-band, 50 ps group delay	[45]

3.6. Integrated in-plane FPs

This subsection presents an analysis of the resonator propagation losses, and quality factors experimentally evaluated for the in-plane FPs incorporating family A DBRs and considering different duty cycle values.

The designed and fabricated FP cavities follow the schematic depicted in Fig. 3.1 and consist of two identical DBR sections with a low-refractive index region characterized by a width of W_1=1.3 µm, while the high-refractive index region has a width of W_2=2.5 µm. The width of the resonant cavity is assumed to be $W_4 = W_3 = W_1$. The mirror sections are defined by N=100 uniform gratings and N_T=20 linearly apodized DBR on each side of the cavity.

The total grating number $N + N_T$ is deliberately limited to ensure sufficient transmission through the mirrors for in-plane FP characterization, while the apodized grating numbers are engineered to maximize the intrinsic Q_i factor. In particular, the tapered (or apodized) DBRs facilitate adiabatic mode conversion between the waveguide mode and the grating Bloch mode, avoiding the large Bloch-mode mismatch loss typical at the waveguide-grating interfaces [19] especially for strongly coupled gratings (as in a 1D photonic crystal), where light experiences multiple reflections and re-transmissions across the interface that amplify scattering losses. Following the approach used in [19], it is possible to extract details about the propagation losses (α) due to the integrated in-plane FP resonators. Specifically, it has been analyzed the contribution losses for two FPs characterized by DC=50% and DC=70%, fixing the values of cavity length to L=900 µm that enables high Q-loaded operation.

The FP resonances were characterized with a tunable-laser source in continuous-sweep mode (sweep rate 1 nm s^{-1}, acquisition 100 kSample s^{-1}) and detected on a high-speed Germanium photodiode (New Focus, 800-1750 nm, Model 2033). From these high-resolution experimental measurements, by fitting them according to the equations valid for an in-line resonator described in [33] extracted the resonant peak FWHM values, and the intrinsic, coupled and loaded quality factors.

Fig. 3.13(a) reports the resulting normalized FP transmission plot, with the fitting of the sharper resonance, for DC=70%. At λ=1572.89 nm, the FP features a very high loaded Q-factor of $Q_l = 3.48 \cdot 10^5$, that refers to a FWHM of around 4.5 pm, and an intrinsic quality factor $Q_i = 1.045 \cdot 10^6$. When DC=50%, the loaded Q-factor results $Q_l = 1.075 \cdot 10^5$, corresponding to a FWHM of around 15.4 pm, while $Q_i = 3.97 \cdot 10^5$ (Fig. 3.13(b)).

The propagation loss coefficient α for the two FP resonators can be defined as function of the extracted intrinsic quality factor, the resonant FP mode λ_{res}, and the group index n_g of the waveguide resonant cavity as follows [19]:

$$\alpha \approx \frac{2\pi n_g}{Q_i \lambda_{\text{res}}}. \tag{3.1}$$

The group index of the fundamental guided mode was extracted as a function of the wavelength using the FDE solver in Lumerical MODE, for a straight waveguide cavity with a width of 1.3 µm. The solver provides the effective and group indices by solving Maxwell's equations on the waveguide cross-section. Specifically, for the in-plane FP cavity characterized by DC=50%, the simulated group index is extracted at $\lambda_R = 1558.65$ nm, corresponding to a simulated group index $n_g = 1.9587$.

In contrast, for DC=70%, the group index is calculated $\lambda_R = 1572.89$ nm, yielding $n_g = 1.9539$. The resulting cavity losses result $\alpha_{DC=50\%} \approx 0.1986 \frac{1}{cm}$ and $\alpha_{DC=70\%} \approx 0.07468 \frac{1}{cm}$, for DC=50% and 70%, respectively. These values assess that the higher duty cycle (DC = 70%) reduces scattering losses and validate the low-loss performance of the engineered gratings, which underpins the high Q-factors achieved in the resonators.

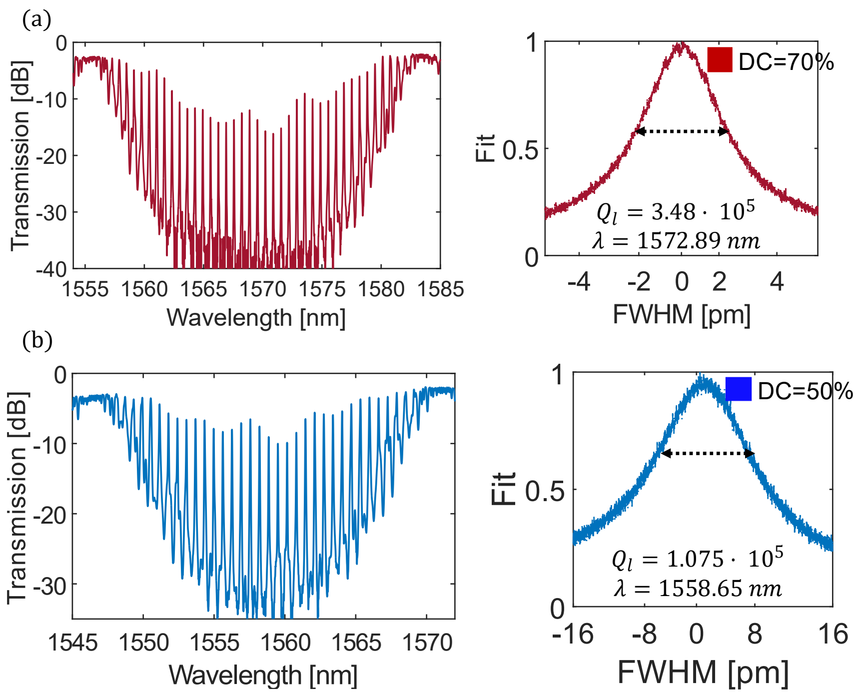

Fig. 3.13: Experimental normalized transmission spectra and Lorentzian fits for SC-FPs with differing duty cycles: (a) DC=70%, (b) DC=50%.

3.7 Integrated side-coupled FPs

This section details on the fabricated SC-FP resonators whose design schematic was illustrated in Fig. 3.3(a) and employing the DBR architectures whose characterization has been reported in Section 3.5. All the SC-FPs feature a combination of uniform and apodized grating mirrors, for a total of N+N_T =2000 grating periods, in order to achieve high reflectivity within the stopband. A preliminary study is first carried out on the output transmission response of the SC-FP resonant dips using an end-fire optical setup, following extraction of dispersion parameters, quality factor, and reflectivity. Accurate DBR design plays a central role in controlling the resonator-induced dispersion and provides a powerful degree of freedom beyond waveguide cross-section engineering alone. In this work, the impact of mirror corrugation width and apodisation profile on the group delay and phase response of the DBRs is systematically investigated, and their resulting influence on the spectral properties of the cavity modes is highlighted. Furthermore, the high tunability of the SC-FP platform is exploited by co-optimizing the cavity length and coupling gap, together with the choice of DBR family, to realize either ultra-high-Q resonances or device configurations that prioritize large on-resonance peak reflectivity, depending on the targeted applications.

3.7.1 Engineering of integrated dispersion

As detailed in Section 2.3.2, the DBR reflection phase $\phi_{DBR}(\omega)$ defines an effective penetration length L_{eff}, consequently introducing a frequency-dependent length contribution to the FP cavity beyond the physical separation between the reflectors L. This penetration length is strictly linked to the wavelength-dependent group delay $\tau(\lambda)$, given by the derivative of the grating phase response, so that the effective optical length of the entire SC-FP cavity and therefore its free spectral range, becomes explicitly frequency dependent.

While models for modelling cavities with uniform and apodized DBRs have been theoretically established [21], in this section the main emphasis is placed on the experimental demonstration that engineering the grating architecture, and in particular the apodized DBR taper length, enables precise control over the integrated dispersion of the resonator. In the optical-frequency domain f, the integrated dispersion $D_{\mathrm{int}}(\mu)$is defined as:

$$D_{int,f}(\mu) = f_\mu - (f_0 + D_{1,f} \cdot \mu), \tag{3.2}$$

where $\mathrm{f_0}$ and $\mathrm{f_\mu}$ denote the measured optical frequencies at the center of the stopband and at resonance with relative longitudinal number μ, respectively, where $\mu = \mathrm{m} - \mathrm{m_0}$. The reference Fabry-Perot mode is indicated with $\mathrm{m_0}$, placed at the center of the stopband, while generic mode index is defined with m that considers integer values. Thus, $\mu = 0$ corresponds to the reference resonance ($m = m_0$), $\mu = \pm 1$ to the first neighboring resonances on either side, $\mu=\pm 2$ to the next pair, and so on. $D_{n,f} = \frac{\partial^n f_\mu}{\partial \mu^n}\Big|_{\mu=0}$ are the n-th order dispersion coefficients, such that $D_{1,f}$ is the FSR at the center of the stopband. The integrated dispersion $D_{int,f}(\mu)$ are retrieved by fitting the experimentally measured resonant frequencies f_μ with a cubic polynomial as:

$$f_\mu = f_0 + D_{1,f} \cdot \mu + \frac{D_{2,f}}{2} \cdot \mu^2 + \frac{D_{3,f}}{6} \cdot \mu^3. \quad (3.3)$$

Consequently, $D_{1,f}$, $D_{2,f}$, and $D_{3,f}$, are extracted from the fit coefficients.

By considering the end-fire setup described in Section 3.4, the SC-FPs are characterized in transmission, and the output spectra of resonators incorporating the three DBR families are collected to experimentally retrieve the integrated dispersion using Eq. (3.3).

Figure 3.14(a–d) reports the transmission response of SC-FP resonators based on the family A DBR (P = 500 nm, W_1 = 1.3 µm, W_2 = 2.5 µm), for progressively increasing apodized grating length N_T, from $N_T = 0$ in (a) up to $N_T = 1000$ in (d), with the cavity length fixed to $L = 900$ µm and a coupling gap $G = 500$ nm. As the apodisation in the grating increases, a higher number of SC-FP modes appears within the same DBR stopband, providing a denser set of resonances.

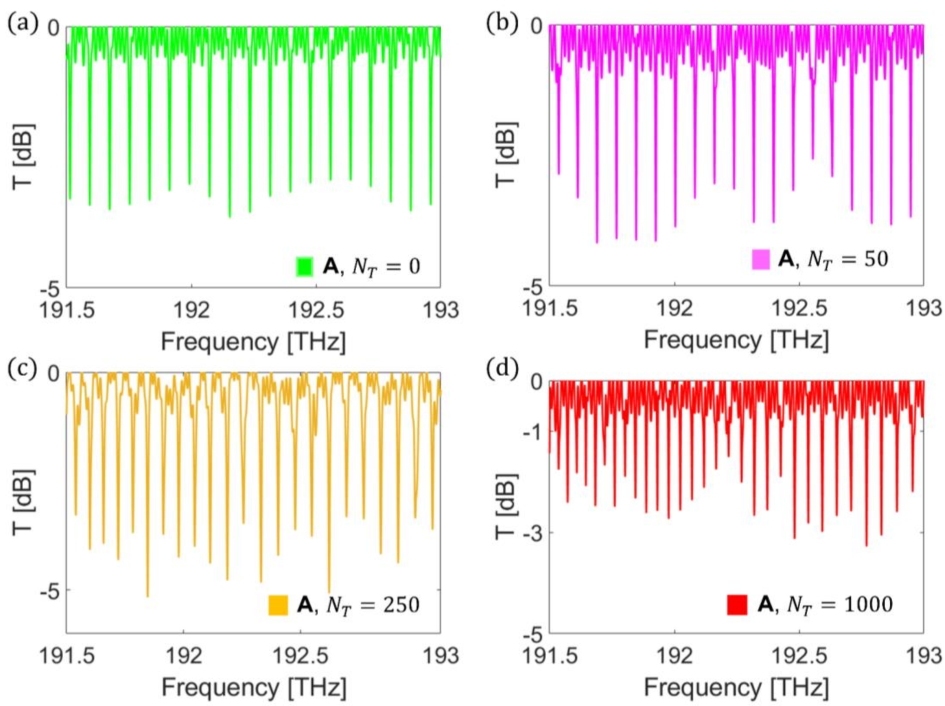

Fig. 3.14: Output transmission response for family A-based SC-FPs incorporating: (a) $N_T = 0$, (b) $N_T = 50$, (c) $N_T = 250$, (d) $N_T = 1000$. Density of supported SC-FP modes are raising in the transition from shorter to longer apodised grating lengths.

The same analysis is extended to the family B architecture. By using the same coupling gap and cavity length, the SC-FP resonator employing the family B DBR ($P = 500$ nm, $W_1 = 0.8$ μm, $W_2 = 2.1$ μm, $W_3 = 1.3$ μm) is characterized in transmission, as reported in Fig. 3.15(a). To enable a direct comparison with this configuration, the family C architecture (air-gap structure) is designed with the same number of uniform and apodized grating periods. Fig. 3.15(b) presents the corresponding transmission spectrum for this device, which uses modified grating parameters ($P = 526$ nm, DC $= 70\%$, $L = 370$ μm)

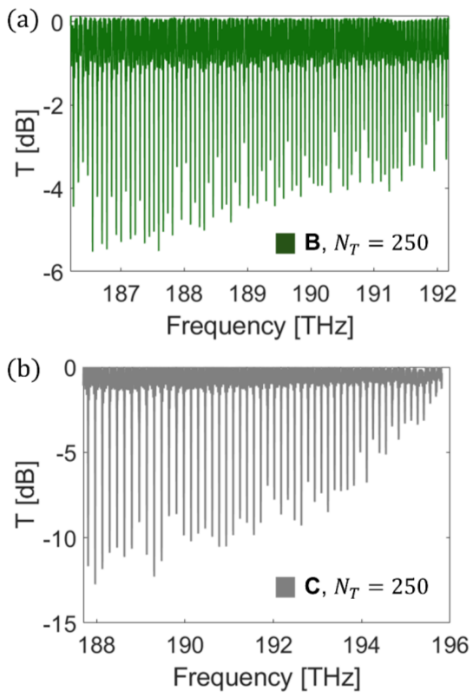

Fig. 3.15: Output transmission response for (a) family B-based, and (c) family C-based SC-FPs incorporating N =1750 and $N_T = 250$. The broaden stopband achieved by the two DBR architectures enable resonances extending over 6 THz frequency range.

From the measured transmission spectra, the experimental resonant frequencies f_μ are extracted and the integrated dispersion of the SC-FP architectures employing the three DBR families is presented in Fig. 3.16, as a function of optical frequency. In particular, Fig. 3.16(a–d) shows the different dispersion profiles for SC-FPs-based on family A gratings induced by varying the apodized grating length N_T. Increasing the number of apodized periods N_T from $N_T = 0$ (no apodisation) to $N_T = 1000$ drives a controlled transition from near-zero to strongly anomalous dispersion.

For short tapers ($N_T = 0$ and $N_T = 50$), $D_{int,f}(\mu)$ evolves from ≈ 10 GHz to ≈ −10 GHz as the resonance frequency shifts from 191.5 THz to 193 THz, remaining nearly flat at the bandgap center and indicating a strongly suppressed second-order term while dominant third-order dispersion.

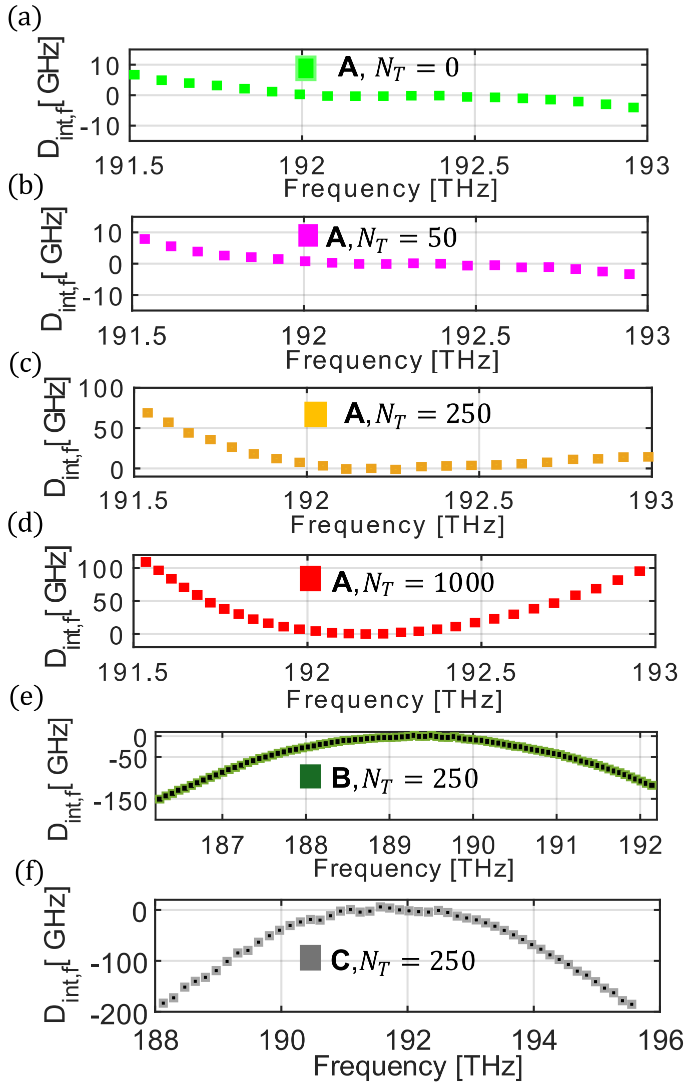

Fig. 3.16: Integrated dispersion $D_{int,f}$ tailoring enabled by different DBR geometries. (a)-(d) Progressive transition from nearly flat to highly anomalous dispersion achieved by increasing the number of taper periods N_T, considering same family A DBR structure. Highly normal dispersion supported by broadband-based reflectors: (e) family B and (f) family C gratings.

In contrast, for $N_T = 250$ and $N_T = 1000$, $D_{int,f}(\mu)$ results predominantly positive and follows a pronounced parabolic trend, evidencing a marked anomalous-dispersion regime with $D_{int,f}(\mu) > 100\ GHz$. At fixed cavity length and taper number $N_T = 250$, SC-FPs based on family B DBRs invert the dispersion sign compared to family A devices, yielding to a normal-dispersion regime with peak values of $D_{int,f}(f) \approx$ -150 GHz, as shown in Fig. 3.16(e). The normal dispersion regime is also observed for air-gap SC-FP, which use the same apodized grating length but a shorter cavity length (≈370 µm). For family C DBRs, (P=526 nm, DC=70%) the air-gap SC-FP achieves larger normal dispersion, with peak $D_{\mathrm{int},f}(f)$≈ -190 GHz (Fig. 3.16(f)).

These results demonstrate that DBR tailoring allows precise dispersion control, enabling the selection of either normal or anomalous integrated dispersion at a target operating wavelength, without engineering the waveguide cross-section. This capability is particularly beneficial for applications such as dissipative Kerr solitons and parametric frequency-comb generation [46]. The dispersion properties of the SC-FP resonators are further analyzed in Fig. 3.17 by plotting the fitted first-order coefficient $D_{1,f}$ and second-order coefficient $D_{2,f}$ as functions of optical frequency for the three resonator families.

For family A devices, Fig. 3.17(a) shows that $D_{1,f}$ is almost flat for $N_T = 0$ and $N_T = 50$, indicating a nearly frequency-independent FSR of about 80 GHz and 75 GHz, respectively, and hence only very weak second-order dispersion.

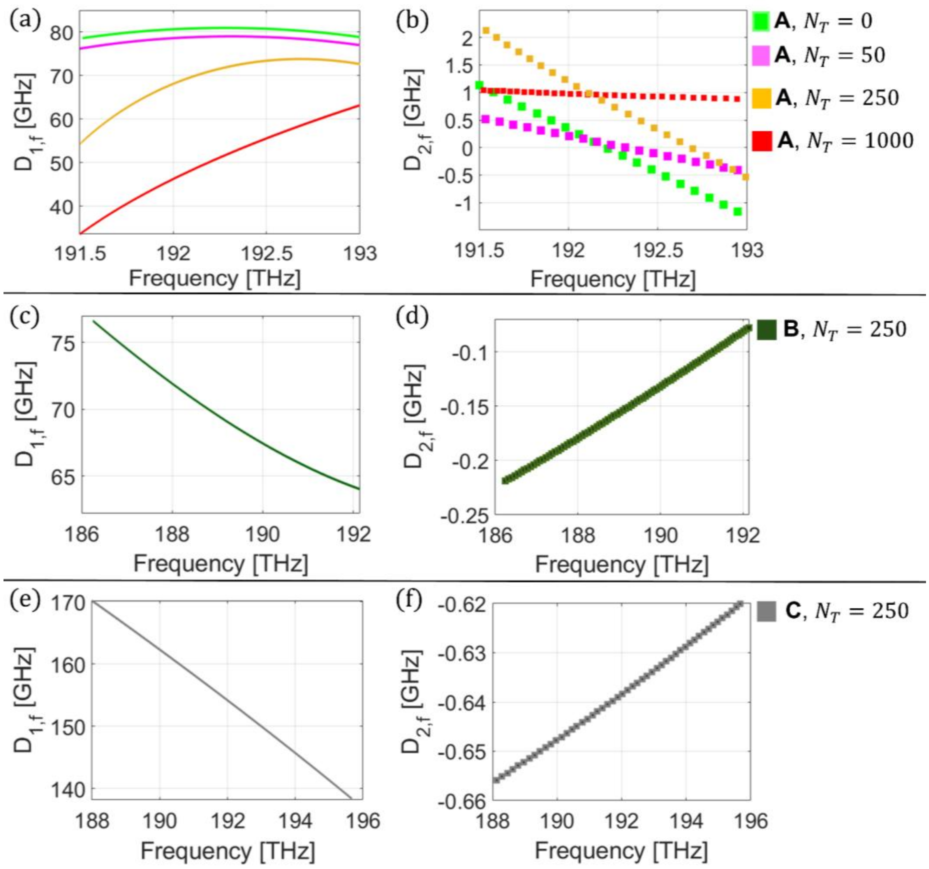

Fig. 3.17: Fitted experimental first order (left column) and second order dispersion (right column) coefficients for: (a-b) family A-, (c-d) family B-, and (e-f) family C-based SC-FP resonators.

In detail, $D_{2,f}$ exhibits very small values that cross from positive to negative around zero (Fig. 3.17(b)), while the magnitude of $D_{3,f}$ increases to about -50 MHz and -130 MHz for $N_T = 50$ and $N_T = 0$, respectively as detailed in Fig. 3.18(a).

When N_T is increased to 250, $D_{1,f}$ starts to show a clear frequency dependence, and for $N_T = 1000$ it varies strongly from about 35 GHz to 62 GHz towards higher frequencies, yielding a strongly monotonic trend with a pronounced positive slope. This reflects a strictly positive second-order dispersion $D_{2,f} \approx 1$ GHz with an almost vanishing $D_{3,f} \approx 0$ MHz, fully consistent with the smooth quadratic integrated-dispersion envelope reported in Fig. 3.16.

For family B (Fig. 3.17 (c), (d)), and family C (Fig. 3.17(e), (f)) SC-FPs, the fitted $D_{1,f}$ shows a strong, nearly linear negative slope across the stopband, with average values of approximately $D_{2,f} \approx -0.15$ GHz and $D_{2,f} \approx -0.64$ GHz, respectively. These results indicate that the FSR decreases monotonically with increasing optical frequency and that both resonators operate in a regime of pronounced normal second-order dispersion, confirming the broad, concave-down $D_{\text{int},f}$ profiles in Fig. 3.16(e), (f).

The third-order dispersion coefficients extracted in Fig. 3.18(b), (c) are finite but remain comparatively small, with $D_{3,f}$ values on the order of 1.7 MHz and 0.7 MHz, respectively.

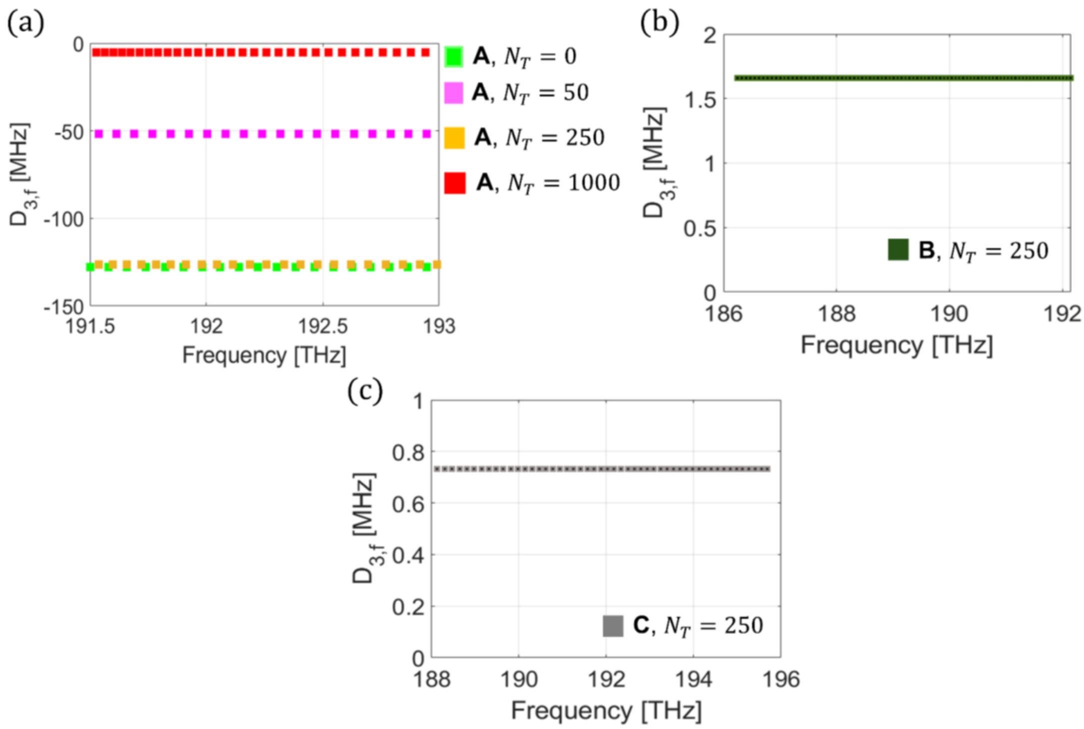

Fig. 3.18: Third order dispersion coefficient as function of the optical frequency for (a) family A, (b) family B, and (c) family C-based SC-FPs.

Moreover, this change in the dispersion response reported for longer tapered DBR sections in family A devices correlates with the resonator FSR response. Fig. 3.19(a) shows the steepening of the FSR slope, while Fig. 3.19(b) reports the corresponding increase in the penetration length L_{eff} toward smaller frequencies, experimentally extracted at the lower edge (191.5 THz), center (192.15 THz), and upper edge (192.86 THz) of the stopband. Specifically, L_{eff} accounts for the additional penetration length beyond the physical geometric cavity length L=900 μm in the resonator. When the number of tapers is increased to $N_T = 250$ and $N_T = 1000$, the FSR shows a pronounced slope and strong frequency dependence.

For longer tapering sections ($N_T = 1000$), L_{eff} nearly doubles between lower band edge and the stopband center, indicating significant frequency-dependent penetration into the DBR mirrors, whereas its variation remains negligible for short tapers.

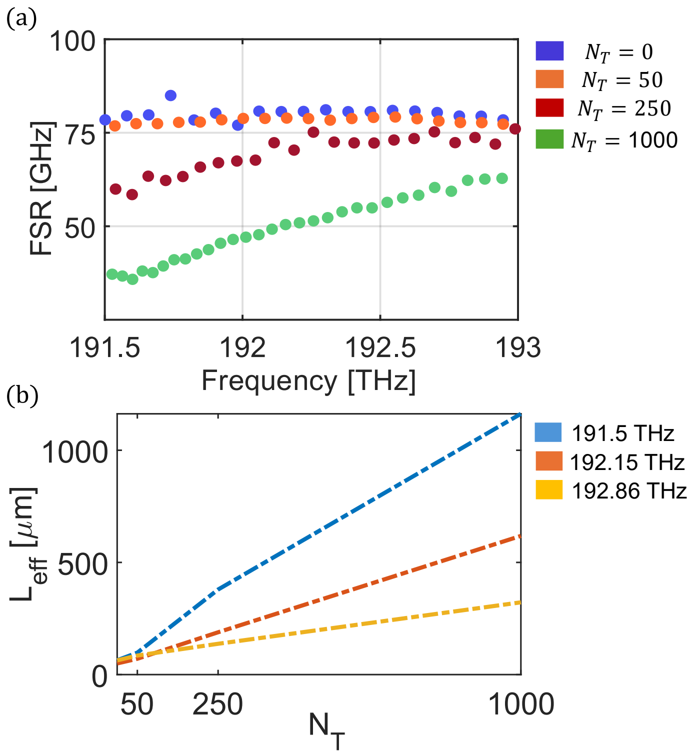

Fig. 3.19: FSR response of SC-FPs based on family A DBRs with fixed cavity length L =900 μm and gap G=500 nm, for different apodised grating lengths N_T. (b) Corresponding experimentally extracted frequency-dependent penetration length L_{eff} , showing increased field extension at the stopband edges for longer DBR tapering sections. For N_T=1000, $L_{\text{eff}} \approx$ 500 μm at stopband centre and $L_{\text{eff}} \approx$ 1000 μm at lower band edge.

This effect has also been analyzed for different cavity lengths. For shorter cavities ($L = 120$ μm), increasing the taper length significantly distorts the FSR, whereas for longer cavities ($L = 900$ μm) the influence of apodization becomes weaker, leading to a correspondingly reduced impact of the DBR penetration length (Fig. 3.20).

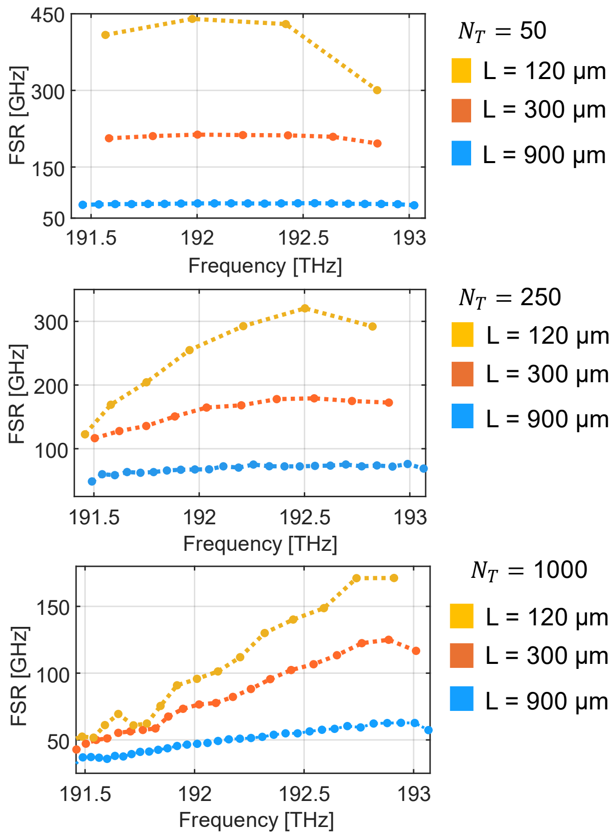

Fig. 3.20: Effect of different apodisation grating periods and cavity length on the FSR response.

Consistently, Fig. 3.21 presents the FSR response of SC-FP resonators incorporating uniform family A DBRs extracted for different cavity lengths. Increasing the cavity length results in a progressive flattening of the FSR curve across the measured frequency range [21], confirming that this behavior in both apodized and non-apodized gratings arises from the reduced relative contribution of the DBR penetration length.

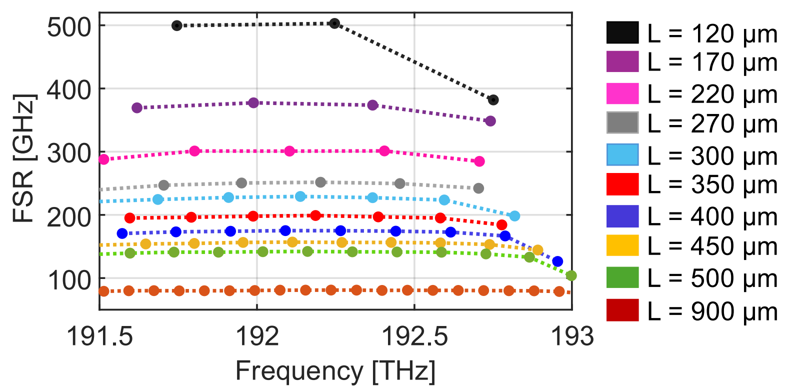

Fig. 3.21: Experimental FSR versus frequency for SC-FP cavities based on family A uniform gratings (N_T=0) with different cavity lengths. A progressive flattening of the FSR is observed for longer cavities L=900 μm, where modes near the stopband center exhibit an "almost constant" FSR≈80 GHz.

A final investigation is explored on the influence of different grating apodisation profiles variations on the FSR response for a fixed cavity length $L = 300$ µm, gap G=500 nm, and same taper length N_T=250.

Particularly, Figure 3.22 compares the SC-FPs employing a cubic (Mn=3), quadratic (Mn=2), and linear apodisation (Mn=1) apodisation profiles in the DBR corrugations. The quadratic apodisation profile produces the least pronounced concavity in the FSR, exhibiting a more uniform spectral response compared to the linear and cubic cases that possess the strongest concave parabolic FSR response. These findings underline that, beyond the taper length, the specific apodisation profile provides an additional handle to engineer the dispersion of DBR-based SC-FP resonators and tailor their spectral response to the requirements of a given photonic function.

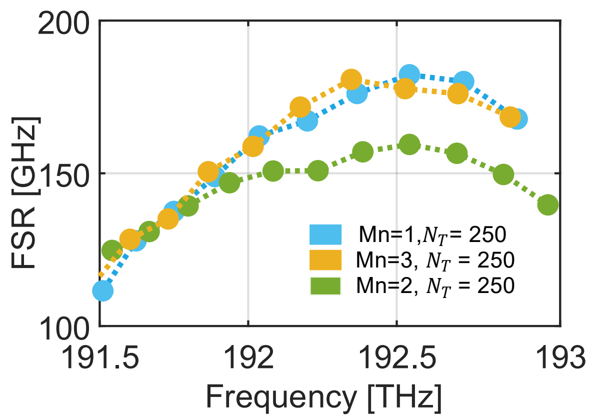

Fig. 3.22: Effect of apodisation profile order Mn on the FSR performance. Measured FSR response for SC-FP resonators with linear (Mn=1), quadratic (Mn=2), and cubic (Mn=3), with fixed cavity length L=300 µm and number of gratings N=1750, N_T=250.

3.7.2 High-Q resonator performance

Beyond dispersion control, the SC-FP geometry enables co-optimization of the loaded quality factor Q_l through systematic variation of cavity length and coupling gap. The SC-FP resonances have been characterized with a tunable-laser source in continuous-sweep mode and detected on a high-speed Germanium photodiode by considering the same settings detailed in Section 3.6. Fitting these high-resolution experimental measurements according to the equations valid for a side-coupled resonator, described in Section 2.5.3, enables it to experimentally retrieve the loaded quality factors.

In family A-based SC-FPs, it has been fixed L = 900 µm and G = 600 nm, while introducing longer apodized gratings. The loaded Q-factor increases from 9.3×10^4 (N_T = 0) up to 2.04×10^5(N_T = 1000). This enhancement is attributed both to the improved mode-matching ensured by the smooth transition between the cavity and the DBR sections, and the enhanced penetration length, as demonstrated in Fig. 3.19(b), that drastically extends the geometrical cavity length when $N_T = 1000$ apodized gratings are considered.

However, the optimal Q-factor of $Q_l \approx 2.3\times10^5$ that corresponds to FWHM≈ 6.7 pm, is achieved when in the family A-based SC-FP is set $N_T = 250$, $G = 400$ nm, $L = 900$ µm, while the coupler waveguide and the FP cavity width W_4 is increased from 1.3 µm to 1.8 µm (Fig. 3.23, yellow markers).

The broadening of the resonant cavity waveguide reduces field overlap with the etched sidewalls and the relative scattering losses due to the roughness interaction, boosting the Q-factor. However, a wider cavity imposes stricter constraints on the coupling gap, as the side-coupler bend must remain sufficiently close (maximum G=400 nm) to ensure proper mode matching and maintain pronounced SC-FP resonance dips.

The second architecture highlighted in Fig. 3.23, represented with green markers, achieves $Q_l \approx 2.0\times10^5$. In this resonator, the resonant cavity width is kept constant to $W_4 = W_3 = W_1 = 1.3$ µm and is characterized by a geometrical length $L = 900$ µm, but the gap is set to 600 nm, and the number of apodized DBR is increased to N_T=1000 enhancing the performance of the Q-factor.

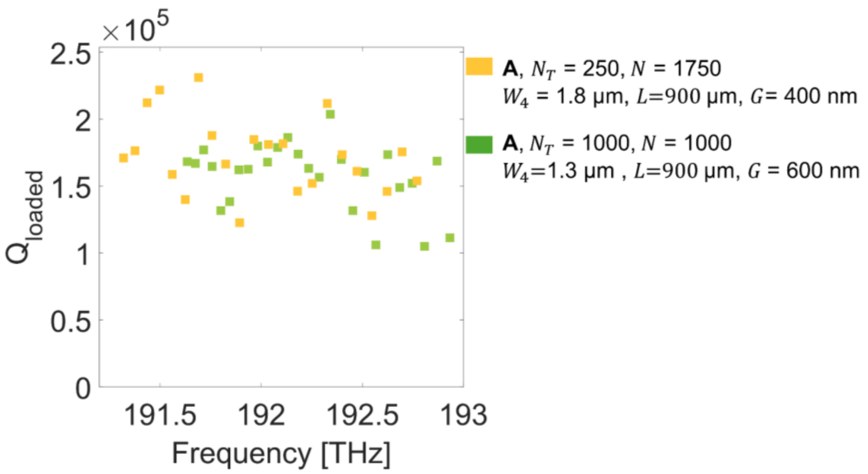

Fig. 3.23: Loaded quality factors (Q_l) extracted from high-resolution measurements for family A DBR SC-FPs, comparing the best performance achieved when considering $W_4 = 1.8\ \mu$m (yellow trace) and $W_4 = 1.3\ \mu$m.

Regarding the other architectures, SC-FP resonators incorporating family B gratings exhibit $Q_l \approx 1.3\times10^5$, for $L = 900$ µm, $G = 600$ nm and $N_T = 250$; while SC-FPs based on family C, characterized by $N_T = 250$, $L = 370$ µm $G = 600$ nm, $W_2 = 2300$ nm, DC = 50%, yields a peak $Q_l \approx 9.6\times10^4$ as highlighted in Figure 3.24.

The abrupt discontinuity at the air-gap interfaces and relative mode-mismatch introduces additional scattering and radiation loss, inducing an overall decreasing of Q-factor in the air-gap structures.

All the parameters described in this section result from a systematic optimization of the cavity and grating geometry during the design process.

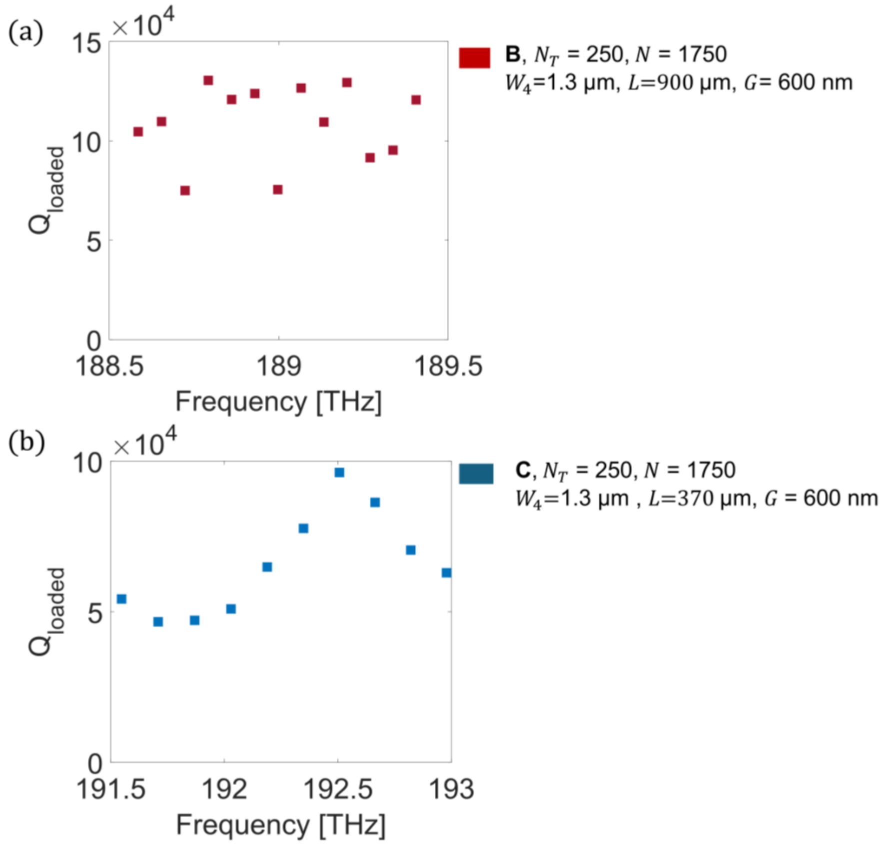

Fig. 3.24: Loaded quality factor for SC-FPs based on (a) family B, and (b) family C DBR.

3.7.3 Resonant mirror: reflectivity analysis

For laser integration, the effective peak reflectivity is a primary figure of merit that determines the suitability of SC-FP devices as resonant mirrors. This reflectivity is strongly governed by the underlying grating architecture and by the coupling gap engineered in the SC-FP. The latter sets the resonator operating regime; in particular, operating in the over-coupled regime is advantageous in the SC-FP configuration, as it enables higher achievable reflectivity at the input waveguide port. For this purpose, the reflection spectra $R(f)$ were measured using a three-port fiber circulator for SC-FPs incorporating the three DBR families,

For family A and B-based resonators, we consider the same apodized grating periods N_T = 250, duty cycle DC=50%, cavity length L = 300 μm and coupling gap G = 400 nm. The family C SC-FP configuration differs only by a shorter cavity length ($L = 300\,\mu$m), while all other design parameters are kept identical. The normalized reflection spectra of the three architectures are reported in Fig. 3.25(a–c).

Enhancement in the on-resonance peak reflectivity (R_{peak}), combined with an increase in the maximum inter-peak extinction ratio $ER_{inter\text{-}peak} \approx R_{peak}/N_{bg}|_{dB}$, where N_{bg} is the average background noise level, also due to parasitic FP arising from reflections at the chip cleaved facets, is observed in family B and family C-based SC-FPs.

Specifically, $ER_{inter\text{-}peak}$ reaches ≈6.35 dB for family B and ≈5.7 dB for family C, with a high density of well-defined reflection peaks over a 6-THz span, whereas SC-FPs integrating family A DBRs exhibit a degraded reflection response, with a maximum peak of ≈ 4.9 dB.

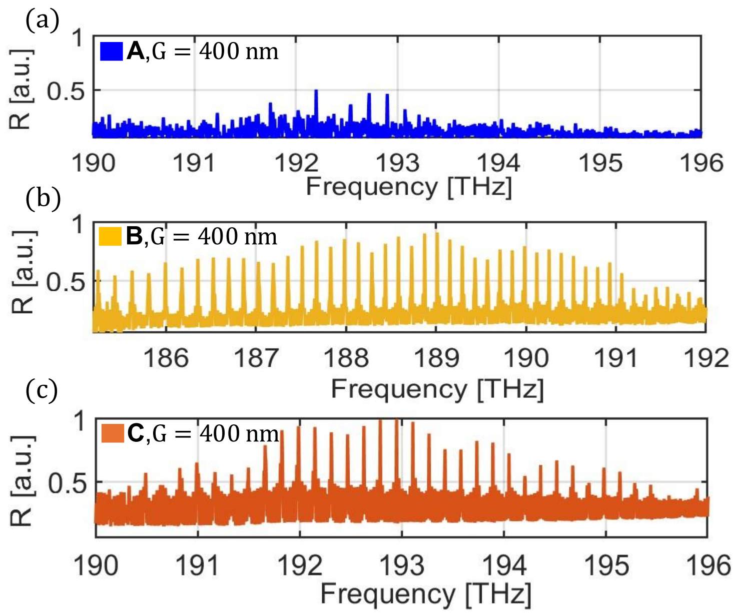

Fig. 3.25: (a-c) Comparison between the normalized experimental reflectivity spectra of SC-FP based on family A, B, and C DBRs, for fixed $N_T = 250$, G= 400 nm.

Among these structures, the coupled quality factor (Q_c) remains invariant, while the improved behavior can be attributed to the enhanced intrinsic quality factor (Q_i) provided by the specific choice of DBR family and the associated intrinsic loss mechanisms. The intrinsic quality factor is obtained by fitting the transmission of the devices compared in Fig. 3.25 with high-resolution measurements (with settings analogous to Section 3.7.2) according to the Eq. (2.80).

Family B configuration exhibits the best performance with peak value exceeding $Q_i > 1.5 \cdot 10^5$, as reported in Fig. 3.26 (yellow markers), while for family C and A it assesses to $Q_i \approx 1 \cdot 10^5$ (orange markers) and $Q_i \approx 0.4 \cdot 10^5$ (blue markers), respectively.

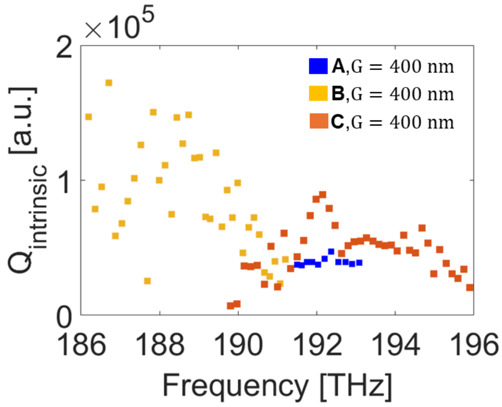

Fig. 3.26: Experimental intrinsic quality factor values for the three different SC-FP architectures: (blue) family A, (yellow) family B, and (orange) family C gratings sharing the same gap G=400 nm.

The impact of the coupling gap variation in SC-FP resonators is investigated not only in terms of loaded quality factor, but also for its simultaneous effect on the transmission dips at the output port and the reflection peaks at the input port. In this analysis, the same family C SC-FP configuration used in Fig. 3.25 is considered, while the coupling gap is varied from $G = 600$ nm to $G = 300$ nm. Fig. 3.27 shows the evolution of the extinction ratio (ER) of the transmission (T) dips: for G=600 nm ER≈3 dB, G=500 nm exceeds 5 dB, G=400 nm is almost 10 dB, while for G=300 nm it results peak ER of 15 dB, clearing showing the increased ER with smaller gaps.

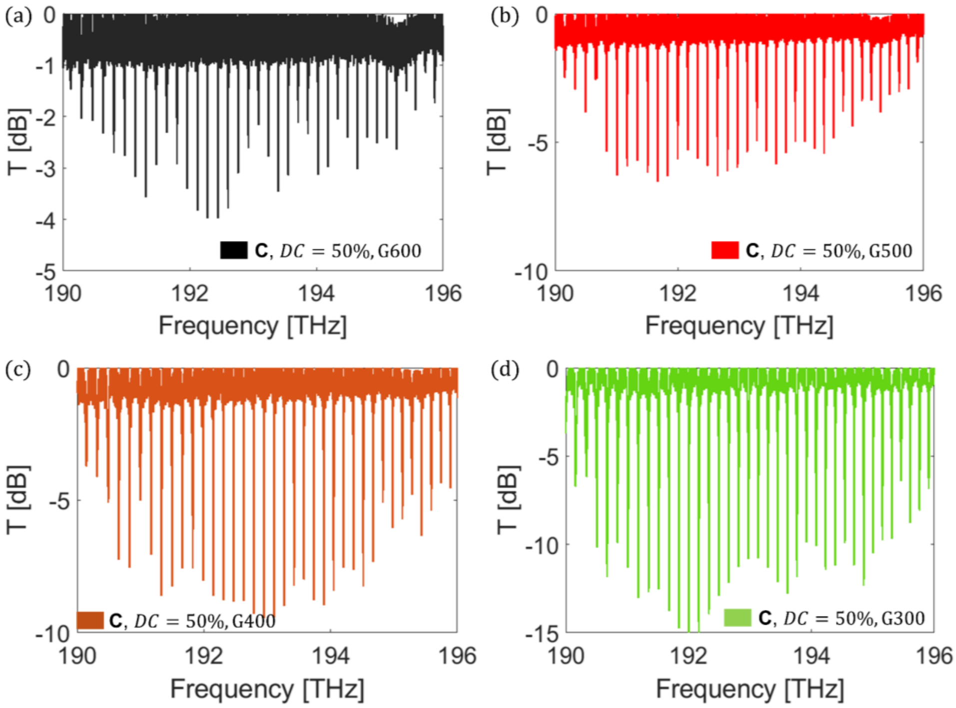

Fig. 3.27: Transmission response of the family C-based SC-FP resonators for decreasing gap values: dips extinction raises passing from *G*=600 nm to *G*=300 nm.

This trend observed in transmission is corroborated by the analysis of the normalized reflection peaks, reported in Fig. 3.28 for $G = 500$ nm and $G = 300$ nm. As the coupling gap decreases, the peak reflectivity increases from $ER_{inter\text{-}peak} \approx 4.6$ dB at $G = 500$ nm (red trace) to $ER_{inter\text{-}peak} \approx 6.8$ dB at $G = 300$ nm (green trace). All resonators considered in the reflection analysis operate in the over-coupled regime ($Q_i > Q_c$), as confirmed in Fig. 3.29 for two example gap values (a) G=600 nm and (b) G=400 nm.

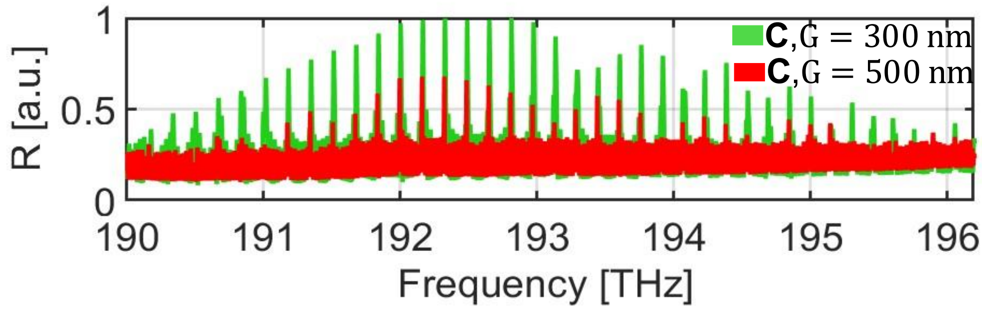

Fig. 3.28: Air-gap SC-FP (N_T = 250): increase in resonance peak intensity and inter-peaks extinction ratio with decreasing gap from 500 nm to 300 nm.

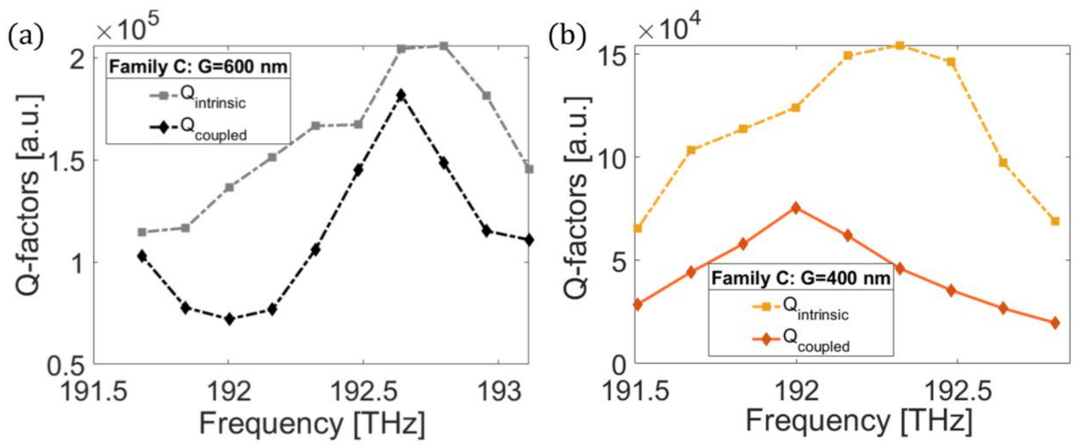

Fig. 3.29: Experimental intrinsic and coupled quality factor values for SC-FP based on family C DBR with (a) *G*=600 nm, and (b) *G*=400 nm. Over-coupling regime is demonstrated over the entire frequency range.

These measurements confirm that broadband, high-contrast DBRs (families B and C), combined with appropriate coupling-gap engineering, can deliver SC-FP mirrors with significantly enhanced peak reflectivity and extinction ratio, which is essential for high-performance hybrid laser cavities and wavelength-selective reflectors.

3-References

[1] Li, Bin, et al. "Towards monolithic low-loss silicon nitride waveguides on a mature 200 mm CMOS platform." *Optik* 250 (2022): 168309.

[2] Ranno, Luigi, et al. "Multi-material heterogeneous integration on a 3-D photonic-CMOS platform." *Optical Materials Express* 13.10 (2023): 2711-2725.

[3] Kaur, Paramjeet, et al. "Hybrid and heterogeneous photonic integration." *APL photonics* 6.6 (2021).

[4] Shekhar, Sudip, et al. "Roadmapping the next generation of silicon photonics." *Nature Communications* 15.1 (2024): 751.

[5] Siew, Shawn Yohanes, et al. "Review of silicon photonics technology and platform development." *Journal of Lightwave Technology* 39.13 (2021): 4374-4389.

[6] Stojanović, Vladimir, et al. "Monolithic silicon-photonic platforms in state-of-the-art CMOS SOI processes." *Optics express* 26.10 (2018): 13106-13121.

[7] Mai, Andreas, Christian Mai, and Patrick Steglich. "From Lab-on-chip to Lab-in-App: Challenges towards silicon photonic biosensors product developments." *Results in Optics* 9 (2022): 100317.

[8] Stern, Brian, et al. "Compact narrow-linewidth integrated laser based on a low-loss silicon nitride ring resonator." *Optics letters* 42.21 (2017): 4541-4544.

[9] Shahbaz, Muhammad, Muhammad A. Butt, and Ryszard Piramidowicz. "Breakthrough in silicon photonics technology in telecommunications, biosensing, and gas sensing." *Micromachines* 14.8 (2023): 1637.

[10] Wang, Qiming. "Investigation progress on key photonic integration for application in optical communication network." *Science in China Series F* 46.1 (2003): 60-66.

[11] Zhang, Jiangwen, Aadithya G. Shankar, and Xihua Wang. "On-chip lasers for silicon photonics." *Photonics*. Vol. 11. No. 3. MDPI, 2024.

[12] Ji, Xingchen, et al. "Methods to achieve ultra-high quality factor silicon nitride resonators." *APL Photonics* 6.7 (2021).

[13] Puckett, Matthew W., et al. "422 Million intrinsic quality factor planar integrated all-waveguide resonator with sub-MHz linewidth." *Nature communications* 12.1 (2021): 934.

[14] Cui, Shuai, et al. "Compact microring resonator based on ultralow-loss multimode silicon nitride waveguide." *Advanced Photonics Nexus* 2.4 (2023): 046007-046007.

[15] Saber, Md Ghulam, et al. "Transversely coupled Fabry–Perot resonators with Bragg grating reflectors." *Optics Letters* 43.1 (2017): 13-16.

[16] Wildi, Thibault, et al. "Dissipative Kerr solitons in integrated Fabry–Perot microresonators." *Optica* 10.6 (2023): 650-656.

[17] Ji, Xingchen, et al. "Ultra-low-loss on-chip resonators with sub-milliwatt parametric oscillation threshold." *Optica* 4.6 (2017): 619-624.

[18] Zhang, Yang, Sylvain Veilleux, and Mario Dagenais. "Fabry-Perot Bragg grating nanoresonator with ultrahigh intrinsic Q based on low-loss silicon nitride." *Optics Express* 31.21 (2023): 34688-34696.

[19] Xie, Shengjie, et al. "On-chip Fabry–Pérot Bragg grating cavity enhanced four-wave mixing." *ACS Photonics* 7.4 (2020): 1009-1015.

[20] Xu, Hongnan, et al. "Million-Q integrated Fabry-Perot cavity using ultralow-loss multimode retroreflectors." *Photonics Research* 10.11 (2022): 2549-2559.

[21] Comis, Farah, et al. "Experimental analysis and modeling of the penetration depth of uniform and apodized integrated Bragg reflectors." *Optics Express* 32.26 (2024): 47447-47457.

[22] Tosi, Mauricio, et al. "Analysis of Uniform Waveguide Bragg Gratings in a Silicon Nitride Platform." *2024 Conference on Lasers and Electro-Optics (CLEO)*. IEEE, 2024.

[23] Butt, Muhammad A., Nikolay L. Kazanskiy, and Svetlana N. Khonina. "Advances in waveguide Bragg grating structures, platforms, and applications: an up-to-date appraisal." *Biosensors* 12.7 (2022): 497.

[24] Yao, Kaiyuan, and Yaocheng Shi. "High-Q width modulated photonic crystal stack mode-gap cavity and its application to refractive index sensing." *Optics express* 20.24 (2012): 27039-27044.

[25] Yang, Da-Quan, et al. "Photonic crystal nanobeam cavities for nanoscale optical sensing: A review." *Micromachines* 11.1 (2020): 72.

[26] Yu, S.-P., Jung, H., Briles, T. C., Srinivasan, K. & Papp, S. B. Photonic-Crystal-Reflector Nanoresonators for Kerr-Frequency Combs. *ACS Photonics* 6, 2083–2089 (2019).

[27] Zhang, Yang, et al. "Over 100 million Q silicon nitride Fabry–Perot Bragg nanoresonators enabled by advanced tapered gratings." *Optics Letters* 50.23 (2025): 7348-7351.

[28] Monopoli, Davide, et al. "Fabry-Pérot cavity in SiN for non-linear applications." *British and Irish Conference on Optics and Photonics*. Optica Publishing Group, 2024.

[29] Ulanov, Alexander E., et al. "Laser diode self-injection locking to an integrated high-Q Fabry–Perot microresonator." *Optics Letters* 49.21 (2024): 6261-6264.

[30] Zhao, Yong, et al. "Side-coupled Fabry-Perot resonator filter based on dual-waveguide Bragg grating." *Journal of Lightwave Technology* 40.19 (2022): 6454-6464.

[31] Morichetti, Francesco, et al. "Coherent backscattering in optical microring resonators." *Applied Physics Letters* 96.8 (2010).

[32] Oskooi, Ardavan, et al. "Robust optimization of adiabatic tapers for coupling to slow-light photonic-crystal waveguides." *Optics express* 20.19 (2012): 21558-21575.

[33] Xu, Yong, et al. "Scattering-theory analysis of waveguide-resonator coupling." *Physical Review E* 62.5 (2000): 7389.

[34] Badri, S. Hadi, et al. "Broadband refractive index sensor using photonic molecule architecture with subwavelength grating mirrors on silicon nitride." *Optics Express* 33.26 (2025): 54166-54176.

[35] Pan, Kai, Debin Meng, and Yunjie Wang. "An ultra-broadband, and low loss 3-dB optical power splitter with curved adiabatic taper." *Optics Communications* 569 (2024): 130729.

[36] KLayout Documentation: https://www.klayout.de/doc-qt5/klayout.pdf

[37] https://www.ansys.com/.

[38] https://www.lionix-international.com/.

[39] Vorobev, Artem. *2D materials for hybrid laser wavelength tuning*., Ph.D. Diss. Polytechnic University of Bari, 2023.

[40] Saghaei, Hamed, Payam Elyasi, and Bhavin J. Shastri. "Sinusoidal and rectangular Bragg grating filters: Design, fabrication, and comparative analysis." *Journal of Applied Physics* 132.6 (2022).

[41] Kehl, Florian, et al. "Design of a label-free, distributed Bragg grating resonator based dielectric waveguide biosensor." *Photonics*. Vol. 2. No. 1. MDPI, 2015.

[42] Durán-Valdeiglesias, Elena, et al. "Dual-polarization O-band silicon nitride Bragg filters with high extinction ration." *Europe Conference on Integrated Optics (ECIO)*. 2018.

[43] Wang, Xu. Silicon photonic waveguide Bragg gratings. Ph.D. Diss. University of British Columbia, 2013.

[44] Du, Zhenmin, et al. "Silicon nitride chirped spiral Bragg grating with large group delay." *APL Photonics* 5.10 (2020).

[45] Mortazy, Ebrahim, et al. "Chirped Bragg grating in silicon based rib waveguide." *2011 7th International Workshop on Fibre and Optical Passive Components*. IEEE, 2011.

[46] Helgason, Óskar B., et al. "Dissipative solitons in photonic molecules." *Nature Photonics* 15.4 (2021): 305-310.

Chapter 4: Multi-wavelength laser emission via fiber-assisted HECL

This chapter presents the application of integrated SC-FP resonators, acting as resonant reflectors, in a fiber-assisted hybrid external-cavity laser configuration. The external-cavity combines the SC-FP, fabricated on an 800-nm-thick silicon nitride PIC, with a fiber-based reflector and a commercial fiber-coupled SOA. This configuration produces multi-wavelength laser (MWL) emission as the result of the overlap between SOA gain ripple, the SC-FP reflection peaks, and the supported longitudinal modes of the fiber-PIC cavity. The integrated SC-FP resonators employ engineered Bragg gratings that enable precise control of spectral reflectivity, dispersion, and achieving loaded quality factors up to 6.5×10^5 with on-resonance reflectivity reaching 57%.

The hybrid laser exhibits multi-wavelength emission aligned to the SC-FP resonances, with multiple longitudinal modes of the hybrid cavity competing within each resonance. When isolating single resonances, coherent pulse trains with corresponding radiofrequency linewidths as narrow as ~3 kHz are observed. The system spontaneously generates multiple identical pulse profiles within the laser cavity, effectively multiplying the repetition rate and reveals transitions toward partially mode-locked states. These results establish SC-FP resonators as promising wavelength-selective reflectors for compact, multi-wavelength HECLs, highlighting their potential for advanced applications such as low-phase-noise microwave generation, WDM carriers, coherent ranging, and multi-comb spectroscopy. The results shown in this chapter have led to the publication of a journal paper in *Journal of Lightwave Technology*, listed as [j2] in the list of publications section.

4.1 Multi-wavelength laser architectures

Multi-wavelength lasers (MWLs), have emerged as critical enablers for next-generation photonic systems, driven by their ability to deliver multiple discrete, stable emission lines across broad gain bandwidths with precise spacing, and frequency-stable laser sources [1-3]. These lasers address fundamental challenges in frequency shaping of multimode emission, transforming broadband amplified spontaneous emission into equidistant lines suitable for applications spanning datacom/telecommunications [4],[5], radiofrequency (RF) signal generation [6], coherent light detection and ranging (LiDAR) [7],[8], laser ranging [9], spectroscopy [10], and multi-comb metrology [11]. Deployable MWL architectures demand compact footprints, energy efficiency, low phase noise (sub-kHz linewidths), uniform power distribution, high side-mode suppression ratios (SMSR >40-60 dB), and thermal stability.

One of the most promising routes to realize such multi-wavelength laser operation is through hybrid external-cavity lasers that integrate a passive optical resonator on a photonic integrated circuit with an external gain element, such as fiber-based gain media like erbium-doped fiber amplifiers (EDFAs) [12],[13], semiconductor optical amplifiers such as SOAs [14], and RSOAs [15], or erbium-doped waveguide amplifiers (EDWAs)[16].

Hybrid external-cavity lasers overcome the limitations of silicon's indirect bandgap by heterogeneously integrating III–V gain media, while avoiding the material waste, alignment difficulties, and scalability challenges associated with conventional die- or wafer-bonding techniques. [17]. Early demonstrations employed fiber-coupled gain chips for their simplicity and inherently low coupling losses, but recent advances in integrated high-gain on-chip amplifiers have enabled direct coupling to photonic integrated circuits, delivering superior optical phase stability, enhanced wavelength tunability, and significantly narrower linewidths [18-22].

The gain chip is precisely aligned and either butt-coupled, evanescently coupled, or wire-bonded to the PIC bus waveguide input and the wavelength-selective resonant reflector. Integrated thermal phase shifters and heaters provide fine-tuning of resonance alignment, and the laser cavity is closed through the resonator's wavelength-selective reflective feedback.

Experimental demonstrations of fiber-free HECL using this butt-coupling scheme are detailed in Chapter 5.

Advances in high-Q SiN resonators have revolutionized on-chip nonlinear optics by enabling soliton-based frequency comb generation in compact, low-loss waveguides through four-wave mixing driven by SiN's strong third-order nonlinearity [23-25]. The injection of intense coherent light into these resonators allows the formation of dissipative soliton states, and when such SiN cavities are embedded in external-cavity lasers, they unlock mode-locked hybrid laser operation via coherent amplification of periodic pulse trains, providing a viable alternative to schemes based on active modulation or integrated saturable absorbers [15],[26-28].

In this context, hybrid SiN–III–V systems can simultaneously deliver narrow optical linewidths, low RF phase noise, and engineered dispersion profiles that are compatible with soliton regimes.

As discussed in Section 3.1, while MRRs have been the dominant platform for on-chip comb generation due to their compact footprint and high-Q resonator performance, they face intrinsic limitations such as resonance splitting from surface scattering [24], [29], modal crosstalk, thermal instability, and restricted dispersion engineering, that can constrain their use in coherent MWL systems. In contrast, photonic-crystal-based resonators implemented, for instance, as in-line [30] or side-coupled Fabry–Pérot cavities [31] have emerged as a competitive alternative, combining ultra-high Q-factors with fine-grained control of dispersion through engineered bandgaps [32].

Such structures maintain a compact footprint while providing strong, spectrally selective reflection and the ability to confine nonlinear interactions like four-wave mixing to specific defect modes within the photonic stopband, thereby enabling an accurate balance between dispersion and nonlinearity necessary for soliton formation.

In this chapter, the applicability of integrated SiN-based side-coupled Fabry–Pérot resonators for multi-wavelength lasing and pulse-train generation in hybrid ECL systems is demonstrated for the first time. Variants of integrated SC–FP structures on a SiN platform are combined with a fiber-pigtailed SOA, and the external-cavity includes relatively long fiber sections so that the overall configuration sits midway between fully fiber-based and chip-integrated architectures.

In practice, the SOA is fiber-coupled into the SiN chip, and fiber components still participate in setting the external-cavity length and free spectral range, leading to observable competition among longitudinal modes, RF beat notes within individual resonances, and spontaneous transitions to coherent pulse trains at repetition rates corresponding to integer multiples of the cavity FSR.

This intermediate configuration thus exploits integrated SC–FP resonators as wavelength-selective reflectors while still leveraging fiber-based cavity lengths to access low repetition rates and high nonlinear dynamics.

Despite its partially fiber-based nature, this SC–FP ECL platform establishes a clear pathway toward fully butt-coupled, chip-scale integrated MWL sources in which the gain element is directly coupled with the SiN PIC. By migrating from fiber-pigtailed to butt-coupled gain elements and progressively replacing fiber delay with low-loss on-chip SiN waveguides and resonators, the same design principles can yield compact, thermally stable, multi-wavelength hybrid lasers with low phase noise and engineered soliton dynamics.

Such butt-coupled integrated MWL sources opens new pathways toward low-phase-noise microwave generation, WDM optical networks, coherent LiDAR, and multi-comb spectroscopy, within a scalable SiN–III–V photonic integration framework.

4.2 PIC characterization

The designed and experimentally tested PICs consists of a series of side-coupled Fabry–Pérot cavities. These optical resonators are implemented on an 800-nm-thick silicon nitride core fully embedded within silicon dioxide, fabricated using a multi-project wafer (MPW) process provided by LIGENTEC SA [33] foundry. This platform marks a transition from the technology described in Section 3.3. Unlike contact photolithography, where the photomask is brought into direct contact with the wafer, stepper photolithography uses a projection-based approach that reduces the mask image and exposes it onto the wafer in discrete steps. This enables finer patterning, sub-micron feature resolution, and improved alignment accuracy, while also avoiding the mechanical risks associated with direct mask-wafer contact. Compared with the EBL-based process used at Glasgow, the LIGENTEC platform offers lower patterning resolution, with a minimum feature size of approximately 200 nm, whereas EBL combined with etching can typically reach the 50-100 nm range. In return, it provides low-loss waveguides with strong mode confinement under silica upper cladding, which is particularly attractive for nonlinear photonic applications and for assessing scalability and edge-coupling performance in a mass-production-oriented environment.

The waveguide core is surrounded by SiO_2 cladding layers, consisting of a 6.6 µm top oxide and a 4 µm bottom oxide. The low-loss SiN material, combined with this buried silicon dioxide structure, enhances mode confinement, for both TE and TM polarizations and provides improved thermal stability. A detailed cross-section of the single-mode waveguide, characterized by a width of 1 µm, is illustrated in Fig. 4.1.

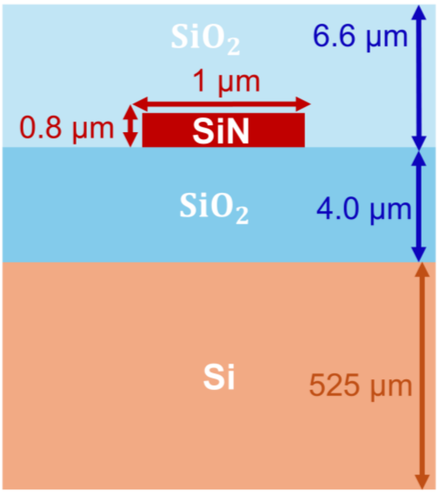

Figure 4.1: Cross-section of LIGENTEC AN800 single mode waveguide. 800-nm-thick SiN layer is buried in SiO_2 cladding (6.6 µm top cladding and 4 µm bottom cladding).

Each integrated SC-FP cavity incorporates two identical on-chip DBR mirrors, implemented using rectangular lateral corrugations patterned along the sidewalls of the fundamental-mode waveguide with an initial width W_a. The unit cell of each DBR mirror is defined by three geometrical parameters: the waveguide width, the corrugation depths, and the grating periodicity (P). This periodic modulation generates a photonic stopband that efficiently reflects light within a specific wavelength range to operate in the C-band window, forming the Fabry–Pérot cavity.

To optimize mode matching and enhance the intrinsic quality factor (Q_I), the mirrors integrate a tapered corrugation section of N_T periods in the grating section, linearly increasing the corrugation width from W_a to W_b along the propagation direction. This smooth corrugation variation reduces abrupt impedance mismatches at the mirror interface, minimizing back-reflection and suppressing scattering losses. Furthermore, within the SC-FP cavity, a linear tapering of the waveguide width from W_a to $W_c > W_a$ over a length L_T is employed to reduce the mode overlap with sidewall roughness and boost the loaded Q-factor (Q_L).

The side-injection of light into the cavity is achieved by means of an optical coupler based on third-order Bézier bends with a bending radius of R_b = 75 µm, designed to reduce bending losses within the bus waveguide. The vertical spacing between the bus waveguide (used for light injection) and the FP section is 10 µm, optimized to maintain low coupling loss and minimize cross-talk between adjacent devices [31]. The SC-FP schematic and the design parameters are reported in Fig. 4.2.

A carefully engineered gap G, varied from 300 nm to 600 nm, is placed between the Bézier bend of the coupler and the straight section of the cavity waveguide, both having a width of W_c. This precisely controlled evanescent coupling region enables weak coupling between the two waveguides, ensuring efficient excitation of the cavity mode while reducing the overall insertion and scattering losses due to indirect light injection.

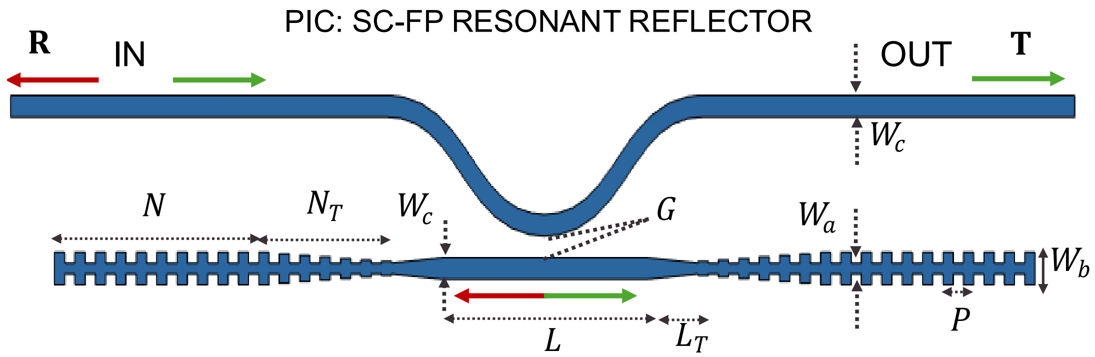

Figure 4.2: The structure of the implemented SC-FP resonator and its main parameters are illustrated.

Each SC-FP cavity supports both TE and TM modes and is characterized by DBR sections in which the combination of uniform and apodized gratings satisfies the required total number of mirror periods $N + N_T$=2000.

However, the spectral response, including stopband position, insertion loss, and extinction ratio (ER), depends strongly on the selected polarization. This polarization dependence is systematically exploited in the design of the different cavity configurations. In this study, three optimized SC-FP designs are investigated, referred to as Device01, Device02, and Device03.

Device01 and Device02 target TE mode operation with DBR corrugation widths of W_b=1.8 μm and W_a=1.0 μm, corresponding to high- and low-refractive index regions, and a periodicity of P=434 nm, providing a stopband of ~10 nm, centered around 1537 nm.

Device03 operates in TM polarization and demonstrates dispersion engineering. It incorporates N = 500, W_a= 0.6 μm (enabling single-mode operation [24]), and W_b =1.2 μm, consequently broadening the stopband from ~10 nm to ~20 nm, due to the higher index contrast. The periodicity of the DBR (P=460 nm) ensures that the operation TM stopband overlaps SOA gain bandwidth to provide efficient TM-polarized lasing, as will be discussed in next paragraph. The experimental stopbands of the two on-chip DBRs, designed for TE polarization, and fabricated with different grating periodicities, are illustrated in Figure 4.3. These test DBRs, integrated on the same PIC, are realized with a reduced number of grating periods (N = 500) and tested by means of the end-fire setup detailed in Section 3.4.

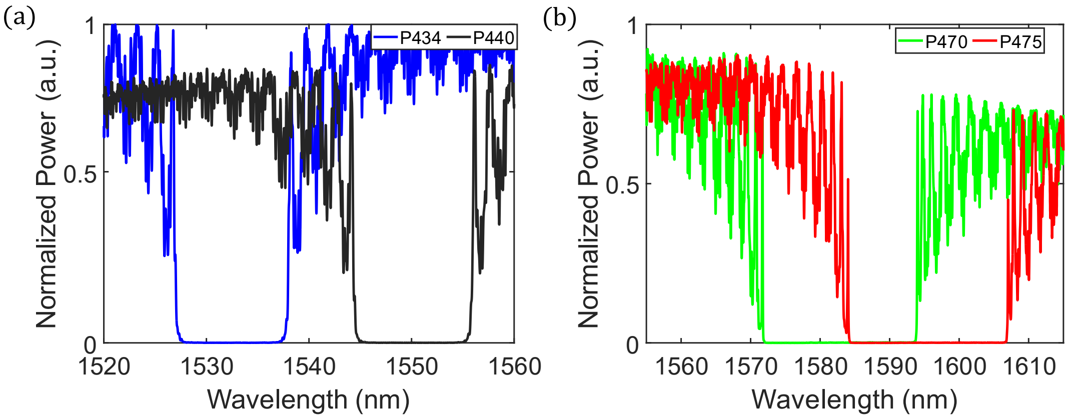

Figure 4.3: Measured TE-polarized transmission of the two different on-chip DBR architectures implemented in the SC-FPs. (a) DBRs with W_b=1.8 μm, W_a=1.0 μm, and (b) DBRs with W_b=1.2 μm and W_a=0.6 μm. The plots show two different periodicity values and the relative shift in the stopband position.

For compact hybrid lasers, the wavelength-selective resonator must be designed through a careful trade-off between high peak reflectivity and loaded Q-factor. A higher reflectivity reduces the total optical losses of the hybrid cavity and enhances optical feedback to the gain section, whereas an increased loaded Q-factor generates narrower resonances in the SC-FP structure, effectively limiting the number of longitudinal modes that can compete within each laser line. The reflectivity of the SC-FP cavities is primarily governed by the coupling gap, the cavity round-trip time, and the internal propagation losses.

The on-resonance reflectivity of a side-coupled cavity scales as $R = (Q_L/Q_C)^2$[34], as reported in Eq. (2.80), where Q_L and Q_C denote the loaded and coupling Q-factors, respectively. To explore the effect of different coupling regimes and cavity geometries, the three devices implement distinct sets of design parameters, including variations in cavity length, coupling gap, and waveguide width. Figure 4.4(a-c) shows the passive transmission characterization of all three SC-FPs, recorded using an OSA with 5 pm resolution.

Device01 maximizes resonance finesse and peak reflectivity. It incorporates a cavity length of $L = 600$ µm and a coupling gap $G = 500$ nm to minimize coupling losses and enhance the loaded Q-factor. Each DBR mirror includes $N = 1950$ grating periods and $N_T = 50$ tapered periods, allowing a smooth optical transition and strong mode confinement. During testing, Device01 achieved the highest reflectivity ($R \approx 57\%$) and a finesse of approximately 360, producing sharp, high-contrast resonances suitable for stable single- or few-mode lasing.

Device02 features longer cavity length, $L = 1200$ µm, doubles the density of cavity modes within the DBR stopband compared to Device01 and the average FSR reduces from 107 GHz to about 56 GHz (Fig. 4.5(a)). At the same time, the coupling gap is set to $G = 400$ nm, which raises the coupling strength and ensures Efficient cavity coupling, despite the longer round-trip path. Device02 shares the same DBR corrugation structure as Device01 (N=1950, N_T=50) and they both implement an optimized waveguide width W_c=1.6 μm.

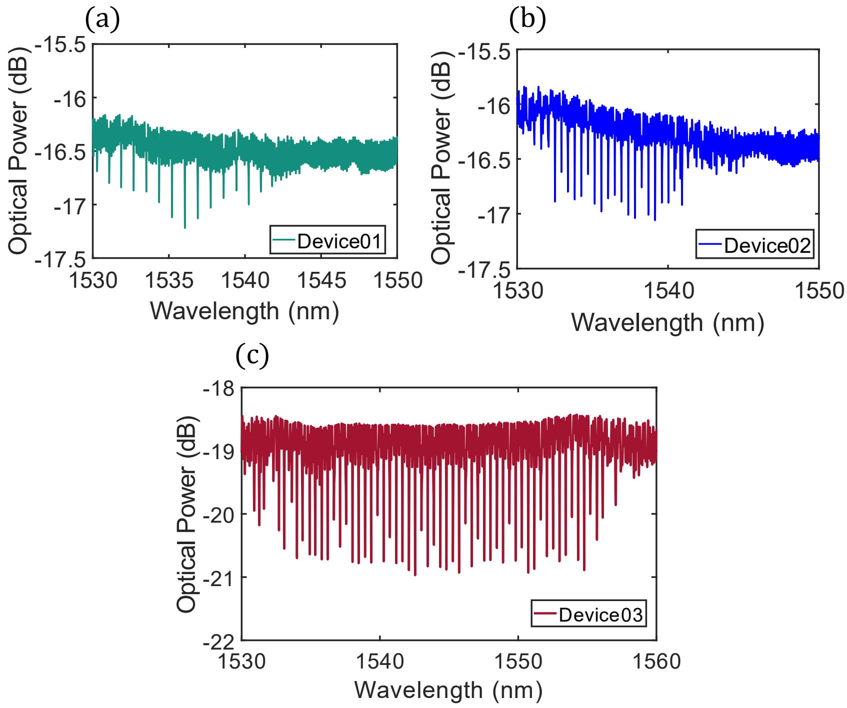

Figure 4.4: Transmission response of (a) Device01, (b) Device02, and (c) Device03 normalized to the input light source used for passive characterization. The SC-FPs are characterized via end-fire optical setup considering TE polarization for Device01 and Device02, while TM-mode for Device03.

Device03 extends the design concept to achieve TM-polarized operation. Figure 4.6 presents the passive transmission spectra of Device03 under both TE and TM excitation, showing a clear blue-shift in the resonant-mode envelope for the TM mode (blue trace) relative to the TE mode (yellow trace). The TM response allows to match the operating wavelength desired for hybrid laser experiments and exhibits a higher extinction ratio of the resonant dips.

This design integrates DBR reflectors with $N = 450$ total periods and $N_T = 50$ tapered sections, using corrugation widths of 0.6 μm and 1.2 μm to enhance index contrast. The cavity waveguide broadens linearly from 0.6 μm to 1.6 μm, reducing sidewall-roughness scattering and improving the overall Q-factor.

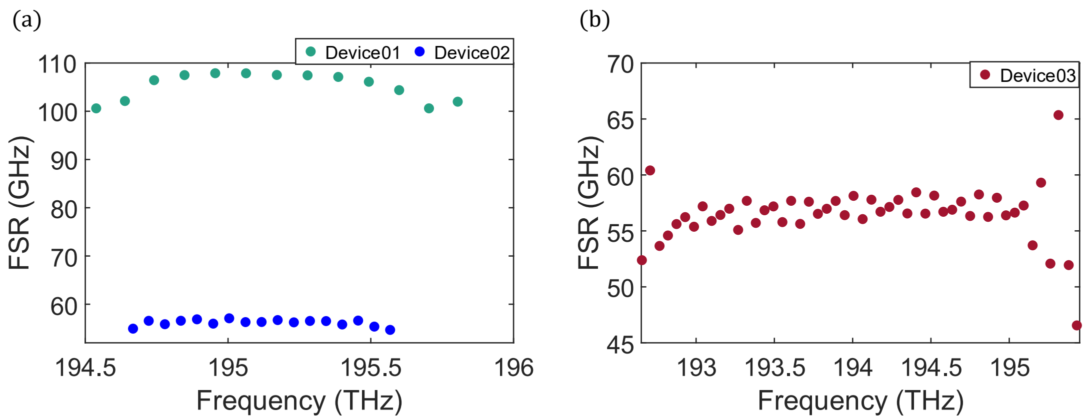

Figure 4.5: Experimental SC-FPs FSR as function of frequency: average values of ≈56 GHz for both Device02 and Device03, and ≈107 GHz for Device01.

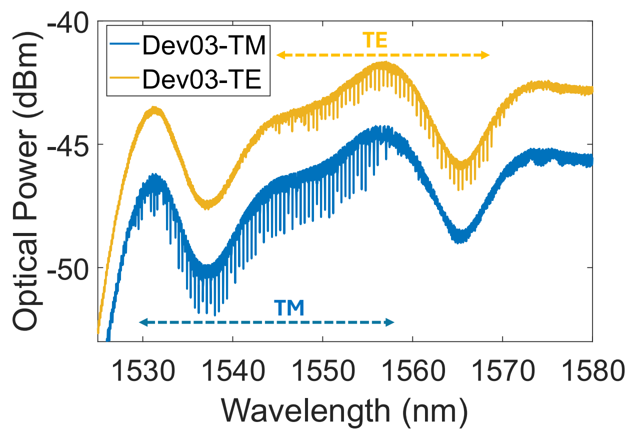

Figure 4.6: Passive transmission spectra of Device 03 measured under TE (yellow) and TM (blue) excitation. The transmission characterization of the devices is operated with a free space edge-coupling setup that includes a polarization cube to select the input polarization to the chip.

The cavity geometry is consistent with Device02, employing a length $L = 1200$ μm and a coupling gap $G = 400$ nm. The combination of the longer cavity and stronger feedback yields a denser resonance spectrum, supporting approximately 50 modes, with FSR comprise between 55 GHz and 57 GHz, significantly higher number than in Devices01 and 02.

High-resolution transmission spectra for Devices 01, 02, and 03, acquired using the optical setup and settings described in Section 3.6, appear in Figure 4.7(a–c).

These traces offer precise characterization of the resonant dips and enable reliable extinction ratio extraction. The measured extinction ratio values reach ER≈15 dB for Device01, ER≈5 dB for Device02, and ER≈10 dB for Device03, clearly demonstrating the distinct coupling regimes engineered into each SC-FP design.

Numerical fitting of the transmission resonant dips, based on the side-coupled resonator model reported in Eq. (2.81), yields optimal FWHM values of 2.3 pm, 2 pm, and 5.5 pm for Devices 01, 02, and 03, respectively. These linewidths correspond to the peak loaded, intrinsic and coupled Q-factors detailed in Figure 4.7(d–f).

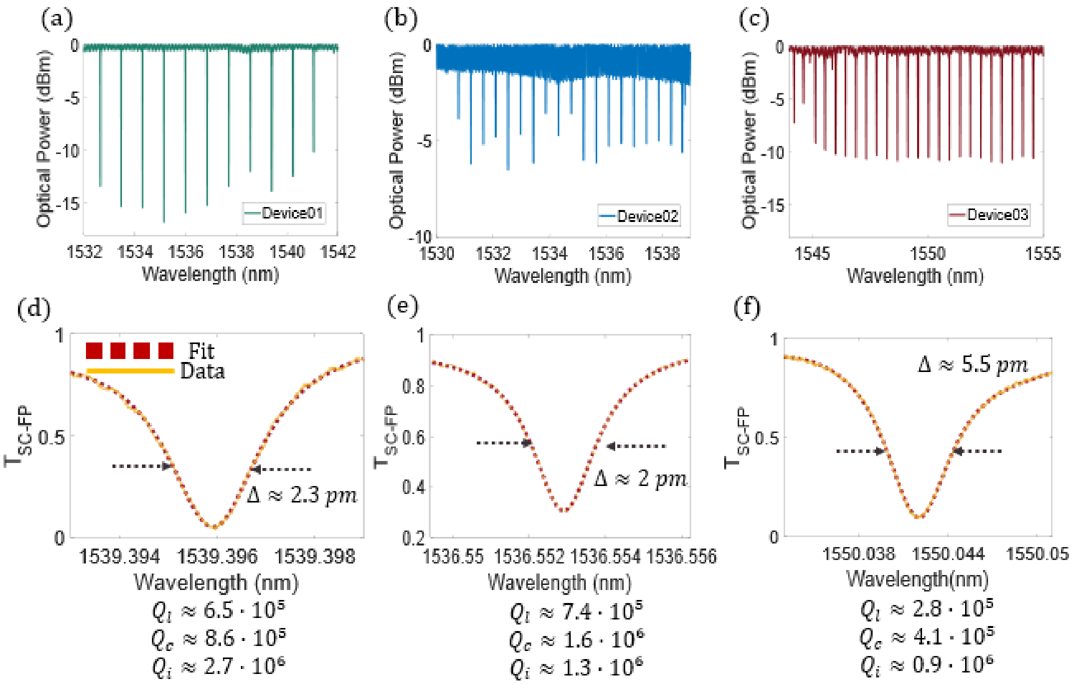

Figure 4.7: Normalized optical spectra obtained after high-resolution measurements highlight different extinction rates for (a) Device01, (b) Device02 and (c) Device03. (d-f) Optimal resonance fitting: extracted peak loaded, coupled and intrinsic Q-factors for Devices 01,02,03, respectively.

From the same analysis, it is possible to evaluate the experimental peak reflectivity at resonance (R), which measures approximately 57.1%, 21.4%, and 46.6% across the three devices. This reflectivity obeys the standard relation $R = (Q_L/Q_C)^2$ for side-coupled Fabry–Pérot resonators (Eq. (2.80)) [14],[34].

Figures 4.8(a), (b) provide detailed insight into the dispersion characteristics of the three SC-FP devices, building directly on the high-resolution transmission analysis. In these plots, the integrated dispersion $D_{\text{int}}(\mu)$is defined in the angular-frequency domain as $D_{\text{int}}(\mu) = \omega_\mu - (D_0 + D_1\mu)$, where $\omega_\mu$is the experimentally measured angular frequency of the μ-th resonance (with $\mu = 0$at the bandgap center), and the coefficients $D_i$are obtained from a polynomial fit of the form

$\omega(\mu) = \sum_{i=0}^{3} D_i \, \mu^i$. For clarity, $D_{\text{int}}(\mu)/(2\pi)$ is expressed in GHz and plotted as a function of optical frequency $f_\mu = \omega_\mu/2\pi$.

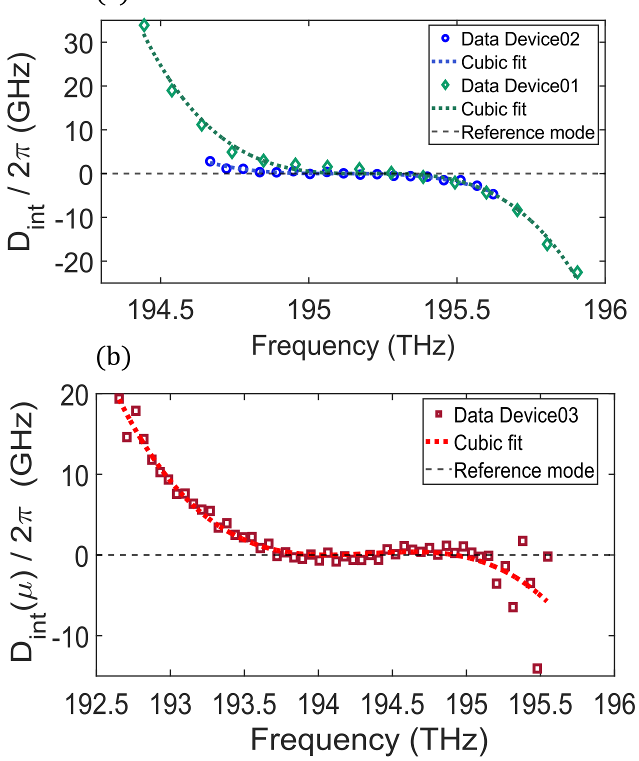

Figure 4.8: Comparison of the integrated dispersion behavior for (d) Device01 (green), Device02 (blue), and (e) Device03 (red) in the frequency domain.

The second-derivative analysis reveals distinct dispersion profiles for the three designs. All devices exhibit low second-order dispersion near the center of the bandgap, but their behavior differs significantly away from this point. Device01 shows a pronounced change in concavity around $\mu = 0$, indicating a clear transition from normal to anomalous dispersion, together with a substantial third-order contribution at the bandgap edges. Device02, in contrast, remains almost flat and close to zero, with only a weak curvature variation and an almost antisymmetric evolution around the central frequency. Device03 displays a strongly asymmetric integrated-dispersion profile: near the central frequency, $D_{\text{int}}(\mu)$is close to zero but slightly positive, while toward lower frequencies the curve bends sharply upward (strongly anomalous dispersion), and toward higher frequencies it stays nearly flat before eventually bending downward into the normal-dispersion regime.

As a result, a larger number of modes in Device03 lie in the anomalous-dispersion region ($D_{\text{int}}(\mu) \geq 0$).

These results confirm that SC-FPs enable effective dispersion engineering through the choice of cavity length, waveguide width, and DBR geometry, providing a practical platform for tailored modal-dispersion control. This functionality is particularly attractive in ECLs, where the SC-FP not only acts as an integrated wavelength-selective reflector but also shapes the dispersion and nonlinear evolution of the circulating light, thereby reshaping the optical envelope that is fed back into the fiber loop [24],[32],[35].

4.3 External-cavity architectures

In this section, the fiber-assisted external-cavity architectures implemented in this thesis, incorporating the SC-FP resonant reflectors described above, are introduced and progressively detailed. Initial experiments employ a laser cavity in which the mirrors are formed by an integrated SC-FP resonator and a three-port fiber-based circulator. The latter enables the optical power, amplified by a fiber-coupled high-power EDFA or by a non-linear fiber-pigtailed SOA used as gain elements, to be reflected into the PIC.

This first fiber-based ECL configuration serves as a preliminary testbed: it demonstrates multi-wavelength emission, confirms that lasing occurs exactly at the passive SC-FP resonances, and verifies the time stability of a large number of simultaneously excited lasing lines. However, the employed circulator-based scheme requires relatively long fiber paths, which limit the cavity free spectral range and make the setup less compact and less suited for practical integration.

To overcome these limitations, the external-cavity is progressively shortened and simplified, while still relying on fiber coupling to the PIC. This evolution leads to the proposed configuration, where a Sagnac-based loop mirror acts as the fiber-end reflector.

In this final design, a linear SOA connects directly to an optical fiber coupler, forming a compact loop that simultaneously provides gain, reflection, and nonlinear interaction. Adjusting the feedback topology and the SOA contribution within the loop alters the feedback conditions and effective amplification in the fiber loop, thereby modifying the lasing excitation dynamics. The laser has been characterized also in frequency domain to assess coherence, mode-competition and stability as will be further demonstrated.

4.3.1 Circulator-based external-cavity setup

Prior implemented external-cavity configuration exploits a commercial three-port fiber circulator as fiber-based feedback, while the SiN PIC acts as the integrated resonant reflector. The connection between the two mirrors is realized partly in free space, through the end-fire measurement setup described in Section 3.4, and partly in fiber, accessed via port 2 of the circulator, as shown in Fig. 4.9. The fiber-coupled gain element, together with a polarization controller, is connected between port-3 and port-1 of the circulator. In each cavity round trip, the signal undergoes optical amplification according to the amplifier's gain, ensuring that all light reflected from the PIC is amplified once before being re-injected into the chip, and this process continues until the amplifier reaches its saturation power. The external-cavity formed between the effective reflection from the on-chip SC-FP reflector and the circulator–gain feedback, results in a total fiber length of approximately 12 m. This long cavity yields a small free spectral range but allows straightforward implementation with standard telecom components. For these experiments, Device03 operated in TE polarization has been chosen as on-chip reflector, because both the EDFA and SOA-NL provide maximum gain close to 1560 nm, overlapping well with the location of the SC-FP resonances. The implemented setup is shown in Figure 4.9.

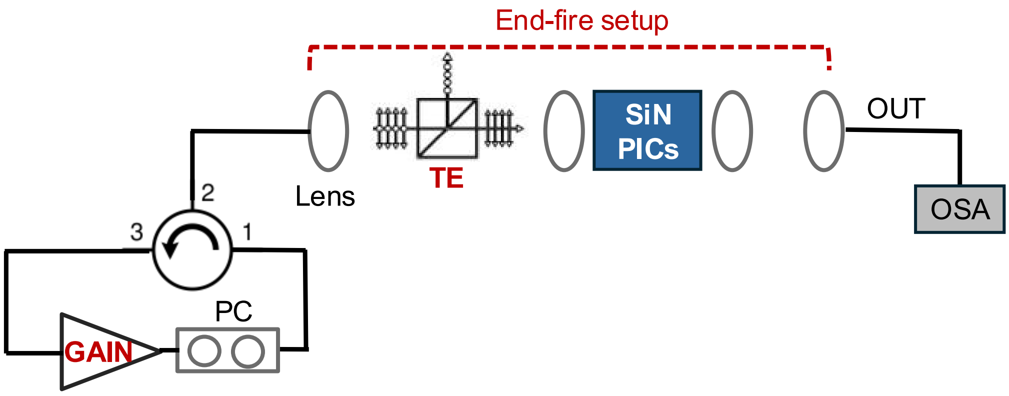

Figure 4.9: Circulator-based HECL setup. The SiN PIC incorporating the SC-FP reflector is partially aligned to a free-space end-fire stage and partially fiber-coupled via a three-port fiber circulator, whose loop contains the gain element (EDFA or nonlinear SOA).

At the initial stage, the cavity employs an EDFA to generate multi-wavelength emission, exploiting its nearly flat gain profile centered at 1550 nm with an effective bandwidth of approximately 20 nm. By gradually increasing the EDFA pump power and optimizing the polarization state in fiber, the system reaches the lasing threshold and generates multi-wavelength emission. The observed lasing lines align spectrally with the passive SC-FP resonances, confirming that the integrated reflector defines the longitudinal mode positions and that many cavity modes can lase simultaneously (Fig. 4.10).

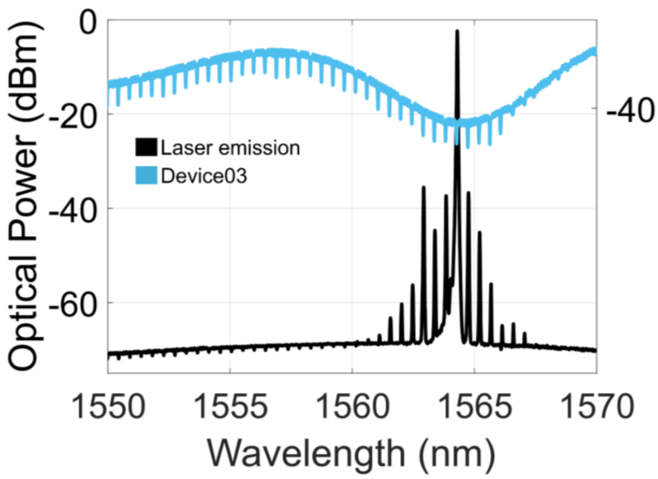

Figure 4.10: EDFA-based multi-wavelength laser emission (black) overlapping with the passive resonant dips of the TE-polarized of Device03 SC-FP (light blue).

Additionally, polarization variation in the circulator feedback (obtained by the rotation of the polarization paddles) and small coupling alignment changes in the PIC modify the amplified signal in the loop and allow different subsets of modes to be excited, as shown in Fig. 4.11(a). Once the alignment and the polarization are fixed, time stability analysis has been checked. Fig. 4.11(b) shows that the multi-wavelength emission envelope remains largely stable between the first measurement taken at time (t_1) and a fifth one (t_5) acquired after 20 minutes, apart from a slight decrease in power caused by a gradual loss of alignment efficiency at the stages.

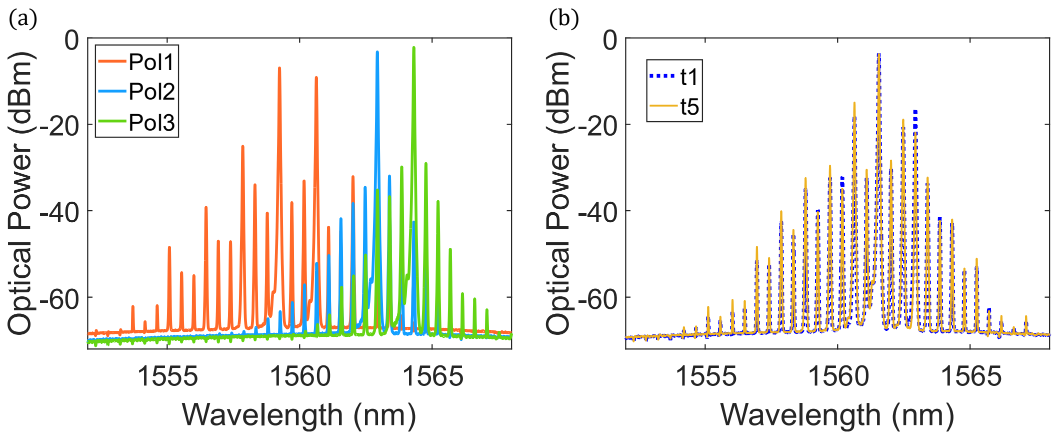

Figure 4.11: Multi-wavelength emission as a function of variation in the polarization by rotating the PC paddles, exciting different subsets of the supported resonant modes. (b) Time stability of the multi-wavelength laser envelope, showing traces recorded at different instants separated by 20 minutes, with t1 and t5 illustrating the temporal stability achieved over this time span.

Despite the high density of lasing lines obtained with the EDFA-based circulator cavity, the long additional fiber required by the input and output fiber of the amplifier extends the external-cavity length over 12 meters and makes the system more mechanically and polarization-sensitive, which in turn perturbs the loop-gain dynamics. To investigate the effect of different amplification mechanism in the loop and to move toward a gain configuration more compatible with future integration, the EDFA is replaced by a non-linear SOA (SOA-NL-OEC-1550 from the Centre for Integrated Photonics Ltd (CIP)) placed in the same circulator arm.

The butterfly packaged SOA-NL provides gain with peak centered at around 1560 nm, still matching to the SC-FP resonant modes. Indeed, multi-wavelength laser performance, as reported in Figure 4.12, shows the good overlap between the passive SC-FP resonances and the laser lines, when the SOA-NL is driven at around 250 mA.

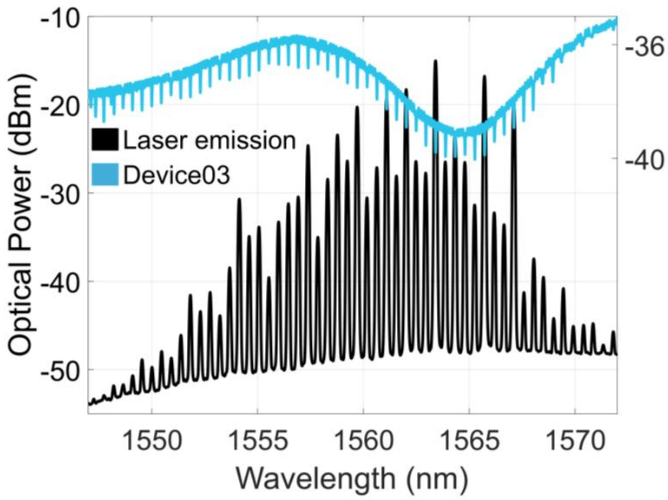

Figure 4.12: SOA-NL multi-wavelength laser emission (black): check overlap between passive resonant dips of the TE-polarized of Device03 SC-FP (light blue). A denser set of lasing lines occurs compared to EDFA-based results.

Employing the SOA-NL in the loop, the laser cavity still emits at the corresponding SC-FP modes, but its spectrum becomes more sensitive to the SOA driving current and the input polarization state, reflecting the influence of carrier-induced refractive-index changes and gain saturation on the hybrid cavity. The evolution of the ECL spectrum as a function of SOA current is summarized in Figure 4.13.

When the current is increased from 150 mA to 350 mA, it leads to a denser and broader laser envelope, with more SC-FP modes reaching threshold and contributing to the overall multi-wavelength output. In both gain configurations, the circulator-based setup serves as a reference ECL, demonstrating that the SC-FP reflector reliably selects the lasing wavelengths and supporting the later transition to more compact Sagnac-loop-based cavities.

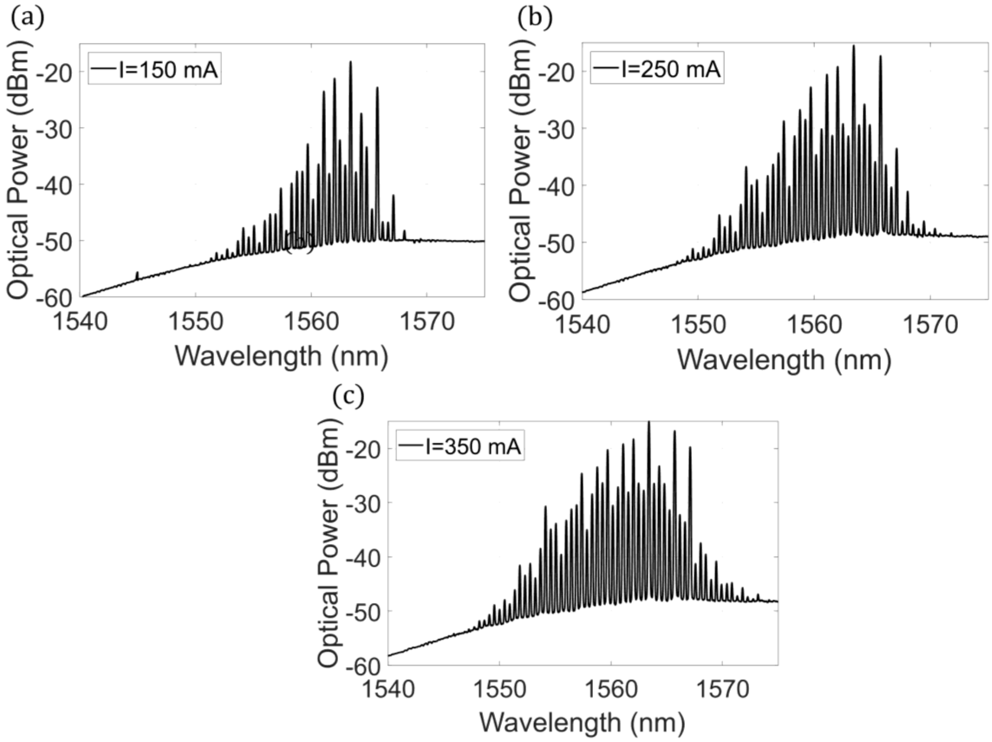

Figure 4.13: Evolution of the ECL spectrum with increasing SOA drive current. Just above threshold, only a few modes within a narrow spectral span are observed. As the current approaches the SOA saturation current, a denser and broader laser envelope appears. Laser emission is shown for SOA currents of (a) 150 mA, (b) 250 mA, and (c) 350 mA.

4.3.2 Sagnac-based loop mirror

The final hybrid fiber-SiN chip based external-cavity employed for multi-wavelength laser system is depicted in Fig. 4.14. The PIC is accessed from both ends via lensed optical fibers, with a polarization-maintaining input fiber preserving the state of polarization injected into the chip.

The gain medium is a butterfly-packaged, fiber-pigtailed SOA (SOA-L-OEC-1550, CIP Photonics) providing about 14 dB optical gain centered at 1545 nm in the linear regime. The SOA fibers are connected to a commercial optical fiber coupler (FC) and wrapped inside a polarization controller (PC), forming a Sagnac-type loop [36]. For device operation and characterization, a NIR camera is employed in the optical setup to assist with the alignment of the lensed fibers to the PIC. Light reflected from the PIC enters the FC, splits into two counter-propagating beams that both traverse the SOA once per round trip and then recombines coherently; the coupling ratio K of the splitter sets the effective feedback reflectivity R_S toward the PIC based on the relation $R_S = 4K(1-K)$.

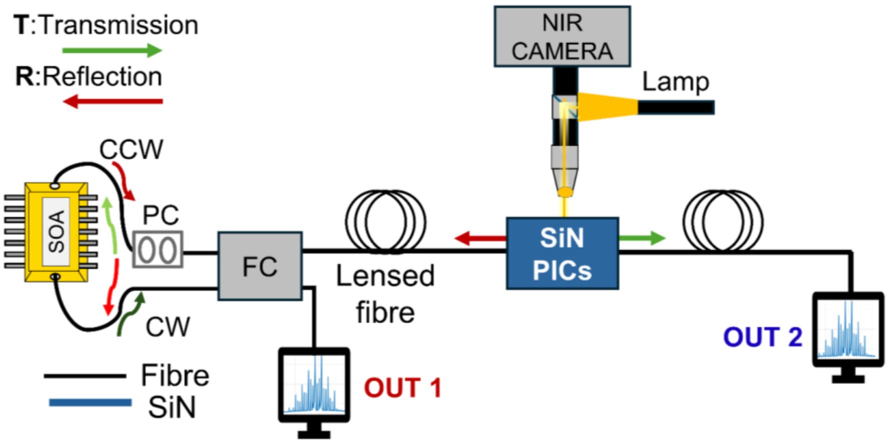

Figure 4.14: Schematic of the Sagnac-based ECL. The cavity is composed by a Sagnac-based fiber reflector, which includes a fiber-coupled SOA as gain element, coupled via a lensed fiber to a SiN PIC side-coupled Fabry–Pérot resonant reflector, acting as the on-chip resonant mirror.

The first configuration under analysis considers a 90/10 fiber splitter connected to the input lensed fiber, creating an unbalanced Sagnac-type loop (UBSL). In this architecture, the fiber splitter results in an effective reflection of approximately R_S≈35% from the Sagnac loop towards the PIC. Consequently, the ECL output port is accessed from the fourth port of the splitter (OUT 1), where roughly 65% of the power is directed at the output, excluding losses. Replacing the 90/10 splitter with a nominal 50/50 coupler results in a balanced Sagnac loop (BSL) configuration, in which the second lensed fiber serves as the ECL output port (OUT 2). The effective reflection of the Sagnac loop towards the PIC depends on the real imbalance of the fiber splitter; based on the nominal fabrication specifications, this "balanced" configuration is expected to provide a reflection exceeding 97%.

Despite the coupling losses that limit intracavity power, the SOA nonlinear response remains comparable to the nonlinear effects in the SC-FP cavity. In both UBSL and BSL, clockwise (CW) and counterclockwise (CCW) propagating beams meet inside the SOA, enabling cross-phase modulation (XPM); together with the PC this leads to nonlinear polarization rotation (NPR) [37]. In the unbalanced loop, the asymmetry further induces an effective nonlinear reflectivity toward the PIC [38]. The combined action of XPM and cross-gain modulation (XGM) produces an intensity-dependent transmission and loss, which can suppress mode competition [39],[40].

At the same time, the Sagnac topology sets the external-cavity length and thus the FSR , while the overall hybrid laser performance in terms of coherence, emitted power and spectral response is governed by the interplay of SOA gain, PIC coupling losses, nonlinear effects in both the SOA and SC-FP, and polarization/chromatic dispersion in both fiber and SC-FP. Lasing stability is additionally affected by temperature drifts and acoustic fluctuations acting on the lensed fibers and the PIC. In this context, Sagnac-loop configurations incorporating an SC-FP resonator reliably generate multi-wavelength laser emission.

Using the SC-FP as the on-chip reflector, the laser operates in a robust multi-wavelength regime: the interval of active resonances supporting lasing emission can be controlled through adjusting the SOA bias current and fiber-based polarization control, enabling operation across several or even all SC-FP resonances. The lasing polarization is determined by the combined effect of the PC settings and the on-chip SC-FP resonator selectivity. The system naturally converges to a state where the polarization of the light returning to the chip aligns with the guided mode of the high-Q SC-FP resonances, minimizing round-trip loss.

For example, Fig. 4.15(a) shows two representative multi-wavelength lasing profiles, (i) and (ii), obtained in the unbalanced Sagnac configuration using Device 02 as the reflector. By applying small adjustments to the PC paddles, different subsets of SC-FP modes are selectively excited while still operating within the same stopband. When the SC-FP is replaced by an on-chip DBR with the same corrugation widths and periodicity considered in the SC-FP, but a reduced number of grating periods (N = 500), the emission reported in Fig. 4.15(b) highlights the gain curve imposed by the SOA, not supporting spaced multi-line response.

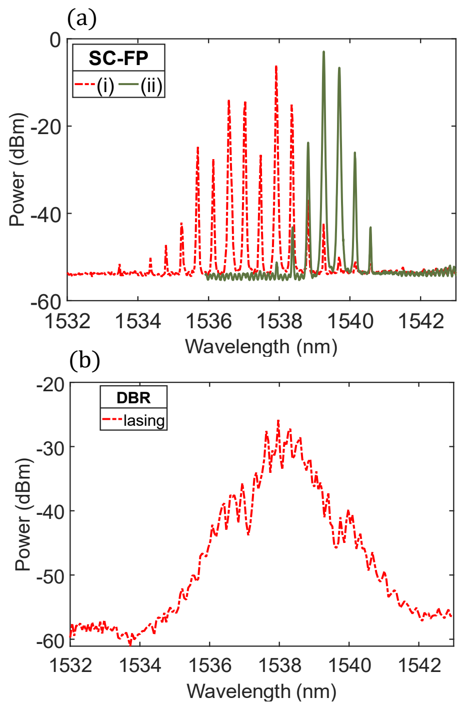

Figure 4.15: (a) Multi-wavelength laser emission when on-chip SC-FP resonator is employed as reflector. Small changes in the lensed fiber alignment in input and adjustments of the polarization controller can result in different subsets of lasing lines emitted: (i) and (ii) illustrate that Device 02 can support different multi-line lasing regimes. (b) In contrast, it is reported the laser emission spectrum when an on-chip DBR, with the same corrugation widths and periodicity as the DBR sections integrated in the SC-FP, replaces the SC-FP as reflector.

4.3.2.1 HECL supported longitudinal modes

To isolate the contribution of the fiber-feedback network independently of the on-chip resonator, three reference external-cavity configurations, without the SC-FP mirror, has been implemented as illustrated in Fig. 4.16. The setup comprises a pure fiber laser (FL), obtained by considering a cavity formed by two single-mode fiber (SMF) reflectors (Fig. 4.16(a)), and two hybrid ECL variants using an on-chip DBR with the two alternative Sagnac fiber loops UBSL, and BSL (Fig. 4.16(b)).

Specifically, replacing the SC-FP resonators with on-chip DBRs allows estimation of the FSR of the supported longitudinal modes while keeping the external path and total cavity length identical to within a few millimeters. In contrast, comparing the fiber laser with the BSL architecture using the on-chip DBR makes it possible to isolate the respective roles of the loop topology and the integrated reflector, since both configurations maintain nearly identical external paths and cavity lengths.

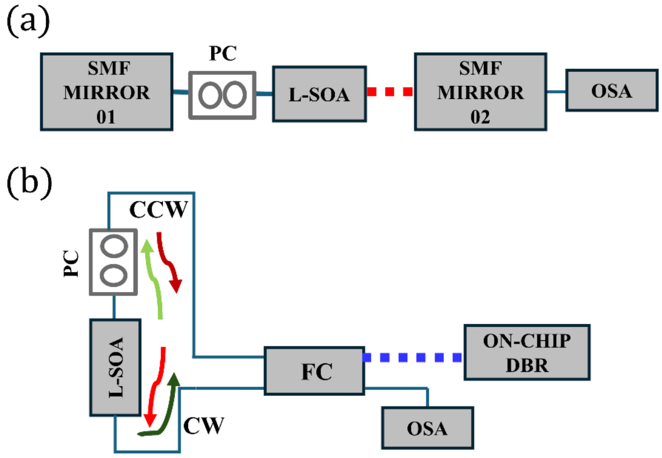

Figure 4.16: Laser emission system in the absence of SC-FP mirror. Sagnac-based loop mirror combined with (i) SMF fiber reflector or (ii) on-chip DBR.

To detect the spacing among the external-cavity longitudinal modes, the emitted spectrum is first isolated using a wavelength-selective switch characterized by a bandwidth (BW) of 50 GHz, selected output using a photodetector (BW=1.6 GHz), followed by amplification (gain G) and sampling with a real time oscilloscope (BW= 16 GHz,), as depicted in Fig. 4.17(a). The fast Fourier transform (FFT) analysis was performed using a time base of 40 µs/div over 10 divisions, corresponding to a 400 µs acquisition window, with a sampling rate of 3.13 GSa/s, resulting in approximately 1.25 Mpts and a frequency resolution of about 2.5 kHz. Figure 4.17(b) shows the FFT traces acquired for the FL reference (Fig. 4.17 (a)) and for the unbalanced Sagnac loop combined with the on-chip DBR (Fig. 4.17(b)).

Although the longitudinal-mode spacing is too small to be resolved with the optical spectrum analyzer, the longitudinal modes beating gives rise to a set of RF tones separated by the external-cavity FSR. Assuming a group index of approximately $n_g \approx 1.468$ for standard single-mode silica fiber in the C-band, the corresponding round-trip cavity lengths are reported in Table 4.1, together with the values obtained for the balanced Sagnac loop with DBR.

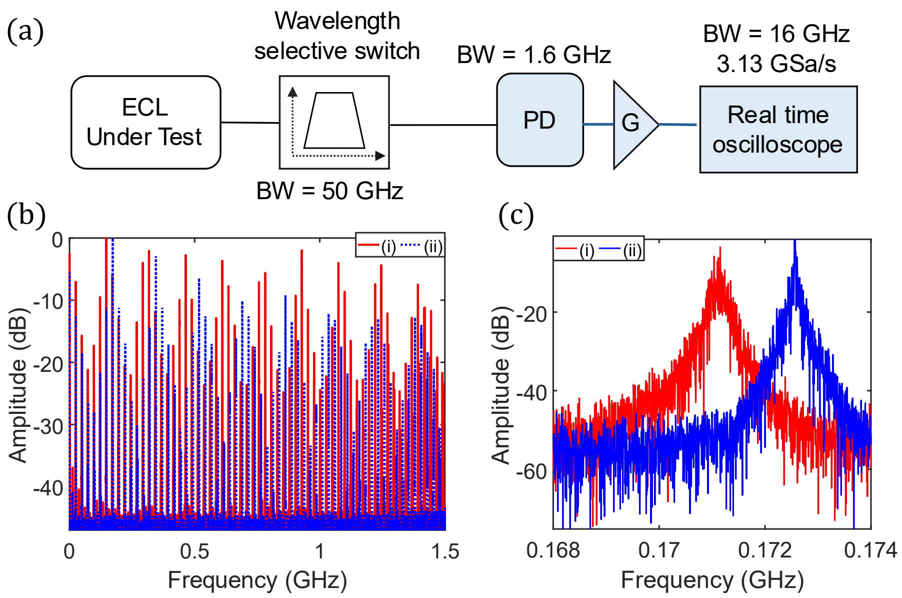

Figure 4.17: (a) Single-wavelength laser RF analysis setup: a single emitted wavelength is filtered and sent to the photo detector (PD) and real time oscilloscope, after amplification (G). (b) FFT magnitude response resulting from the beating of external-cavity longitudinal modes: red trace for (i) and blue trace for (ii). (c) Zoomed view of a single harmonic for both cases: the RF linewidth for the on-chip DBR case results sharper than the fiber mirror.

Table 4.1: Experimental FSRs a between the longitudinal modes beating in the four external-cavity configurations used as reference after the FFT of the RF signal. The corresponding round trip length is estimated by L = c/(ng · FSR). The fourth and fifth columns represent the average FWHM of the RF set and the first non-zero local maximum of the RF envelope.

Configuration	RF measured FSR	L round trip length	RF FWHM	Parasitic modulation
UBSL + DBR	≈ 24.8 MHz	≈ 8 m	≈ 180 kHz	≈ 172 MHz
BSL +DBR	≈ 19.7 MHz	≈ 10 m	≈ 127 kHz	≈ 98.3 MHz
FL	≈ 24.7 MHz	≈ 8 m	≈ 300 kHz	≈ 147 MHz

Moreover, Figure 4.17(c) presents a zoom of the main RF peaks; the extracted RF full width at half maximum is about 300 kHz for the FL configuration and 180 kHz for the UBSL with DBR, indicating improved coherence in the latter case. The RF envelope observed for the UBSL with DBR differs from that of the FL reference, showing that it is not purely determined by the fiber SOA or the fiber coupler, but by their specific arrangement in the loop. Overall, strong RF harmonics are observed across the entire photodetector bandwidth, revealing rich multimode beating within the external-cavity.

4.3.2.2 HECL frequency analysis

Competition between longitudinal modes has a strong impact on the performance of the external-cavity laser. The SC-FP resonators implemented in this laser architecture exhibit resonance linewidths larger than 254 MHz, which exceeds the external-cavity free spectral range of 24.8 MHz and 19.7 MHz reported in Table 4.1 for the unbalanced and balanced Sagnac configurations, respectively. As a result, several tens of external-cavity longitudinal modes can oscillate within what appears as a single spectral line at the resolution of the optical spectrum analyzer. To reveal the coexistence of these modes, a single SC-FP resonance is isolated and analyzed in the RF domain using the setup of Fig. 4.17(a).

The corresponding RF spectrum, reported in Fig. 4.18(a) by the blue trace, arises from the beating of the longitudinal modes occurring at the photodetector, confined within one SC-FP resonance. When a SC-FP is used as reflector, the harmonic content is mainly restricted to frequencies below 0.5 GHz, consistent with the spectral filtering imposed by the resonator linewidth.

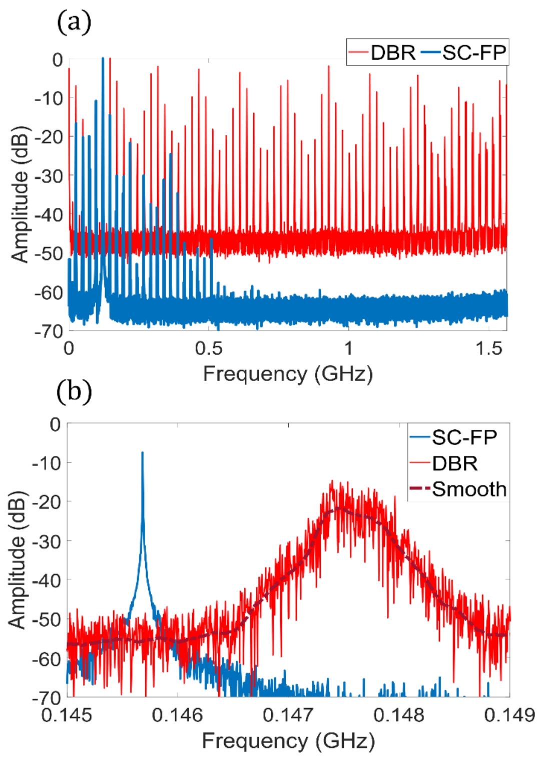

Figure 4.18: (a) (b) FFT magnitude resulting from the beating modes: red trace for the DBR and blue one for SC-FP are reported up to 1.565 GHz range. In the red trace, FFT amplitudes below the noise threshold were omitted for clarity. (c) Zoomed view of a single harmonic for both cases: the RF linewidth results much sharper when the SC-FP acts as resonant mirror in the cavity

For comparison, the RF spectrum obtained when the on-chip DBR is used as the reflector (red trace) is also shown. Although both configurations share almost identical longitudinal FSRs, since the external fiber path and cavity length differ by few hundreds of micrometers, their RF signatures differ markedly. The DBR-based cavity produces broadband, noisy RF harmonics extending across the entire photodetector bandwidth, with typical harmonic linewidths on the order of several hundred kilohertz. In contrast, the SC-FP-based cavity yields much narrower RF components, with linewidths below 15 kHz, demonstrating a substantial improvement in the relative coherence of the external-cavity modes. This narrowing of the RF harmonics is observed for both Device01 and Device02; however, the system showed a limited stability, resulting in RF components characterized by different linewidths and amplitude fluctuations on the millisecond timescale. Among the two fiber loop configurations and devices tested, Device02 with the BSL configuration exhibited the best RF performance (Fig. 4.19).

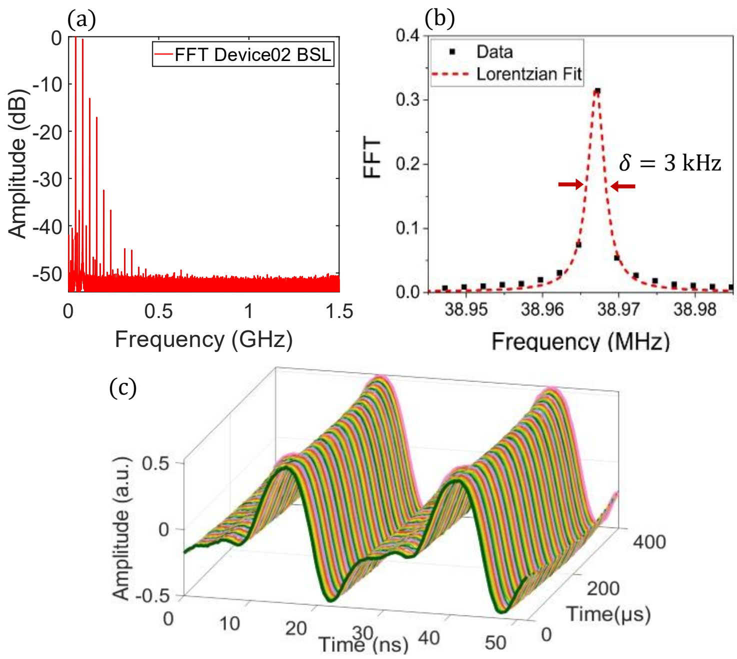

Figure 4.19: FFT results under BSL setup and Device02 integrated mirror: (a) an inter-harmonic spacing of 38.9 MHz, i.e. twice the fundamental FSR for a BSL, and (b) Lorentzian fitting of the FFT trace. (c) The time evolution of the pulses across a 400 μs time window.

The FFT of a 400 μs time trace exhibits a set of RF tones spaced by twice the cavity FSR, each with a linewidth of approximately 3 kHz. This value approaches the frequency resolution imposed by the acquisition window (about 2.5 kHz), indicating that the laser reaches a highly coherent operating state. Furthermore, this configuration supports multi-wavelength lasing at significantly lower SOA drive currents (around 220 mA) than required in the unbalanced loop (approximately 400 mA), confirming the advantage of the balanced Sagnac architecture in terms of efficiency and coherence. In addition to the RF linewidth analysis discussed above, the system can transiently access regimes in which the longitudinal modes reorganize into distinctly spaced structures in the frequency domain. As shown in Fig. 4.20(a), the RF spectrum initially displays a fundamental spacing equal to the FSR of the unbalanced Sagnac loop (as reported in Table 4.1, in Section 4.3.2.1).

When the polarization controller in the fiber loop is adjusted and small changes are applied to the input alignment of Device01, the inter-harmonic spacing can spontaneously shift to approximately 48.6 MHz and 96 MHz, i.e. nearly integer multiples of the fundamental frequency.

In this process, the polarization variations modify the feedback conditions and the effective amplification in the fiber loop, while the on-chip polarization state and lasing wavelength remain fixed owing to the wavelength-selective optical filtering used in the RF analysis. These coherent states persist only over short time intervals of the order of 200 μs, with more than 50 dB suppression of the previous harmonic pattern, and similar behavior is observed for several devices and fiber configurations.

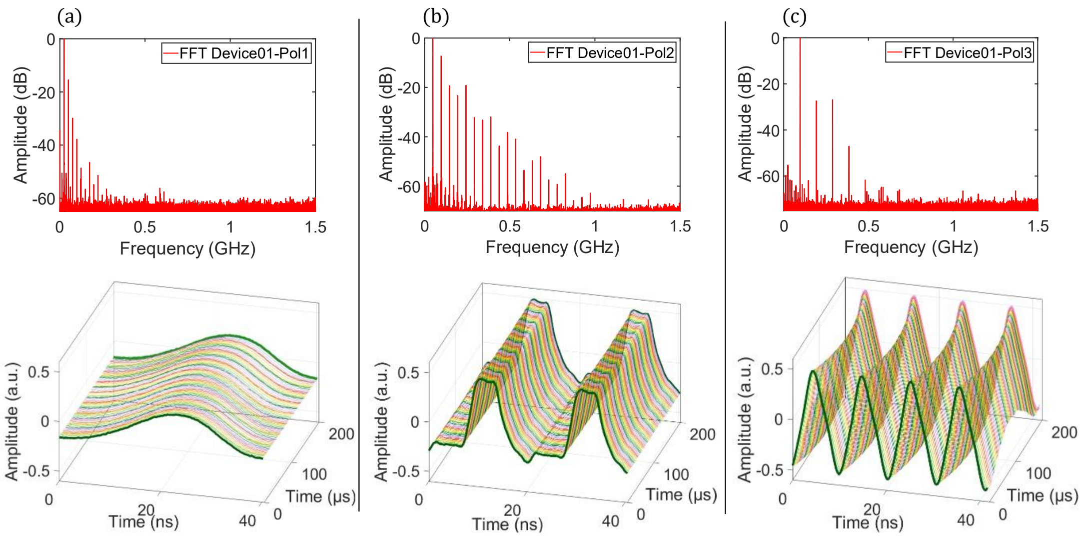

Figure 4.20: RF components and time evolution for Device01 in UBSL configuration: from (a) to (c) the harmonics spacing varies from ~24.7 MHz to ~48.6 MHz and ~96.2 MHz, obtained by small adjustments of the polarization-controller paddles and minor changes in the input alignment. Top row: FFT of a 200 μs time trace. Bottom row: time trace evolution. The x-axis scans a ~ 40 ns interval. The y-axis scans a 200 μs time-lapse.

The lower row of Fig. 4.20 illustrates the corresponding temporal dynamics within the acquisition window. The oscilloscope traces are segmented according to the measured RF periodicity; sequences of 50 periods are averaged and plotted as a function of time.

The resulting pulse trains exhibit clearly distinct profiles, corresponding to single-pulse, double-pulse, and four-pulse patterns that spontaneously form and circulate within the external-cavity laser. These higher-frequency states are intrinsically unstable and reappear intermittently, yet they frequently coincide with RF spectra of enhanced coherence, characterized by linewidths narrower than 10 kHz (Fig. 4.21).

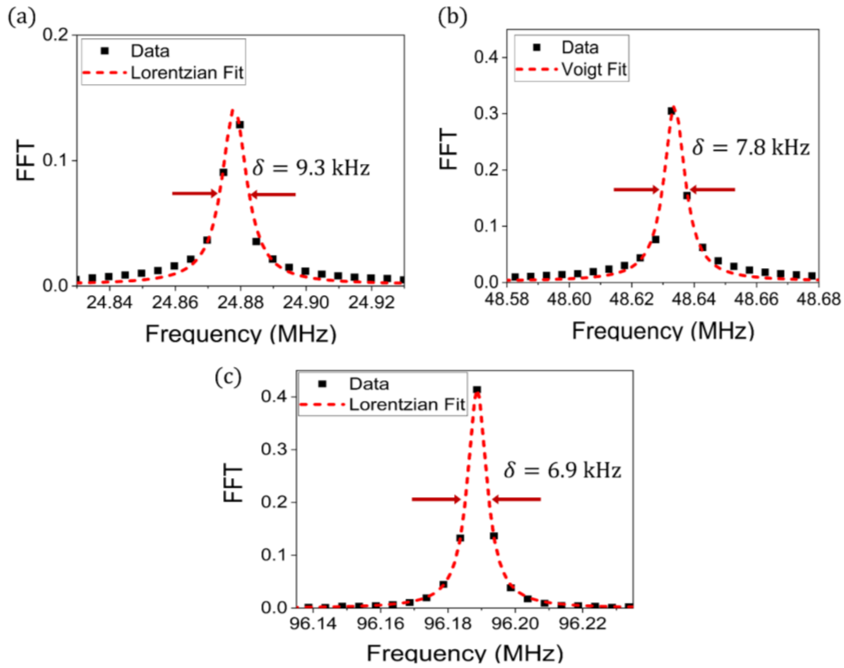

Figure 4.21: Linewidth of the RF components for inter-harmonic spacings of ~24.7 MHz, ~48.6 MHz and ~96.2 MHz, is (a) ~9.3 kHz, (b) ~7.8 kHz and (c) ~6.9 kHz respectively.

For Device03 operated with the unbalanced Sagnac loop, the same qualitative behavior observed for Devices01 and 02 is preserved, confirming the robustness of this operation regime. In this case, the RF harmonic content extends up to about 1 GHz, while the inter-harmonic spacing remains close to 24.8 MHz, consistent with the external-cavity FSR. The corresponding RF tones exhibit linewidths of approximately 11 kHz (Fig. 4.22).

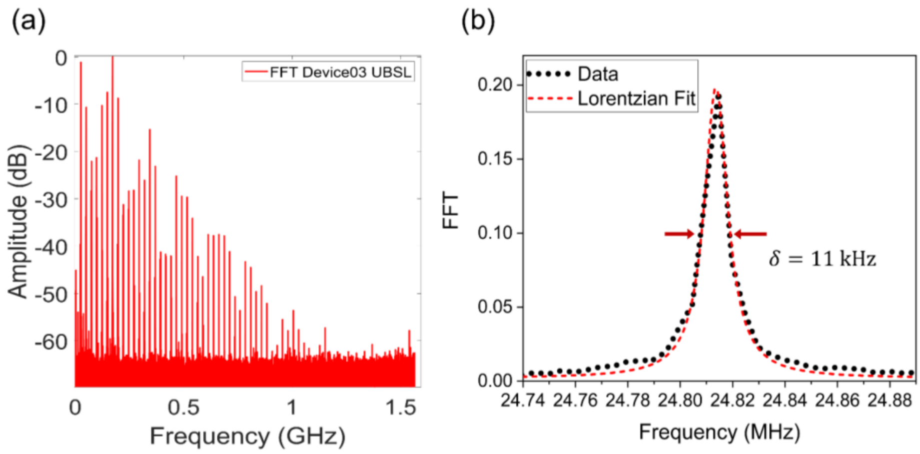

Figure 4.22: ECL based on Device03 and UBSL configuration: (a) inter-harmonic spacing of ~ 24.8 MHz (b) optimal linewidth of ~11 kHz.

4.3.2.3 Towards optical frequency comb generation

To investigate the coherence of the multi-wavelength laser and assess its potential for comb-like operation, the analysis is extended beyond single-resonance frequency measurements to the mutual coherence between different lasing wavelengths. This is achieved through an electro-optic down-conversion scheme that transfers the optical spacing set by the SC-FP free spectral range (≈56 GHz), which exceeds the photodiode bandwidth, into the RF domain. Device02, which exhibits the best RF linewidth performance, is selected for this study, and the corresponding experimental schematic is shown in Fig. 4.23.

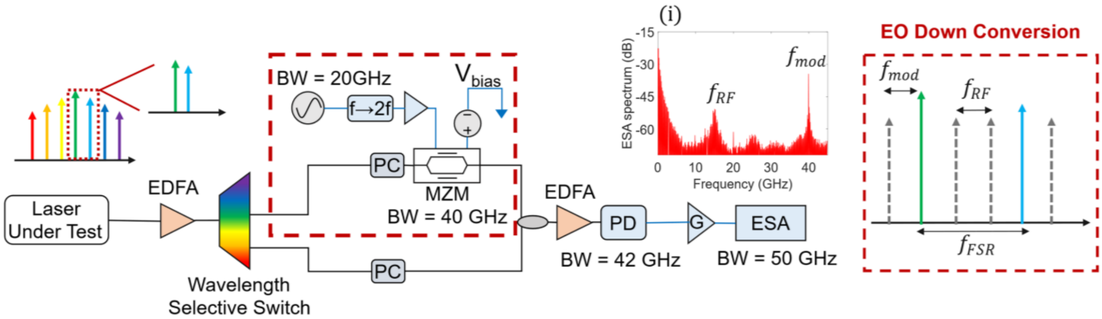

Figure 4.23: Experimental setup for comb-line mutual coherence measurement. Two lines from a wavelength-selective switch are electro-optically down-converted with a 40 GHz MZM, detected on a high-BW PD, and analyzed on an ESA. Polarization controllers are used to improve the modulation depth and optimize the generated sidebands. Single-wavelength modulation translates the comb spacing into a RF beat, within the PD bandwidth to quantify coherence.

The emitted multi-wavelength laser output placed around 1540 nm (Fig. 4.24(a)) is first amplified with an EDFA and routed to a programmable wavelength-selective switch that isolates the two strongest lines of the multi-wavelength spectrum.

Narrow, wavelength-selective optical filter channels suppress neighboring modes and approximately equalize the optical powers of the selected lines. (Fig. 4.24(b)).

After polarization alignment, one of the lines is injected into a high-speed Mach–Zehnder modulator (MZM) driven at 40 GHz, generating coherent modulation sidebands around that carrier. The modulated line is then recombined with the unmodulated line and amplified via an EDFA.

In the optical domain, the OSA confirms the presence of strong sidebands around each carrier resulting by the modulation process, as shown in Fig. 4.24(c). The recombined optical signal is detected on a high-bandwidth photodiode so that optical mixing between the sidebands and the unmodulated carrier down-converts the optical spacing into the RF domain. For Device02, with a spacing between lines of approximately 56 GHz, the 40 GHz drive generates RF components at 56 GHz − 40 GHz = 16 GHz and 56 GHz + 40 GHz = 96 GHz; but only the 16 GHz beat note lies within the bandwidth of the photodiode and the 50 GHz electrical spectrum analyzer (ESA).

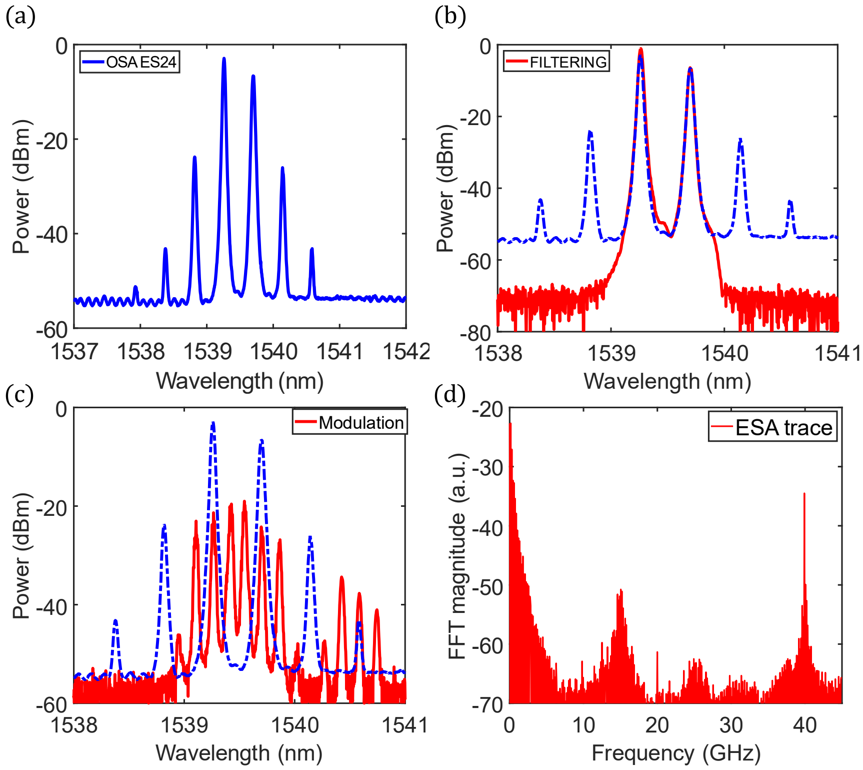

Figure 4.24: Full details on the electro-optic down conversion process. (a) SC-FP passive characterization is shown. (b) The two high-power lines are filtered from the multi-wavelength laser. (c) The modulation process generates sidebands in addition to the carriers, as shown in the OSA trace. (d) ESA plot shows a spectral component at the modulation frequency and a broader noise pedestal at the frequency of the RF tone $f_{RF} \sim 16\ GHz$, as expected.

The modulation conditions are adjusted to suppress the original carriers and enhance the sideband transmission. The ESA trace reported in Fig. 4.24(d) clearly shows a distinct 16 GHz RF tone superimposed on a large noise pedestal characterized by a FWHM of approximately 1 GHz, indicating substantial excess phase and frequency noise of the beating modes. This behavior points to two main limitations: (i) longitudinal modes within each emission line display unstable dynamics on the ESA acquisition timescale, and (ii) the mutual coherence between modes belonging to different lines is incomplete.

Such behavior is typical of multimode external-cavity lasers, where groups of longitudinal modes lase asynchronously and are subject to mode competition, mode hopping, and continual energy redistribution within the cavity [41],[42]. As a result, although the hybrid ECL can transiently display narrow RF tones and travelling pulse trains, the electro-optic down-conversion measurements indicate that, in its current implementation, the source operates as a partially coherent multi-wavelength laser rather than as a fully phase-locked optical frequency comb.

4-References

[1] Virte, Martin, and Pablo Marin-Palomo. "Integrated multi-wavelength lasers for all-optical processing of ultra-high frequency signals." Applied Physics Letters 123.18 (2023).

[2] Zhuang, Dongwei, et al. "Tunable multi-wavelength generation of an integrated self-injection locking laser based on the Vernier effect." Optics Letters 50.7 (2025): 2215-2218.

[3] Coddington, Ian, Nathan Newbury, and William Swann. "Dual-comb spectroscopy." Optica 3.4 (2016): 414-426.

[4] Zhao, Jie, et al. "Multi-wavelength DFB laser with high mode stability and uniform spacing for optical I/O technology." Journal of Lightwave Technology 42.14 (2024): 4874-4881.

[5] Torres-Company, Victor, et al. "Laser frequency combs for coherent optical communications." Journal of Lightwave Technology 37.7 (2019): 1663-1670.

[6] Capmany, José, et al. "Microwave photonic signal processing." Journal of lightwave technology 31.4 (2012): 571-586.

[7] Lukashchuk, Anton, et al. "Photonic-electronic integrated circuit-based coherent LiDAR engine." Nature Communications 15.1 (2024): 3134.

[8] Trocha, Philipp, et al. "Ultra-fast optical ranging using quantum-dash mode-locked laser diodes." Scientific Reports 12.1 (2022): 1076.

[9] Zhu, Zebin, and Guanhao Wu. "Dual-comb ranging." Engineering 4.6 (2018): 772-778.

[10] Marshall, Joanna, George Stewart, and Gillian Whitenett. "Design of a tunable L-band multi-wavelength laser system for application to gas spectroscopy." Measurement science and technology 17.5 (2006): 1023-1031.

[11] Ye, Jun, Harald Schnatz, and Leo W. Hollberg. "Optical frequency combs: from frequency metrology to optical phase control." IEEE Journal of selected topics in quantum electronics 9.4 (2003): 1041-1058.

[12] M. Peccianti, A. Pasquazi, Y. Parket al. “Demonstration of a stable ultrafast laser based on a nonlinear microcavity,” Nat. Commun., vol.3, no.765, Apr. 2012.

[13] Jyu, Siao-Shan, et al. "250-GHz passive harmonic mode-locked Er-doped fiber laser by dissipative four-wave mixing with silicon-based micro-ring." IEEE Photonics Journal 5.5 (2013): 1502107-1502107.

[14] Liles, Alexandros A., Kapil Debnath, and Liam O’Faolain. "Lithographic wavelength control of an external cavity laser with a silicon photonic crystal cavity-based resonant reflector." Optics Letters 41.5 (2016): 894-897.

[15] Vissers, Ewoud, et al. "Hybrid integrated mode-locked laser diodes with a silicon nitride extended cavity." Optics Express 29.10 (2021): 15013-15022.

[16] Liu, Yang, et al. "A photonic integrated circuit–based erbium-doped amplifier." Science 376.6599 (2022): 1309-1313.

[17] Roelkens, Günther, et al. "III-V/silicon photonics for on-chip and intra-chip optical interconnects." Laser & Photonics Reviews 4.6 (2010): 751-779.

[18] Wildi, Thibault, et al. "Phase-stabilised self-injection-locked microcomb." Nature Communications 15.1 (2024): 7030.

[19] Pintus, Paolo, et al. "Demonstration of large mode-hop-free tuning in narrow-linewidth heterogeneous integrated laser." Journal of Lightwave Technology 41.21 (2023): 6723-6734.

[20] Gong, Hai, et al. "Mode-hopping suppression of external cavity diode laser by mode matching." Applied optics 53.4 (2014): 694-701.

[21] Iadanza, Simone, et al. "Thermally stable hybrid cavity laser based on silicon nitride gratings." Applied optics 57.22 (2018): E218-E223.

[22] Bakoz, Andrei P., et al. "Wavelength stability in a hybrid photonic crystal laser through controlled nonlinear absorptive heating in the reflector." Light: Science & Applications 7.1 (2018): 39.

[23] Herr, Tobias, Michael L. Gorodetsky, and Tobias J. Kippenberg. "Dissipative Kerr solitons in optical microresonators." Nonlinear optical cavity dynamics: from microresonators to fiber lasers (2016): 129-162.

[24] Wildi, Thibault, et al. "Dissipative Kerr solitons in integrated Fabry–Perot microresonators." Optica 10.6 (2023): 650-656.

[25] Xie, Shengjie, et al. "On-chip Fabry–Pérot Bragg grating cavity enhanced four-wave mixing." ACS Photonics 7.4 (2020): 1009-1015.

[26] Klaver, Yvan, et al. "Self-mode-locking in a high-power hybrid silicon nitride integrated laser." Optics letters 47.1 (2021): 198-201.

[27] Grelu, Philippe, and Nail Akhmediev. "Dissipative solitons for mode-locked lasers." Nature photonics 6.2 (2012): 84-92.

[28] Shen, Boqiang, et al. "Integrated turnkey soliton microcombs." Nature 582.7812 (2020): 365-369.

[29] Bogaerts, Wim, et al. "Silicon microring resonators." Laser & photonics reviews 6.1 (2012): 47-73.

[30] Zhang, Yang, Sylvain Veilleux, and Mario Dagenais. "Fabry-Perot Bragg grating nanoresonator with ultrahigh intrinsic Q based on low-loss silicon nitride." Optics Express 31.21 (2023): 34688-34696.

[31] Monopoli, Davide, et al. "Fabry-Pérot cavity in SiN for non-linear applications." British and Irish Conference on Optics and Photonics. Optica Publishing Group, 2024.

[32] Comis, Farah, et al. "Experimental analysis and modeling of the penetration depth of uniform and apodized integrated Bragg reflectors." Optics Express 32.26 (2024): 47447-47457.

[33] https://www.ligentec.com/

[34] Xu, Yong, et al. "Scattering-theory analysis of waveguide-resonator coupling." Physical Review E 62.5 (2000): 7389.

[35]Ulanov, Alexander E., et al. "Laser diode self-injection locking to an integrated high-Q Fabry–Perot microresonator." Optics Letters 49.21 (2024): 6261-6264.

[36] Duling, I. N., et al. "Operation of a nonlinear loop mirror in a laser cavity." IEEE journal of quantum electronics 30.1 (1994): 194-199.

[37] Zhou, Xuefang, et al. "Multi-wavelength SOA fiber laser with ultra-narrow wavelength spacing based on NPR effect." IEEE Photonics Journal 12.5 (2020): 1-8.

[38] Doran, N. J., and David Wood. "Nonlinear-optical loop mirror." Optics letters 13.1 (1988): 56-58.

[39] Sulaiman, Abdul Hadi, et al. "Nonlinearity effect on multiwavelength fiber laser based on Sagnac loop mirror interferometer." Jurnal OptoElektronik (2021).

[40] Aliza, Hanun Enani Muhamad, et al. "Flatness Investigation of Multiwavelength SOA Random Fiber Laser Based on Sagnac Loop Mirror." 2023 9th International Conference on Computer and Communication Engineering (ICCCE). IEEE, 2023.

[41] Slepneva, Svetlana, et al. "Dynamics of a short cavity swept source OCT laser." Optics express 22.15 (2014): 18177-18185.

[42] Yacomotti, Alejandro M., et al. "Dynamics of multimode semiconductor lasers." Physical Review A—Atomic, Molecular, and Optical Physics 69.5 (2004): 053816.

Chapter 5: Butt-coupled HECL integration: from two chips to single chip

Chapter 5 examines the evolution of hybrid external-cavity lasers based on side-coupled Fabry–Perot resonators, progressing from the hybrid fiber–chip architecture detailed in Chapter 4 to a fully integrated HECL platform incorporating both the gain element and the cavity feedback on-chip. The SiN resonant mirrors are butt-coupled to a reflective semiconductor optical amplifier (RSOA), drastically reducing the external-cavity length from meters to the millimeter scale and mitigating polarization instability and mechanical fluctuations associated to fiber-based configurations. Two configurations are explored: a two-chip hybrid HECL, where the SiN PIC is butt-coupled to an external RSOA gain chip, with air-gap in between, via optical alignment between two stages, and a heterogeneous laser based on micro-transfer printing (μ-TP) integration of RSOAs onto SiN.

The first butt-coupled approach between two distinct chips delivers proof-of-concept for a single-mode lasing governed by the SC-FP cavity design, achieving sub-100kHz linewidths and very high side-mode suppression ratio (SMSR) exceeding 50 dB, but requires high-precision alignment, thermal stabilization, and accurate wavelength tuning to ensure laser frequency stability. Building on these results, μ-TP-based butt-coupled HECL enables scalable, wafer-scale co-integration of RSOAs directly onto same silicon substrate of the SiN resonant-mirror PICs, preserving good laser stability, high SMSR (above 40 dB), and narrowing the laser linewidth to around 47 kHz.

5.1 HECL dynamics

This section details the conditions enabling laser emission in the hybrid external-cavity laser model defined in Section 2.5.2, describing all the constituent structures. In this HECL architecture the gain section comprises an RSOA with HR and AR facets butt-coupled to the passive waveguide of the SiN PIC, that is a side-coupled Fabry–Pérot resonator incorporating Bragg grating mirrors acting as wavelength-selective reflector. The hybrid laser emission dynamics arise from the interplay between the spectrally rippled gain of the RSOA (whose peak-to-peak gain ripple assesses to around 3 dB), originating from the internal Fabry–Pérot cavity enclosed by the two facets, the discrete set of ECL modes supported by the external-cavity extending from the HR facet to the effective SC-FP reflection peaks delivered, which ultimately select the lasing wavelength (Fig. 5.1).

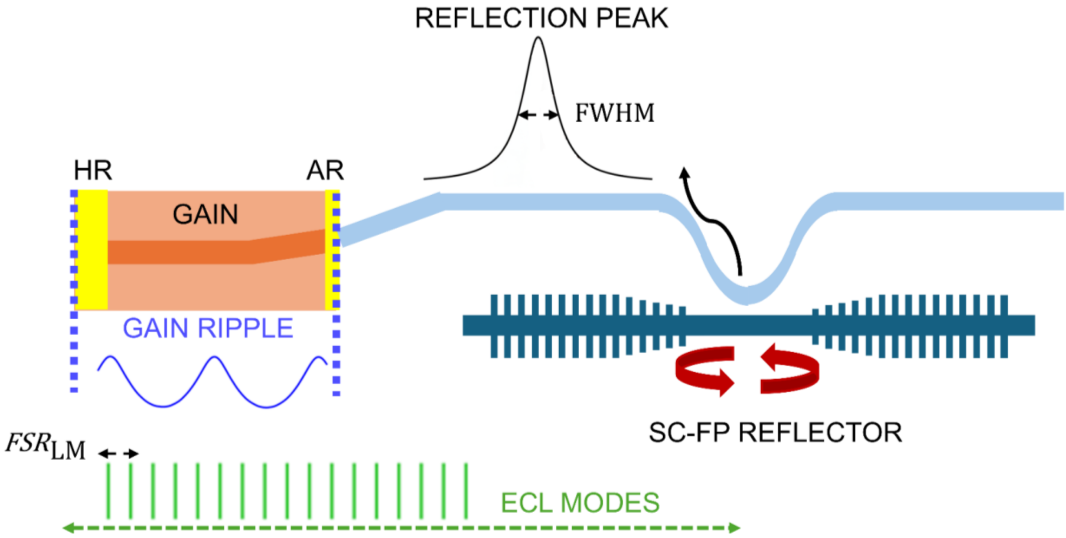

Fig. 5.1: Schematic of the proposed three-mirror external-cavity laser. Butt-coupling between RSOA gain element and the resonant reflector based on SC-FP. Illustrations of the reflection peak provided from the SC-FP, gain ripple amplification due to the RSOA and supported ECL modes of the laser architecture.

Single-mode lasing is obtained when one reflection peak of the side-coupled Fabry–Pérot resonator overlaps with a maximum of the RSOA gain ripple at a specific longitudinal-mode frequency, so that the product of gain and feedback for that mode most strongly exceeds the total losses compared to all competing modes. This condition is favored when the external-cavity free spectral range FSR_{LM} is larger than or comparable to the FWHM f the reflector resonance, $FSR_{\text{LM}} \gtrsim$ FWHM, ensuring that at most one longitudinal mode lies within a given reflection peak. This regime requires very sharp, high-Q resonances (Q of order 10^5–10^6) and/or a short external-cavity length on the centimeter scale, as illustrated in Fig. 5.2(a).

If several longitudinal modes fall within the same reflection peak, they may lase simultaneously or undergo mode hopping, resulting in unstable emission. In experiments, lasing behaviors such as those illustrated in Fig. 5.2(b) and Fig. 5.2(c), are therefore frequently encountered, and achieving stable single-mode operation requires careful engineering of the cavity design together with appropriate alignment and tuning procedures.

Additionally, the influence of control parameters, such as injection current in the RSOA, temperature variation and nonlinear effects on each constituent element of the external-cavity, and their impact on the resulting dynamics, is analyzed in detail in the following section.

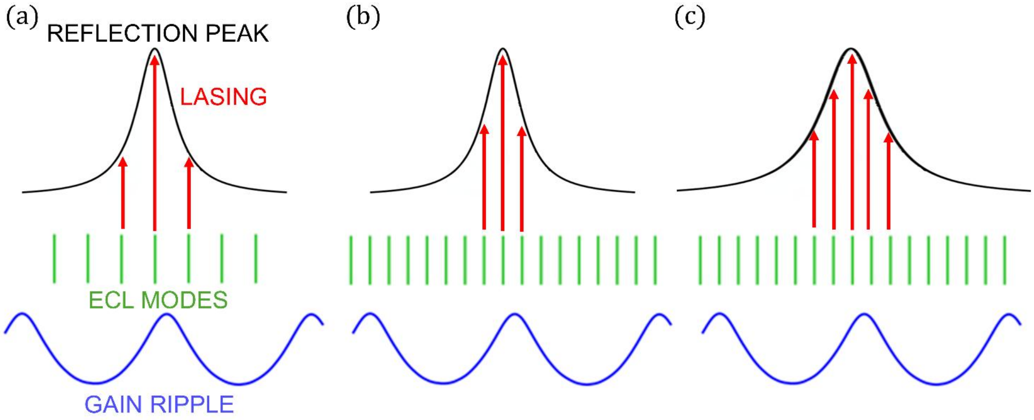

Fig. 5.2: (a) Ideal condition for stable single-wavelength laser (SWL) emission. (b) Mode hopping between longitudinal ECL modes within a single SC-FP reflection peak, arising when the ECL free spectral range FSR_{LM} is shorter than the reflection peak FWHM, as occurs with a longer external-cavity length compared to case (a). (c) With fixed $\mathrm{FSR}_{\mathrm{LM}}$, a broader reflection peak dramatically increases the mode-hopping tendency by accommodating multiple ECL modes.

5.1.1 Thermal and carrier-induced effects in the RSOA

The RSOA, that constitutes the active section of the hybrid laser, is characterized by spectral and phase characteristics that are strongly dependent on both injection current and temperature, which together determine the carrier density and thermal state of the gain medium.

5.1.1.1 Influence of injection current at fixed sink temperature

When the injection current is varied and the heat-sink temperature remains nominally constant, two concurrent phenomena occur in the III–V active medium: carrier-induced effects and self-heating.

At low to moderate injection levels, carrier-induced mechanisms dominate: increasing the current raises the carrier density above the transparency density (N_{tr}), establishing population inversion that directly enhances the material gain $g_m(N) \propto (N - N_{tr})$ through stimulated emission dominance, slightly broadens the gain spectrum due to band filling and state filling across the density of states, and blue-shifts the gain envelope. These variations modify the refractive index and, consequently, the effective index of the guided mode and optical path length of the RSOA. The resulting phase shift manifests as a small displacement of the gain ripple pattern.

At higher currents, thermal effects become increasingly dominant as resistive heating within the junction elevates the local temperature above that of the heat sink. The refractive index then increases via the positive thermo-optic coefficient, while the material gain decreases due to carrier redistribution and a higher transparency carrier density. This produces an overall red shift of the

ASE gain spectrum. Consequently, as the current increases, the RSOA transitions from carrier-dominated (blueshift) to thermally dominated (redshift) behavior, ultimately leading to gain saturation.

5.1.1.2 Influence of temperature at fixed injection current

When the RSOA current is held constant and its temperature is varied through a thermoelectric cooler (TEC) stage, the underlying mechanisms are primarily thermal-related. An increase in temperature raises the real refractive index of the III–V material, proportionally increasing the effective index of the guided mode and the optical phase accumulated per round trip; consequently, both the ASE spectrum and the overlapped ripple pattern shift toward longer wavelengths. In parallel, elevated temperature increases the transparency carrier density, requiring more carriers to achieve population inversion and consequently reducing the peak gain. Instead, the enhanced carrier scattering and thermal redistribution broadens the spectrum.

5.1.2: Temperature and power-induced effects in the PIC

The SC-FP resonator reflector's behavior is strongly influenced by both temperature and intracavity optical power. It supports discrete high-Q resonant modes determined by the cavity geometry and effective index profile; increasing the temperature within the resonator induces thermo-optic effects in the core material (SiN in this work), raising the refractive index and causing a red-shift of the resonance wavelengths. The surrounding passive waveguides (SU-8, SiN waveguides and converters) along the optical path contribute in additional phase shifts according to their thermo-optic coefficients, negative for SU-8 (blue-shifting under heating) and positive for SiN (inducing smaller red-shifts), resulting in combined temperature-dependent tuning of both the SC-FP resonance position and the overall optical phase between the resonator and RSOA, thereby modifying the longitudinal mode condition.

Additionally, a portion of the circulating intracavity power couples into the high-Q SC-FP resonator mode. Due to the resonator's small mode volume and high-quality factor, this creates localized optical intensities orders of magnitude higher than in the access waveguides. Absorption within the SiN cavity, due to intrinsic losses, defect states, or nonlinear absorption phenomena (such as TPA, FCA, etc.), produces localized heating that further increases the refractive index, red shifting the resonance wavelength and establishing a feedback loop between optical power, absorption, and resonance position. Consequently, the SC-FP reflector functions as a power-dependent tunable mirror, with its effective reflectivity varying according to both the thermal environment and intracavity intensity.

5.1.3: Coupled dynamics in HECL

In the external-cavity configuration, the lasing condition is determined by the interplay of three key elements: the RSOA gain spectrum and phase (controlled by injection current and temperature), the SC-FP resonance spectrum and its power-dependent thermal shift, and the global cavity phase and length (set by the RSOA and passive waveguides), which together define the longitudinal modes. Perturbations in current or temperature can thus induce mode hopping, either between longitudinal modes of the HECL within a single reflection peak (as summarized in Section 5.1) or between distinct SC-FP resonances spaced by their FSR. The latter arises when the broad RSOA gain envelope overlaps multiple SC-FP resonances, prompting the laser to switch to the mode offering the lowest threshold whenever the gain–resonance overlap for one becomes unfavorable; such resonance hopping is driven by the concurrent spectral shifts of both the RSOA (due to current or temperature) and the SC-FP (due to thermal and power-induced effects).

A more complex scenario arises from the combined thermal interaction between the subsystems. Increasing the RSOA current raises the intracavity power, enhancing SC-FP cavity heating and red-shifting the reflector resonance, while simultaneously modifying the RSOA index and gain spectrum through self-heating. External heating, via chip temperature or integrated heaters, further shifts both SC-FP resonances and passive waveguide phases. As a result, the variations in laser wavelength and output power with respect to current or heater power arise from the nonlinear interaction between the RSOA and the SC-FP subsystems. Moreover, nonlinear effects within the high-Q SC-FP cavity (such as Kerr-based nonlinearities, thermo-optic bistability) can further modulate the laser dynamics and introduce additional instabilities.

5.2 Two-chip butt-coupled HECL architecture

The hybrid external-cavity laser comprises a commercial angled-facet RSOA chip, that is an active III/V diode bar with one HR facet and an AR-coated input/output facet, butt-coupled to a 300 nm-thick SiN PIC incorporating SC-FP reflectors. The gain and PIC chips are mounted on two separate 5-axis stages and optically coupled in free-space as referred in Section 1.3.1.2 as two-chip butt-coupled hybrid integration scheme. The laser output is collected via a lensed fiber, while fine-tuning on the alignment at both stages can be achieved using piezo controllers. Both the RSOA and the PIC are temperature-controlled by independent TEC controllers, which can either maintain the same setpoint or apply a relative temperature offset to stabilize the wavelength or tune the RSOA gain peak.

The hybrid laser optical setup and schematic are depicted in Figure 5.3(a) and Fig. 5.3(b), respectively. Figure 5.3(b) highlights the angled input waveguide of the SC-FP, which is designed to match the angled facet of the RSOA ridge waveguide. Furthermore, the SiN waveguide at the gain section interface is widened to approximately 2.3 µm before being tapered down to a single-mode width of 1.3 µm (in air cladding) to optimize mode matching between the RSOA ridge and the SiN waveguide. The mounted commercial RSOAs used in this work include a short-cavity device of 250 µm (from CST-Global) and a longer 2.5 mm device (from SemiNex) offering higher peak gain, enabling the exploration of different device features and corresponding laser characteristics.

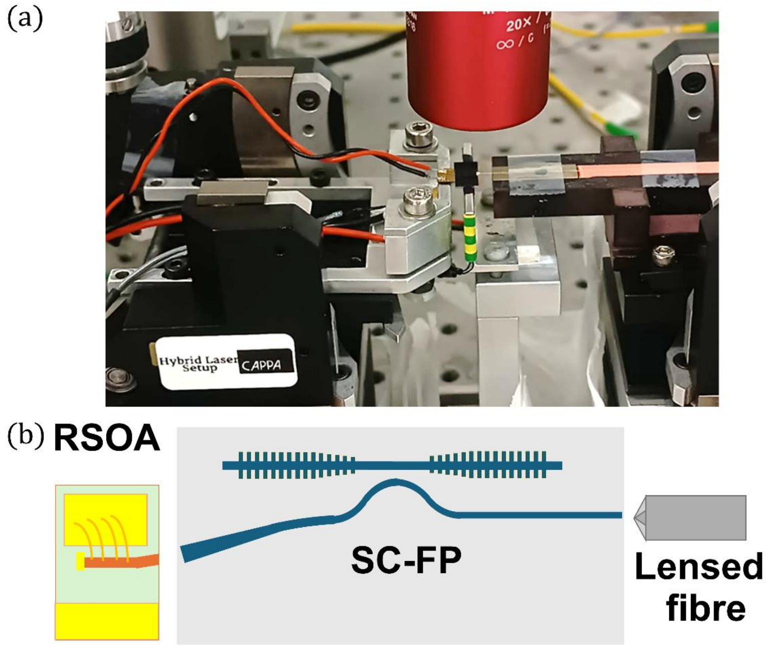

Figure 5.3: (a) Experimental setup of the hybrid external-cavity laser, showing the butt-coupling between the RSOA gain chip and the SC-FP chip, with output collected by a lensed fiber. (b) Schematic representation of the HECL, where mode-matching between the RSOA and SC-FPs is enhanced through angled and wider SiN waveguides in the coupler at the interface.

Light emitted from the anti-reflection-coated facet of the RSOA is coupled into the SiN PIC, where the integrated SC-FP cavity (whose architecture has been reported in Section 3.2), formed by DBRs, acts as a wavelength-selective resonant mirror. The cavity design provides high reflectivity at resonance while maintaining sufficient transmission to ensure strong spectral filtering and controlled optical feedback. In each cavity loop, light is amplified by the RSOA, resonantly reflected by SC-FP modes, recirculated to sustain lasing, and partially transmitted for output collection through the lensed fiber. The zoomed view of the HECL setup is highlighted in Figure 5.4(a), while Fig. 5.4(b) illustrates a zoom in the input coupling between the RSOA and the SiN, observed at a NIR camera. When the RSOA current exceeds the lasing threshold, one or more peaks appear at the resonant wavelengths of the SC-FP cavity. The two-chip butt-coupled system forms a compact external-cavity spanning just a few millimeters, avoiding fiber-induced polarization instability and mechanical fluctuations.

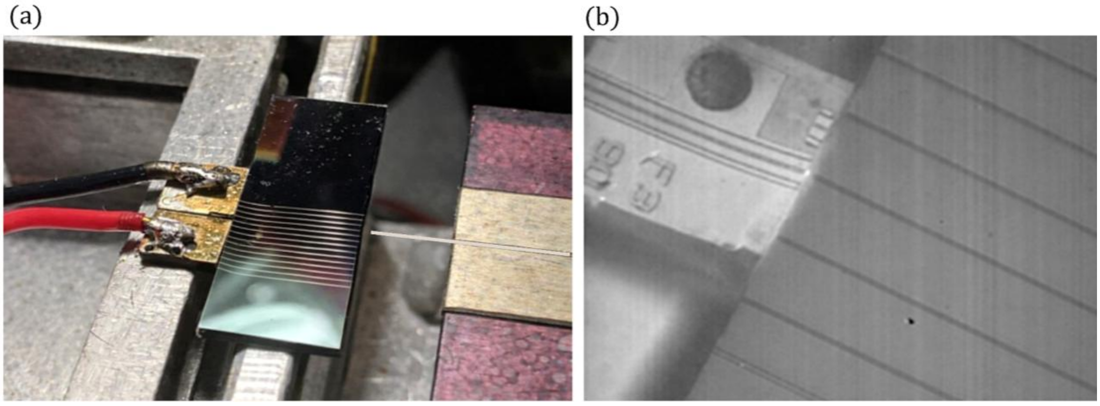

Figure 5.4: (a) Two-chip butt-coupling HECL setup. (b) NIR camera zoom view of the input alignment between angled RSOA and SiN waveguide.

The SC-FP's free spectral range and mode selection are tailored through DBR parameters to enable single-mode or multi-mode operation across the C-band gain profile; electrical pumping of the RSOA via wire bonds drives the process, with the low-loss SiN platform providing stable feedback that yields to narrow-linewidth emission.

5.2.1 PIC fabrication

The PIC is realized through in-house fabrication at Tyndall National Laboratory by Dr. Artem S. Vorobev and Dr. Nicola Maraviglia, using EBL process and dry-etching technique. A LioniX 300-nm-thick SiN core is deposited via PECVD on 2.2 μm-thick thermally grown SiO_2 bottom cladding over a 525 μm-thick bulk silicon substrate.

Compared to the EBL steps detailed in Section 3.2, the fabrication process reported in Fig. 5.5 considers a 400 nm thick layer of positive-tone CSAR 62 (Chemical Semi-Amplified Resist) electron-beam resist, that is spin-coated onto the surface and soft-baked at 180 °C to stabilize the film (Fig. 5.5 (d)), and exposed using a high-voltage electron-beam writer to define the SC-FP patterns. After CSAR development (with ZED-N50 solution for 90 seconds) the patterns were transferred into the 300 nm SiN layer via dry etching. The polymer-based CSAR was then fully stripped using O_2 plasma and immersion in 1165 remover (Fig. 5.5(h)), yielding a clean SiN surface.

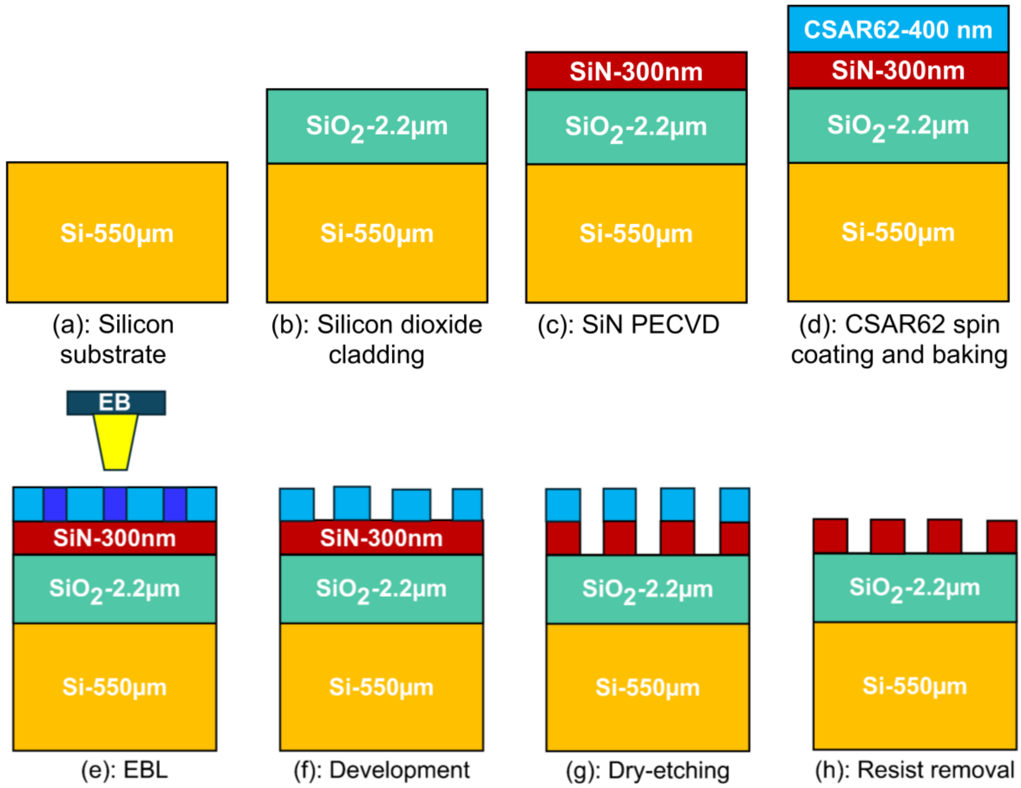

Figure 5.5: Description of the PIC-fabrication flow for 300 nm thick SiN on 2.2 µm SiO2 platform.

5.2.2 Passive resonators design

The schematic of the designed side-coupled Fabry–Pérot cavity with the key design parameters is depicted in Fig. 5.6(a). It incorporates Bragg grating reflectors with rectangular corrugation profiles featuring corrugation widths of W_1=1.3 µm and W_2=2.5 µm, combining apodized sections (N_T=250 periods), and uniform sections (N=1750 periods), while side-coupling injection follows the same design defined in Chapter 3.

Figure 5.6(b) shows the SEM images assessing feature fidelity and sidewall quality, with particular focus on the DBR corrugations, tapered grating section, and upper portion of the bent coupler waveguide in the fabricated device. The DBRs and SC-FPs were characterized using the passive optical setup described in Section 3.4. The experimental stopbands of the on-chip DBRs span approximately 10 nm across the C-band, as shown in Fig. 5.7 for periodicities of Λ = 490 nm and Λ = 494 nm, using fully uniform sections with N = 1000 periods and rectangular corrugation widths matching those in the resonators.

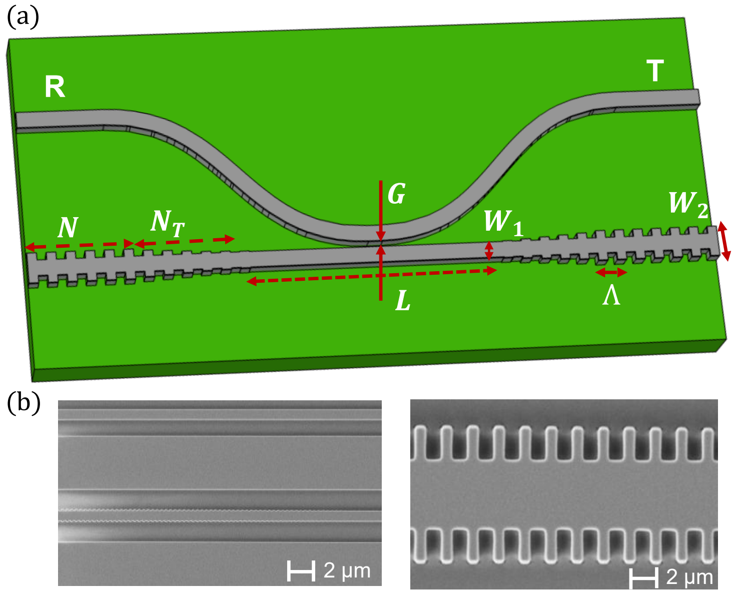

Figure 5.6: (a) Schematic of the side-coupled Fabry–Pérot resonator, showing the main design parameters and the reflection (R) and transmission (T) ports where peaks and dips appear, respectively. (b) SEM images of the fabricated device at ~2 µm resolution, highlighting patterns precision.

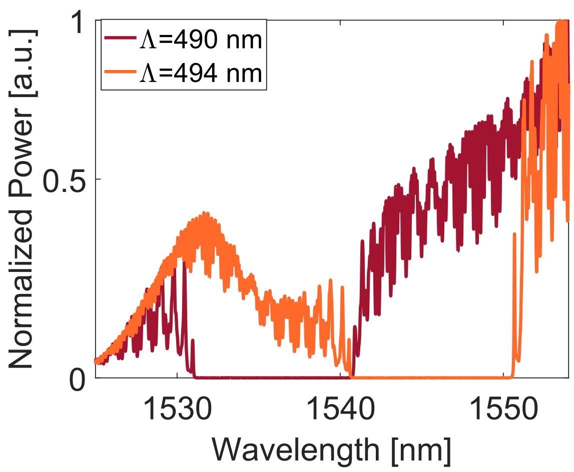

Figure 5.7: Measured DBR stopband for λ=490 nm (red), and λ=494 nm (orange), both characterized in transmission.

In this study, the primary design parameters investigated are the cavity lengths (L) and the coupling gaps (G), varied to evaluate their impact on the resonator performance. Figure 5.8(a) and 5.8(b) presents the resonant transmission dips (with extinction ratios) for the shorter (L=120 µm) and longer (L=900 µm) cavities at both G=500 nm and G=600 nm. These parameters are selected as trade-off between sharper resonances for enhanced spectral selectivity and side-mode suppression and need for higher reflectivity peaks essential for effective optical feedback in the hybrid laser.

Apodized (or tapered) DBRs combined with longer cavities and optimized gaps yield maximum loaded Q-factors of approximately 8×10^4 and 1×10^5, when if fixed *L*=900 µm and are considered *G*=500 nm and *G*=600 nm, respectively. Moreover, Fig. 5.8 (c) and 5.8(d) report the SC-FP free spectral range response as function of wavelength for *L*=120 µm and *L*=900 µm, respectively.

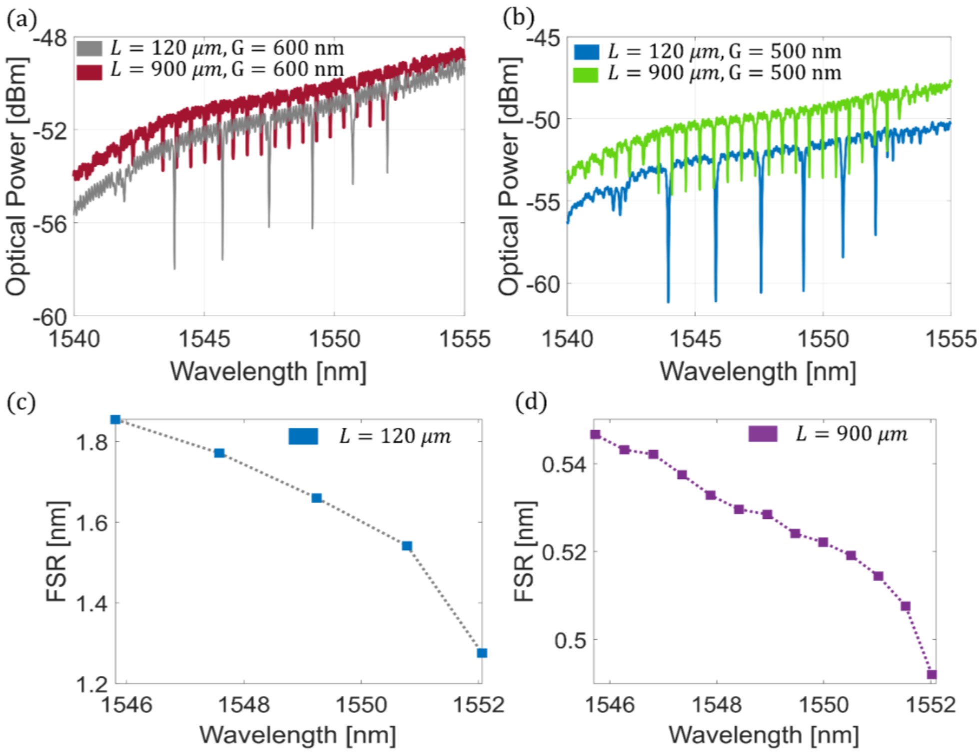

Figure 5.8: Measured transmission spectra of SC-FP resonators for coupling gaps G=600 nm (a) and G=500 nm (b), comparing short (L=120 µm) and long (L=900 µm) cavities. The FSR response for the two cavities is defined in (c) and (d) at 1545.8-1552 nm range. All the resonators feature a fixed periodicity of 494 nm.

5.2.3 Short cavity RSOA: HECL performance

The gain chip consists of a commercially available RSOA gain chip from CST-Global mounted on an AlN ceramic tile and glued to an aluminum sub-mount holder. The RSOA is wire-bonded via gold pads to both the current and temperature controllers, and both the RSOA and SiN chips are actively temperature-stabilized using TEC controllers during the experiments. The RSOA is a 250 µm-long aluminum indium gallium arsenide (AlInGaAs) ridge waveguide amplifier, featuring a back facet coated with a HR film (R > 90%) and a front facet with an AR coating to suppress back-reflections within the amplification loop. Gain is provided by quaternary AlInGaAs QWs, where the incorporation of aluminum ions deepens the potential well and reduces carrier leakage at elevated temperatures.

Moreover, this enhances high-temperature performance and enables a compact 250 µm device length, significantly shorter than alternative designs, allowing cost-efficient use of III–V materials. The intrinsic gain chip amplification has been experimentally determined as a function of driving current by edge-coupling alignment of the RSOA to a lensed output fiber as shown in the setup picture in Fig. 5.9(a). For this characterization, alignment was optimized to maximize the collected power measured at the power meter, under a fixed ambient temperature of T=25 °C for the RSOA. Figure 5.9(b) shows a 3D colormap of the RSOA amplified spontaneous emission, with wavelength on the vertical axis, drive current on the horizontal axis, and measured optical power encoded in the color scale, specifically for drive currents swept from 0 mA to 100 mA in 10 mA steps. From this emission map, it is possible to identify the wavelength range over which the RSOA provides optical gain. For simplicity, in this thesis the 3D plot will be used as a proxy for the RSOA gain response. Specifically, the RSOA gain peak results located at approximately 1535 nm, with a bandwidth of approximately 50 nm. The device exhibits a saturation current near 70 mA, and the maximum gain occurs around 65 mA.

(a)

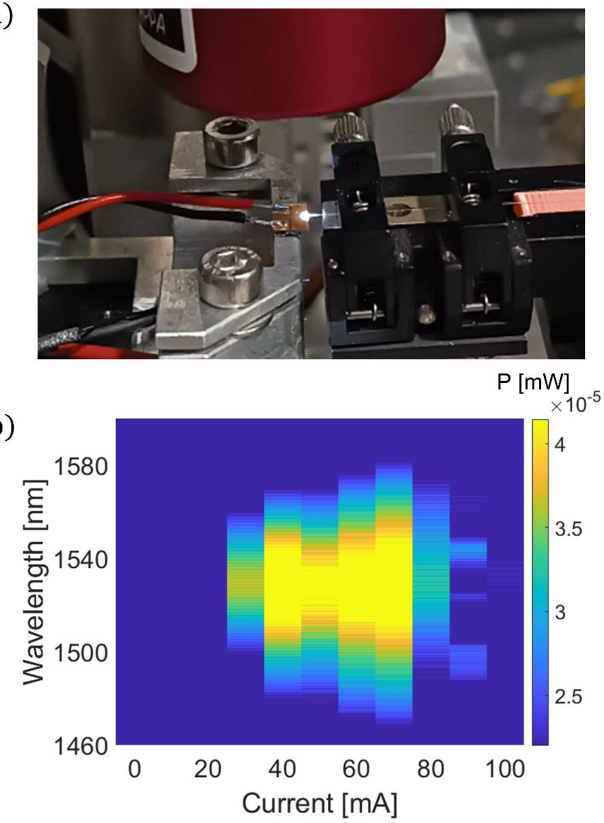

(b)

Figure 5.9: (a) Illustration of the alignment between RSOA gain and lensed fiber at the optical setup. (b) RSOA amplified spontaneous emission (power indicated in mW) as a function of the driving current (0-100 mA), and wavelength. The colorbar indicates the minimum and maximum measured power, ranging from 21 µW to 42 µW.

The maximum power collected at the lensed fiber results around 40 μW, this low power coupling is due to the RSOA reduced amplification capability and the lack of mode-matching between the gain ridge waveguide and the output fiber.

The lasing experiments were carried out by mounting the RSOA chip and the SiN passive PIC on two precision five-axis alignment stages, and edge-coupling the angled ridge waveguide of the laser to the angled input of the SC-FP couplers, as shown in Fig. 5.10(a). Optimum coupling was achieved by maximizing the lasing power above threshold while monitoring the average output power on a power meter. The laser emission from each passive resonator was collected with a lensed fiber mounted on a third alignment stage and by means of an optical splitter 90% of the power was measured at the OSA and 10% at the power meter.

Once proper alignment between the stages in Fig. 5.3(a) is achieved both in input and output section of the SiN, laser emission can occur in the hybrid EC. Specifically, the input alignment between the PIC and the RSOA enable the strength of the feedback from the RSOA resonant peaks, while the output alignment fix the laser power level and extinction. Lasing emission is further confirmed by the NIR camera image in Fig. 5.10, which shows clear light scattering within the Fabry–Pérot resonant cavity.

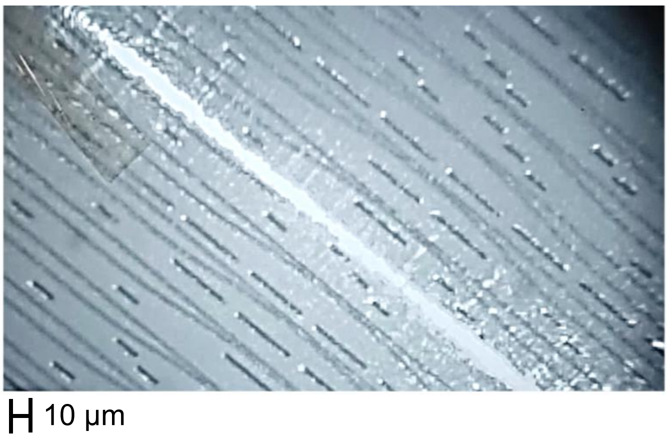

Figure 5.10: NIR camera view of scattered light visible along the FP cavity when lasing occurs.

Before analyzing the laser dynamics and features, a preliminary analysis of the contributions arising from parasitic reflections at the various interfaces along the optical path of the external-cavity laser has been presented. These residual reflections give rise to low-finesse Fabry–Pérot-like cavities. Figure 5.11 shows the schematic of the implemented HECL, highlighting these interfaces.

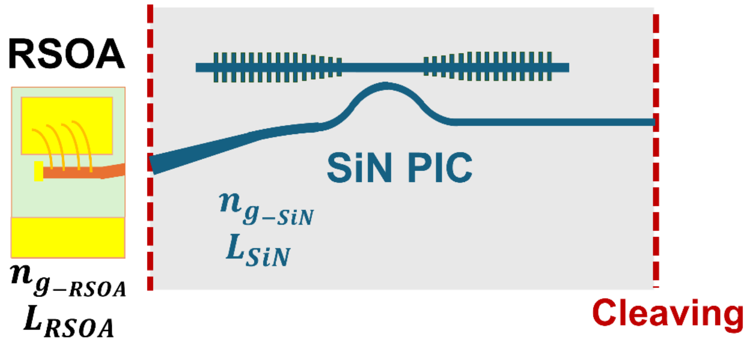

Figure 5.11: Schematic of HECL architecture showing RSOA section, SiN PIC, and PIC cleaving lines. Less than 6 μm air-gap section exists between RSOA and PIC in the free-space edge-coupling alignment.

The RSOA facets form the first "FP-like cavity", which produces fringes whose spacing (FSR_{RSOA} expressed in nanometers) is estimated as follows:

$$FSR_{\mathrm{RSOA}} = \lambda^2/(2 \cdot n_{g-RSOA} \cdot L_{RSOA}) \tag{5.1}$$

where $L_{\mathrm{RSOA}} = 250\ \mu m$ is the RSOA length and the group index $n_{g,\mathrm{RSOA}} \approx 3.448$ is estimated at the operating wavelength at the center of the grating stopband (λ=1545 nm). The RSOA mirrors produce fringes spaced around 1.3 nm apart.

This Fabry–Pérot interference appears as a gain-ripple envelope in the measured spectra. Figure 5.12(a)) shows this response outside the DBR stopband to isolate the pure gain contribution. The RSOA gain chip is positioned at an air-gap (distance (L_{AIR}) of approximately 1–3 μm from the SiN PIC, according to the specific alignment established during butt-coupling. Because this distance is small relative to the gain chip length, the air-gap (n_{g-AIR}=1) butt induces only a negligible variation in the FSR of the parasitic Fabry–Pérot cavity formed at the angled SiN waveguide interface. Consequently, the corresponding value obtained as $FSR_{\mathrm{RSOA-SiN}} = \lambda^2/(2 \cdot n_{g-RSOA} \cdot L_{RSOA} + n_{g-AIR} \cdot L_{AIR})$, is effectively identical to that of the isolated RSOA gain chip described in Eq. (5.1).

A second set of fringes arises from the SiN chip facets after the cleaving process. This contribution is also visible just during the passive characterization of the resonator at the end-fire setup. Indeed, during the characterization of the passive SC-FP dips in transmission, the spectrum in Fig. 5.12(b) reports fringes spaced FSR_{SiN} ≈100 pm. From this value, it is possible to retrieve indirectly the total length of the PIC after cleaving according to the expression: $FSR_{SiN}=\lambda^2/(2 \cdot n_{g-SiN} \cdot L_{CHIP})$. Evaluating the group index of the single-mode SiN waveguide using the FDE solver in Lumerical at the operating wavelength of 1545 nm yields a group index of 1.954 for a waveguide width $W = 1.3$ μm. Consequently, the total chip length is approximately L_{CHIP} ≈6.1 mm.

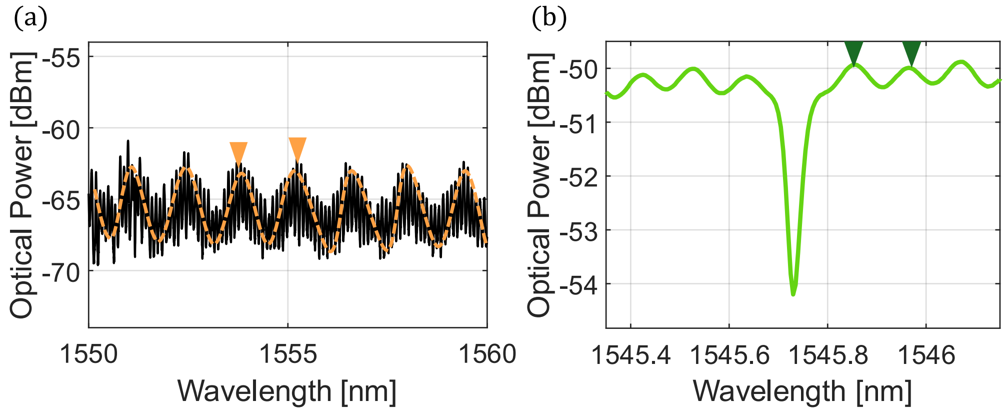

Figure 5.12: (a) Analysis of the FSR_{RSOA} RSOA gain ripples spaced around 1.3 nm. (b) Passive resonant dip supported by the SiN SC-FP: the chip facets (after cleaving) support FP fringes spaced FSR_{SiN}≈100 pm.

The longitudinal modes supported by the HECL are determined by considering the total external-cavity formed between the HR facet of the RSOA and the reflectivity peaks of the SC-FP resonators. Neglecting the term related to the free-space (air-gap) separation between the two alignment stages, that corresponds to a deviation on the order of a few micrometers (≈ 4 µm), the spacing between these modes, denoted as FSR_{LM}, is evaluated as:

$$FSR_{\mathrm{LM}} = \frac{\lambda^2}{2(n_{g\text{-RSOA}}L_{\mathrm{RSOA}} + n_{g\text{-SiN}}L_{\mathrm{SiN}}) + \frac{\lambda^2}{\pi}\frac{d^2\Phi_{\mathrm{DBR}}(\lambda)}{d\lambda^2}}. \quad (5.2)$$

This contribution encompasses the path along the RSOA gain medium (L_{RSOA}), the SiN waveguide optical path (L_{SiN}) considered from the chip cleaving facet to approximately half of the evanescent coupler (assessed to be around L_{SiN} ≈2.5 mm), and the penetration depth into the DBR gratings, with the dispersive-related term $\frac{\lambda^2}{\pi}\frac{d^2\Phi_{\mathrm{DBR}}(\lambda)}{d\lambda^2}$ as detailed in Section 2.3.2.

In absence of this last dispersion term, the average longitudinal-mode spacing is approximately 207 pm. Because the high-Q SiN resonators under study exhibit FWHM values narrower than 50 pm, fulfilling the condition FWHM< FSR_{LM}, and the gain ripples are relatively weak and widely spaced (i.e., FSR_{RSOA} =1.3 nm ≫ 50 pm), the simultaneous excitation of multiple external-cavity longitudinal modes within the same resonant reflection peak is unlikely.

Among the fabricated SC-FPs described in Section 5.2.2, the first experiments consider a resonator with grating period Λ = 494 nm, gap *G* = 500 nm, and the shortest designed cavity length *L* = 120 µm. These parameters yield approximately six resonant modes within 1544–1554 nm (Fig. 5.8(b)), aligned with the RSOA gain bandwidth.

By performing high-resolution measurements (with settings identical to the ones reported in Section 3.6), these SC-FP modes feature an average loaded Q-factor Q_L=2.4×10^4, and a coupled Q-factor Q_C=7.5×10^4 that yields an average on-resonance reflectivity R_{res}≈10%, estimated by using Eq. (2.80) detailed in Section 2.5.3.

Figure 5.13 presents a 3D color-map plot of the emitted SC-FP-based laser power as a function of the RSOA driving current ranging from 45 mA to 70 mA, and the wavelength when both SiN and gain chips are cooled to a constant temperature of T = 25 °C, via TEC controllers.

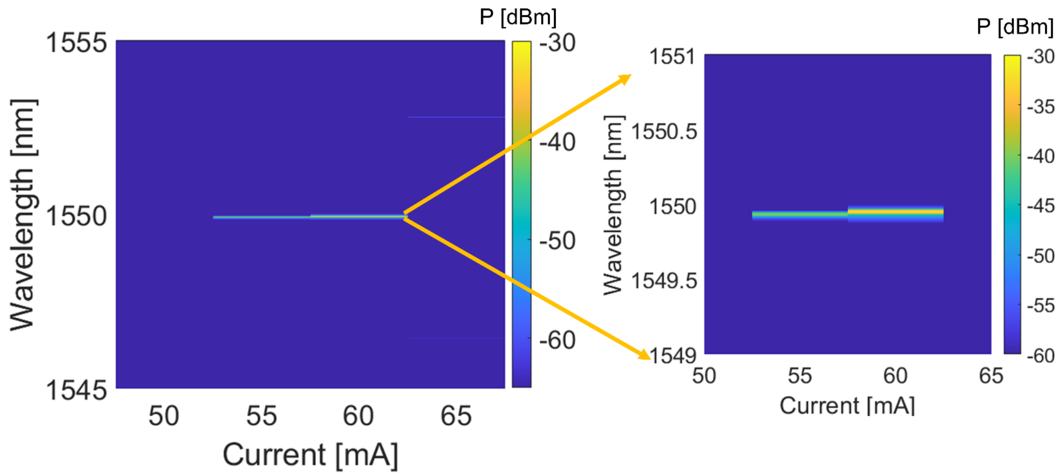

Figure 5.13: Emitted power (indicated in dBm) as a function of the applied RSOA current (from 45 mA to 70 mA) and wavelength for the SC-FP-based HECL at T = 25 °C. The zoom-in view highlights a laser threshold at I_{TH}≈52.5 mA and shows mode-hop-free operation over 10 mA current variation.

The laser shows a threshold current of I≈52.5 mA and operates in a mode hopping-free regime between 52.5 mA and 62.5 mA, with minor wavelength shifts of ~10–15 pm over this current variation. At I=60 mA, the hybrid laser operates in single-wavelength mode and achieves a SMSR greater than 40 dB at a wavelength of approximately 1549.95 nm, as shown in Fig. 5.14(a). Moreover, the use of independent TEC controllers for the RSOA and the SiN PIC enables a systematic investigation of the lasing characteristics under controlled relative temperature offsets between the two chips. In this regard, Figure 5.14(b) shows the lasing emission evolution when the SiN PIC temperature varies from T=20 °C to T=30 °C, while the RSOA temperature is fixed to T=25 °C and the current is kept constant to I=60 mA.

The lasing mode red shifts with the increasing temperature with a variation of around 12 pm/°C. This effect arises from the SiN thermo-optic effect, driven by the material's thermo-optic coefficient (TOC). The high mode confinement in the SiN core and the low TOC of the SiO_2 substrate enhance the resonator temperature sensitivity. As the temperature rises, the effective refractive index of the passive chip changes, which shifts the SC-FP reflection peaks and effectively lengthens the external-cavity, thereby modifying the lasing conditions.

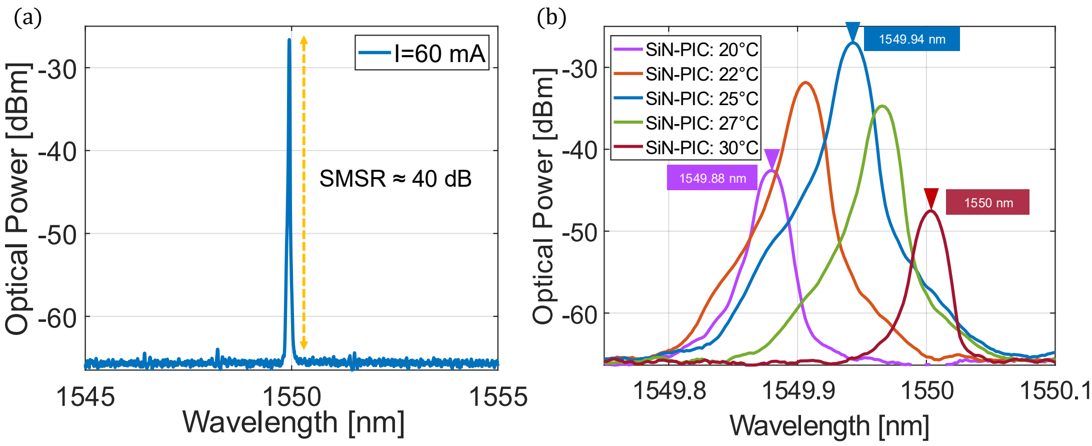

Figure 5.14: (a) Single-mode lasing at 1549.95 nm (SMSR ≈40 dB, I=60 mA). (b) Relative temperature variation analysis between RSOA (fixed to T=25°C) and the SiN sample that varies from T=20°C to T=30°C. Redshifts lasing of around 12 pm/°C, via SiN thermo-optic effect, is demonstrated.

The lasing emission has been also achieved when the wavelength-selective resonant reflector incorporates a longer cavity (L = 900 µm), while considered the same coupling gap (G=500 nm). From the passive characterization, this SC-FP configuration possesses resonant dips characterized by higher average Q-factors compared to the previous device, respectively a loaded Q-factor Q_L=7.8×10^4, and a coupled Q-factor Q_C=2×10^5, that results in an average on-resonance reflectivity R_{res}≈15%.

If the longer geometrical cavity enhances the Q-factors performance, it impacts in a reduced resonator FSR (as illustrated in Fig. 5.8(d)) featuring in more resonant peaks within the same DBR stopband and RSOA gain response. This makes resonance hopping between adjacent SC-FP modes more evident as illustrated in the 3D laser plot in Fig. 5.15(a), appearing as abrupt kinks when the lasing wavelength jumps with the current variation.

These hops result from concurrent residual thermo-optic redshifts of both the RSOA gain ripple (due to self-heating effect) and SC-FP resonances (due to intracavity absorption heating), which periodically misalign the optimal gain–resonance overlap, favoring adjacent modes with lower threshold. These observations provide an experimental demonstration of the laser dynamics discussed in Section 5.1 and constitute a direct continuation of the theoretical and numerical analysis presented in [1].

However, the independent TECs for the RSOA and PIC can reduce thermal crosstalk between gain and passive chips, improving alignment stability and partially suppressing hopping. The sharper resonances and the corresponding experimental higher on-resonance reflectivity enabled by this design, enables single-wavelength emission at 1545.5 nm characterized by a SMSR=45 dB when I=65 mA (Fig. 5.15 (b)). Laser linewidth characterization in the frequency domain will be addressed in Section 5.3, using the same SiN PIC with a higher gain RSOA (longer cavity) to assess full HECL features.

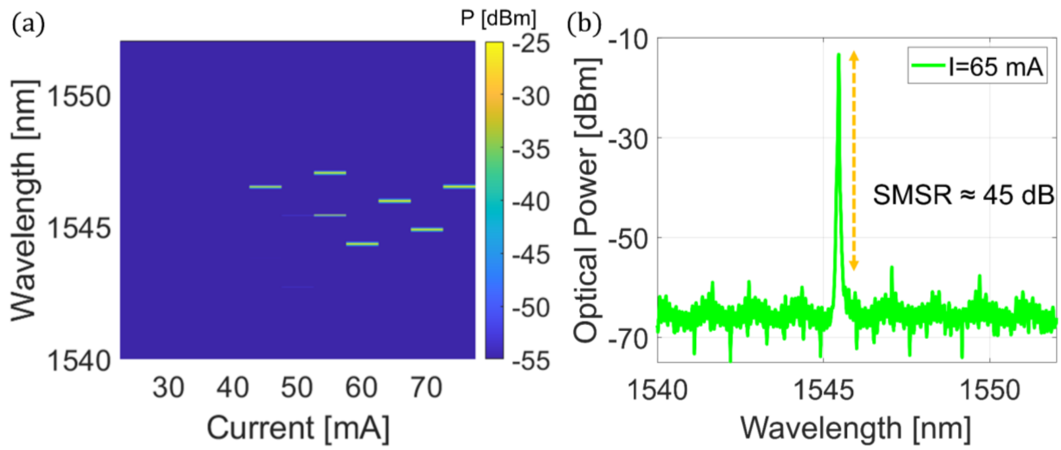

Figure 5.15: (a) Emitted HECL power (colorbar reports values spanning from -25 dBm to -55 dBm) as a function of the applied RSOA current and wavelength. The lasing map shows resonant hopping effect with the current variation. (b) Single-mode lasing emission at 1545.5 nm, exhibiting SMSR≈45 dB at *I*=65 mA.

5.2.4 Longer cavity RSOA: HECL performance

The RSOA considered in this section is high-gain chip-on-carrier (COC) device from SemiNex (model COC-179), optimized for operation in the C-band. It comprises a four-channel ridge-waveguide array with a channel spacing of 127 µm and a maximum 3-dB gain bandwidth of approximately 80 nm when each channel is driven at its maximum current. Each ridge waveguide has a length of 2.5 mm, ten times longer than RSOA used in the previous section.

The gain chip is packaged according to flip-chip laser technology (ridge waveguides are on the bottom side), consequently the mount was flipped (Fig. 5.16(a)) to expose the top view part of the ridge waveguides (Fig. 5.16 (b)).

The employed RSOA simultaneously provides four lasing outputs, with two of these spot-excited ridges shown in the NIR camera image acquired in Fig. 5.16(b). The current set to the RSOA driver is distributed among the four outputs, such that each ridge effectively receives one quarter of it. To ensure proper cooling during the experiments, the maximum current for laser emission was limited to 300–400 mA. At this low-operating current, the gain spectrum offers a high amplification over a reduced bandwidth of roughly 30 nm centered at 1540 nm for T = 20 °C and 1543 nm for T = 25 °C, exhibiting a red-shift with the increased temperature (Fig. 5.17). For all the laser experiments that will be presented in this section, both the RSOA and SiN chips were temperature-stabilized at T=20 °C.

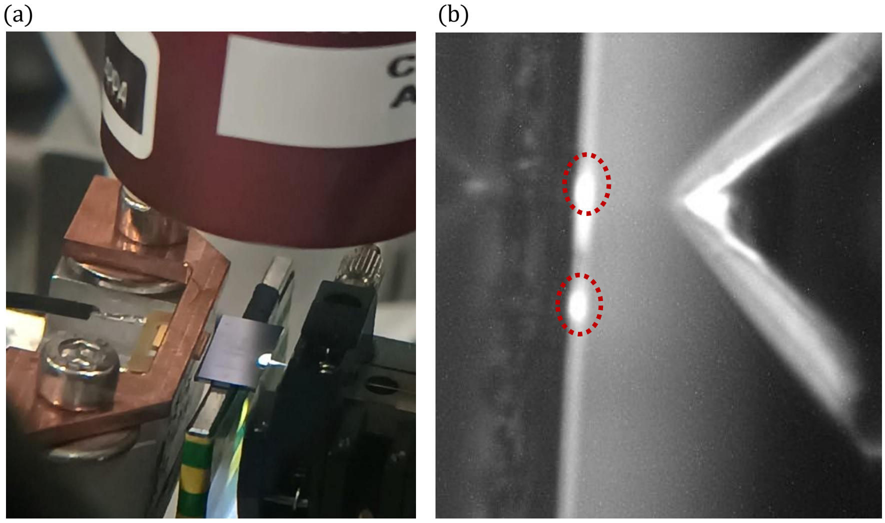

Figure 5.16: (a) Flip-chip RSOA on flip mount view. (b) SEM image of the excited spot on two RSOA ridge waveguides, and lens fiber alignment for laser gain curve characterization.

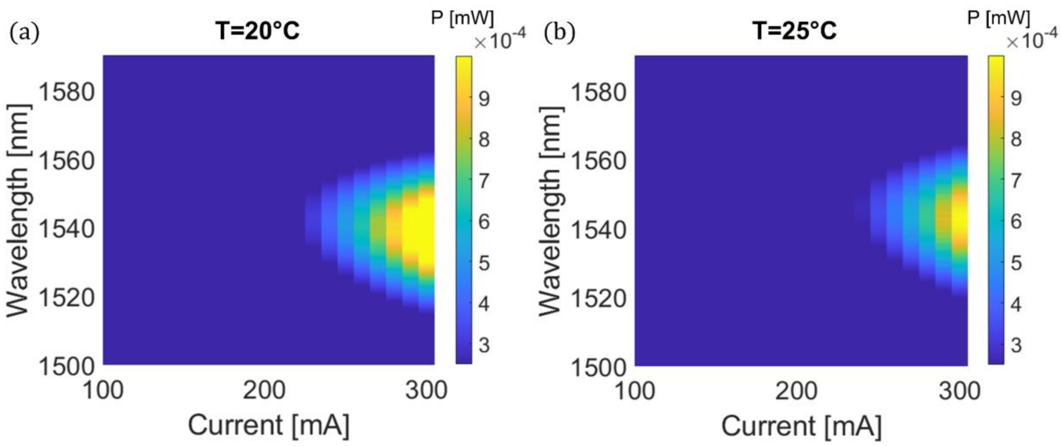

Figure 5.17: RSOA amplified spontaneous emission response: emitted power (in dBm) as a function of the RSOA injection current and wavelength range for (a) T=20°C, and (b) T=25°C. The ASE spectra report ≈30 nm bandwidth centered at 1540 nm for T=20°C, and at 1543 nm for T=25°C. In this configuration, the longer cavity RSOA ensures to collect two orders of magnitude higher power in the output compared to Fig. 5.9. The colorbar indicates the minimum and maximum measured power, ranging from 280 µW to 980 µW.

Building on the analysis carried out in previous section on the FP parasitic cavities deriving from the different interfaces in the hybrid laser cavity, it can be assessed that at λ =1545 nm, the longer RSOA cavity introduces gain modulated ripples spaced FSR_{RSOA}≈130 pm, exactly ten times narrower due to L_{RSOA} ≈ 2.5 mm used. Moreover, building on the Eq. (5.2) previously defined, neglecting the DBR-induced dispersion term and considering the same L_{SiN} and $n_{g_{-SiN}}$ values, the ECL modes are spaced approximately FSR_{LM}≈88 pm. After considering the dispersive DBR response, it will be demonstrated to be further reduced. The chip facets cleaving-related contribution matches the prior case, given that the PIC under test is identical.

By employing the same SC-FP design (L = 900 µm, G = 500 nm) as in the short-cavity RSOA-based HECL, laser emission is also demonstrated for the longer-cavity RSOA.

Fig. 5.18(a) reveals a linear laser characteristic, as expressed by the light-current (L–I) curve, when the current is varied from 180 mA to 350 mA at step of 10 mA. The threshold current is set at around $I_{\mathrm{TH}} \approx 240$ mA and a maximum total output power of around $P_{\mathrm{out}} = 0.8$ mW is achieved for a current of I=350 mA.

Figure 5.18(b) shows the 3D color-map depicting the lasing emission spectra and power as a function of the RSOA drive current, revealing superior mode stability certified by the reduced resonant-based hopping compared to the short-cavity RSOA results. Specifically, the hops are confined to two specific SC-FP resonances that are spaced by FSR ≈ 0.55 nm, e.g., 1548.9 nm and 1549.45 nm in the shown picture. A more detailed analysis on the laser emitted spectra across five distinct drive currents from 300 mA to 350 mA (at 10 mA steps), is reported in Fig. 5.18(c).

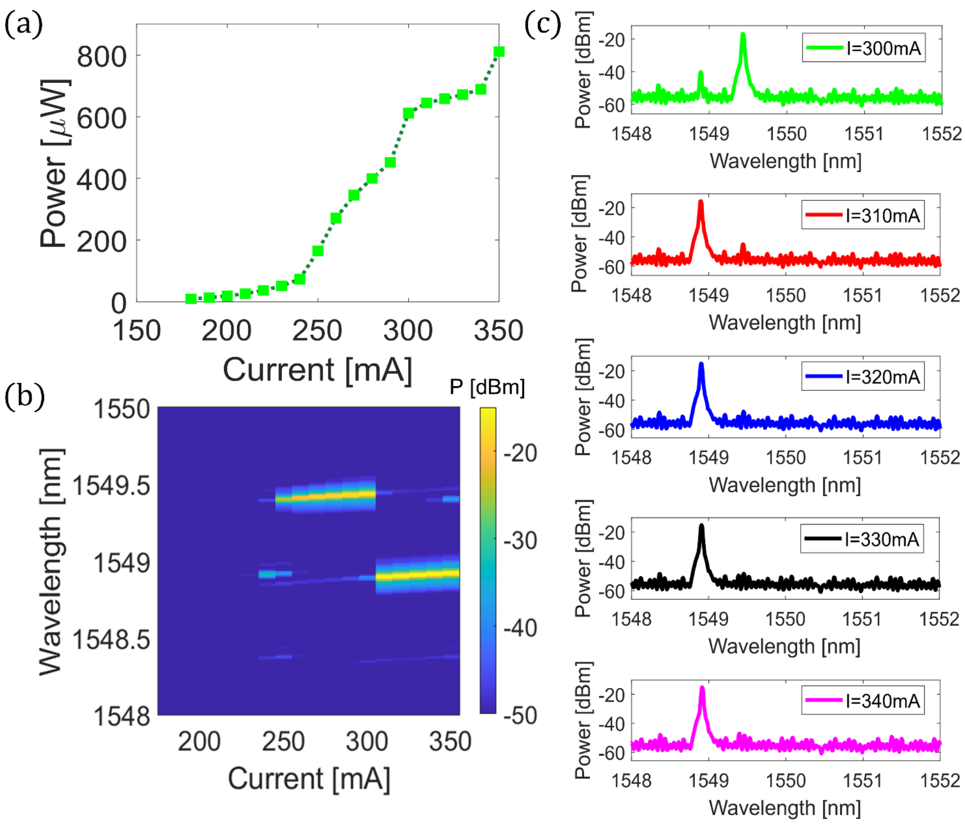

Figure 5.18: (a) Laser characteristic: threshold results around ~180 mA, while the output power reaches 0.8 mW, without reaching the saturation current. (b) Emitted laser power (colorbar shows values spanning from -15 dBm to -50 dBm) with respect to wavelength and applied RSOA current. (c) Lasing emission subplots: spectra evolution when current is varied from 300 mA to 340 mA.

Specifically, as shown in Fig. 5.18(b), the lasing peak shifts from 1549.55 nm to 1548.90 nm when the drive current is increased from I=300 mA to I=310 mA. For higher currents, between I=310 mA and I=350 mA, the emission wavelength remains stable, and the laser maintains robust single-mode operation throughout this range.

From high-resolution measurements (with settings identical to the ones reported in Section 3.6), the SC-FP resonant dips for the device under test are characterized by a FWHM in the order of 20 pm. Although the resonant reflection peaks result sharper than the ECL modes spacing, the high and narrowly spaced gain ripples can increase the impact of the other ECL-based parasitic reflections, enabling excitation of multiple longitudinal modes (multimode behavior).

In this context, Fig. 5.19 shows two lasing states achieved at the same current of I=340 mA: (i) single-mode and (ii) four modes excitation. Specifically, it can be observed that the spacing between the modes in the case (ii) experimentally proves that the effect of the grating penetration length is to reduce the longitudinal modes spacing from FSR_{LM}≈88 pm to approximately FSR_{LM}≈60 pm. However, by accurate temperature stabilization and alignment, it can be ensured precise ECL mode–gain curve–SC-FP reflection peak overlap for one single longitudinal mode for stable single-wavelength emission.

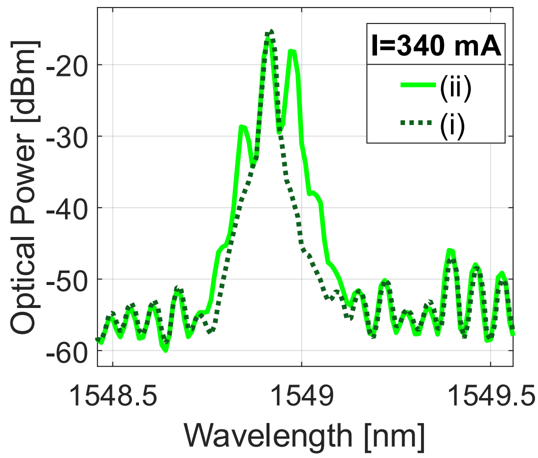

Figure 5.19: Laser stability dynamics. When driving current is set to I=340 mA, both (i) single-mode, and (ii) “multi” modes can be excited.

The linewidth of the achieved HECL is measured using the heterodyne technique, whose schematic is illustrated in Fig. 5.20. The laser line emitting at λ_0=1548.9 nm, corresponding to the condition (i) in Fig. 5.19, beats with a tunable laser source, set at a wavelength as close as possible to λ_0, through a 50/5 fiber coupler (FC). A high-bandwidth photodiode (45 GHz) detects the resulting beat signal with frequency offset Δf, and an electrical spectrum analyzer processes it by applying a FFT operation.

For the FFT measurement, the oscilloscope was configured with a time base of 4 μs/div over 10 horizontal divisions, yielding a 40 μs acquisition window. By fixing a sampling rate of 12.5 GSa/s, this resulted in 500k points record and an FFT frequency resolution of 25 kHz. Figure 5.21 (a) shows the RF harmonic resulting from the FFT operation on the time trace, that is placed at approximately 578 MHz. The zoomed-in view of the FFT component (Fig. 5.21(b)) shows a linewidth of around $\Delta\omega \approx 74$ kHz, extracted via Lorentzian fitting.

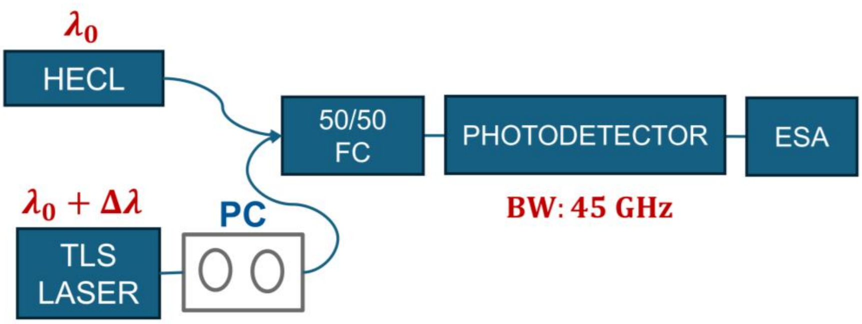

Figure 5.20: Schematic of the heterodyne laser linewidth characterization technique.

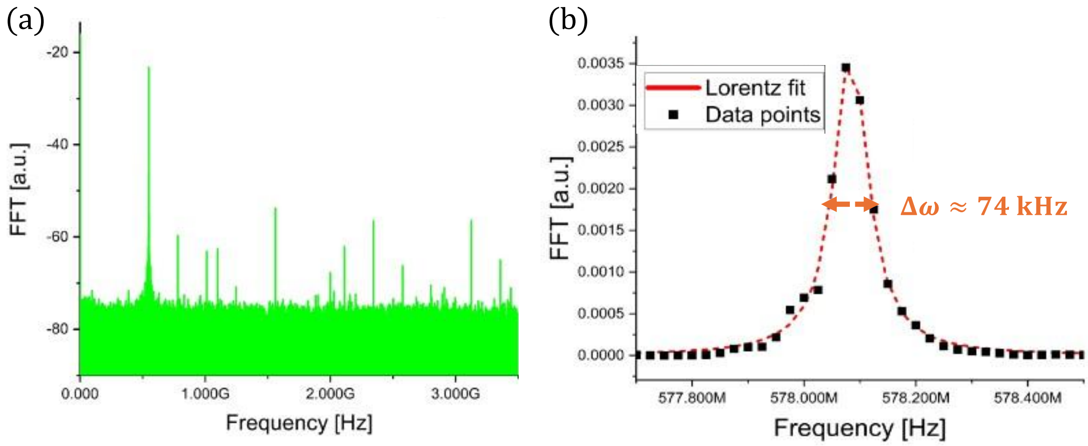

Figure 5.21: (a) FFT spectrum extracted from ESA: the beating tone is produced at ≈578.1 MHz. (b) Lorentzian fit of the FFT component and linewidth estimation (~74 kHz).

As the injection current further increases from I=340 mA to I=420 mA, enhancing the gain capability of the RSOA, the laser no longer supports emission on a single SC-FP resonance. The emission occurs clearly from two adjacent SC-FP resonances spaced ≈0.52 nm apart. However, instability in the alignment leads to multiple longitudinal modes overlapping with these resonances as reported in Fig. 5.22. This last result can be regarded as a proof of concept for future multi-wavelength operation, which could be enabled by stabilizing the alignment setup, reducing the FSR, and engineering the dispersion of the SC-FP modes.

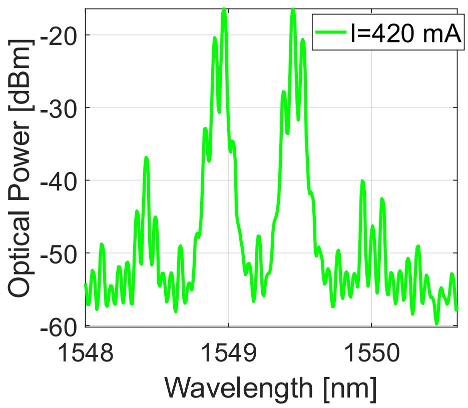

Figure 5.22: Lasing emission of two SC-FP resonances overlapping with ECL longitudinal modes excitation.

For a shorter SC-FP cavity with $L = 120\ \mu$m and coupling gap $G = 500$ nm, the L–I curve shows a linear response with output power halved compared to the longer cavity (discussed above), due to the lower Q-factor from reduced cavity length. The laser spectrum is analyzed over a nearly mode-hop-free tuning range (Fig. 5.23(b)), where the lasing wavelength red-shifts by ~10 pm per mA of RSOA current, despite TEC stabilization. This, reflects residual thermo-optic effects in both subsystems (as detailed in Section 5.1.3).

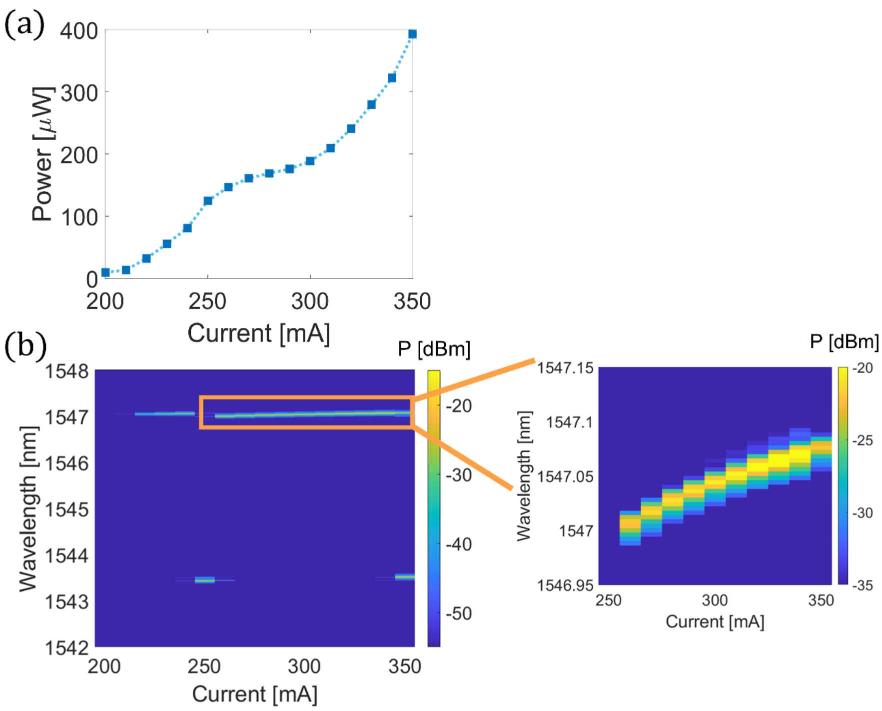

Figure 5.23: (a) L-I curve for SC-FP based HECL featuring L=120 um and G=500 nm. (b) Emitted power (in dBm) as a function of the RSOA injection current and wavelength for the SC-FP-based HECL. Mode-hop-free operation demonstrated over 100 mA current range; redshift along the same single-wavelength condition due to RSOA heating effects with the increased current as reported in the zoomed view.

Increasing RSOA current causes self-heating effect (raising its effective index, red-shifting the gain peak and the Fabry–Pérot ripple), while simultaneously increasing intracavity power that thermally redshifts the SC-FP resonance via absorption heating. These concurrent red-shifts partially compensate within the external-cavity phase condition, enabling smooth tracking of the dominant longitudinal mode rather than discrete hopping. A zoomed view of this behavior for current values between 300 and 320 mA is shown in Fig. 5.24.

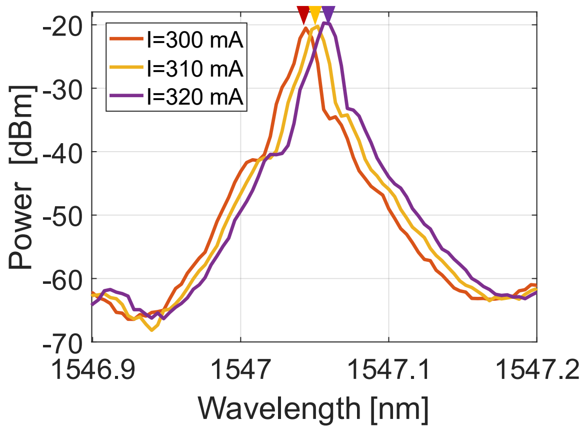

Figure 5.24: Driving the RSOA current from 300 mA to 320 mA at 10 mA steps, it can be observed that the lasing peak red shifts of around 10 pm.

The final device under test refers to a SC-FP architecture incorporating a higher coupling gap (G=600 nm) and a short cavity (L= 200 µm), in order to assess the robustness of the HECL architecture. The increased gap reduces the on-resonance SC-FP reflectivity, resulting in a lower output power (Fig. 5.25(a)) and more marked resonance hopping (Fig. 5.25(b)).

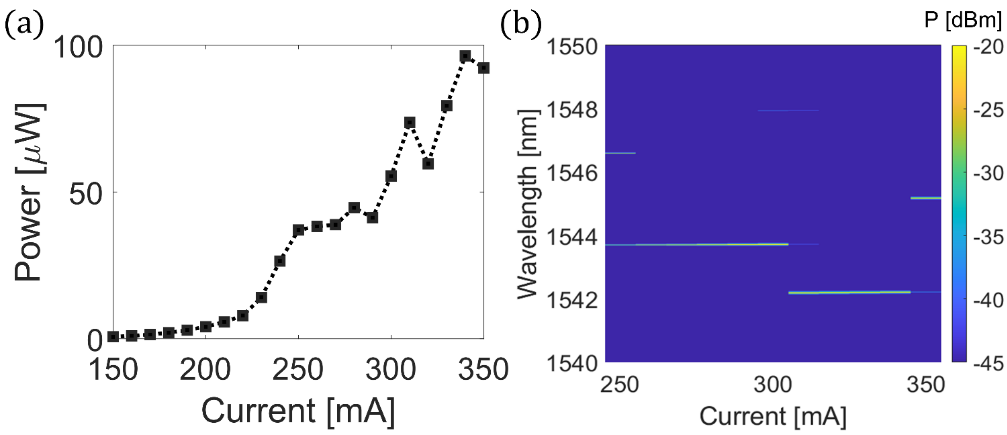

Figure 5.25: (a) L-I laser response when a SC-FP incorporating L=200 um, and G=600 nm is considered. (b) Emitted laser power (spanning from -20 dBm to -45 dBm) as a function of the applied RSOA current and wavelength.

Compared to the G = 500 nm, L = 120 μm configuration, the narrower and sharper resonance provide single-wavelength emission characterized by a SMSR exceeding 50 dB at an RSOA drive current of I =325 mA (Fig. 5.26).

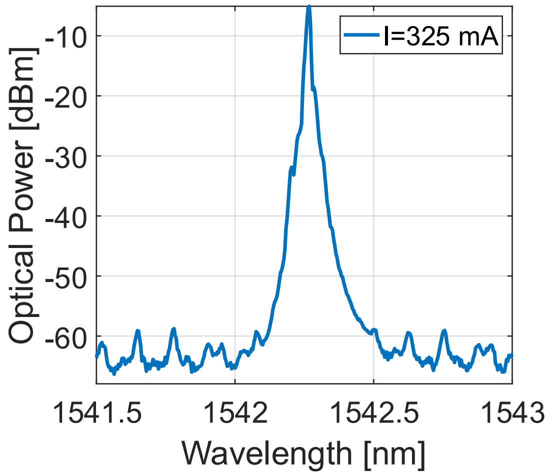

Figure 5.26: Single-wavelength emission extracted at I=325 mA. Optimal SMSR value of ≈50 dB is measured.

For the FFT measurement, the oscilloscope was configured with a time base of 3.2 μs/div over 10 horizontal divisions, yielding a 32 μs acquisition window; with a sampling rate of 12.5 GSa/s, this resulted in 400000 points record and an FFT frequency resolution of 31.25 kHz. The laser linewidth measures approximately 110 kHz, as determined by the Lorentzian fit of the FFT component located at 788.5 MHz, shown in Figure 5.27.

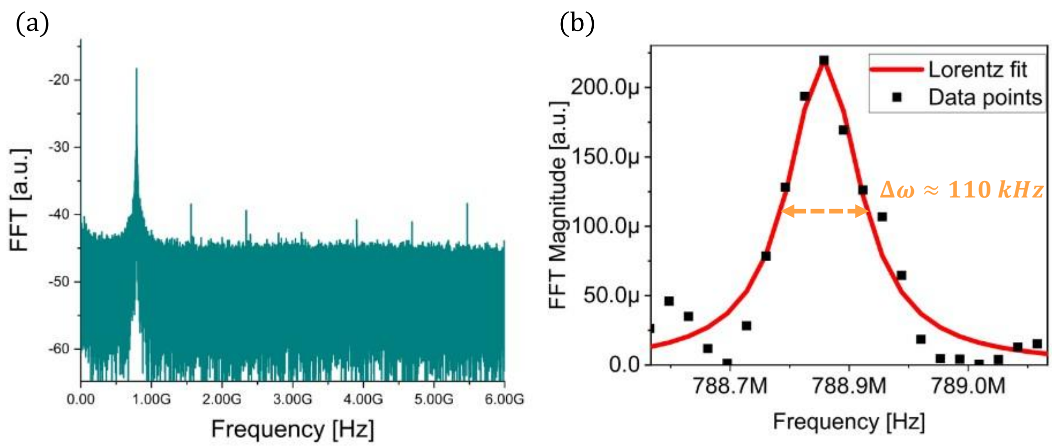

Figure 5.27: (a) FFT analysis of the HECL: the RF tone is located at ≈788.5 MHz and is characterized by a linewidth of ≈ 110 kHz, after Lorentzian fitting (b).

5.3. Micro-transfer printing

Micro-transfer printing (μ-TP) is a heterogeneous integration technique (as detailed in Section 1.4.3) employing patterned elastomer stamps to selectively pick-up and release microscale devices from their native substrates onto non-native target substrates (Fig. 5.28) [2-4]. In μ-TP, fully processed III–V devices are fabricated on their native III–V wafer and then "printed" onto a separate passive photonic platform using an elastomeric stamp made of PDMS. This approach offers several compelling advantages that make it potentially the most scalable integration strategy such as sub-micron alignment accuracy that enables device positioning with placement precision of ±0.5 μm (3σ) for efficient optical coupling to underlying waveguides and cost-effectiveness by avoiding waste of expensive III-V material through selective printing of only required devices [4]. Moreover, it supports massive parallel transfer for high-throughput, wafer-scale integration, facilitates heterogeneous integration of III-V gain materials like RSOAs with low-loss SiN or SOI platforms, and allows independent optimization of active and passive components on their native substrates [5],[6]. Critically, this decoupling addresses trade-offs in other schemes, such as evanescent coupling versus thermal management and gain, while pre-fabrication simplifies target processing and enables pre-print yield testing. Prior work has established the versatility of μ-TP for silicon photonic integration: DFB lasers on SOI achieving 35 dB SMSR [7], efficient on-chip green light generation via second-harmonic generation in SiN-LN hybrid waveguides [8], compact lithium niobate modulators on SiN [9], modulated membrane distributed reflector lasers with 40 dB SMSR [10], and single-mode hybrid external-cavity lasers based on 1D photonic crystal resonators with 40 dB SMSR [11].

In this section, it will be demonstrated a fully integrated butt-coupled μ-TP HECL based on the heterogeneous integration of a transfer printed III-V RSOA gain element onto SiN PICs incorporating SC-FPs reflectors. For silicon nitride fabrication, EBL-based patterning is preferred because its higher resolution provides the design flexibility required for precise mode matching and alignment in the butt-coupled configuration. Specifically, this work shows that careful engineering of the resonator parameters, together with optimization of the transfer printing process across two fabrication iterations, leads to a clear improvement in waveguide-coupled optical power, a reduced device footprint, and the realization of a more compact integrated laser.

In the following section, the main process flow for III–V transfer printing onto a SiN-based chip is presented, with the transfer printing process carried out by Dr. Fatih B. Atar (researcher in the III-V Materials and Devices group) at Tyndall National Institute.

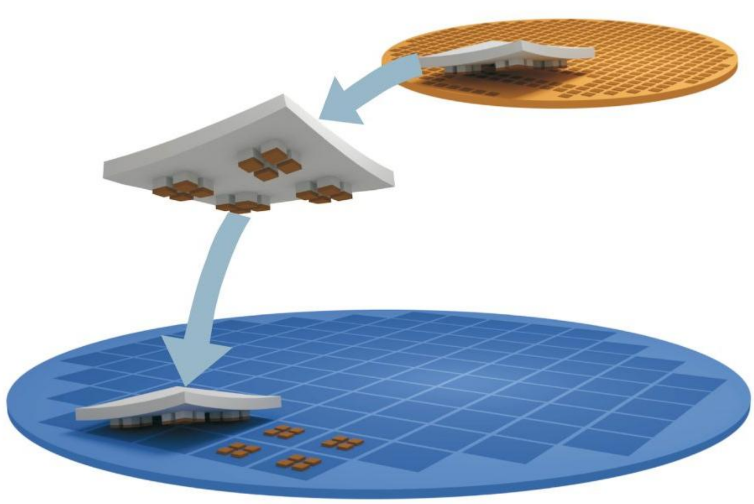

Figure 5.28: Schematic illustration of the three-step micro-transfer printing process, showing (i) release of the III–V coupons from the source wafer, (ii) pick-up with an elastomeric stamp, and (iii) transfer and alignment onto the target photonic wafer [12].

5.3.1 μ-TP RSOA fabrication process

In the μ-TP process, the active devices are first fully fabricated on their native III-V source wafer and only then transferred to the silicon photonic target wafer. For the InP RSOAs, the epitaxial stack is grown on a selectively etchable sacrificial release layer, which enables later undercut and device release [13]. The ridge waveguides are then defined lithographically, metallized for electrical contact, and encapsulated with a dielectric or photoresist overcoat to passivate the device and protect the quantum wells and other active layers from the release etchant. This is particularly important because the release chemistry selectively attacks the AlInAs sacrificial layer and stops on InP, but it can also etch the AlInGaAs quantum wells if they are not encapsulated. The encapsulation is then patterned to open windows only around the perimeter of each coupon, where photoresist tethers are formed to hold the devices in place during processing while still allowing clean fracture during pick-up.

After the tethers are defined, the sacrificial layer exposed in these openings is selectively removed in a controlled wet etch, which laterally undercuts the devices and leaves the RSOA coupons suspended above the source substrate while still anchored by the thin tethers. The resulting array of suspended coupons is then ready for transfer printing without any further processing on the source wafer. Device pick-up relies on the viscoelastic adhesion of the PDMS stamp: the stamp is brought into contact with the source wafer so that its posts conformally contact the selected RSOA coupons, and is then rapidly retracted. The high peel velocity increases adhesion at the PDMS-device interface, causing the tethers to break and allowing the coupons to detach from the source substrate and remain attached to the stamp. In this way, entire arrays of RSOAs can be lifted in a single step, enabling high-throughput wafer-scale transfer [14-16].

5.3.2 SiN PIC and SU-8 spot-size converters

In parallel with the source-wafer preparation, the SiN photonic chip is independently fabricated adopting the same fabrication steps detailed in Section 3.2 but considering 1.5 µm-thick thermally grown SiO_2 bottom cladding instead of 8 µm. To improve butt coupling between the transfer-printed III-V coupon and the SiN waveguide, a 2 µm-thick SU-8 spot converter was introduced, providing an intermediate mode-matching section between the edge-emitting III-V device and the passive SiN circuit. In the first iteration, these converters were realized via mask lithography and subsequently using an EBL process, followed in both cases by a 200°C hard bake step. The coupon and BOX thicknesses are engineered to optimize the vertical alignment between the center of the mode on the III–V ridge waveguide and the mode on the SU-8 side, so that the ridge facet is not buried in SiO_2 but lies close to, or slightly above, the SiN core, with any residual offset compensated by appropriately designed mode converters.

In this context, EBL-based patterning is preferred because its higher resolution provides the design flexibility required for precise mode matching and alignment in the butt-coupled configuration. Moreover, the PIC needs to be engineered to host the III-V printed coupons. The process begins by etching a local recess into the SiO_2 cladding at the intended RSOA locations, ensuring that after transfer printing the III-V gain section rests directly on the high-thermal-conductivity silicon substrate (Fig. 5.29(b)).

This process step represents a key optimization, as the direct RSOA-Si interface leverages the substrate's high thermal conductivity to provide a short, low-resistance heat path that substantially improves heat extraction from the active region. This work overcomes the limitations of the first HECL demonstrations in [11], where µ-TP-bonded RSOAs were placed directly on an insulating SiO_2 stack (Fig. 5.29 (a)) with a <10 nm vapor-coated BCB layer and could only be operated under low-duty-cycle pulsed driving. In those earlier devices, the poor thermal path through the oxide caused strong self-heating under continuous-wave bias, leading to wavelength drift and performance degradation. Very short current pulses with a small duty cycle (for example, 0.1 % at 20 kHz) were therefore employed to provide sufficient instantaneous current for lasing while greatly reducing the time-averaged heating compared with CW operation, thereby stabilizing the chip temperature and refractive index and limiting thermal roll-over and wavelength drift.

Subsequently, a thin BCB film (~50 nm) is spin-coated into the recess and partially cured, forming a compliant adhesion layer that robustly secures the printed coupon while maintaining optical access to the underlying SiN waveguide and supporting efficient thermal coupling. During printing, the PDMS stamp carrying the released RSOA coupons is aligned to the SiN PIC using lithographically defined fiducial markers on the GDS files for both wafers.

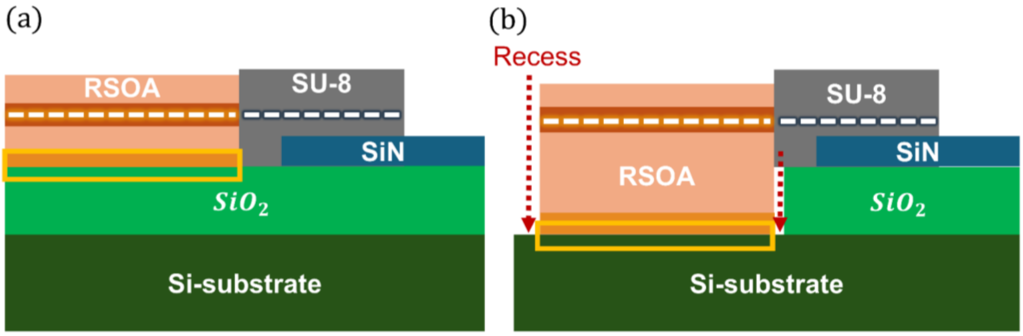

Figure 5.29: Schematic cross-sections of RSOA recess (a) before, and (b) after SiO_2 etching at the interface with SU-8 and SiN. Direct transfer onto Si substrate reduces thermal dissipation.

Adiabatic inverse tapers are fabricated on the photonic chip between the SU-8 (spin-on polymer) and SiN waveguides (Fig. 5.30). These structures act as spot-size converters and consist of an SU-8 waveguide tapered down from 3 µm to ~1.5 µm width over a taper length of 250 µm, while the SiN waveguide expands from a sharp 0.12 µm tip width to 1.3 µm, that is the single-mode width of the side-coupler implementation.

The wider SU-8 section at the interface with the RSOA, precisely matches the mode area of the RSOA ridge waveguide output, minimizing coupling losses at the III–V/SiN interface, enabling efficient butt-coupling. The entire inverse taper structures maximize the power transfer into the SiN resonator. In the output section, the converters are mirrored to enhance also the output power collection.

As it will be detailed later, SEM inspection of RSOA coupon positions enables custom alignment markers for precise EBL-based SU-8 converter placement, an advantage over fixed photomask designs, yielding enhanced power coupling.

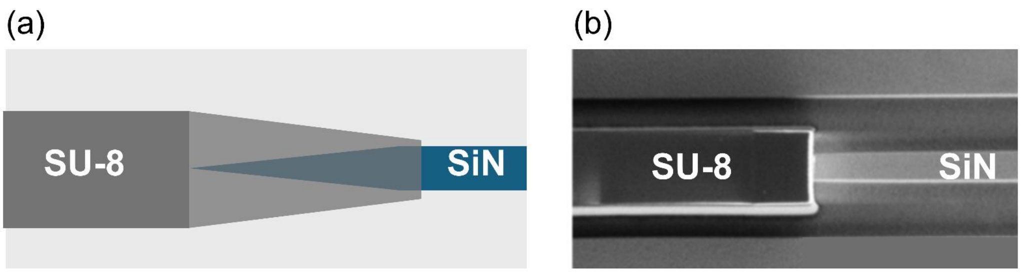

Figure 5.30: (a) Inverse taper design schematic. (b) SEM picture of the fabricated taper: zoom-in on the interface between SU-8 and SiN waveguide.

5.3.3 μ-TP HECL architecture

A key advantage of micro-transfer printing is that the SiN passive circuitry and RSOA gain chips can be fabricated via fully decoupled process flows, consequently enabling independent design and process optimization for each. The resulting μ-TP HECL integrates an RSOA gain chip printed directly onto a silicon nitride PIC featuring side-coupled Fabry–Pérot cavities as the resonant cavity reflectors, with edge coupling achieved via precisely aligned SU-8/SiN inverse-taper converters for low-loss mode matching (as detailed previously).

The HECL architecture is schematized in Fig. 5.31. The printed RSOAs are characterized by a variable cavity length of 300 μm, 500 μm, and 700 μm but they all exhibit a gain curve peak at around 1560 nm, with a ~30/35 nm bandwidth, when temperature is set to 12°C.

By increasing the driving current in the coupons or temperature in the system, it induces a redshift of the gain peak. However, it has been adopted to have a low operating temperature (T=12°C or T=15°C) to avoid thermal instability.

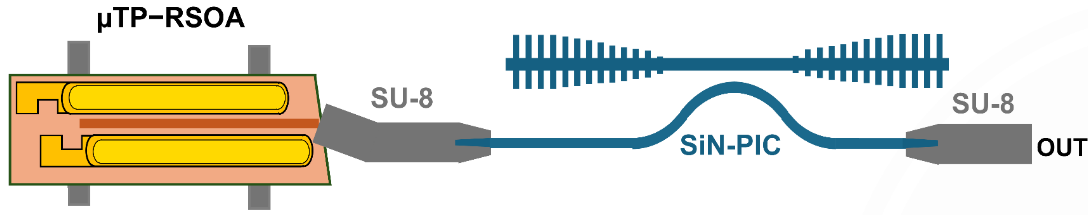

Figure 5.31: Schematic of the external-cavity laser architecture. The μ-TP RSOA is butt-coupled by means of a SU-8 spot-size converter to SiN-PIC. The latter is coupled to another SU-8 converter to maximize output collected power.

The passive SC-FP resonators incorporates a bus waveguide evanescently coupled to a high-Q Fabry-Pérot cavity bounded by two symmetric DBRs: each with rectangular lateral corrugations (W_1 = 1.3 μm, W_2 = 2.5 μm, yielding ~17 nm stopband), and combining N = 1750 uniform grating periods with N_T = 250 linearly apodized periods, building on the design strategy implemented in Section 5.2.2.

The grating periodicities are engineered to ensure spectral overlap with the transfer printed RSOA gain, investigating DBRs with Λ=500 nm, 506 nm, and 512 nm. The fabricated devices consider coupling gaps varying from 400 nm to 600 nm, and different cavity lengths considering both shorter cavities (L = 120 μm) and longer ones (L = 600 μm).

This parametric sweep enables investigation of the trade-off between achieving high-Q FP resonant modes, which favors narrow resonances and low intra-cavity loss, and maximizing the effective peak reflectivity seen by the gain chip. Understanding this balance is crucial, since it directly impacts lasing performance in terms of threshold, slope efficiency, and spectral purity of the hybrid external-cavity device.

Representative SEM pictures of the DBR grating sections, the μ-TP RSOA coupons, and the SU-8/SiN spot-size converter are provided in Figs. 5.32 and 5.33, to check fabrication fidelity.

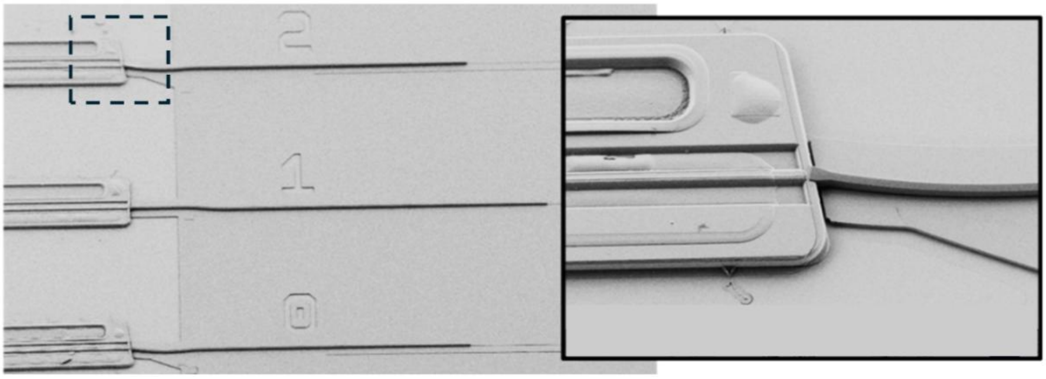

Figure 5.32: SEM image illustrating the interface between the SU-8 and the RSOA coupon.

(a) (b)

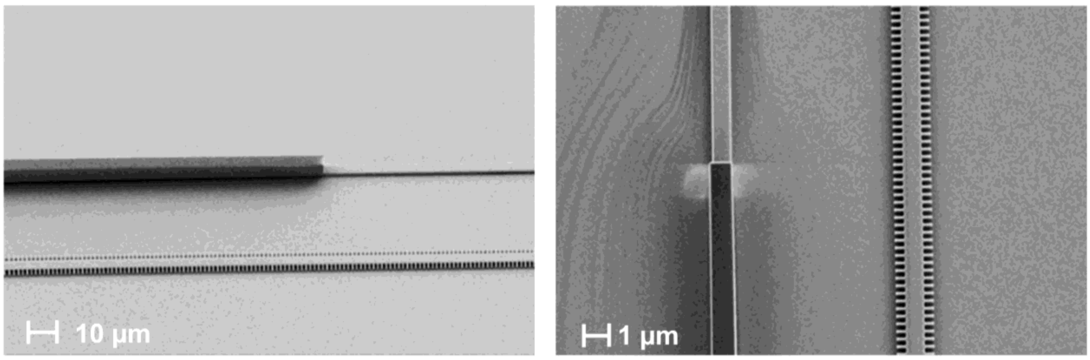

Figure 5.33 (a) SEM picture of the interface between SU-8 and SiN waveguide in the fabricated inverse taper. (b) Zoomed view of the on-chip DBR in the bottom part of the side-coupler.

5.3.4 Fringes analysis: HECL interfaces reflection

Following the considerations and approach used in Section 5.2.3 and 5.2.4 for the two-chip butt-coupled laser, an estimation of all the possible parasitic FP reflections occurring at the interfaces of the μ-TP external-cavity, as well as the longitudinal mode spacing are performed. A schematic of the HECL interfaces is depicted in Fig. 5.34. This effect can be estimated by analyzing seven distinct Fabry-Pérot interference contributions arising from interface discontinuities along the optical path.

All these contributions incorporate the interactions between the RSOA facets, SU-8 and SiN interfaces, PIC chip facets, with final evaluation of the predicted spacing between the external-cavity longitudinal modes supported by the system after the SC-FP reflection. These calculations are based on the conventional free spectral range formula FSR= $\frac{\lambda^2}{2\, n_g\, L}$, where λ is the operating wavelength is assessed to 1550 nm, while n_g and L are the corresponding group index and the geometrical length of the specific region under analysis.

Specifically, the group index analysis has been performed by using the FDE solver in Lumerical, while the FSR of the parasitic FP cavities are evaluated and reported below considering an RSOA cavity length of 700 µm, but can be analogously obtained for shorter RSOA t lengths of 500 µm and 300 µm, as listed in Table 5.1.

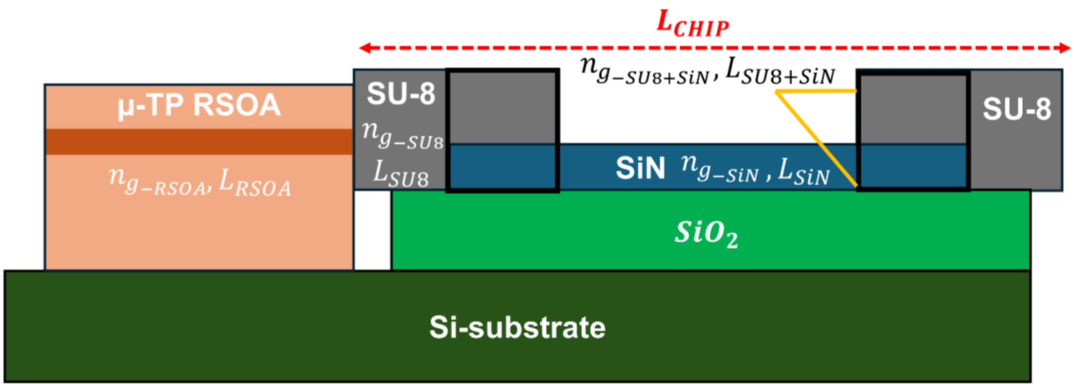

Figure 5.34: HECL cross-section schematic: illustration of all the interfaces along the optical path.

The primary parasitic Fabry–Pérot reflections arise from the transfer printed RSOA's two facets. Despite AR coating on one side, these residual reflections still form a low-finesse FP-like cavity, that superimposes a periodic modulation (ripple) on the net RSOA gain spectrum and can be defined as:

$$\mathrm{FSR_I} = \frac{\lambda^2}{2n_{g,\mathrm{RSOA}}L_{\mathrm{RSOA}}}. \tag{5.3}$$

By assuming $n_{g,\mathrm{RSOA}} = 3.448$, for long RSOA coupons ($L_{\mathrm{RSOA}} = 700\ \mu\mathrm{m}$), $\mathrm{FSR_I} \approx 0.5\ \mathrm{nm}$. The following interface discontinuity along the optical path is between the SU-8 waveguide and the start of the tip width of the SiN taper that adds to the pure RSOA optical path. By considering a group index $n_{g,\mathrm{SU8}} = 1.58616$, and a geometrical length $L_{\mathrm{SU8}} = 282\ \mu\mathrm{m}$ for the SU-8 waveguide with SiO_2 bottom cladding, it results:

$$\mathrm{FSR_{II}} = \frac{\lambda^2}{2(n_{g,\mathrm{RSOA}}L_{\mathrm{RSOA}} + n_{g,\mathrm{SU8}}L_{\mathrm{SU8}})}. \tag{5.4}$$

This contribution assesses to $\mathrm{FSR_{II}} \approx 420\ \mathrm{pm}$.

The third interface accounts also for the cross-section in which SU-8 and SiN coexist, and their top and bottom cladding are air and silicon dioxide, respectively. This inverse-taper section extends for $L_{\text{SU8+SiN}} = 250\ \mu\text{m}$. Given the structure detailed in 5.3.2, the group index of this cross-section accounts for the average value between the start and end widths of both SiN and SU-8 waveguides, yielding $n_{g,\text{SU8+SiN}}$=1.9736. At the end of the SU-8 section, the related FP reflection spacing results:

$$\text{FSR}_{\text{III}} = \frac{\lambda^2}{2(n_{g,\text{RSOA}}L_{\text{RSOA}} + n_{g,\text{SU8}}L_{\text{SU8}} + n_{g,\text{SU8+SiN}}L_{\text{SU8+SiN}})}. \tag{5.5}$$

By substituting the parameters described above, it results $\text{FSR}_{\text{III}} \approx 358$ pm. Regarding the longitudinal modes supported by the HECL, they are determined by the total external-cavity formed between the HR facet of the RSOA and the reflectivity peaks provided by the SC-FP resonators. The spacing between these modes, denoted as FSR_{IV}, is evaluated as:

$$\text{FSR}_{\text{IV}} = \frac{\lambda^2}{2(n_{g,\text{RSOA}}L_{\text{RSOA}} + n_{g,\text{SU8}}L_{\text{SU8}} + n_{g,\text{SU8+SiN}}L_{\text{SU8+SiN}} + n_{g,\text{SiN}}L_{\text{SiN,1}}) + \frac{\lambda^2}{\pi}\frac{d^2\Phi_{\text{DBR}}(\lambda)}{d\lambda^2}}, \tag{5.6}$$

where $n_{g,\text{SiN}} = 1.9764$ is the group index retrieved by considering a single-mode SiN waveguide (whose width is W=1.3 μm) covered by HSQ, while the SiN path is accounted starting from the end of SU-8 to half of the side-coupler ($L_{\text{SiN,1}} = 1073\ \mu\text{m}$), for approximation.

Temporary neglecting the dispersion contribution term $\frac{\lambda^2}{\pi}\frac{d^2\Phi_{\text{DBR}}(\lambda)}{d\lambda^2}$, Eq. (5.6) gives $\text{FSR}_{\text{IV}} \approx 220$ pm. FSR_{V} considers all the SiN region (L_{SiN}) up to the start of the SU-8 output taper, consequently it accounts the sum of $L_{\text{SiN,1}}$ and $L_{\text{SiN,2}}$= 1582.251 μm.

$$\text{FSR}_{\text{V}} = \frac{\lambda^2}{2(n_{g,\text{RSOA}}L_{\text{RSOA}} + n_{g,\text{SU8}}L_{\text{SU8}} + n_{g,\text{SU8+SiN}}L_{\text{SU8+SiN}} + n_{g,\text{SiN}}L_{\text{SiN}})}. \tag{5.7}$$

This value assesses to $\text{FSR}_{\text{V}} \approx 140$ pm.

Adding in the optical length the section in which SiN waveguide and SU-8 overlap in the output section, that is still $L_{\text{SU8+SiN}} = 250\ \mu\text{m}$, is possible to retrieve fringes spaced $\text{FSR}_{\text{VI}} \approx 132$ pm, as obtained from:

$$\text{FSR}_{\text{VI}} = \frac{\lambda^2}{2(n_{g,\text{RSOA}}L_{\text{RSOA}} + n_{g,\text{SU8}}L_{\text{SU8}} + 2\,n_{g,\text{SU8+SiN}}L_{\text{SU8+SiN}} + n_{g,\text{SiN}}L_{\text{SiN}})}. \tag{5.8}$$

The final contribution takes into account the full optical path between the RSOA HR facet and the cleaved end facet of the chip. The additional section refers to a pure SU-8 waveguide region that extends for $L_{\text{SU8,2}} \approx 1300\ \mu\text{m}$, consequently producing FSR_{VII} that is derived as:

$$\mathrm{FSR_{VII}} = \frac{\lambda^2}{2(n_{g,\mathrm{RSOA}}L_{\mathrm{RSOA}} + n_{g,\mathrm{SU8}}L_{\mathrm{SU8}} + 2\, n_{g,\mathrm{SU8+SiN}}L_{\mathrm{SU8+SiN}} + n_{g,\mathrm{SiN}}L_{\mathrm{SiN}} + n_{g,\mathrm{SU8}}L_{\mathrm{SU8,2}})}. \quad (5.9)$$

This spacing is around $\mathrm{FSR_{VII}} \approx 108$ pm, resulting similar to the sample cleaving contribution detailed in Section 5.2.3.

All the FSRs related to the RSOA cavity lengths L_{RSOA} = 300 µm, 500 µm and 700 µm are summarized in Table 5.1.

Table 5.1: Predicted FSR contributions calculated for the three different implemented RSOA cavity lengths.

FSR label	L_{RSOA} = 300 µm	L_{RSOA} = 500 µm	L_{RSOA}= 700 µm
FSR I	1.16 nm	0.70 nm	0.50 nm
FSR II	0.811 nm	0.553 nm	0.420 nm
FSR III	0.608 nm	0.451 nm	0.358 nm
FSR IV	0.293 nm	0.251 nm	0.220 nm
FSR V	0.166 nm	0.152 nm	0.140 nm
FSR VI	0.155 nm	0.143 nm	0.132 nm
FSR VII	0.123 nm	0.115 nm	0.108 nm

*For FSR VII, is omitting the DBR dispersion-related contribution in the calculation.

5.3.5 Probe station setup

The optical setup used for the transfer printed HECL characterization is depicted in Fig. 5.35(a). A single stage hosts the photonic chip, comprising both the III-V gain section and the silicon nitride passive side-coupled FPs, all mounted on a high-thermal-conductivity copper layer for efficient heat dissipation. Both the chip and the gain coupons are thermally regulated through a TEC controller, which maintains a stable operating temperature (in these experiments fixed to around T=12 °C) to ensure repeatable laser performance and wavelength stability. Each gain coupon is electrically excited via two DC probes positioned on the gold contact pads of the RSOA ridge waveguide, with a NIR camera used for the alignment, as shown Fig. 5.35(b). These probes (Cat-Whisker type), controlled through high-precision micro-manipulators, deliver bias current from an external low-noise current source.

A second stage consists of a three-axis stage (as the one reported in the end-fire setup) in which is mounted a lensed single-mode fiber to collimate and focus the beam allowing efficient output optical power collection. The collected light is then routed to a power meter for direct output power measurement, and to the OSA for spectral response investigation in terms of laser SMSR and linewidth evaluation.

(a) (b)

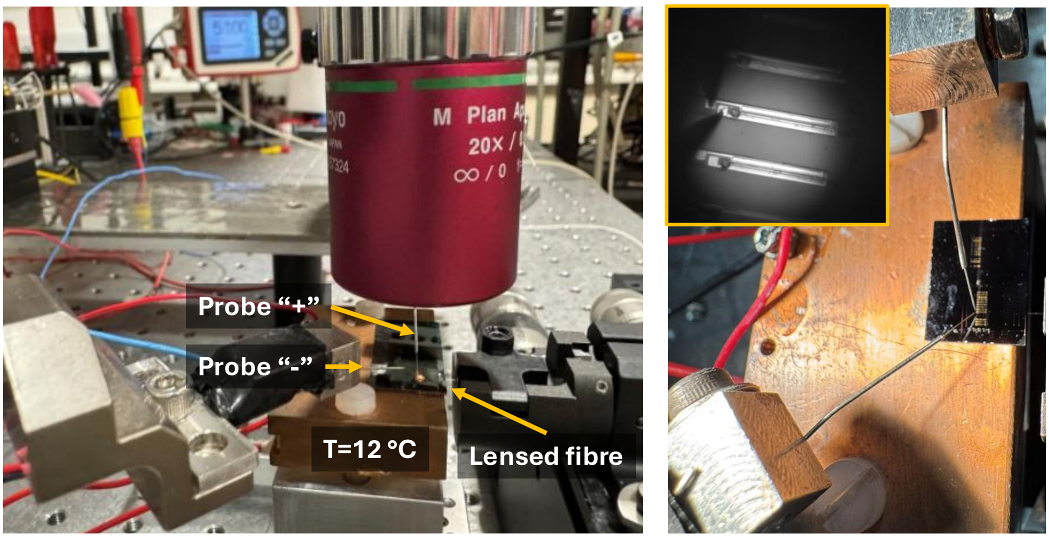

Figure 5.35: (a) Probe station experimental setup. (b) Focus on the probe alignment on the RSOA contact pads.

The NIR camera provides additional insight into the HECL operation before and after lasing operation. For example, Fig. 5.36(a) reports the amplified spontaneous emission from the RSOA and Fig. 5.36(b) the weak scattering spot at the interface between the SU-8 and the SiN inverse taper, visible in the NIR camera when the drive current is set to 29 mA. In this bias condition, the hybrid cavity does not reach the laser threshold.

Under higher bias, increased carrier injection in the III–V region enables higher optical gain and produce lasing in the hybrid external-cavity defined by the on-chip feedback element. Specifically, Figs. 5.37(a),(b) show the behavior along the chip at a drive current of 90 mA. At this operating point, a much stronger scattered-light contribution is observed both at the RSOA coupon and in the coupler/mirror region, confirming that lasing has been established.

Furtherly increasing the RSOA drive current (I = 155 mA), the HECL delivers an output power of approximately 450 µW. The NIR image in Fig. 5.37(c) clearly depicts the output facet of the PIC aligned to the lensed fiber during laser emission.

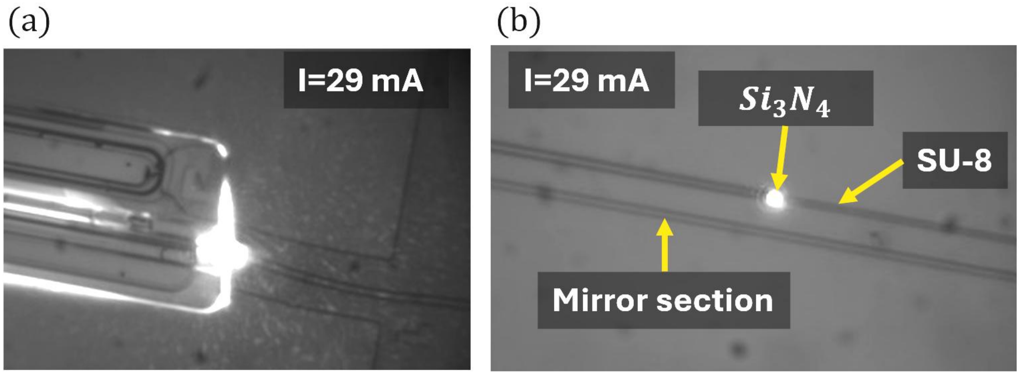

Figure 5.36: (a) RSOA coupon excitation biasing with I=29 mA. (b) Light scattering view from NIR camera between SU-8 and SiN, in absence of lasing emission.

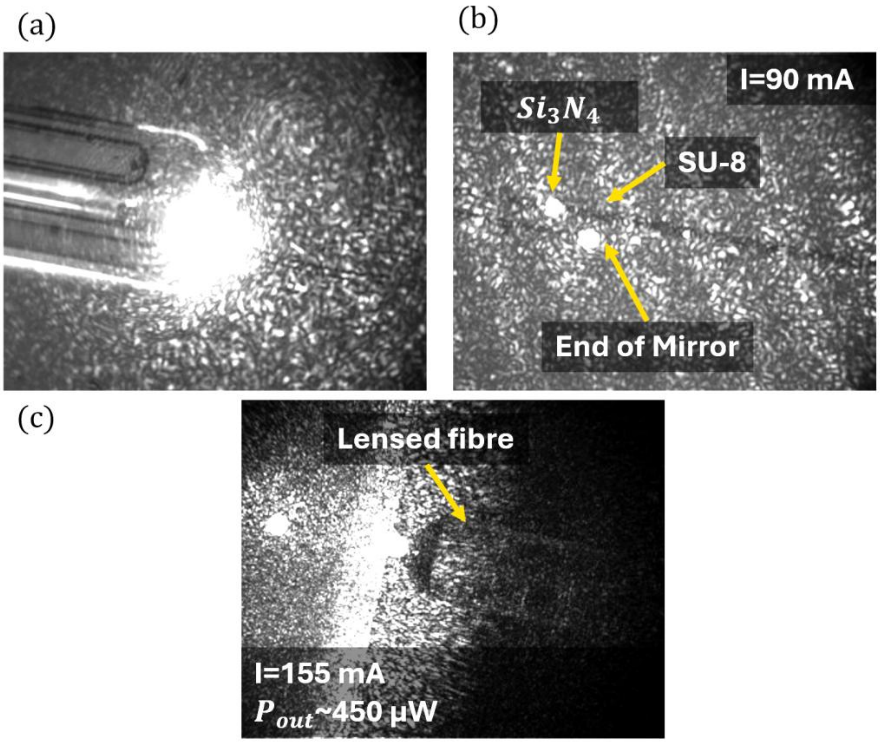

Figure 5.37: Analysis of the light scattering along the full optical path of the HECL, during laser emission. It depicts (a) the RSOA coupon, (b) the mirror and inverse taper section, and (c) the output alignment with the lensed fiber.

5.3.6 First iteration results

The first iteration of the transfer printed HECL demonstrates a clear proof of concept, showing that lasing emission can be obtained both from an on-chip DBR reflector and from a wavelength-selective side-coupled Fabry–Pérot reflector.

The HECL architecture follows the configuration described in Fig. 5.31, employing gain coupons characterized by a 500 µm long ridge waveguide, transfer printed onto a SiN PIC fabricated according to the process detailed in Section 5.2.1. Laser characterization has been carried out in the Tyndall laboratories. In this fabrication run, the SU-8 converters were realized using a photomask process rather than electron-beam lithography.

The architecture enables single-wavelength lasing operation in a fully integrated system, with a SMSR of approximately 20/25 dB. Post-fabrication inspection, however, reveals a not optimized alignment between the gain coupons and the SU-8 converters, which reduce the measured output power to only tens of microwatts.

5.3.6.1 DBR-based laser emission

The Bragg reflectors consist of rectangular corrugation-profile gratings, defined by waveguide widths of $W_1 \approx 1.3$ µm in the narrow section and $W_2 \approx 2.5$ µm in the wider section. The structure comprises $N = 150$ uniform grating periods and $N_T = 50$ apodized periods on both the left and right sides, while maintaining a 50% duty cycle. The implementation of apodized grating periods on the DBR architecture is employed to provide a smooth transition between the single-mode waveguide width region (W_1) and the high-contrast corrugated waveguide width (W_2), reducing radiation loss contributions as detailed in Section 3.1. The grating periodicity is set to Λ=508 nm so that the Bragg stopband is centered on the RSOA gain spectrum. The schematic of the implemented DBR is shown in Figure 5.38.

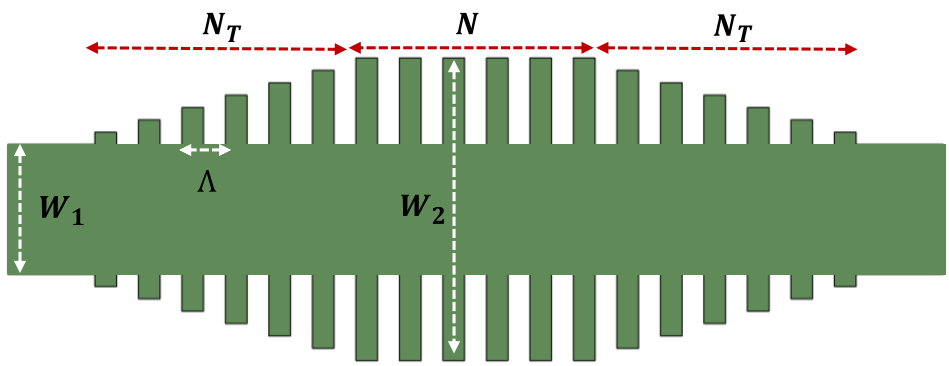

Figure 5.38: Schematic of the implemented on-chip DBR with the summarized key design parameters.

At a temperature of approximately T=15°C for both the RSOA and the SiN PIC, single-wavelength lasing emission is demonstrated, when the on-chip DBR is used as reflector, designed to have around 80% reflectivity. Specifically, as depicted in Figure 5.39, when the injection current is set to I=80 mA a weak lasing line, among the supported cavity modes, emerges on the DBR stopband. The achieved laser has a SMSR of about SMSR≈15 dB and shifts toward longer wavelength ECL modes when current rises to 100 mA (Fig. 5.39, purple trace).

This shift is consistent with the self-heating effect in the RSOA and the increasing intracavity power, that red-shifts the gain curve, the SC-FP resonance via absorption heating, and modify the external-cavity laser condition as already detailed before. In addition, these measurements provide also an experimental demonstration of the grating stopband, which confirms to be characterized by a width of 17 nm with a central Bragg wavelength λ_B≈1581 nm.

Among the interfaces-related contributions examined in Section 5.3.3, in the lasing spectrum is overlapped the gain ripple arising from the ASE of the RSOA as observed in Fig. 5.39 outside the stopband (approximately peak-to-peak gain ripple of 5 dB around -60/65 dBm level): the observed fringes spacing of around 0.7 nm corresponds exactly to the predicted values retrieved by using the formula $\mathrm{FSR_I} = \frac{\lambda^2}{2n_{g,\mathrm{RSOA}}L_{\mathrm{RSOA}}}$ for a cavity length $L_{\mathrm{RSOA}} \approx 500$ µm.

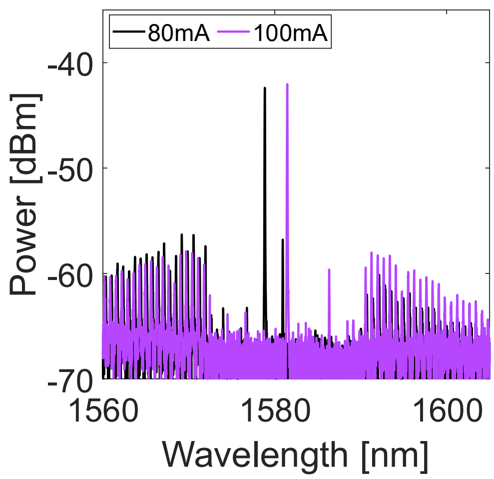

Figure 5.39: Single-wavelength laser emission extracted at I=80 mA (black trace) and I=100 mA (purple trace), when the DBR is used as reflector.

5.3.6.2 Side-coupled FP-based laser emission

Among the different designed resonator architectures (described in Section 5.3.3), laser emission is firstly investigated for a SC-FP resonator which features a grating period $\Lambda = 500$ nm, DC=50%, coupling gap G=400 nm, and cavity length $L = 120$ µm. This configuration is expected to maximize the intensity of the reflection peaks while reducing the loaded Q-factor of the output resonant dips. Under the same temperature conditions used for the DBR-based emission (T = 15 °C), a dominant single lasing peak superimpose over the SC-FP resonant dips when the driving current is set to I=80 mA, 90 mA, and 96 mA, as shown in Fig. 5.40.

The output spectra report single-wavelength lasing emissions exhibiting a SMSR of approximately SMSR≈20–25 dB, combined with resonant hopping effect occurring for different current values.

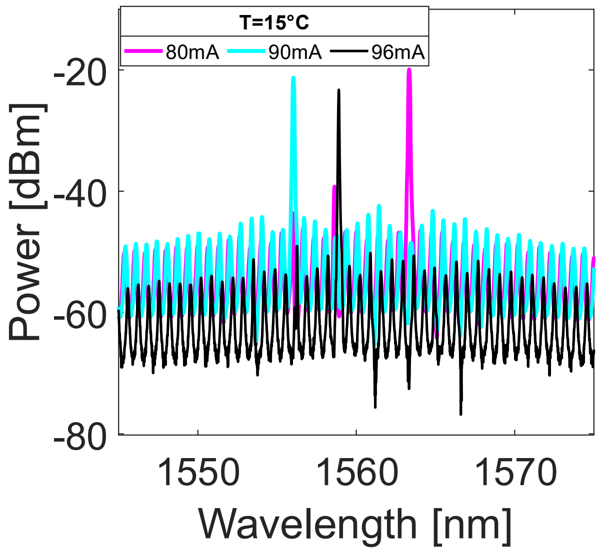

Figure 5.40: Single-wavelength lasing: resonant hopping occurs between different SC-FP resonances at different driving current in the RSOA.

Even though the on-chip output power is only on the order of tens of microwatts, both the SC-FP resonances and the lasing mode are clearly distinguishable over the ripple-gain background. The low power level is attributed to presence of air-gaps between the SU-8 spot-size converter and the printed RSOA, confirmed by SEM inspection (Fig. 5.41).

Mask lithography for the SU-8 patterns, does not allow precise customization of the SU-8 placement, so the RSOA coupons cannot be perfectly aligned with them, and the coupling efficiency is reduced. Moreover, lasing emission was tested at fixed current (I = 70 mA) while varying the TEC temperature from 12 °C to 15 °C, as shown in Fig. 5.42.

The laser exhibits a redshift consistent with the combined thermo-optic effect in both the RSOA gain peak and SC-FP resonances, accompanied by the corresponding adjustment of the external-cavity longitudinal mode condition.

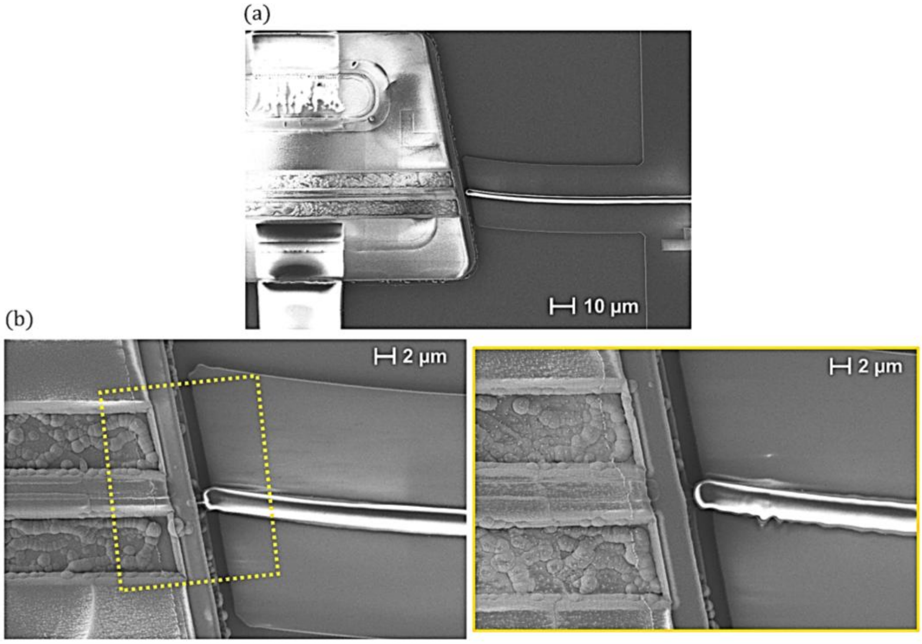

Figure 5.41: (a) SEM image depicting the coupling between RSOA and SU-8 converter. (b) Zoom on the air-gap existing between the RSOA interface and SU-8.

The emitted line, that features SMSR≈25–28 dB, sits on top of the passive resonant dips of the SC-FPs (visible in Fig. 5.42(a)), which have FSR varying from 2.6 nm to 1.7 nm, set by the geometric cavity length (L=120 µm) plus the additional penetration length into the DBR section. Fig. 5.42(b) shows the parasitic FP reflection fringes derived from the RSOA gain, spaced 0.7 nm, that features a peak-to-peak gain of 10 dB around -55 dBm power level.

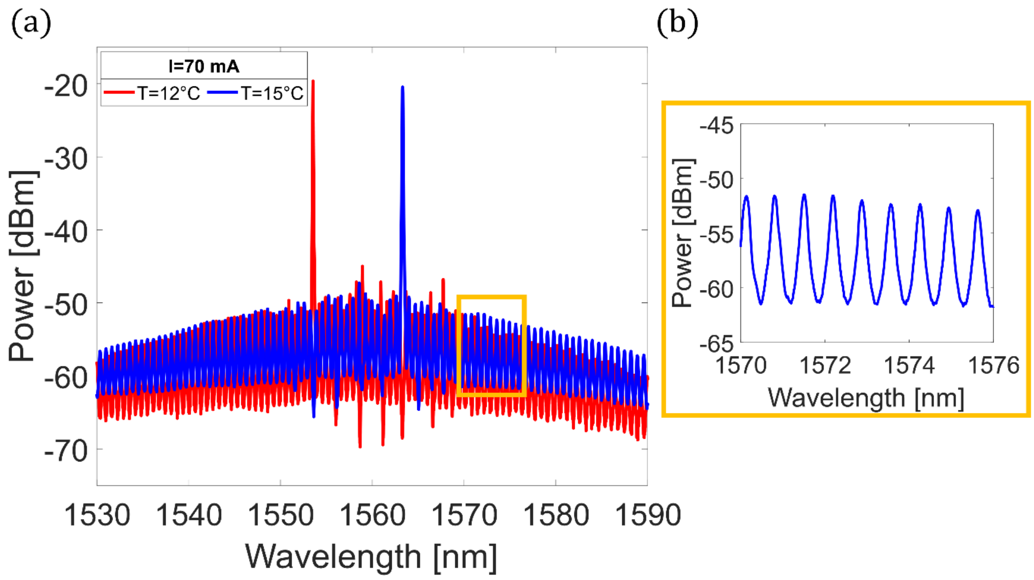

Figure 5.42: (a) Single-wavelength emission for two different operating temperature conditions: T=12°C, and T=15°C. for a fixed current of I=70 mA. (b) Zoom of the ASE gain ripples spaced 0.7 nm.

5.3.7 Second iteration results

In the second iteration of the HECL, a key modification concerns the fabrication of the SU-8 spot-size converters. Unlike the first prototype, where these converters were patterned using mask lithography, this process employs EBL technique.

After transfer printing the RSOA coupons, their positions are precisely assessed through SEM imaging, guiding the EBL patterning of the SU-8 section to ensure optimal alignment and coupling efficiency. Figure 5.43 shows SEM images confirming the successful RSOA–SU-8 alignment and the reduced air-gap achieved.

(a)

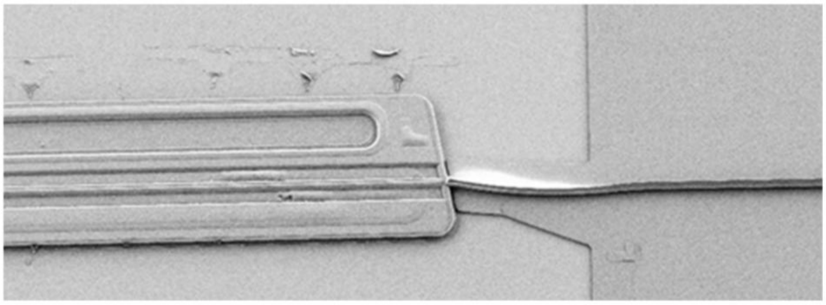

(b)

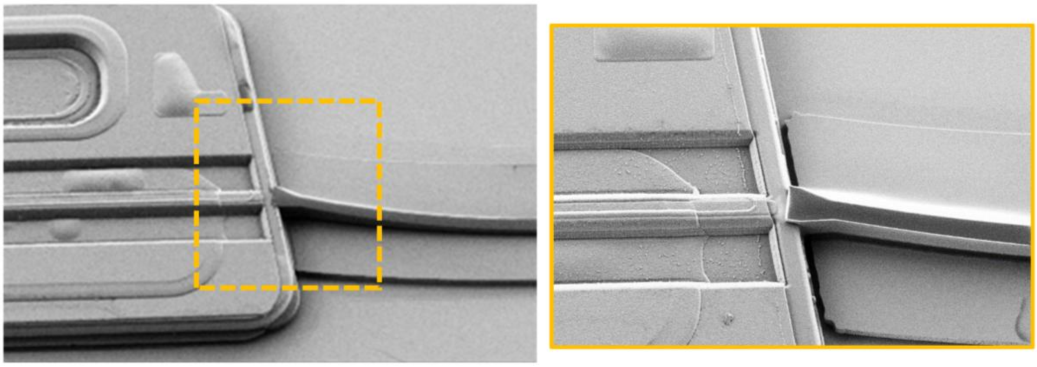

Figure 5.43: a) SEM image of the coupling between RSOA and SU-8 converter realized by EBL. (b) Zoom on the interface: better alignment exists between the RSOA coupon and the SU-8 waveguide.

This refinement led to a substantial performance improvement, achieving a peak power output exceeding 0.6 mW compared to only tens of microwatts in the first iteration. In addition, the laser spectra exhibit SMSR exceeding 40 dB under single-wavelength operation. The enhanced output power and spectral purity enabled heterodyne linewidth measurements, revealing a laser linewidth below 50 kHz, below the resolution limit of the measurement setup.

5.3.7.1 Side-coupled FP reflection measurements

The SiN SC-FP resonators are fabricated following the same process flow described in Section 5.3.5. Prior to the comprehensive analysis of the laser performance, reflection measurements have been conducted on the SC-FP structures to determine the spectral positions of the reflection peaks associated with each implemented grating periodicities (500 nm, 506 nm, and 512 nm).

The aim of this preliminary investigation is to verify the resonant reflectors fabrication repeatability across the two iterations, and to identify the configuration whose reflection peaks best overlaps the RSOA gain bandwidth. The reflection response of the SC-FP resonators is extracted using a broadband laser source (ASE ranging from 1520 nm to 1620 nm) coupled via a fiber-based three-port optical circulator to the output port of the HECL as shown in the setup in Fig. 5.44. A polarization controller was employed to ensure precise excitation of the TE polarization mode during the measurement procedure.

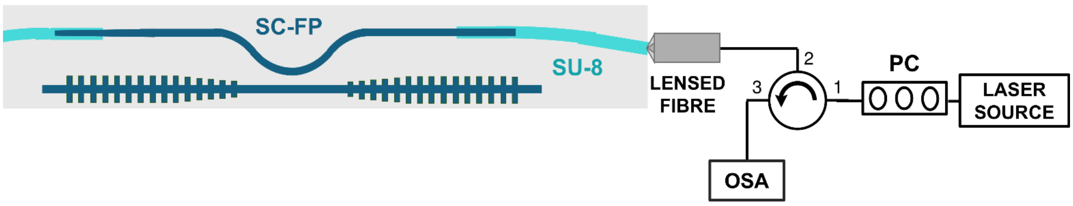

Figure 5.44: Schematic of the experimental setup implemented for measuring the SC-FP reflection peaks.

From this experimental setup, the normalized reflection spectra of a SC-FP, featuring $L = 120\ \mu$m, $G = 500$ nm, N=1750, N_T=250, and $P = 500$ nm as design parameters, are reported in Fig. 5.45(a).

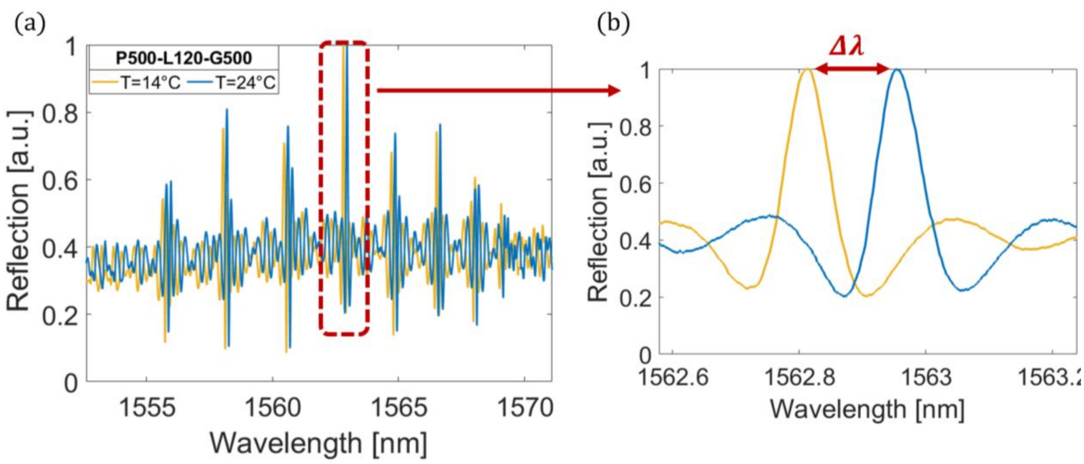

Figure 5.45: (a) Normalized SC-FP reflection spectra for T=14°C (yellow) and T=24°C (blue), when periodicity is fixed to P=500 nm. (b) The highlighted reflection peak reports a redshift of around Δλ≈140 pm.

These spectra are normalized to the laser source and scaled to ensure visualization clarity, and are extracted at two operating temperatures, T=14°C (yellow trace) and T = 24°C (blue trace), respectively. The SC-FP resonator under test, supports resonance peaks within the 1555–1570 nm wavelength range when $P = 500$ nm is considered. The ten-degree temperature variation applied to the SC-FP reveals a red-shift of each resonance by about $\Delta\lambda \approx 140$ pm (Fig. 5.45(b)), corresponding to a temperature rate variation of around 14 pm/°C, consistent with the behavior previously observed in Fig. 5.14. Moreover, it exhibits an FSR response ranging from approximately 2.5 nm to 1.5 nm as shown in Fig. 5.46.

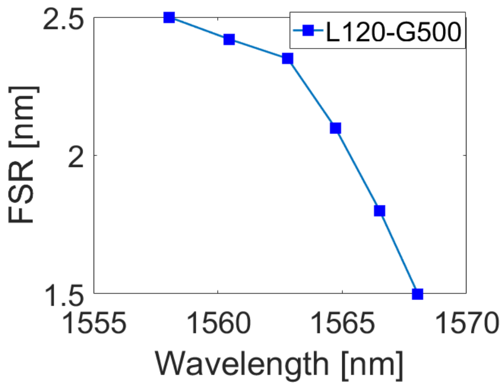

Figure 5.46: FSR response extracted for the SC-FP resonator with $L = 120$ μm, $G = 500$ nm.

This grating periodicity provides an optimal spectral alignment with the RSOA gain peak; therefore, the subsequent subsection will majorly discuss the laser performance achieved for this specific periodicity value. Conversely, when T=14°C and the grating periodicity is set to $P = 506$ nm, the resonance envelope experiences a spectral shift of approximately 15 nm towards longer wavelength compared to Fig. 5.45, with SC-FP peaks spanning between 1570 nm and 1585 nm, as illustrated in Fig. 5.47.

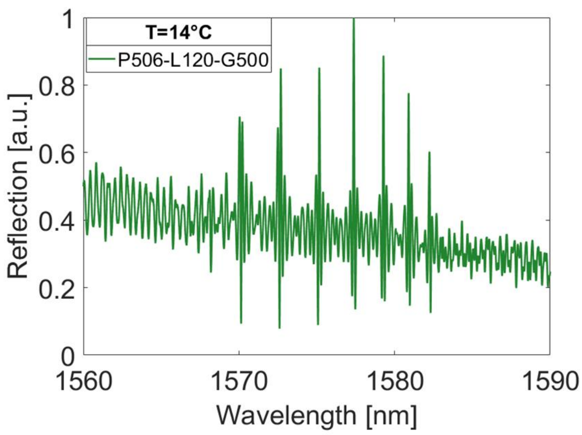

Figure 5.47: Normalized SC-FP reflection spectra for T=14°C, when periodicity is fixed to P=506 nm.

5.3.7.2 SC-FP laser emission characterization

The emission performance of the HECL is investigated by using the same resonant reflector described in Section 5.3.6.2 (G=400 nm, and L= 120 µm). During the characterization, the chip temperature is stabilized at T = 12°C, while the laser output power reported in Fig. 5.48(a) and the corresponding emission spectra in Fig. 5.48(b) are recorded as the injection current is increased from 25 mA to 155 mA in steps of 5 mA.

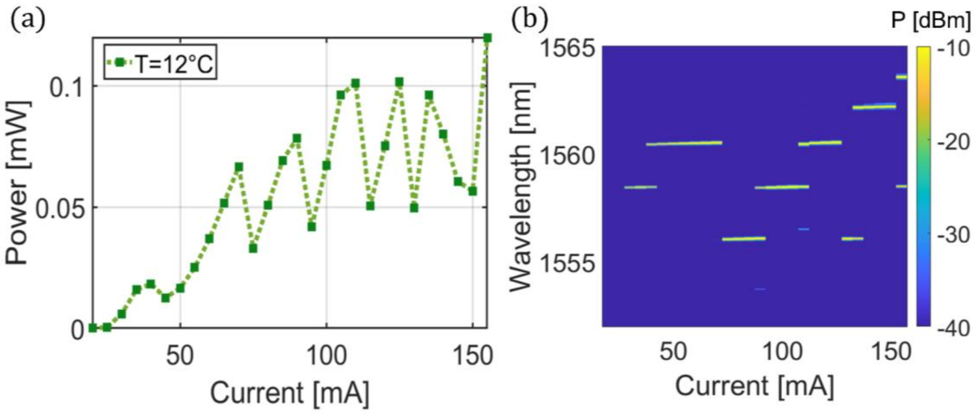

Figure 5.48: (a) L-I curve jumps from lower to higher laser power, reaching around 0.12 mW at I=150 mA. (b) Emitted HECL power as a function of the RSOA injection current and wavelength (colorbar shows power values spanning from -10 dBm to -40 dBm).

Resonant hopping is still observed as the current is varied, both in the L–I curve, where the output power exhibits discrete jumps from lower to higher values, and in the 3D color-map, plotted over a range from −40 dBm to −10 dBm. When the current is fixed at $I = 125$ mA, the laser spectrum exhibits a side-mode suppression ratio of approximately SMSR≈40 dB, which represents a marked improvement over the 25 dB obtained in the first iteration (Fig. 5.49).

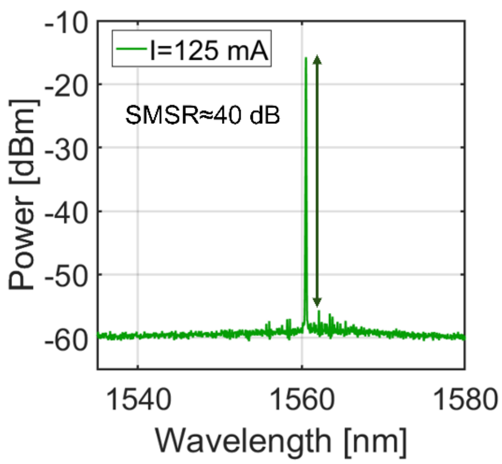

Figure 5.49: (a) Single-wavelength laser emission placed at 1560.53 nm and characterized by SMSR≈ 40 dB, for 125 mA driving current.

The enhanced laser spectrum allows to carry out the heterodyne linewidth measurement, using the same experimental configuration shown in Fig. 5.20 and the procedure described in Section 5.2.4. By acquiring a total time trace of 40 μs, and keeping a sampling rate of 12.5 GSa/s, the FFT operation on the heterodyne beat note reveals a spectral component at approximately 552.9 MHz (Fig. 5.50(a)). A zoomed-in view of the fundamental tone (Fig. 5.50(b)) reports the Lorentzian fit of the RF harmonic, yielding to extract a linewidth of $\Delta\omega \approx 47$ kHz.
This measured linewidth falls below the minimum resolution reliably supported by the employed instrumentation, as the typical TLS linewidth reported in the datasheet is around 100 kHz. Nevertheless, the result clearly evidences a substantial improvement compared to the laser emission shown in the two-chip butt-coupled HECL configuration, which exhibited minimum linewidths of approximately 74 kHz and 110 kHz, respectively.

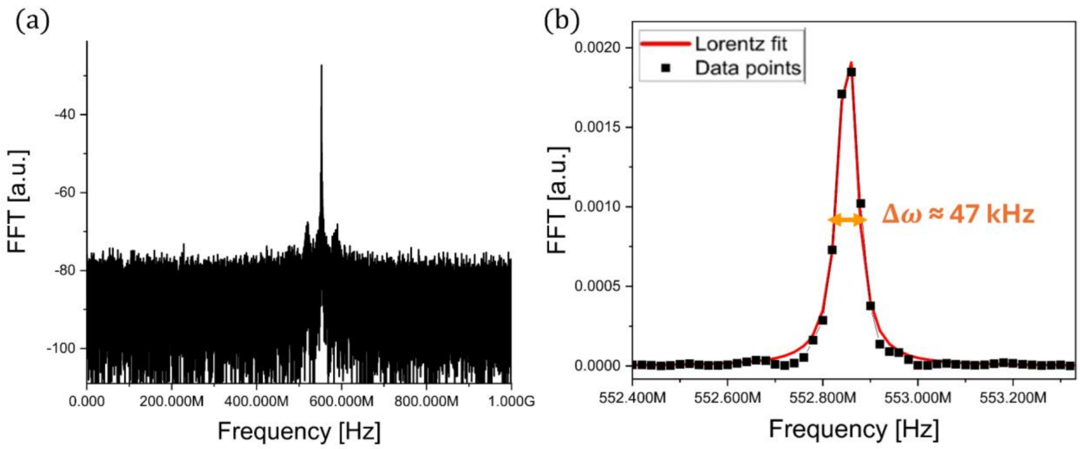

Figure 5.50: (a) FFT analysis of the HECL: the RF tone is located at ≈552.9 MHz and is characterized by a linewidth of ≈ 47 kHz, after Lorentzian fitting (b).

An analogous analysis is performed for a SC-FP resonator with same coupling gap ($G = 400$ nm) but a longer cavity length ($L = 600\ \mu$m). The collected output power raises from 0.1 mW to 0.2 mW, as shown in the L-I curve in Fig. 5.51(a), but the high density of modes in the DBR stopband induces a more relevant resonant hopping among the supported SC-FP modes (Fig. 5.51 (b)).

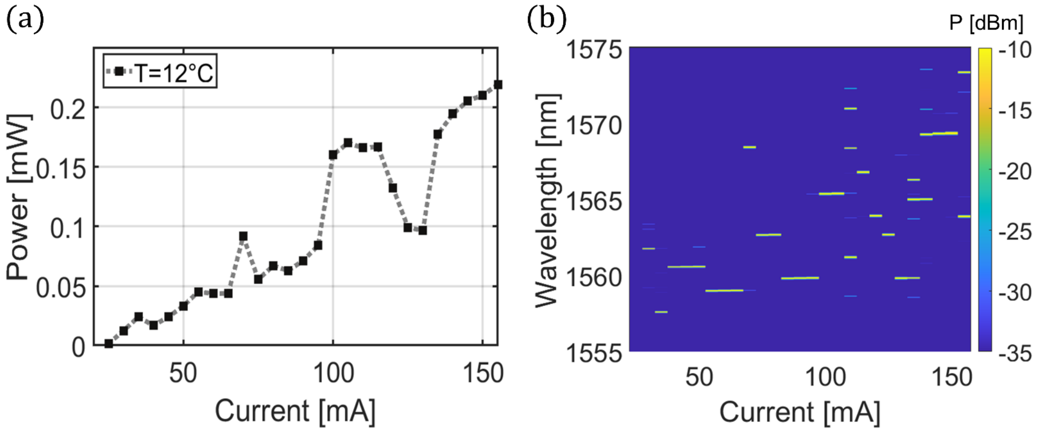

Figure 5.51: (a) Laser characteristic: threshold results around ≈30 mA, while the output power exceeds 0.2 mW, without reaching the saturation current. (b) Emitted HECL power (values spanning from -10 dBm to -35 dBm) versus RSOA drive current and wavelength.

At $I = 150$ mA, the dominant single-wavelength laser peak rises from -18 dBm to approximately -5 dBm, but the SMSR assesses around 35 dB (Fig. 5.52).

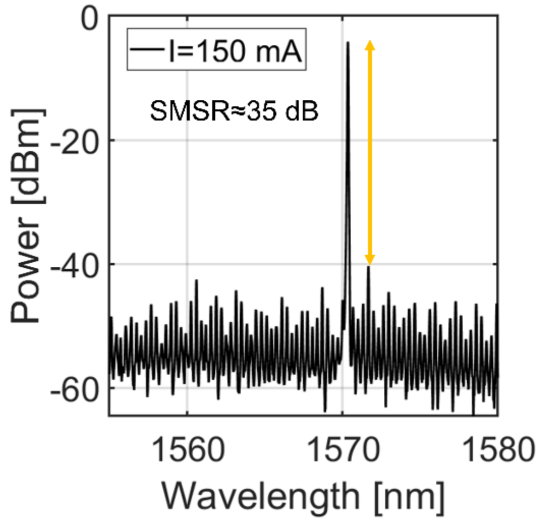

Figure 5.52: Single-wavelength emission placed in 1570.35 nm, extracted at I=150mA. Optimal SMSR value of ≈35 dB is measured.

Using the same FFT acquisition settings as for the previous device under test, the linewidth analysis yields a RF beat note located at 427.28 MHz and wide 48 kHz, as shown in Fig. 5.53(b). The RF component superimposes with the electronic noise floor, as visible in Fig. 5.53(a). In order to distinguish the pure electronic noise in the RF spectrum, it is considered the FFT trace in absence of laser emission, showing these components location in Fig. 5.54.

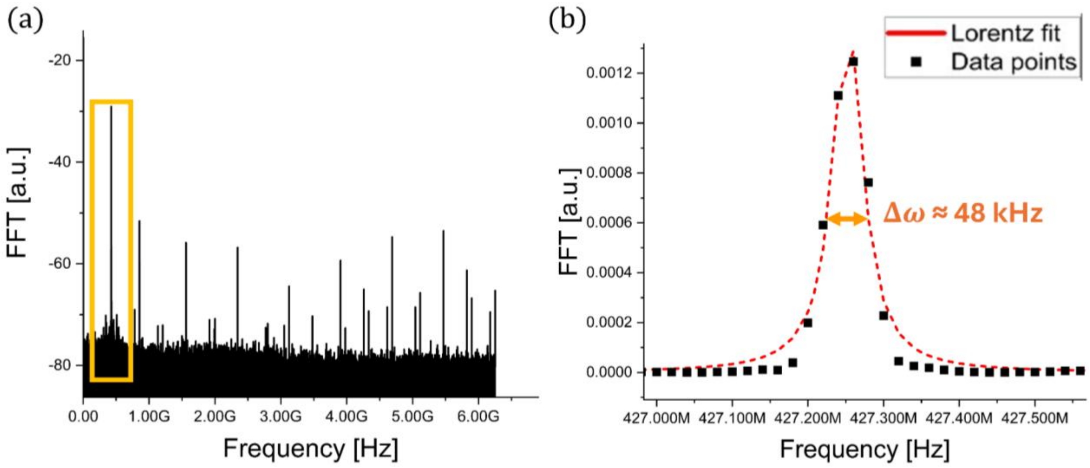

Figure 5.53: (a) FFT analysis of the HECL: the RF tone is located at ≈427.28 MHz and is characterized by a linewidth of ≈ 48 kHz, after Lorentzian fitting (b).

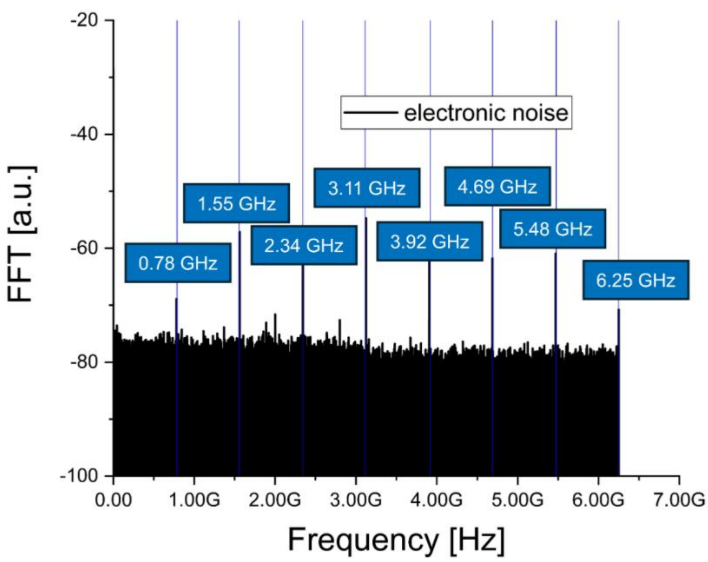

Figure 5.54: (a) FFT RF spectrum showing electronic noise from internal clock sources in the oscilloscope, where timing clocks leak into detected signals.

A final investigation regards the lasing emission when is employed a resonant reflector incorporating *L*=600 µm and *G*=500 nm. The laser analysis is performed by cooling the chip to two different temperature regimes, T=12 °C and T=14 °C, respectively.

This device shows the optimal output power, reporting a linear laser characteristic with peak power values of 0.4 mW (for T=12°C) and exceeding 0.6 mW (for T=14°C) as depicted in Fig. 5.55(a) and Fig. 5.56(a). However, the inspection of the 3D color-map plots in Fig. 5.55(b) and Fig. 5.56(b) reveals marked resonant hopping across the current, with a clear redshift in the emitted laser wavelengths when the temperature is increased from 12 °C to 14 °C, particularly in the range from 100 mA to 150 mA.

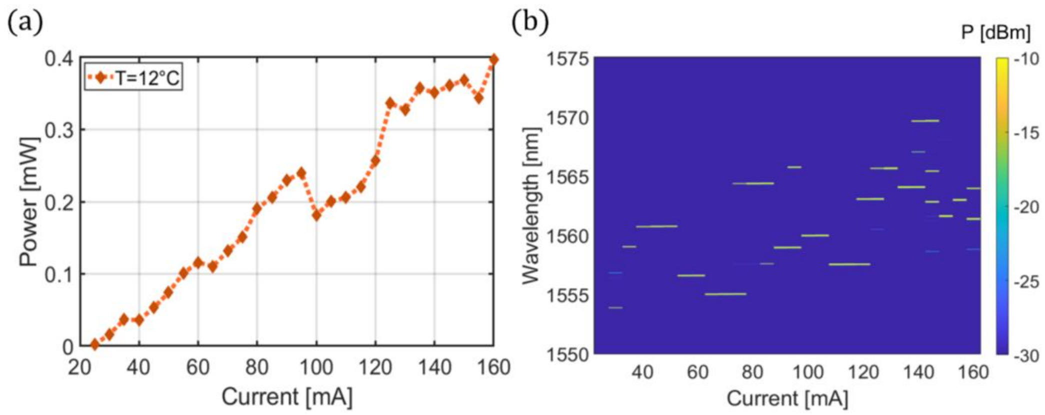

Figure 5.55: (a) Linear laser characteristic at T=12°C with output power reaching 0.4 mW, without reaching the saturation current. (b) Emitted laser power as a function of the RSOA current and the wavelength (colorbar power values span from -10 dBm to -30 dBm).

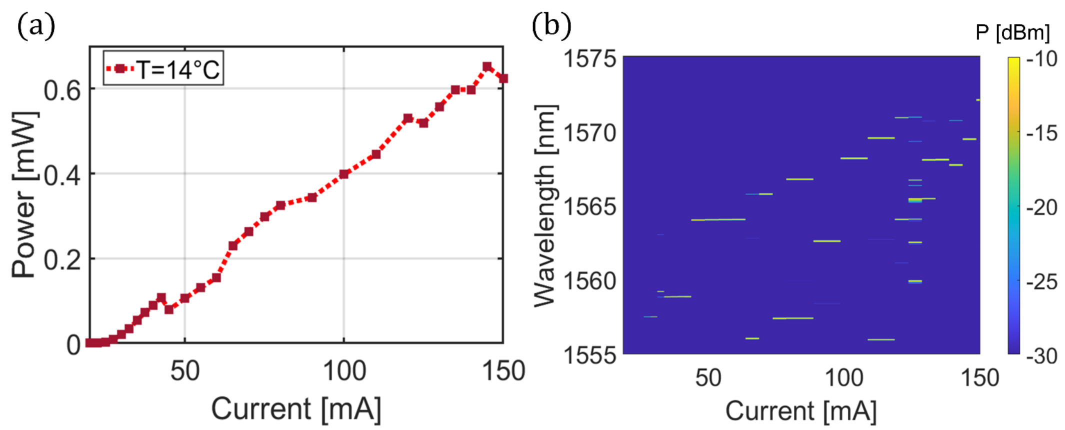

Figure 5.56: (a) Linear laser characteristic at T=14°C with output power exceeding 0.6 mW, without reaching the saturation current. (b) Emitted laser power with respect to RSOA injection current and wavelength (colorbar depicts power values span from -10 dBm to -30 dBm).

5.3.8 Future optimizations on the transfer printed HECLs

The transfer printed HECLs demonstrated in this work provides a clear proof of concept that stable single-wavelength operation can be realized in a highly compact hybrid external-cavity laser. This result marks an important step toward the final integration pathway envisioned in this thesis, enabled by advanced heterogeneous hybrid integration techniques. Future implementations should further optimize power coupling performance by employing more efficient spot-size converters between the RSOA and the SiN PIC.

The implemented polymer-based taper replacement with a higher-index material (such as silicon) that is more closely matched to the RSOA refractive index, has been demonstrated in [17] as efficient solution at the cost of slightly increased process complexity compared to SU-8 EBL technique. In addition, dedicated mode converters between the SiN waveguide and lensed fibers could be introduced to maximize the collected output power or ideally integrate transfer printed photodetectors, enabling an ultra-compact, packaged HECL, as discussed in Chapter 6.

Optimization of butt coupling between the different sections alone does not resolve the parasitic reflections arising from discontinuities in the optical cavity, which remain a major limitation. For this reason, evanescent coupling has emerged as a particularly promising solution for Si/SiN-based μ-TP lasers [17], as it can strongly suppress such parasitic reflections while efficiently transferring the optical field from the gain section into the passive core waveguides. This approach, however, relies on carefully engineered adiabatic tapers to ensure low-loss and wavelength-dependent power transfer.

From an operational point of view, the main challenge for single-wavelength HECLs lies in suppressing both resonant hopping and mode hopping between longitudinal modes within a single SC-FP reflection peak. The latter phenomenon can be mitigated by increasing the cavity Q-factor (sharper resonances) and/or shortening the external-cavity length to the centimeter scale, in order to approach a one-to-one overlap between a single SC-FP reflection peak, a supported longitudinal cavity mode, and the gain spectrum. Reduction of the resonant-hopping effect has been proved being obtained by adopting shorter geometrical cavity in the FP resonator in order to support only few, widely spaced reflection peaks in the DBR stopband.

This design choice entails a trade-off: shortening the cavity length reduces the Q-factor and thus the resonance sharpness, whereas increasing the coupling gap to compensate for the shorter cavity improves the Q-factor but lowers the overall reflectivity. Alternatively, the coupler and resonator architecture can be engineered to enhance both the extinction ratio and the reflectivity of a specific Fabry–Pérot resonance within the stopband, thereby enforcing stable single-mode operation. This selectivity can be achieved by employing wavelength-dependent side-couplers or by optimizing mode-matching conditions for a targeted resonance.

Furthermore, the integration of phase-shifting gratings [18],[19], typically introducing a π-phase discontinuity, offers a powerful mechanism for spectral control. By creating a narrow transmission window within the broader stopband, phase-shifted gratings intrinsically lock the laser emission to a precise resonant frequency, simultaneously improving side-mode suppression and reducing sensitivity to environmental fluctuations that typically trigger mode hopping.

A significant limitation of this approach is the relatively low loaded Q-factor observed experimentally, measured at approximately $Q \approx 1.4 \times 10^4$ [18] in SiN, and $Q \approx 1.2 \times 10^4$ [19] in SOI platforms. Consequently, the FWHM of the phase-shifted reflection peak, particularly when utilized in an evanescent coupling scheme, is on the order of 130 pm. This broad resonance width is insufficient to ensure stable single-longitudinal-mode operation in non-ultra-compact cavities, as it allows for mode-hopping between the longitudinal modes supported by the external-cavity.

5-References

[1] Butler, Sharon Marie. *Wavelength Swept Photonic Crystal Laser*, Ph.D. Diss. Munster Technological University of Cork, 2021.

[2] Loi, Ruggero, et al. "Transfer printing of AlGaInAs/InP etched facet lasers to Si substrates." *IEEE Photonics Journal* 8.6 (2016): 1-10.

[3] Zhang, Jing, et al. "Transfer-printing-based integration of a III-V-on-silicon distributed feedback laser." *Optics express* 26.7 (2018): 8821-8830.

[4] Roelkens, Gunther, et al. "Micro-transfer printing for heterogeneous Si photonic integrated circuits." *IEEE Journal of selected topics in quantum electronics* 29.3: Photon. Elec. Co-Inte. and Adv. Trans. Print. (2022): 1-14.

[5] Wang, Zhechao, et al. "Novel light source integration approaches for silicon photonics." *Laser & Photonics Reviews* 11.4 (2017): 1700063.

[6] Roelkens, Günther, et al. "III-V/silicon photonics for on-chip and intra-chip optical interconnects." *Laser & Photonics Reviews* 4.6 (2010): 751-779.

[7] Ghosh, Samir, et al. "Scalable transfer printing approach to heterogeneous integration of InP lasers on silicon-on-insulator waveguide platform." *Applied Physics Letters* 125.8 (2024).

[8] Sumon, Md Saiful Islam, et al. "Efficient on-chip green light generation via frequency upconversion in SiN–transfer-printed LN hybrid waveguides." *Optics Letters* 50.10 (2025): 3281-3284.

[9] Badri, S. Hadi, et al. "Compact modulators on silicon nitride waveguide platform via micro-transfer printing of thin-film lithium niobate." *Scientific Reports* 15.1 (2025): 11681.

[10] Maeda, Yoshiho, et al. "Micro-transfer-printed membrane distributed reflector lasers on Si waveguide modulated with 50-Gbit/s NRZ signal." *Journal of Lightwave Technology* 41.12 (2023): 3866-3873.

[11] Atar, Fatih, et al. "First Demonstration of a Fully Integrated Hybrid External Cavity Laser in Edge-Coupling Configuration via µTransfer-Printing." *2024 IEEE Silicon Photonics Conference (SiPhotonics)*. IEEE, 2024.

[12] https://x-celeprint.com/.

[13] O'Callaghan, James, et al. "Comparison of InGaAs and InAlAs sacrificial layers for release of InP-based devices." *Optical Materials Express* 7.12 (2017): 4408-4414.

[14] Zhang, Jing, et al. "Micro-transfer printing InP C-band SOAs on advanced silicon photonics platform for lossless MZI switch fabrics and high-speed integrated transmitters." *Optics Express* 31.26 (2023): 42807-42821.

[15] Roelkens, Gunther, et al. "Present and future of micro-transfer printing for heterogeneous photonic integrated circuits." *APL Photonics* 9.1 (2024).

[16] Corbett, Brian, et al. "Transfer print techniques for heterogeneous integration of photonic components." *Progress in Quantum Electronics* 52 (2017): 1-17.

[17] Poelman, Stijn, et al. "High-power heterogeneously integrated mode-locked laser enabled by a booster amplifier." *Optics Express* 33.26 (2025): 54747-54756.

[18] Husko, Chad, et al. "Phase-shifted Bragg gratings in a foundry silicon nitride platform." OSA Continuum 4.3 (2021): 933-939.

[19] Zhao, Yong, et al. "Side-coupled Fabry-Perot resonator filter based on dual-waveguide Bragg grating." Journal of Lightwave Technology 40.19 (2022): 6454-6464.

Chapter 6: Refractive index sensing and space applications

This final chapter discusses the future perspectives and potential applications of the side-coupled Fabry–Pérot resonators investigated throughout the thesis, with a particular focus on their use as compact refractive index (RI) sensors. The sensing performance of a simple SC-FP architecture is first examined through experiments involving NaCl solutions and deionized water as analytes. The analysis highlights the resonance wavelength shift and the corresponding limit of detection, which serve as the main figures of merit for assessing the device sensitivity.

The concept is then extended to more complex configurations based on coupled SC-FP resonators, forming so-called photonic molecules. These structures enable multi-parameter sensing, as the resonance splitting provides two independent spectral readouts for each original SC-FP mode. In this framework, both the resonance wavelength shifts, and the extinction ratio variations induced by the presence of the analyte are considered, further enhancing the sensing capability. The potential of the photonic molecule sensor architecture is also extended to the implementation of air-gap SC-FPs, which can substantially improve the interaction volume with the surrounding environment. Experimental demonstrations confirm the enhanced sensitivity of such air-gap implementations compared to conventional SC-FP designs.

The potential of SC-FP-based HECLs for refractive index sensing is further explored. A compact, stable, narrow-linewidth single-wavelength laser enables sensing of liquids or gases, while arrays of HECLs support heterodyne schemes to achieve very low limits of detection (LODs). Finally, future development of multi-wavelength HECLs in space are discussed building on prior demonstrations in free-space optical links, atomic clock networks, spectroscopy, remote atmospheric sensing, and astronomical applications.

6.1 Passive SC-FP for RI sensing

The passive SC-FP resonator, whose design is presented in the schematic of Fig. 3.3 in Chapter 3, has been effectively employed for refractive-index sensing under different upper cladding conditions. The analyzed structure comprises a cavity length $L = 600\ \mu$m, separated by a coupling gap G=700 nm bounded by two DBR sections with $N = 1975$ uniform periods and $N_T = 25$ apodized periods on each side. The gratings feature a rectangular corrugation whose widths are $W_1 = 1.3\ \mu$m, $W_2 = 2.5\ \mu$m, and duty cycle is 50%.

The upper cladding environment is modified by depositing droplets of deionized (DI) water and aqueous NaCl solutions with different concentrations onto the resonator surface, in addition to the reference characterization with air cladding. Sensing relies on changes in the surrounding refractive index, due to the presence of an analyte, which modifies the guided mode's effective index in the FP cavity and shifts the resonance wavelengths ($\Delta\lambda$). In this context, the transmission spectra recorded for the different analytes are acquired at the OSA, as depicted in Fig. 6.1(a).

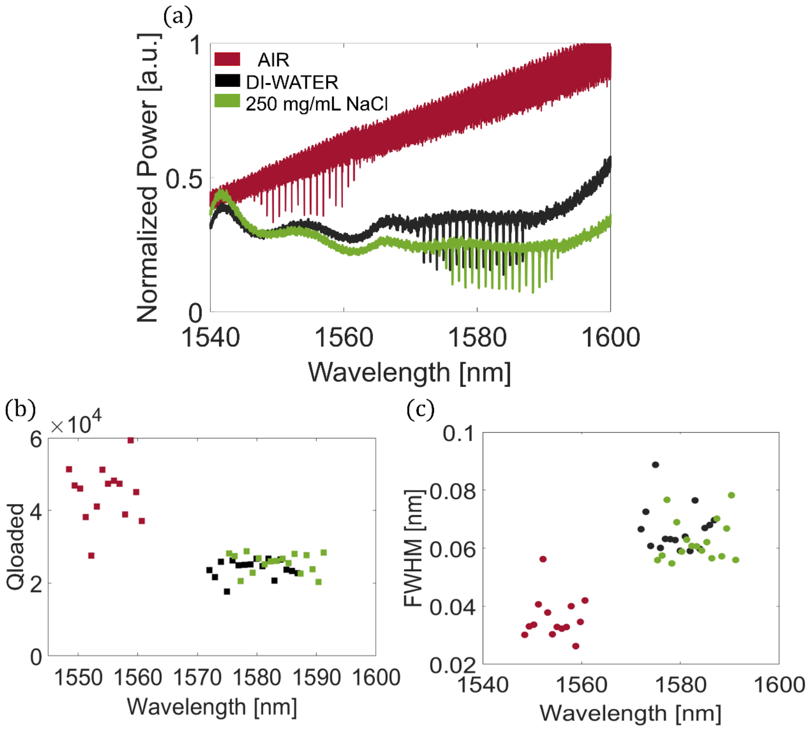

Figure 6.1: (a) SC-FP experimental transmission response when air (red), DI-water (black), and NaCl solution (green) are considered as upper cladding. Comparison between loaded Q-factors (b), and FWHM values (c) for the different upper claddings.

To transduce the resonances shift into a comparable sensor metric, a key parameter is the sensitivity $S = \frac{\Delta\lambda}{\Delta n_c}$, which quantifies the wavelength shift $\Delta\lambda$ per unit refractive index change Δn_c in the cladding medium. Moreover, the use of DI water and NaCl solutions leads to additional optical losses that significantly impact cavity performance. These losses arise mainly from increased absorption in the liquid cladding and enhanced scattering at the waveguide–liquid interface, as the refractive-index contrast between the core and cladding is reduced.

Consequently, the loaded Q-factor and the FWHM exhibit noticeable degradation, decreasing from average values of $Q_L \approx 5\times10^4$ and FWHM ≈30 pm in air to around $Q_L \approx 2.5\times10^4$ and FWHM ≈70 pm in DI water and 250 mg/mL NaCl solution, respectively, as shown in Fig. 6.1(b–c). This degradation reflects the increased attenuation of the resonance field interacting with the external medium and highlights the inherent trade-off between optical confinement and sensitivity in evanescent-field sensing configurations.

The sensitivity of the fabricated device is experimentally determined by analyzing the spectral shift between the last resonance measured in air and in DI water, as expressed in Eq. (6.1). Additionally, Eq. (6.2) reports the analogous spectral shift observed when comparing the spectra measured in DI water and in a 250 mg/mL NaCl solution. Spectral shifts of the resonance peaks are monitored to evaluate the refractive-index sensitivity of the SC-FP sensor as shown in Fig. 6.2.

$$S_{\lambda,AIR\,-\,DI\,WATER} = \frac{\Delta\lambda}{\Delta n_c} = \frac{(1586.83 - 1561.55)\,nm}{(1.3162 - 1)} \approx 79.95\,nm/RIU \tag{6.1}$$

$$S_{\lambda,DI\,WATER-NaCl} = \frac{\Delta\lambda}{\Delta n_c} = \frac{(1591.17 - 1586.83)\,nm}{(1.36 - 1.3162)} \approx 99\,nm/RIU \tag{6.2}$$

where the refractive index value for DI-water and the NaCl solutions are obtained from the data reported in Ref. [1]. Another parameter that can be derived from the device response is the minimum detectable refractive-index change, also known as the limit of detection (LOD). This figure of merit represents the smallest refractive-index variation that can be distinguished by the sensor and is calculated as [2]:

$$LOD_{AIR\,-\,DI\,WATER} = \frac{\lambda_{RES}}{Q_L\, S_{\lambda,AIR\,-\,DI\,WATER}} \approx 6.58 \times 10^{-4}\,RIU \tag{6.3}$$

$$LOD_{DI\,WATER-NaCl} = \frac{\lambda_{RES}}{Q_L\, S_{\lambda,DI\,WATER-NaCl}} \approx 5.32 \times 10^{-4}\,RIU \tag{6.4}$$

where the Q_L values and sensitivities in Eqs. (6.3), (6.4) are extracted from Figs. 6.1(b) and 6.2.

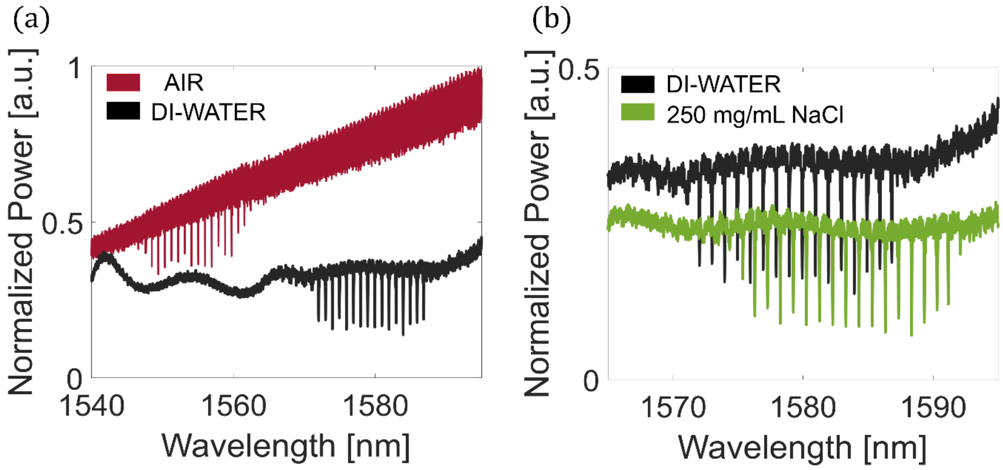

Figure 6.2: Overview of the resonances shift $\Delta\lambda$: (a) between air and DI-water cladding, and (b) between DI-water and 250 mg/mL NaCl concentration.

6.2 SC-FP based photonic molecule for RI sensing

A photonic molecule (PM) is formed by the optical coupling of two or more micro-resonators whose evanescent fields overlap strongly enough that their individual resonances hybridize into collective super-modes [3].

When resonators such as microrings or Fabry–Pérot cavities are placed in close proximity, the evanescent field of one perturbs the optical mode of the other, splitting the original single resonance into a characteristic pair of eigenfrequencies: a lower-frequency symmetric (bonding) super-mode, where fields in the two resonators oscillate in phase, and a higher-frequency antisymmetric (antibonding) super-mode, where they oscillate out of phase. This behavior occurs in direct analogy with the electronic states of diatomic molecules. The splitting magnitude, known as the coupling strength or resonance splitting λ_{split}, scales inversely with the physical separation between resonators [4-6] and depends on the overlap integral of their evanescent fields. This electromagnetic coupling produces new optical properties, including mode splitting, tailored line shapes, and enhanced field interactions, which can be leveraged for spectroscopy [4],[5], modulation [6], signal processing [7], and advanced sensing [8].

In this section, the use of two coupled SC-FP architectures, referred to as the main and auxiliary Fabry–Pérot resonators, is demonstrated for the realization of a photonic molecule, as illustrated in Fig. 6.3, and exploited as a compact refractive index sensor. Specifically, the electric field profiles of the anti-symmetric and symmetric modes in the resonant cavity of the main FP are illustrated in the red box in Fig. 6.3.

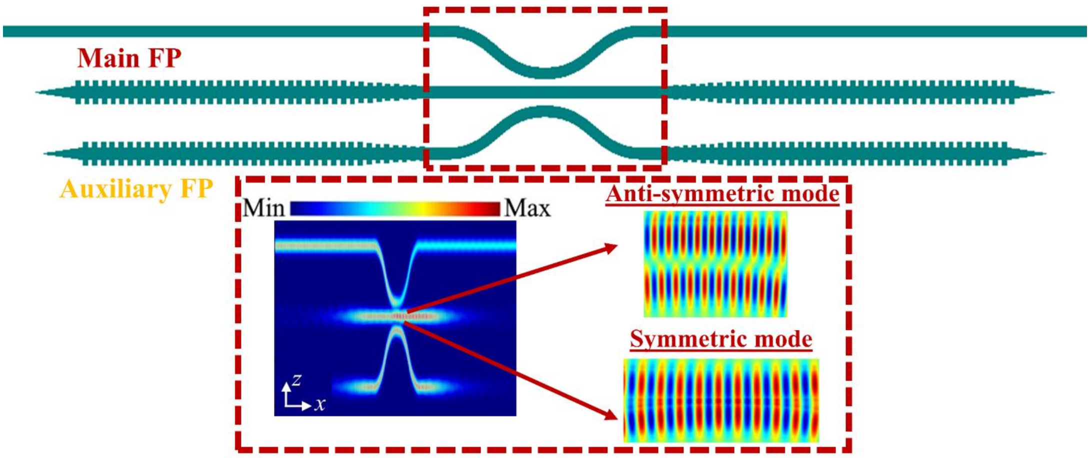

Figure 6.3: Schematic of the photonic molecule architecture based on two coupled SC-FP resonators. Zoom-in of the coupling region illustrating the formation of symmetric and anti-symmetric super-modes.

The input optical signal is side-coupled into the main FP resonator via a bent waveguide, spaced *D*=13 µm from the FP cavity, and implemented as a Bézier curve with optimized bending radii

(L_{bend}=150 μm) selected to minimize field distortion and loss, as detailed in Chapter 3. The main FP resonator is evanescently coupled to the auxiliary FP resonator via a tunable coupling gap that tunes the strength of the resonance splitting in the resulting photonic molecule. Each FP resonator consists of a cavity length L enclosed by engineered DBR mirrors, either uniform or apodized, to control mirror reflectivity and penetration length.

The fabricated PM is realized on 300 nm-thick LioniX SiN platform by means of the same fabrication process detailed in Section 5.2.1. The DBR sections feature a periodicity P = 485 nm, duty cycle DC=50%, corrugation widths W_1=1300 nm, and W_2=2400 nm, while combining N_{BG}=2000 uniform grating periods and N_{taper}=50 apodized grating period. The main and auxiliary FPs are symmetric, and employ L=789×P, and G=450 nm. The schematic of the implemented photonic molecule is reported in Fig. 6.4(a), while details of the etched uniform and apodized DBRs are highlighted in yellow boxes in Fig. 6.4(b).

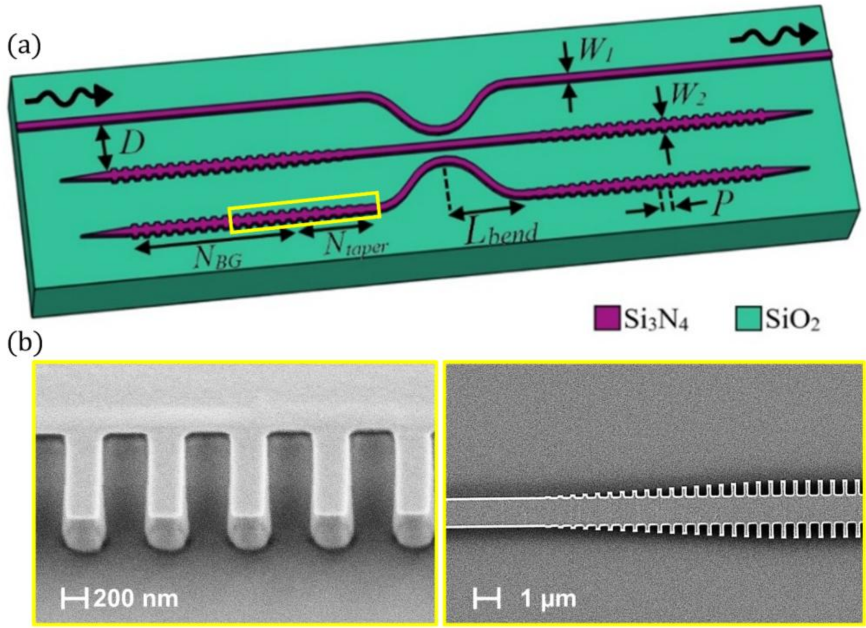

Figure 6.4: (a) Schematic of the designed SC-FP-based photonic molecule, with key design parameters. (b) SEM images of the etched uniform and apodised DBRs.

The transmission response of the structure under air cladding is reported in Figure 6.5(a). When an analyte covers the device, its refractive index affects the coupling strength between the resonators. Therefore, it enables both resonance shifts and changes in resonance splitting, providing a robust and multi-parameter sensing mechanism and read-out for sensor, enhancing sensitivity and reliability.

To test the sensing performance of the photonic molecule, both DI water and different concentrations of NaCl solutions ranging from 0 to 250 mg/ml were prepared and applied as analytes via a single droplet dispensed onto the chip surface. Specifically, based on the analysis of the recorded transmission spectra for DI water and a 250 mg/ml NaCl solution, Fig. 6.5(b) reports the resonance shift ($\Delta\lambda$), the change in extinction ratio (ER_{split}), and the resonance splitting (λ_{split}). ER_{split} represents the difference in the extinction ratios of the resonant dips in transmission spectrum, while λ_{split} is the spacing between the produced split resonances. ER_{split}, $\Delta\lambda$, and λ_{split} can be simultaneously analyzed to accurately evaluate the refractive index of the analyte. As the refractive index of the analyte increases, ER_{split} also rises, indicating a pronounced change in the resonance splitting.

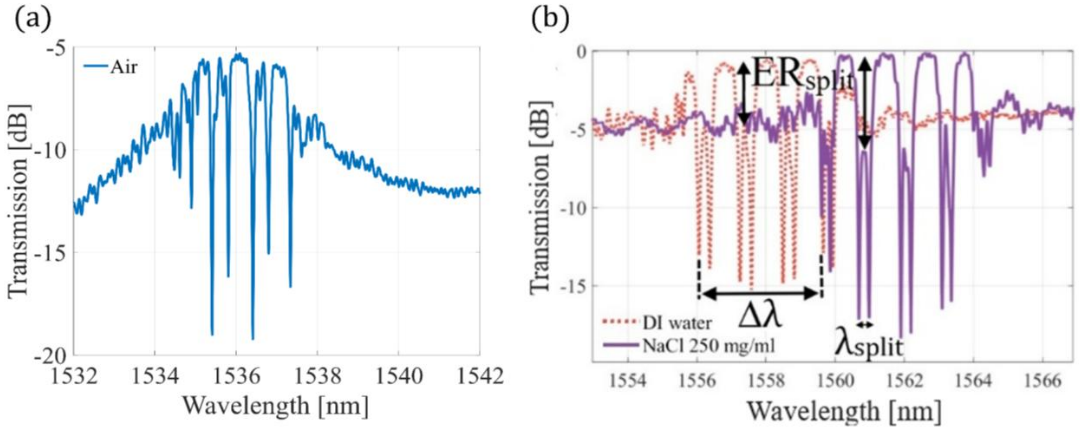

Figure 6.5: Transmission response of the photonic molecule based on *G*=450 nm. (a) air cladding, (b) DI-water and NaCl analyte presence.

For instance, ER_{split} is measured to be 3.89 dB for DI water and increases to 6.25 dBm for an NaCl solution with a concentration of 250 mg/ml.

Additionally, the resonance wavelengths exhibit a shift as the refractive index changes. In particular, when the cladding is changed from DI water to a NaCl solution at 250 mg/ml, the resonance undergoes a wavelength shift of $\Delta\lambda$≈3.54 nm. At the same time, λ_{split} decreases with the increasing refractive index, reporting values of 440 pm in air, 328 pm in DI water, and 296 pm in the 250 mg/ml NaCl solution. The sensor achieves a sensitivity:

$$S_{\lambda,DI\,WATER-NaCl} = \frac{\Delta\lambda}{\Delta n_c} = \frac{(3.54)\,nm}{(1.36-1.3162)} \approx 80.8\,nm/RIU \tag{6.5}$$

By considering higher-Q super-mode characterized by a loaded Q-factor Q_L≈2×10^4, the LOD results:

$$LOD_{DI\,WATER-NaCl} = \frac{\lambda_{RES}}{Q_L\,S_{\lambda,DI\,WATER-NaCl}} \approx 9.7\times10^{-4}\,RIU \tag{6.6}$$

Tuning geometric parameters, such as cavity length, coupling gap, and Bragg grating features, can optimize sensor performance for specific applications. When an identical high coupling gap

(G=600 nm) is implemented between the two side-coupled FPs, enhancements in terms of the sensitivity are achieved as shown in Fig. 6.6.

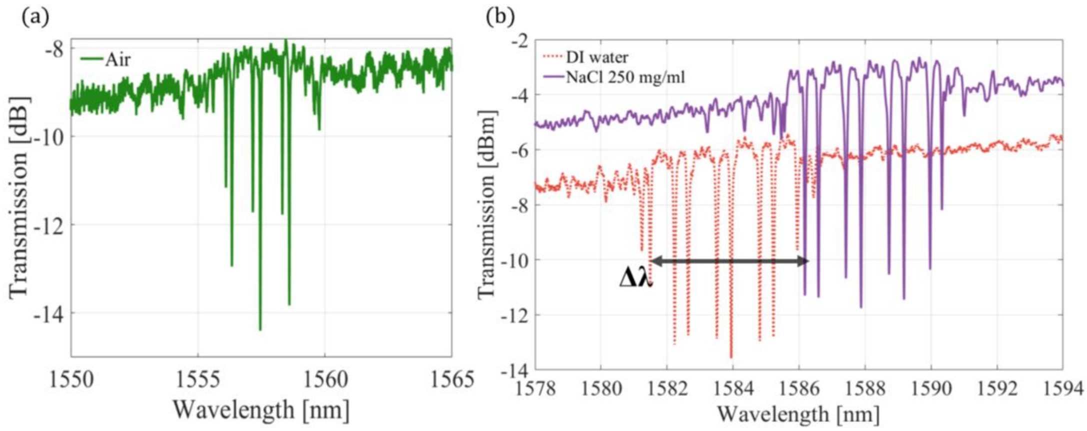

Figure 6.6: Transmission response of the photonic molecule based on *G*=600 nm. (a) air cladding, (b) DI-water and NaCl analyte presence.

Analysis of the sensitivity between DI-water analyte and 250 mg/mL NaCl solution shows a wavelength shift of 4.94 nm between the two envelopes. This shift corresponds to sensitivity:

$$S_{\lambda,DI\ WATER-NaCl} = \frac{\Delta\lambda}{\Delta n_c} = \frac{(4.94)\ nm}{(1.36-1.3162)} \approx 112\ nm/RIU \qquad (6.7)$$

This result is higher compared to Eq. (6.5), valid for G=450 nm. In addition, the loaded Q-factor of ~3.5×10^4 for the split resonant mode in the NaCl case allows the estimation of the LOD as:

$$LOD_{DI\ WATER-NaCl} = \frac{\lambda_{RES}}{Q_L\ S_{\lambda,DI\ WATER-NaCl}} \approx 4\times10^{-4}\ RIU \qquad (6.8)$$

The multi-parameter sensing capability of the proposed photonic molecule ensures reliable detection and precise evaluation of refractive indices for various analytes. These properties position SC-FP photonic molecules as versatile platforms for hybrid lasers, where super-modes select wavelengths within SOA gain, nonlinear optics, and sensors with specific aim for utilizing as refractive index sensors.

6.2.1 SWG Bragg-grating implementation

This subsection extends the SC-FP-based photonic molecule architecture by incorporating subwavelength gratings (SWGs) [9], enabling coupling between air-gap identical SC-FP structures analogous to those presented in Chapter 3.

These SWG mirrors are formed by alternating low-index air regions and high-index SiN regions with a fixed periodicity P_{SWG}, designed to operate in the Bragg regime. The transition from the single-mode resonator cavity waveguide (W_1=1300 nm) to the air gap is achieved through smooth tapering down to a tip width of 20 nm over a length L_{taper}, while W_2 is fixed at either 2300 nm or 3000 nm. SWG-based mirrors offer two primary advantages: enhanced field penetration into the surrounding analyte for improved sensitivity, and broadband high reflectivity potentially over much shorter lengths compared to conventional DBRs, reducing footprint for integrated sensing.

Among the fabricated devices, the geometrical parameters that deliver the best RI sensing performance are: P_{SWG} = 520 nm, f =50%, W_1 = 1300 nm, W_2 = 3000 nm, G=600 nm, L_{bend} = 200 μm, L_{cavity} = 960×P_{SWG}, D = 12 μm, L_{SWG} = 2000×P_{SWG}, and L_{taper} = 100×P_{SWG}. Where, in this representation f refers to the duty cycle. Figure 6.7(a) depicts the schematic of the SWG-based photonic molecule in this thesis, summarizing key design parameters.

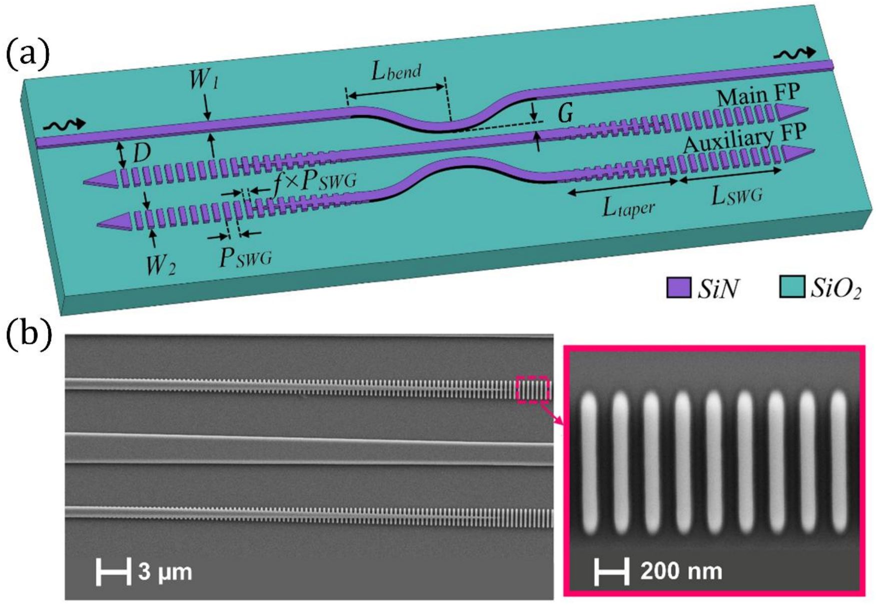

Figure 6.7: (a) Schematic of the SWG-based photonic molecule resonator. (b) SEM images showing the fabricated air-gap gratings and the levels of the PM device.

These parameters yield a stopband width of approximately $\Delta\lambda \approx 90$ nm in air cladding, representing a further enhancement over the air-gap grating results previously reported in Chapter 3 for the family C architecture. Additionally, the reflectivity and dispersion properties of SWG mirrors can be engineered by adjusting the period, duty cycle, and etch depth as already shown for the DBR gratings.

The devices are fabricated on a 300 nm-thick SiN platform with a 3 μm-thick silicon dioxide BOX layer using a deep ultraviolet (DUV) stepper photolithography multi-project wafer process provided by CORNERSTONE [10]. Further details on the fabrication flow and design parameters are reported in [11]. SEM images of the fabricated device, confirming pattern fidelity for the SWG gratings, are shown in Fig. 6.7(b). Under air and DI water claddings (considering W_2=3000 nm and G=600 nm), the photonic molecule exhibits a pair of split resonances corresponding to symmetric and antisymmetric super-modes.

One mode features lower Q-factor with high extinction, while the other has high-Q but lower extinction. This asymmetry can be explained by considering the relative coupling strengths. The main FP, being directly coupled to the bus waveguide, experiences stronger coupling and thus higher coupling loss, leading to a broader resonance with greater extinction, while the auxiliary FP is more weakly coupled to the external waveguide and it experiences reduced coupling loss yielding a narrower linewidth and higher Q-factor. The simultaneous presence of these two modes provides a dual-readout mechanism: the low-Q, high-extinction mode facilitates robust detection under noisy conditions, while the high-Q mode enables high-resolution detection of subtle refractive index changes [11].

When the cladding is changed from air to DI water, the loaded Q-factor decreases because the higher cladding index reduces SWG mirror index contrast and Bragg reflectivity, and water absorption adds extra loss, shortening the photon lifetime. Simultaneously, the wavelength separation between split resonances increases from λ_{split}≈0.26 nm (air) to λ_{split}≈0.46 nm (DI water), as reported in Fig. 6.8, indicating analyte sensitivity of the coupling-induced splitting.

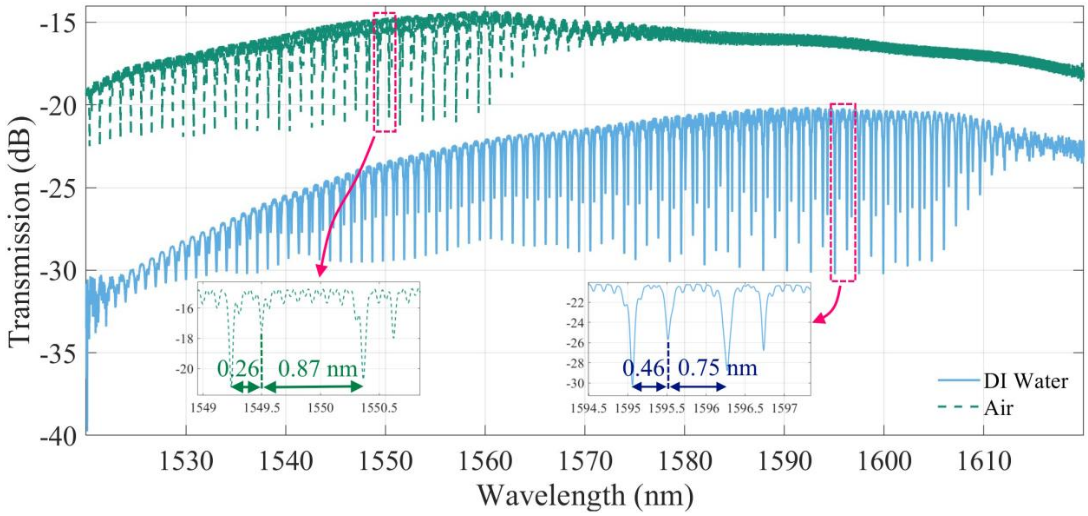

Figure 6.8: Measured transmission spectra of the sensor with G=600 nm and W_2=3000 nm using air (green) and DI water (blue) as upper cladding.

To compare sensing performance between Section 6.1 and Section 6.2 configurations, NaCl solutions from 0 mg/mL (DI water) to 15 mg/mL (in 2.5 mg/mL steps) are applied as analytes on the architecture defined in Figure 6.7(a). Transmission spectra were recorded for each concentration. Analysis of the super-mode resonance shift $\Delta\lambda$ yields a maximum sensitivity:

$$S_{\lambda,DI\,WATER-NaCl} = \frac{\Delta\lambda}{\Delta n_c} = \frac{(0.4\,nm)}{(1.36 - 1.3162)} \approx 166\,nm/RIU \tag{6.9}$$

The refractive index difference between 0 and 15 mg/mL NaCl is calculated using the formulation in [1], while the corresponding wavelength shifts are shown in Fig. 6.9(a). This sensitivity represents a significant enhancement over non-air-gap configurations detailed in the previous subsection. For the higher-Q super-mode (Q_l=2.1 × 10^4), the limit of detection remains comparable to previous sections and is estimated as:

$$LOD_{DI\,WATER-NaCl} = \frac{\lambda_{RES}}{Q_L\,S_{\lambda,DI\,WATER-NaCl}} \approx 4.4 \times 10^{-4}\,RIU \tag{6.10}$$

Moreover, tracking resonance shifts across NaCl concentrations reveals a clear linear trend between $\Delta\lambda$ and analyte concentration (Fig. 6.9(b)), obtained by fitting experimental data points. Deviations from this linearity provide insight into the sensor's response fidelity and reveal any systematic non-idealities.

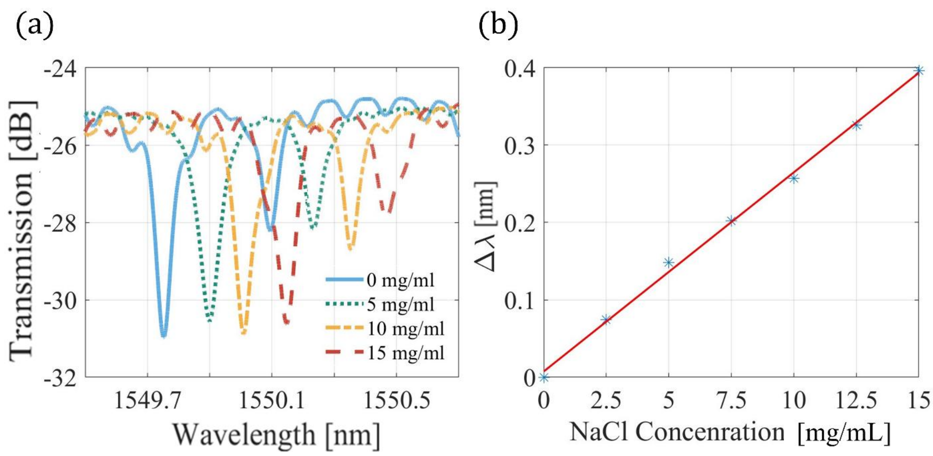

Figure 6.9: Effect of different NaCl concentrations. (a) Transmission plots, and (b) resonance shift response.

6.3 HECL for RI sensing

In HECLs, such as the architectures detailed in Chapter 5, the most promising application is refractive index sensing. The underlying physics arises from evanescent field overlap between the SiN 1D photonic crystal cavity mode on a CMOS-compatible PIC platform and perturbations in the analyte cladding.

The sensing dynamic in HECL is mainly due to two features. Firstly, the fraction of the mode volume extends into the upper asymmetric cladding (either gas or liquid analyte), such that cladding RI perturbation (Δn_c) shifts the effective index n_{eff}, and consequently the resonance wavelength λ_{res}. Moreover, shifts in the resonator resonances modulate the HECL lasing condition, allowing the spectral shift and the sensor's LOD performance to be directly tracked from the laser emission. Its narrow and stable emission further improves the detection limit. A conceptual schematic of the proposed HECL-based RI sensor is shown in Fig. 6.10.

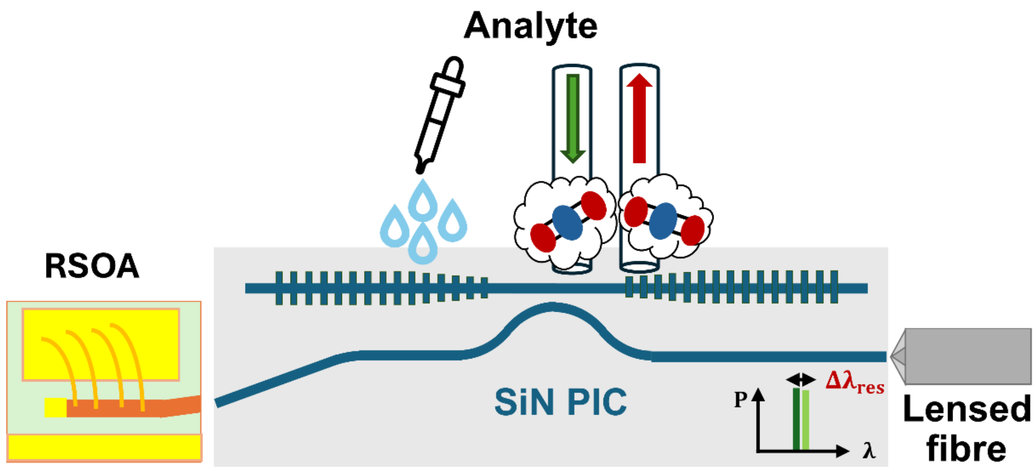

Figure 6.10: Schematic of the HECL architecture: an analyte, introduced as a cladding around the PIC waveguides (via liquid or gas flow), perturbs the external-cavity and is transduced into changes in the laser output, enabling quantitative evaluation of LOD, sensitivity, or discrimination between different analytes.

Ref. [12] compares the performance of a passive high-Q resonator based on 1D photonic crystal cavities with its integration into a hybrid external-cavity laser architecture, achieving mode-hop-free single-mode operation with side-mode suppression ratio >40 dB. While sensitivity remains consistent to around 150 nm/RIU in liquids, comparable to standalone passive cavities, the HECL configuration enhances detection limits by over an order of magnitude (e.g., from ~10^{-3} RIU to <6.6×10^{-5} RIU), owing to the laser's ultra-narrow linewidth versus the broader resonance dips of passive resonators.

Specifically, the HECL operating as a RI sensor, was tested with solutions of sugar in DI water at increasing concentrations from 0% to 25% in 5% steps, demonstrating approximately linear resonance wavelength shifts with sugar concentration. This exceptional sensitivity enables far superior detection of minute concentration changes, compared to conventional optical sensors, paving the way for compact, mass-producible silicon-chip lab-on-a-chip devices ideal for food quality testing, environmental monitoring, and rapid point-of-care medical diagnostics.

In addition, microfluidic integration is transforming passive resonator sensing by enabling continuous, dynamic liquid refractive-index measurements while using low-volume channels that help minimize dispersion. Transitioning from proof-of-concept drop-casting to practical analytical tools, integrated microfluidic channels over optical micro-resonators tightly confine and guide the liquid analyte across the sensing region. They require only tens to hundreds of nanoliters for complete cladding exchange, far more efficient than repeated microliter-scale pipetting used in commercial RI detectors (~60 μL).

This approach drastically reduces sample dilution and peak broadening, yielding flow injection analysis (FIA) and high-performance liquid chromatography (HPLC) peaks with transient full width at half maximum of ~5–6 s, compared to ~10 s for conventional methods [13]. Injection in stop-flow mode, driven by peristaltic or HPLC pumps, generates highly reproducible concentration profiles, enabling accurate calibration curves and LODs down to $\sim 10^{-6}$ RIU under realistic flow conditions, not static droplets. Furthermore, sealed PDMS or pressure-sensitive adhesive (PSA) chips prevent evaporation and cross-contamination while supporting surface functionalization and multi-sensor arrays, key aspects for biosensing and chromatographic applications.

In Ref. [13], using glucose solutions as test samples, the device was benchmarked against a commercial RI detector, achieving a sensitivity of 113 nm/RIU and a LOD of 2.3×10^{-6} RIU (0.014 g/L glucose), in line with prior HPLC demonstrations for sugar separation reported in [14]. Looking ahead, integrating these microfluidic sensing strategies with hybrid external-cavity laser-based interrogation promises even higher sensitivity, frequency stability, and compactness, paving the way toward fully integrated, real-time chemical and biosensing platforms.

6.3.1 Optical heterodyne sensing

The optical heterodyne technique introduced in Chapter 5 for laser linewidth characterization of both the two-chip butt-coupled and transfer-printed HECLs can also be employed as a sensing scheme, enabling the detection of very small refractive-index changes in the cladding.

When a reference laser, typically a tunable laser source acting as the local oscillator (LO), is mixed with the single-wavelength emission from the HECL, their interference generates a beat frequency within the photodetector's RF bandwidth, determined by the HECL resonance wavelength. In this configuration, the fixed LO is combined with the analyte-sensitive HECL output; variations in the upper cladding refractive index shift the photonic crystal cavity resonance, thereby changing the HECL lasing wavelength and, consequently, the beat frequency. Since heterodyne detection can resolve shifts down to the laser's intrinsic linewidth, it provides orders-of-magnitude higher precision than conventional spectrometric methods.

A first demonstration of optical heterodyne sensing exploiting HECL architecture has been achieved in [15]. By varying the gas mixture between N_2 (n = 1.000294) and CO_2 (n = 1.000438) using mass-flow control within a flow chamber, the cladding RI of the HECL changes, leading to a shift in the lasing wavelength and, consequently, in the beating tone. Specifically, an increase in CO_2 concentration induces a red shift in the beat signal.

With a beat linewidth of 1.6 MHz, the system achieved an intrinsic detection limit of 1.59×10^{-7} RIU, significantly surpassing passive resonator sensors (typically $\sim10^{-4}$ RIU) and direct lasing detection, thanks to linewidth-limited resolution. Future developments of HECL-based SC-FP sensors employing heterodyne optical techniques will focus on enhancing coupling efficiency and mechanical stability, thereby boosting LOD performance through minimized phase noise and drift while maintaining linewidth-limited resolution.

This advancement can be achieved through the use of the micro-transfer printing process, enabling the realization of scalable and highly compact RI sensors. Moreover, HECL stability can be further improved by integrating micro-heaters on the PIC at the most sensitive regions of the resonator, such as a section of the Fabry--Pérot cavity, to fine-tune the resonant modes and compensate for the thermal effects discussed in Section 5.1. Another key enhancement should remove the external reference laser, by considering the beating between two identical HECL structures (matched gain chip and SC-FP resonators, within fabrication repeatability limits). The resulting beat frequency shift directly encodes differential RI sensitivity or thermal crosstalk, enabling self-referenced, chip-scale heterodyne detection for ultra-stable, calibration-free sensing. Additionally, the absence of a reference external laser leads to a more integrated system and eliminates the limitations imposed by the LO linewidth; thus, extremely narrow emitted laser lines can significantly enhance the sensor's limit of detection. A schematic of this future development, under the case of two-chips butt-coupled HECLs, is reported on Fig. 6.11.

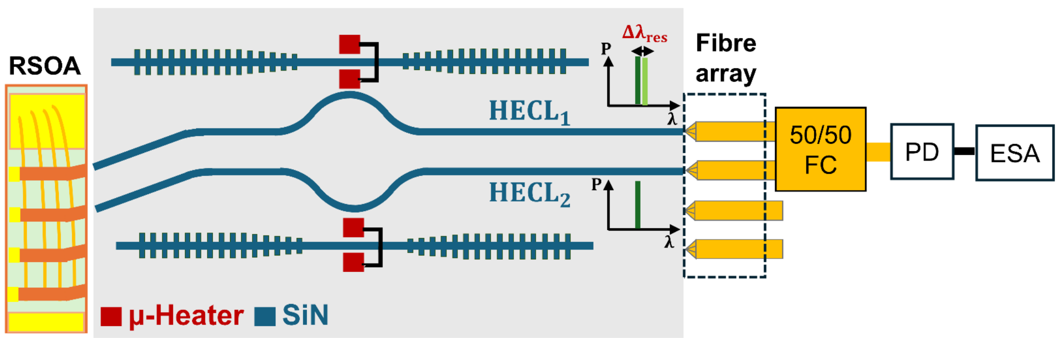

Figure 6.11: Optical heterodyne sensing. Schematic of the dual-HECL architecture, where two SiN external-cavity lasers ($HECL_1$ and $HECL_2$) incorporating integrated microheaters are coupled to a common RSOA gain chip. The laser outputs are collected via a fiber array, combined in a 50/50 optical fiber coupler, and detected on a photodiode (PD); the resulting RF beat note is analyzed on an electrical spectrum analyzer (ESA) to realize optical heterodyne sensing.

As visible in Fig. 6.11, two further enhancements can be considered as part of a continuous, step-by-step evolution of the on-chip sensor. The first concerns the fiber-array output and the fiber-based 50/50 optical fiber coupler, which can be replaced by an integrated PIC-based multimode interferometer (MMI) (Fig. 6.12).

An on-chip MMI splitter/combiner offers increased robustness to fabrication variations, broadband operation, and a significant reduction of the overall footprint, thereby making the sensing system more compact and mechanically stable. The next step concerns the full integration of the active components on the same substrate as the SiN HECLs.

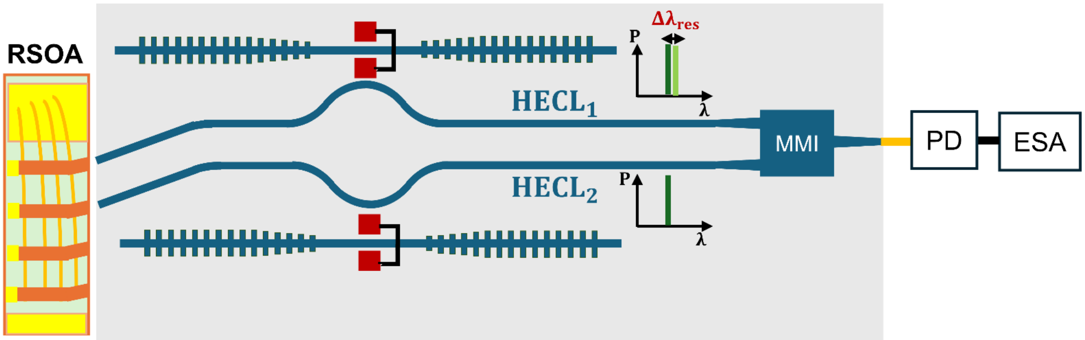

Figure 6.12: Optical heterodyne sensing: the output HECLs are combined by means of on-chip MMI.

By exploiting µ-TP technology, both the RSOA coupons and the photodetector can be integrated directly on the PIC (Fig. 6.13), yielding a highly compact and robust sensor with improved mechanical stability, more efficient alignment-free optical coupling, and reduced packaging complexity. This approach also enables higher reproducibility, lower assembly costs, and enhanced thermal management through direct integration, ultimately improving overall system reliability and scalability.

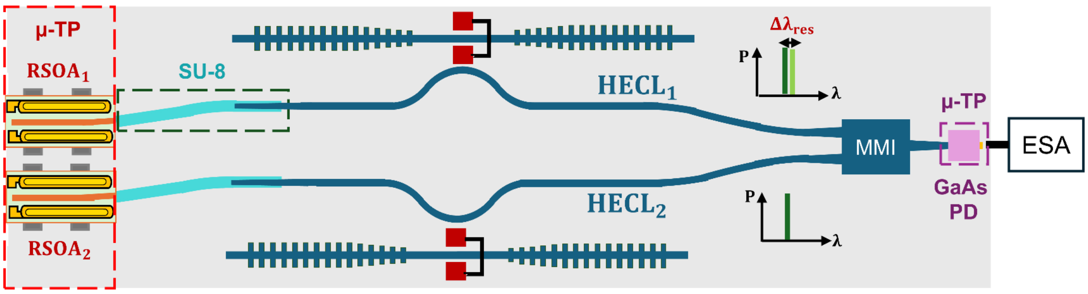

Figure 6.13: Fully integrated optical heterodyne sensing. The RSOA gain element and the photodetector are both transfer printed on the same substrate of the SiN-based dual-HECL architectures. As described in Section 5.3, SU-8 based spot-size converters are used for optimizing mode coupling between RSOA and SiN interfaces.

6.4 OFCs for space applications

Optical frequency comb technology has evolved from early laboratory demonstrations into a fundamental tool for precision metrology in space-based applications. By coherently linking optical and microwave domains, OFCs establish ultra-stable, traceable, and broadband frequency references. This unique property enables a unified hardware platform capable of supporting high-accuracy timekeeping, spectroscopic calibration, and coherent optical communication. Within the context of space applications, OFCs have become integral to numerous advanced systems. They provide absolute wavelength calibration for astronomical spectrographs in exoplanet detection, facilitate optical clock networks for high-precision time and frequency transfer, and underpin emerging experiments dedicated to gravitational wave detection, dark matter searches, dual-comb ranging, and atmospheric spectroscopy. Their exceptional frequency stability and spectral coherence render them ideally suited for space missions demanding metrology-grade performance in highly constrained environments.

The advent of integrated optical frequency combs, notably microcomb and EO-comb architectures, detailed in Section 1.8.2, has introduced a paradigm shift in system design for space deployment. The replacement of bulk or fiber-based cavities with chip-scale resonators and photonic waveguides achieves a substantial reduction in size, weight, and power (SWaP) while improving robustness against mechanical vibration and thermal fluctuations. The alignment-free nature of these integrated platforms makes them inherently compatible with the stringent mechanical and thermal requirements of satellite and deep-space payloads.

This section examines the progression of OFC technology toward space qualification, addressing key technical and environmental challenges as well as major milestones achieved through recent missions. Finally, it discusses future directions for integrated and hybrid photonic comb systems, which are poised to play a pivotal role in next generation spaceborne optical networks.

6.4.1 Free-space optical links

Free-space optical (FSO) links have emerged as a critical technique for distributing ultra stable optical references across long distances where fiber infrastructure is unavailable, including intercontinental links, ground-to-satellite connections, and spaceborne networks. In this context, FSO communication results in a rapidly developing field for both terrestrial and satellite applications [16],[17]. Directional FSO communication systems have been investigated for high data rate links between earth and low earth orbit satellites [18],[19] and for future missions to the moon by NASA [20],[21]. The current record data rate for earth orbit communications is on the order of a single coherent fiber communication channel (i.e. 1-200 Gb/s) [20], and this can only be maintained for a short time before thermal management issues force an extended shutdown. Providing higher data rates continuously between locations needs significant reduction in power consumption while maintaining a compact footprint and weight. In such systems, OFCs act as broadband phase-coherent carriers capable of encoding the stability of a local optical reference and transmitting it to a remote terminal with minimal degradation.

A typical implementation employs an erbium-doped fiber (Er: fiber) frequency comb [22],[23] that is fully phase-locked to a high-finesse optical cavity or optical clock. In this configuration, both the repetition rate (f_{rep}) and carrier–envelope offset frequency (f_0) are stabilized, allowing each comb tooth to inherit the reference's stability. In transmission, one or several comb teeth are typically power amplified using techniques such as distributed feedback (DFB) laser injection and EDFAs. The amplified optical signal is then launched through the turbulent atmosphere toward a remote receiver. At the receiving terminal, a heterodyne beat is generated between the incoming comb light and a locally generated comb. This process enables the transfer of both optical frequency and phase information, effectively replicating the spectral stability of the master comb at the remote site. A principal challenge in FSO links arises from atmospheric turbulence, which introduces path-length fluctuations that manifest as phase noise in the received signal.

This noise dominates at Fourier frequencies below approximately 1 kHz and follows a spectrum consistent with Kolmogorov turbulence theory [24]. Specifically, the optical channel and its associated electromagnetic effects degrade the propagating optical beam. Atmosphere-induced impairments, including scintillation, beam wander, and beam spreading, are generally estimated for an effective optical link design and performance analysis. Most literature studies predominantly address the deployment of analytical and statistical models for characterizing critical link parameters and conducting link budget analyses for various satellite scenarios and propagation directions [25][26]. Conversely, a detailed low-level description of the optical link can be obtained by emulating the behavior of the perturbed field in a flexible and comprehensive way, using experimental testbeds or advanced numerical wave propagators to simulate the propagation of the optical beam from the transmitter to the receiver plane [27].

To mitigate these effects, active phase-noise compensation schemes are implemented. These systems typically measure the round-trip phase fluctuations using a returned optical carrier or pilot tone and apply pre-compensation through actuators such as acousto-optic modulators (AOMs) or electro-optic modulators (EOMs). Control loops with bandwidths on the order of 10–20 kHz can effectively suppress atmospheric and fiber-induced phase noise, achieving reductions to approximately −40 dBc/Hz at 10 Hz and −80 dBc/Hz at 5 kHz [28].

Recent experimental demonstrations highlight the capability of FSO links to preserve optical clock-level stability. For example, an 18 km atmospheric link has achieved fractional frequency instability on the order of 10^{-15}at 0.1 s averaging time [29].

Comb-to-comb stabilization across a 1.3 km free-space link has demonstrated frequency transfer stability of 1.7×10^{-15} at 0.1 s while faithfully transporting the master comb's stability of 1.2×10^{-15} at 1 s across a spectral bandwidth of approximately 4.2 THz, with a mutual linewidth of roughly 1.4 Hz [28] as shown in the schematic in Fig. 6.14(a).

Even longer-range experiments have demonstrated free-space links with fractional instability approaching the 10^{-19} level over 113 km (Fig. 6.14(b)) [30].

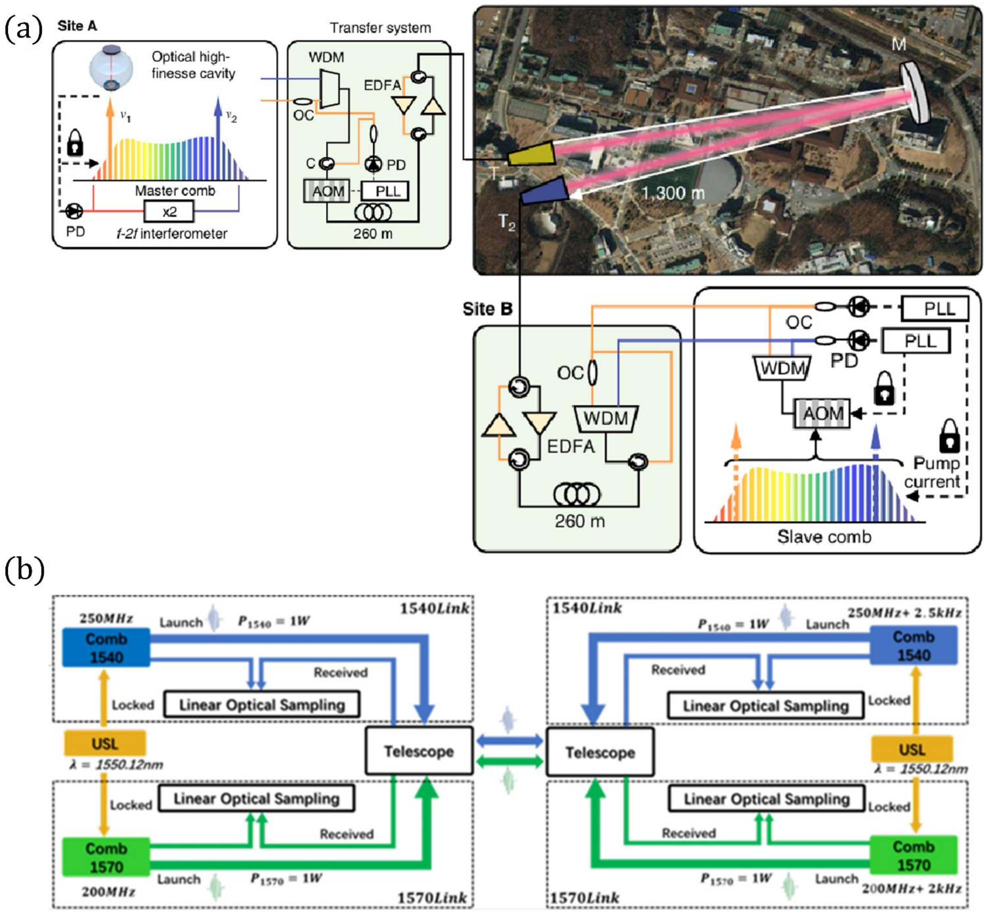

Figure 6.14: (a) Comb-to-comb stabilization demonstrated over a 1.3 km free-space link in [28]. The master comb at Site A, locked to a high-finesse cavity, transmits two optical tones (1531 nm and 1564 nm) through the link to stabilize a slave comb at Site B. (b) Schematic of the 113 km free space time-frequency link, transmitting 1540 nm and 1570 nm channels [30].

These results indicate that atmospheric FSO links are capable of supporting frequency transfer with stability suitable for state-of-the-art optical clocks over distances comparable to ground–satellite paths. For practical deployment in space applications, the fundamental comb hardware remains largely unchanged, but the optical terminals must be integrated with space-qualified telescopes and supporting subsystems.

In particular, robust pointing, acquisition, and tracking (PAT) mechanisms are required to maintain alignment between distant terminals, while adaptive optics may be incorporated to mitigate wavefront distortions caused by atmospheric turbulence [31]. When combined with active phase-noise compensation, these technologies enable the realization of coherent, comb-based optical communication backbones capable of distributing ultra stable time and frequency references in space. Such systems have the potential to complement or replace existing microwave-based time–frequency distribution networks, enabling a new generation of high-precision navigation, fundamental physics experiments, and global optical clock comparisons.

6.4.2 Space-based optical atomic clock networks

Optical atomic clocks represent the forefront of precision timekeeping, with current systems achieving fractional frequency instabilities of 10^{-18}, two orders of magnitude beyond the performance of even the best microwave atomic clocks [32]. OFCs serve as crucial components in optical atomic clocks, enabling the conversion of high-precision optical frequency standards to the microwave domain [33]. The transition from ground-based to space-based optical atomic clocks holds transformative potential. Placing optical clocks in orbit offers advantages such as low vibration noise, thermally stable operation, and reduced sensitivity to Earth's gravitational potential [23]. Several international missions have demonstrated the feasibility of space-deployed fiber-based OFCs:

(i) *KARI, Korea Institute of Space Technology* (2013): the world's first fiber femtosecond laser oscillator meeting space requirements was launched into low Earth orbit (LEO). This (Er: fiber) laser, mode-locked via a SESAM device at a 25 MHz repetition rate and 14 mW output power, maintained stable operation in orbit for over one year, with radiation-induced power attenuation limited to only 8.6% [34].

(ii) *Menlo Systems TEXUS-51 Rocket* (2016): this sounding-rocket mission marked the first operation of an optical frequency comb linked to an onboard optical clock in space. A compact, self-referenced Er: fiber comb performed precision frequency comparison between a rubidium optical clock and a cesium microwave clock. The entire optical-clock–comb system demonstrated stability in rocket environments [35].

(iii) *"DreamSky", China's Tiangong Space Station* (2022): experimental cabin carried a high-precision time-frequency platform containing optical frequency combs, microwave clocks, cold-atom optical clocks, and precision comparison links. This represents the world's first spaceborne cold-atom optical clock, engineered to establish a highly stable, integrated space–time reference system [36].

Space-qualified OFCs enable optical clocks to function as both ultra stable time–frequency references and precision instruments for measuring fundamental constants and relativistic effects (Fig. 6.15).

They offer a pathway to replace current microwave-based timing systems, improving global time dissemination and measurement accuracy by several orders of magnitude. Applications span intercontinental optical clock comparisons, support for a future redefinition of the SI second, relativistic geodesy based on high-precision gravitational red-shift measurements, and enhanced navigation performance when integrated with Global Navigation Satellite Systems (GNSS). Presently, microwave clocks aboard GNSS constellations [37] provide nanosecond-level accuracy, where a few-nanosecond error corresponds to meter-level positional uncertainty.

Space-borne optical clocks stabilized and linked by OFCs could reduce these errors by orders of magnitude while simplifying the GNSS architecture, minimizing the dependence on extensive ground-based monitoring and correction networks.

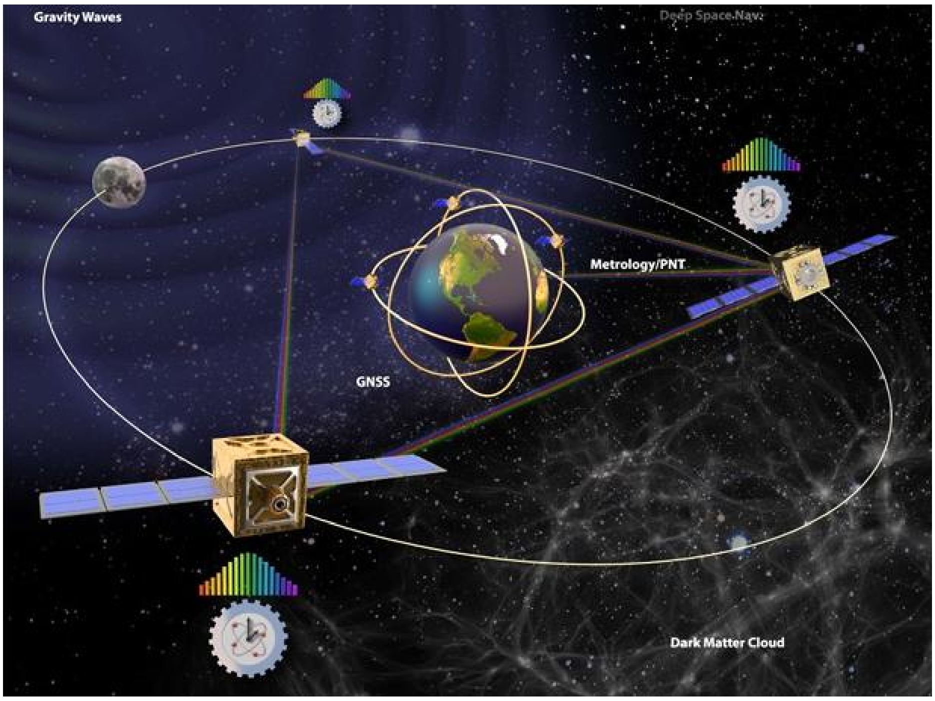

Figure 6.15: Schematic of OFCs deployed as atomic clock networks, enabling precise time synchronization and frequency referencing across distributed nodes [38].

6.4.3 Spectroscopy and atmospheric remote sensing

OFC–based spectroscopy is emerging as a transformative technology for atmospheric and planetary remote sensing, offering broad spectral coverage, high resolution, and rapid data acquisition. Frequency-comb spectroscopy in space mostly appears in dual-comb spectroscopy

(DCS) and space heterodyne spectroscopy concepts, where the OFC acts simultaneously as a set of narrow-linewidth probe lines and as a phase-coherent sampling clock.

In DCS, two combs with slightly different repetition rates, $f_{\mathrm{rep},1}$and $f_{\mathrm{rep},2} = f_{\mathrm{rep},1} + \Delta f$, interrogate a sample; the multi-heterodyne beat down-converts the entire optical spectrum into a radio-frequency comb with spacing Δf, and each RF line corresponds to a particular optical frequency, enabling high-resolution, multiplexed spectroscopy without moving parts. Among its key applications, OFC-based spectroscopy can be used to monitor atmospheric composition, structure, motion, and circulation, as well as climate change indicators, atmospheric chemical reactions, and the origin and evolution of planetary atmospheres. When integrated into spaceborne instruments, comb-based spectroscopy can greatly enhance existing satellite missions for planetary atmospheric detection, such as : GOSAT (Japan, 2009) that monitors global atmospheric carbon monoxide and methane levels [39], OCO-2 (NASA, 2014) studying global climate change through carbon dioxide measurements [40], and TanSat (China, 2016) that consists of a carbon monitoring satellite for climate research [41].

6.4.4 Astronomical applications

OFCs play an important role in both ground- and space-based astronomy, particularly in the calibration of high-resolution astronomical spectrographs used for radial-velocity (RV) measurements [42], [43]. These instruments detect extremely small Doppler shifts in stellar spectrum, enabling the determination of stellar radial velocities, the detection of exoplanets (Fig. 6.16(a)), the characterization of planetary atmospheres, and studies related to cosmological expansion.

In exoplanet searches, the host star and its planet orbit their common center of mass; this motion induces a periodic Doppler shift in the star’s emitted light, producing a small change in the frequency $\Delta\nu$ of stellar spectral lines. Measuring these shifts with sufficient precision requires highly stable spectrograph calibration. OFCs provide an ideal calibration reference by generating a spectrum consisting of a large number of evenly spaced optical modes.

Through the process of self-referencing, both the comb line spacing (repetition rate) and the carrier–envelope offset frequency are stabilized and locked to a radio-frequency standard. Consequently, the absolute frequencies of the comb lines are precisely known and traceable to atomic or GPS-disciplined references, effectively forming an accurate “optical ruler” in frequency space. Conventional calibration sources, such as iodine absorption cells and thorium–argon lamps, suffer from limitations including irregular spectral line distribution, restricted spectral coverage, and limited long-term stability. In contrast, OFCs provide a dense grid of evenly spaced, phase-coherent optical frequencies over a broad spectral range, making them highly suitable for precision spectrograph calibration. In astronomical applications, such systems are commonly referred to as *astro-combs*. For high-precision calibration, these systems require flat spectral power over 350–800 nm and long-term frequency stability better than 10^{-11} over a decade, enabling radial-velocity accuracy at the 1 cm s^{-1} level.

Recent advances have demonstrated compact astro-comb implementations based on micro-resonator frequency combs. In these devices, soliton emissions within an optical micro-resonator generates a stable comb spectrum in the near-infrared region. When referenced to atomic or molecular absorption lines, these soliton microcombs can achieve the frequency stability required for astronomical measurements. A notable demonstration involved a near-infrared soliton microcomb [44] used at the Keck-II telescope to search for the known exoplanet HD 187123b, representing one of the first field implementations of microcomb-based spectrograph calibration (Fig. 6.16(b)). Additionally, worldwide have deployed OFCs for wavelength calibration [23].

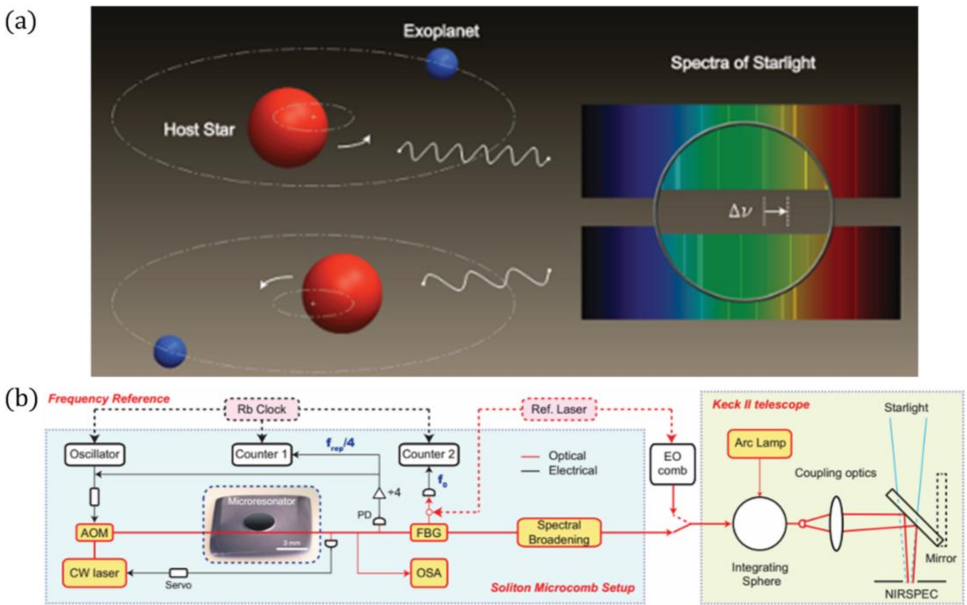

Figure 6.16: (a) Schematic of exoplanet transit spectroscopy: Starlight passes through exoplanet atmosphere during transit, imprinting absorption features (Δλ, Δν) detected in stellar spectrum. (b) Experimental setup for high-resolution spectroscopy using frequency-stabilized laser based on soliton microcomb [44].

Notable systems include: HARPS (High Accuracy Radial velocity Planet Searcher) characterized by 18-25 GHz repetition rate, 1 cm/s calibration accuracy [45], HARPS-N (Northern hemisphere) with 16 GHz repetition rate, 6 cm/s calibration accuracy [46], Habitable-zone Planet Finder (HPF) featuring 30 GHz repetition rate, 1 m/s calibration accuracy, covering 700-1760 nm [47].

6-References

[1] Saunders, John E., et al. "Refractive indices of common solvents and solutions at 1550 nm." *Applied optics* 55.4 (2016): 947-953.

[2] Chrostowski, Lukas, et al. "Silicon photonic resonator sensors and devices." *Laser Resonators, Microresonators, and Beam Control XIV*. Vol. 8236. SPIE, 2012.

[3] Liao, Kun, et al. "Photonic molecule quantum optics." *Advances in Optics and Photonics* 12.1 (2020): 60-134.

[4] Xu, Hongnan, et al. "Breaking the resolution-bandwidth limit of chip-scale spectrometry by harnessing a dispersion-engineered photonic molecule." *Light: Science & Applications* 12.1 (2023): 64.

[5] Zhang, Yujia, et al. "Miniaturized disordered photonic molecule spectrometer." *Light: Science & Applications* 14.1 (2025): 144.

[6] Badri, S. Hadi, et al. "Compact modulators on silicon nitride waveguide platform via micro-transfer printing of thin film lithium niobate." *Scientific Reports* 15.1 (2025): 11681.

[7] Zhang, Mian, et al. "Electronically programmable photonic molecule." *Nature Photonics* 13.1 (2019): 36-40.

[8] Granchi, Nicoletta, et al. "Multimode photonic molecules for advanced force sensing." *Optics Express* 27.26 (2019): 37579-37589.

[9] Cheben, Pavel, et al. "Subwavelength integrated photonics." *Nature* 560.7720 (2018): 565-572.

[10] www.cornerstone.sotonfab.co.uk.

[11] Badri, S. Hadi, et al. "Photonic Molecule-Based Refractive Index Sensor Using Coupled Fabry-Perot Resonators." *The European Conference on Lasers and Electro-Optics*. Optica Publishing Group, 2025.

[12] Iadanza, Simone, et al. "High-Q asymmetrically cladded silicon nitride 1D photonic crystals cavities and hybrid external-cavity lasers for sensing in air and liquids." *Nanophotonics* 11.18 (2022): 4183-4196.

[13] Mendoza-Castro, Jesus Hernan, et al. "Flow Injection-Based Refractive Index Sensing with a Si3N4 Photonic Crystal Nanobeam-Microring Fano Resonator." *ACS Applied Optical Materials* 3.12 (2025): 2946-2959.

[14] Tomasetig, Daniela, et al. "Si3N4 Microring Resonator-Based Refractive Index Sensing for Liquid Samples: Comparing Wavelength Scanning and Fixed-Wavelength Probing." *ACS Measurement Science Au* (2025).

[15] Oliveria, T. O., et al. "Refractive Index Sensing using the optical heterodyne method and Photonic crystal hybrid laser." *CLEO: Applications and Technology*. Optica Publishing Group, 2024.

[16] Jia, Shuaiwei, et al. "150 Gbit/s 1 km high-sensitivity FSO communication outfield demonstration based on a soliton microcomb." *Optics Express* 30.20 (2022): 35300-35310.

[17] Dochhan, Annika, et al. "13.16 Tbit/s free-space optical transmission over 10.45 km for geostationary satellite feeder-links." *Photonic Networks; 20th ITG-Symposium*. VDE, 2019.

[18] www.starlink.com

[19] https://www.aboutamazon.com/news/innovation-at-amazon/amazon-project-kuiper-oisl-space laser-december-2023-update

[20] Robinson, Bryan S., et al. "TeraByte InfraRed Delivery (TBIRD): a demonstration of large-volume direct-to-Earth data transfer from low-Earth orbit." *Free-space laser communication and atmospheric propagation XXX*. Vol. 10524. SPIE, 2018.

[21] Murphy, K. "Lasers Light the Way for Artemis II Moon Mission." *ESC, LEMNOS, Artemis, Lasercommunication (3 June 2021)* (2023).

[22] Lezius, Matthias, et al. "Radiation tolerant frequency comb fiber laser for space applications." *International Conference on Space Optics—ICSO 2022*. Vol. 12777. SPIE, 2023.

[23] Shao, Xiaodong, et al. "Optical frequency comb technology: from ground to space." *Astronomical Techniques and Instruments* 1.2 (2024): 105-116.

[24] Andrews, Larry C., and Ronald L. Phillips. "Laser beam propagation through random media." *Laser*

Beam Propagation Through Random Media: Second Edition (2005).

[25] Carrasco-Casado, Alberto, and Ramon Mata-Calvo. "Space optical links for communication networks." *Springer Handbook of Optical Networks*. Cham: Springer International Publishing, 2020. 1057-1103.

[26] Cantore, Carla, et al. "Link budget analysis of bi-directional LEO and GEO optical feeder links advancing the beam wander model's accuracy." *Scientific Reports* 14.1 (2024): 8579.

[27] Monopoli, Davide, et al. "Emulation of ground-space optical link propagation based on multilayer turbulence models." *International Conference on Space Optics—ICSO 2024*. Vol. 13699. SPIE, 2025.

[28] Yang, Jaewon, et al. "Frequency comb-to-comb stabilization over a 1.3-km free-space atmospheric optical link." *Light: Science & Applications* 11.1 (2022): 253.

[29] Kang, Hyun Jay, et al. "Free-space transfer of comb-rooted optical frequencies over an 18 km open-air link." *Nature communications* 10.1 (2019): 4438.

[30] Shen, Qi, et al. "Free-space dissemination of time and frequency with 10−19 instability over 113 km." *Nature* 610.7933 (2022): 661-666.

[31] Gozzard, D. R., et al. "Stabilized free-space optical frequency transfer." *Physical Review Applied* 10.2 (2018): 024046.

[32] Oelker, Eric, et al. "Demonstration of 4.8× 10−17 stability at 1 s for two independent optical clocks." *Nature Photonics* 13.10 (2019): 714-719.

[33] Diddams, Scott A., Kerry Vahala, and Thomas Udem. "Optical frequency combs: Coherently uniting the electromagnetic spectrum." *Science* 369.6501 (2020): eaay3676.

[34] Lee, Joohyung, et al. "Testing of a femtosecond pulse laser in outer space." *Scientific reports* 4.1 (2014): 5134.

[35] Lezius, Matthias, et al. "Space-borne frequency comb metrology." *Optica* 3.12 (2016): 1381-1387.

[36] Liu, Yun, et al. "Laser system of cold atom optical clock in China Space Station." *ACTA PHYSICA SINICA* 72.18 (2023).

[37] Schmidt, Tobias D., et al. "COMPASSO: In-orbit verification of optical key technologies for future GNSS." *Proceedings of the 53rd annual precise time and time interval systems and applications meeting*. 2022.

[38] Leifer, Stephanie, et al. "Optical frequency combs for space applications." (2015).

[39] Yokota, T., et al. "Global concentrations of CO2 and CH4 retrieved from GOSAT: First preliminary results." *Sola* 5 (2009): 160-163.

[40] Sun, Ying, et al. "OCO-2 advances photosynthesis observation from space via solar-induced chlorophyll fluorescence." *Science* 358.6360 (2017): eaam5747.

[41] Du, Shanshan, et al. "Retrieval of global terrestrial solar-induced chlorophyll fluorescence from TanSat satellite." *Science Bulletin* 63.22 (2018): 1502-1512.

[42] Li, Chih-Hao, et al. "A laser frequency comb that enables radial velocity measurements with a precision of 1 cm s-1." *Nature* 452.7187 (2008): 610-612.

[43] McCracken, Richard A., Jake M. Charsley, and Derryck T. Reid. "A decade of astrocombs: recent advances in frequency combs for astronomy." *Optics express* 25.13 (2017): 15058-15078.

[44] Suh, Myoung-Gyun, et al. "Searching for exoplanets using a microresonator astrocomb." *Nature photonics* 13.1 (2019): 25-30.

[45] Wilken, Tobias, et al. "A spectrograph for exoplanet observations calibrated at the centimetre-per-second level." *Nature* 485.7400 (2012): 611-614.

[46] Li, Chih-Hao, et al. "Green astro-comb for HARPS-N." *Ground-based and Airborne Instrumentation for Astronomy IV*. Vol. 8446. SPIE, 2012.

[47] Ycas, Gabriel G., et al. "Demonstration of on-sky calibration of astronomical spectra using a 25 GHz near-IR laser frequency comb." *Optics Express* 20.6 (2012): 6631-6643.

Conclusions

This thesis has demonstrated the realization of integrated HECL architectures capable of providing both single- and multi-wavelength emission in the C-band by employing engineered SC-FP resonators as reflectors. The ability to combine advanced PIC design with the development of experimental setups for the fabrication and characterization of both passive and active devices has been enabled through the joint PhD programme between the NPEG (NanoPhotonics and Electromagnetics Group) group at the Polytechnic University of Bari and the CAPPA (Centre for Advanced Photonics & Process Analysis) group at Munster Technological University of Cork. This work was further supported by funding from Research Ireland through the IPIC research project framework.

HECLs have emerged as a versatile and powerful class of light sources, constituting strong candidates to supersede conventional monolithically integrated lasers by offering compact, energy-efficient and highly configurable platforms for both single- and multi-wavelength operation in applications spanning optical sensing, spectroscopy, telecommunications and space systems. The integration of high-gain III–V semiconductor optical amplifiers with low-loss, advanced PIC in a carefully engineered external-cavity configuration, allow that these hybrid architectures can fulfill demanding SWaP requirements and high-power and spectral shaping control. In this framework, a novel resonant reflector architecture based on SiN side-coupled Fabry–Pérot cavity employing DBR mirrors is developed as a compact, CMOS-compatible building block for hybrid external-cavity lasers.

In this thesis, a side-coupled Fabry–Pérot resonator is prroposed as alternative tomicroring resonators to overcome intrinsic limitations of traveling-wave geometries in high-Q, dispersion-engineered applications. In microrings, the free spectral range is directly tied to the ring radius, so achieving large FSR requires aggressive miniaturization that increases bend losses and fabrication sensitivity. Moreover, at ultra-high Q, sidewall roughness induces backscattering that couples clockwise and counter-clockwise modes, leading to resonance splitting, spectral instability, and reduced device reproducibility. Dispersion engineering in rings is also constrained by the need to balance waveguide cross-section and curvature, often pushing designs into multimode regimes that require additional mode management. In contrast, a linear FP cavity defines its modal structure through its physical length and mirror phase response, enabling large FSR without bend-related penalties. The standing-wave nature of the cavity inherently avoids mode degeneracy, so backscattering primarily contributes to excess loss rather than stochastic resonance splitting, resulting in a more robust and predictable spectral response, particularly on low-index-contrast platforms such as SiN.

Compared with conventional in-line Fabry–Pérot cavities, the proposed SC-FP architecture offers a key advantage by decoupling mirror functionality from external coupling. In an in-line FP, the DBR mirrors are embedded in the same waveguide that carries the signal, so mirror reflectivity, internal cavity loss, and external coupling are intrinsically linked. Increasing the number of grating periods to improve reflectivity directly reduces through-transmission and raises insertion loss, and any imperfections or roughness in the mirror region immediately perturb the propagating signal in the bus waveguide. By contrast, the SC-FP employs a separate bus waveguide that couples evanescently to a straight cavity terminated by two DBR mirrors. In this scheme, the DBRs are solely responsible for setting the longitudinal mode spectrum, stopband, and dispersion of the cavity, while the external coupling rate is independently engineered by the side-coupler geometry (gap, coupling length, and low-loss bends). This separation enables higher mirror reflectivity, tailored penetration depth, and engineered dispersion without degrading the through-path performance. The total number of grating periods can thus be increased to boost reflectivity and tailor dispersion without incurring the insertion-loss penalty that is unavoidable in an in-line FP where the bus must traverse the corrugated sections. Additionally, scattering and radiation generated within the DBR sections remain largely confined to the resonant cavity and do not directly translate into additional insertion loss on the access waveguide, which is a limitation in both microrings and in-line FPs where the guided signal co-propagates through the corrugated region. Consequently, the SC-FP exhibits high-Q resonant dips in transmission and corresponding reflection peaks, providing a distinct resonant reflector response. In contrast, the implementation of an in-line Fabry–Pérot configuration would typically require optical isolators to suppress detrimental back-reflections to the external laser or gain section and ensure stable operation; however, such components remain challenging to integrate in standard photonic platforms.

The resulting structure offers flexible control over the loaded Q-factor and coupling regime. Furthermore, unlike traveling-wave resonators, the SC-FP exhibits distinct coupling behavior due to its bidirectional propagation and standing-wave nature: there is no coupling condition for which the reflected power vanishes, and the coupling regime can be engineered from under- to over-coupled by adjusting the side-coupler gap and length. Increasing the coupling gap reduces external loading, lowering insertion losses on the bus and increasing the loaded Q, whereas tighter coupling broadens the resonance linewidth and increases the peak reflectivity observed at the input. This enables flexible trade-offs between spectral selectivity, insertion loss, and feedback strength that are not available in a rigid in-line FP geometry, providing a more versatile and fabrication-tolerant platform for high-performance hybrid external-cavity lasers.

In detail, this work proposes a SC-FP resonator structure implemented using integrated Bragg grating reflectors obtained by modulating the waveguide corrugation. The choice of reflectors, however, can in principle accommodate alternative on-chip mirrors such as multimode interferometer (MMI)-based mirrors, Sagnac loop mirrors, multimode retroreflectors. By integrating such mirrors on both sides, a viable Fabry–Pérot cavity can be realized. These approaches are particularly attractive when broadband, wavelength-independent reflection with minimal excess loss is a primary design objective, enabling operation over a wide spectral range while supporting cavities with high intrinsic quality factors.

Conversely, wavelength-dependent reflectors, such as Vernier ring-resonator-based reflective filters, can provide very sharp spectral selectivity. In such configurations, a compound cavity is formed by terminating a bus waveguide with Vernier-based reflectors, resulting in a significantly more complex traveling-wave resonator system. In this case, it becomes essential to account not only for the standing-wave cavity formed between the two reflective filters, but also for the internal dynamics of the Vernier rings themselves. These dynamics are highly sensitive to fabrication variations, temperature fluctuations, and structural imperfections, which can strongly influence the reflection phase, bandwidth, and resonance alignment. As a result, the independent engineering of cavity length, mode spacing, and dispersion becomes considerably more challenging.

Nevertheless, this Vernier-based Fabry–Pérot configuration remains a promising direction and will be explored in future work, provided that suitable control mechanisms are implemented to stabilize the resonator dynamics and mitigate these sensitivities.

The Bragg grating–based approach is selected due to its ability to precisely engineer the cavity spectral response. Unlike broadband reflector concepts, distributed Bragg reflectors provide direct control over reflectivity, bandwidth, and phase (group delay), enabling tailored dispersion, resonance spacing, and modal selectivity. This level of control is intrinsic to the grating design, through parameters such as period, duty cycle, and apodization, and is more difficult to achieve with inherently wavelength-flat reflector approaches without introducing significant additional complexity. Furthermore, the side-coupled architecture enables independent tuning of the external coupling rate, while implementation on a low-index-contrast SiN platform with adiabatic transitions ensures low propagation loss and preserves the engineered phase response. The combination of precise dispersion control and independent coupling flexibility makes SC-FP cavities based on Bragg gratings the most suitable choice for the targeted functionalities in this work.

This architecture offers strong on-chip reflectivity with engineered dispersion, precise and stable wavelength control, and flexible tailoring of the emission regime and output power, enabling high-performance, scalable integrated HECL sources.

Over the course of this thesis, the SC-FP architecture and the associated design choices are detailed, highlighting the tunability of the device achieved through precise sizing of the geometric parameters and Bragg grating structure. After fabrication using an EBL process, the impact of these choices is experimentally demonstrated in terms of resonance spacing, quality factor, spectral envelope, and reflectivity (Chapter 3). The DBR design enables broad stopband operation (exceeding 70 nm in air-gap implementations) and reveals the impact of apodized gratings and their penetration length on the dispersion regime of the resonator and on the Q-factor, due to the improved mode-matching.

The patterned structures demonstrate good agreement with the intended design despite the presence of fabrication tolerances. In practice, deviations from the ideal geometry arise due to etch bias and limitations of the electron-beam lithography (EBL) process, affecting waveguide cross-sections, coupling gaps, and feature sizes, and leading to slight variations in effective index and coupling strength. Within the Bragg gratings, these imperfections manifest as variations in duty cycle and corrugation width, as well as small random fluctuations that introduce fabrication-induced disorder. Radiation losses and disorder-induced scattering are further mitigated by design through smoothly varying, apodized, and adiabatically tapered grating profiles, which ensure gradual mode transitions and suppress out-of-plane scattering. Moreover, the impact of etch-induced rounding on the nominally rectangular corrugations remains limited, preserving a high degree of structural fidelity and resulting in a stopband response that closely matches the design. As a result, although individual building blocks exhibit moderate sensitivity to fabrication deviations, these effects predominantly lead to minor spectral shifts and small excess losses, without significantly degrading the overall cavity performance. Within this robust framework, a systematic exploration of cavity length, coupling length, and coupling gap further provides practical design guidelines for trading off sharp, high-Q resonant dips against enhanced peak reflectivity, effectively enabling the engineering of SC-FP reflectors for different target specifications.

In this regard, the thesis traces a step-by-step pathway toward a fully integrated, compact HECL application based on an SC-FP wavelength-selective reflector and integrated gain sections, evolving from hybrid fiber-assisted coupling (Chapter 4) to fiber-free two-chip butt-coupling and transfer printed HECL configurations (Chapter 5).

In the first approach, the external-cavity combines a SiN PIC incorporating the SC-FP reflector, with a fiber-based balanced and un-balanced Sagnac loop reflector and a commercial fiber-coupled SOA, extending over tens of meters. This configuration yields multi-wavelength emission aligned to the SC-FP resonances, arising from the spectral overlap between the SOA gain ripple, the SC-FP reflection peaks, and the longitudinal modes of the extended cavity, with multiple longitudinal modes competing within each resonance. When individual resonances are isolated, the system supports coherent pulse trains with radio-frequency linewidths as narrow as ~3 kHz and spontaneously generates multiple identical pulse profiles within the cavity, effectively multiplying the repetition rate and indicating the onset of partially harmonic mode-locking. These results confirm the suitability of SC-FP resonators as high-performance wavelength-selective reflectors for multi-wavelength HECLs and highlight their potential for advanced applications such as low-phase-noise microwave generation, WDM carrier formation, coherent LiDAR, and multi-comb spectroscopy.

Building on the fiber–PIC demonstration, two architectures are implemented that further advance the integration and miniaturization of the HECL platform, eliminating fiber from the external cavity and reducing its length from meters to the millimeter scale, while simultaneously enhancing mechanical robustness and polarization stability. The first HECL implements a two-chip butt-coupling scheme between an RSOA gain and the SiN PIC, air-gap spaced, with the two chips mounted on independent 3-axis stages and aligned to optimize coupling from the RSOA ridge waveguide into the on-chip waveguides. This configuration demonstrates laser operation with output powers of around 0.8 mW, side-mode suppression ratios exceeding 45 dB, and preliminary linewidth measurements indicating sub-100 kHz optical linewidths using a heterodyne method. A systematic comparison between shorter and longer RSOA gain chips (lower and higher gain) and between different SC-FP designs is carried out to assess their impact on lasing performance, including output power, spectral purity, and stability. The study highlights that the air gap between the gain chip and the PIC leads to significant coupling losses, which could be mitigated by incorporating spot-size converters to better match the mode profiles of the SiN and RSOA waveguides, although the approach remains highly alignment-sensitive. Moreover, continuous thermal and mechanical stabilization of the stages is required to maintain stable operation, ultimately limiting the long-term stability and practicality of this free-space butt-coupled solution. A more advanced level of heterogeneous integration is then explored, in which the RSOA and the passive SiN structures are co-integrated on the same silicon substrate via transfer printing, enabling the most compact HECL configuration. The alignment and coupling limitations observed in the two-chip butt-coupled scheme are addressed through the design of SU-8 spot-size converters combined with SiN waveguide tapers, forming an inverse taper configuration at both input and output to improve mode matching, and by precisely aligning the SC-FP modes position (consequently the DBR stopband) to the transfer printed RSOA gain spectrum. A key requirement of this approach is achieving precise vertical and lateral alignment between the RSOA and the SU-8/SiN waveguide, which is progressively improved over two fabrication iterations by using fiducial markers in the GDS layout and EBL-defined structures for both SiN and SU-8, guided by SEM inspection. This refinement leads to a substantial increase in coupled power, yielding output powers above 0.6 mW with SMSR values around 40 dB, and linewidth measurements confirming high coherence, with sub-50 kHz linewidths limited by the reference laser in the heterodyne setup. Future work will focus on the integration of on-chip thermal tuning and phase-control elements, to enable active management of the coupled thermal and current-induced effects in the RSOA and resonator, thereby enhancing emission stability and mitigating mode hopping. In combination with shorter external cavities (centimeters scale), larger FP modes spacing and higher-Q resonances, these advances are expected to support stable, reconfigurable multi-wavelength operation and to enable deployment in dense WDM systems, nonlinear optics, and single-frequency on-chip sensing lasers. Table 6.1 summarizes the HECLs demonstrated throughout the thesis, highlighting the progression from partially fiber-based architectures toward more compact integrated platforms. The table compares the main figures of merit, including emission regime, linewidth, SMSR, and peak emitted power, while values that were not reported are marked as “N.R”.

For advanced laser-oriented applications, the main bottleneck limiting the collected output power in both the two-chip butt-coupled and transfer-printed HECL configurations arises from coupling inefficiencies. The relatively low output power is primarily dictated by extrinsic losses at the gain-chip–SiN interface and at the fiber output, while intra-cavity losses in the SiN FP cavity play a secondary role. In particular, coupling from the active to the passive section represents the dominant loss channel and is likely the primary factor responsible for the reduced output power. In the butt-coupled configuration, the absence of dedicated mode converters leads to a significant mode mismatch between the III–V gain section and the SiN waveguide, reducing injection efficiency, while fiber collection via a lensed fiber introduces additional insertion loss.

Although these limitations are partially alleviated in the transfer-printed implementation through inverse-taper spot-size converters between the RSOA and the SiN platform, further optimization of mode matching, polymer waveguide geometry, and alignment accuracy is required to fully improve external efficiency.

Within the cavity, losses are associated with waveguide propagation and residual scattering due to fabrication-induced imperfections, while the contribution of the Bragg gratings remains limited owing to apodized and adiabatic designs that preserve high reflectivity and suppress radiation losses. However, the relatively high reflectivity of the SC-FP resonant mirror may further limit the extracted output power by reducing the outcoupling efficiency.

Overall, these loss mechanisms are consistent with state-of-the-art SiN technology and do not fundamentally constrain device operation, but they do impact threshold and laser efficiency. Consequently, the current output power should be regarded as a proof-of-concept limitation, with clear routes for improvement through optimized coupling strategies, refined fabrication processes, and improved reflectivity engineering for balanced cavity design.

This work also discusses the broader perspectives and applications of the SC-FP resonators developed here, with particular emphasis on their use as compact, integrated refractive-index sensors. The sensing performance of a simple SC-FP architecture is first examined using NaCl solutions and DI water, focusing on resonance wavelength shifts and corresponding limits of detection as primary figures of merit. The concept is then extended to coupled SC-FP resonators, in a photonic molecules scheme, which provide resonance splitting and thereby two independent spectral readouts per mode, enabling multi-parameter sensing based on both wavelength shifts and extinction ratio changes induced by the analyte. In this framework, air-gap SC-FP implementations are introduced to enhance the interaction volume with the environment, with experiments confirming improved sensitivity compared to fully embedded structures, achieving sensitivities on the order of 166 nm/RIU and limits of detection down to approximately 4.4×10^{-4} RIU.

Building on these results, the potential of SC-FP-based HECLs for refractive index sensing is explored, where compact, narrow-linewidth single-wavelength sources support high-resolution liquid or gas sensing.

The active HECL-based resonator does not intrinsically enhance the bulk refractive-index sensitivity compared to an equivalent passive cavity, as the sensitivity (in nm/RIU) is fundamentally determined by the modal overlap with the analyte and the cavity design—which can be optimized through proper grating design, such as sub-wavelength configurations and slot waveguides. The key advantage of active configuration lies instead in the substantial improvement of the limit of detection (LOD), which is significantly better than what can be achieved with passive resonator-based approaches.

By transducing the resonance shift into a narrow and stable lasing emission, the HECL enables much finer resolution of wavelength (or frequency) shifts than passive spectral measurements.

Within this framework, ultra-narrow linewidth HECL emission enables a reduction of the refractive index detection limit by over an order of magnitude ($10^{-5}/10^{-6}$ RIU) compared with passive resonator-based sensors. The sensitivity is further enhanced through heterodyne-based detection, reaching values on the order of 10^{-7} RIU by exploiting MHz-level beat notes, well beyond the capabilities of conventional spectrometric approaches and direct lasing measurements. These considerations make it a powerful approach for high-resolution refractive-index sensing. Multi-wavelength HECL-based OFC sources also show strong potential for space applications, building on comb technologies already demonstrated in free-space optical links, atomic clocks, precision spectroscopy, atmospheric sensing, and astronomy. Hybrid laser platforms are particularly attractive for space photonics, as they combine high performance with robustness and compliance with stringent size, weight, and power constraints, while meeting the demanding requirements of high output power, low phase noise, and long-term frequency stability in free-space optical FSO systems.

Table 6.1: Summary of the key figures of merit of all the hybrid external-cavity lasers demonstrated in this thesis, including fiber-assisted, two-chip butt-coupled, and micro-transfer printed implementations.

SC-FP-based HECL	**External-cavity**	**Emission regime**	**SMSR**	**Linewidth**	**Peak-line power**
Fiber-assisted HECL	Fiber circulator and EDFA/ SOA-NL	MWL: (10 lines) Fig. 4.10	$\approx$ 30 dB	N.R.	-2/3 dBm
		MWL (20 lines) Fig. 4.11	$\approx$ 10 dB		-2/5 dBm
		MWL (50 lines) Fig. 4.12	$\approx$ 1/2 dB		-15 dBm
	Fiber Sagnac reflector and SOA-L	MWL (10 lines) Fig. 4.15	3/5 dB	RF-analysis: 3 kHz Comb-analysis: 1 GHz	-3/-5 dBm
Two-chip butt-coupled HECL	Air-gap between the RSOA chip and SiN PIC	**Short RSOA**			
		SWL: Fig. 5.15	45 dB	N.R.	-13 dBm
		Long RSOA			
		SWL: Fig. 5.19	30/35 dB	74 kHz	-15 dBm
		SWL: Fig. 5.26	50 dB	110 kHz	-5 dBm
µ-TP HECL	Transfer printed RSOA coupon on the SiN PIC	**First iteration**			
		SWL: Fig. 5.42	25/28 dB	N.R.	-20 dBm
		Second iteration			
		SWL: Fig. 5.49	40 dB	47 kHz	-17 dBm
		SWL: Fig. 5.52	35 dB	48 kHz	-5 dBm

List of publications

International Journal Articles

[j1] Monopoli, D., Badri, S.H., Maraviglia, N. et al. “Broadband dispersion-engineered Bragg grating mirrors for integrated side-coupled Fabry–Pérot resonators.” *Scientific Reports* (2026).

[j2] Monopoli, Davide, *et al.* "Multi-wavelength hybrid laser with side-coupled Fabry-Perot silicon nitride resonators." *Journal of Lightwave Technology* 44.8 (2026): 3159-3166.

[j3] Badri, S. Hadi, Monopoli, Davide, Calò, Giovanna, and O’Faolain Liam,” Broadband refractive index sensor using photonic molecule architecture with subwavelength grating mirrors on silicon nitride." *Optics Express* 33.26 (2025): 54166-54176.

[j4]Cantore, Carla, Monopoli, Davide, *et al.* "Link budget analysis of bi-directional LEO and GEO optical feeder links advancing the beam wander model’s accuracy." *Scientific Reports* 14.1 (2024): 8579.

International Conference Proceedings

[c1] Monopoli, Davide, *et al.* "Scalable hybrid laser integration via microtransfer printing for silicon photonic platforms." *Optical Interconnects and Packaging 2026*. Vol. 13903. SPIE, 2026.

[c2] Badri, S. Hadi, Monopoli, Davide *et al.* "Photonic Molecule-Based Refractive Index Sensor Using Coupled Fabry-Perot Resonators." *The European Conference on Lasers and Electro-Optics*. Optica Publishing Group, 2025.

[c3] Monopoli, Davide, *et al.* "Emulation of ground-space optical link propagation based on multilayer turbulence models." *International Conference on Space Optics—ICSO 2024*. Vol. 13699. SPIE, 2025.

[c4] Cantore, Carla, Monopoli, Davide *et al.* "Experimental laboratory emulation of turbulence-induced fading affecting optical feeder links." *International Conference on Space Optics—ICSO 2024*. Vol. 13699. SPIE, 2025.

[c5] Monopoli, Davide, *et al.* "Fabry-Pérot cavity in SiN for non-linear applications." *British and Irish Conference on Optics and Photonics*. Optica Publishing Group, 2024.

[c6] Cantore, Carla, Monopoli, Davide *et al.* "Reconfigurable fading testbed for the investigation of COTS transceivers in OFLs." *2024 11th International Workshop on Metrology for AeroSpace (MetroAeroSpace)*. IEEE, 2024.

[c7] Monopoli, Davide, *et al.* "BPM-based atmospheric turbulence propagator for optical ground-to-space links through extended Rayleigh Sommerfield theory and phase screen generation." *2024 24th International Conference on Transparent Optical Networks (ICTON)*. IEEE, 2024.

[c8] Cantore, Carla, Monopoli, Davide *et al.* "Laboratory emulation of LEO downlink optical feeder link employing commercial transceivers." *2024 24th International Conference on Transparent Optical Networks (ICTON)*. IEEE, 2024.

[c9] Cantore, Carla, Monopoli, Davide *et al.* "An accurate and efficient numerical tool for the analysis and design of optical feeder links." *2023 IEEE 10th International Workshop on Metrology for AeroSpace (MetroAeroSpace)*. IEEE, 2023.

Appendix

Appendix A: Scattering-matrix derivation of the FP etalon

This appendix derives the scattering parameters of the Fabry–Pérot etalon used in Section 2.2.1.

A.1 Scattering parameters calculation

The Fabry–Pérot etalon can be viewed as a two-port network, characterized by the normalized forward- and backward-propagating field amplitudes (a_1, b_1) at the left port and (a_2, b_2) at the right port. The response of this two-port is conveniently described in terms of its scattering matrix **S**, which relates the outgoing waves to the incoming waves at each port. The scattering relation is defined as [1]:

$$\begin{bmatrix} b_1 \\ b_2 \end{bmatrix} = \begin{bmatrix} S_{11} & S_{12} \\ S_{21} & S_{22} \end{bmatrix} \begin{bmatrix} a_1 \\ a_2 \end{bmatrix}, \tag{A.1}$$

where the elements of the matrix $\boldsymbol{S}$ denote the complex amplitude reflection and transmission coefficients between the ports of the Fabry–Pérot section. In particular, S_{11} and S_{22} represent the reflections seen when exciting the structure from the left and from the right, respectively, while S_{21} and S_{12} describe transmission from left to right and from right to left.

Considering Eqs. (2.12-2.14) in the thesis, in this section are reported the derivation of the scattering parameters. To obtain the scattering coefficients S_{11} and S_{21}, the Fabry–Perot section is first excited from the left only. This is implemented by setting the incident field at the right port to zero, $a_2 = 0$, and solving the coupled equations for b_1 and b_2 in terms of a_1.

From the interface relations at the left boundary, Eq. (2.13), and the propagation relation for the backward-propagating field, Eq. (2.12), the internal backward amplitude at the left interface can be expressed as:

$$b_1' = t_1 a_1 + r_1 a_1', b_2' = b_1' e^{j\beta L}, \tag{A.2}$$

where the second equality simply propagates the backward wave from $z = 0$ to $z = L$ inside the dielectric block. At the right interface, with $a_2 = 0$, b_2' in Eq. (2.14) reduces to:

$$b_2' = r_2 a_2', \tag{A.3}$$

The internal forward amplitudes at the two interfaces are related through propagation according to Eq. (2.12), namely $a_2' = a_1' e^{-j\beta L}$. Substituting this expression into Eq. (A.3) gives:

$$b_2' = r_2 a_1' e^{-j2\beta L}. \tag{A.4}$$

Equating the two expressions for b_2' in Eqs. (A.2) and (A.4) yields a single relation between a_1' and a_1:

$$t_1 a_1 + r_1 a_1' = r_2 a_1' e^{-j2\beta L}, \tag{A.5}$$

from which the internal forward amplitude at the left interface is obtained as:

$$a_1' = \frac{t_1}{r_2 e^{-j2\beta L} - r_1} a_1, \tag{A.6}$$

Inserting Eq. (A.6) into the left-interface relation for the reflected field, Eq. (2.14), gives:

$$b_1 = -r_1 a_1 + t_1 a_1' = -r_1 a_1 + t_1 \frac{t_1}{r_2 e^{-j2\beta L} - r_1} a_1. \tag{A.7}$$

This expression can be simplified by rewriting the denominator in terms of the round-trip factor $r_1 r_2 e^{-j2\beta L}$. After mathematical calculations, it yields:

$$b_1 = \frac{-r_1 + t_1^2 r_2 e^{-j2\beta L}}{1 - r_1 r_2 e^{-j2\beta L}} a_1, \tag{A.8}$$

and therefore, the reflection coefficient seen from the left side is:

$$S_{11} = \frac{b_1}{a_1} = \frac{-r_1 + t_1^2 r_2 e^{-j2\beta L}}{1 - r_1 r_2 e^{-j2\beta L}}. \tag{A.9}$$

For the transmitted field, b_2 expression in Eq. (2.14) when $a_2 = 0$, Eq. (A.6) reduces to:

$$b_2 = t_2 a_2'. \tag{A.10}$$

By inserting Eq. (A.6) for a_1' into the forward amplitudes at the two interfaces described by the propagation relation $a_2' = a_1' e^{-j\beta L}$ (Eq. (2.12)), gives:

$$b_2 = t_2 a_2' = t_2 a_1' e^{-j\beta L} = t_2 \frac{t_1}{r_2 e^{-j2\beta L} - r_1} e^{-j\beta L} a_1, \tag{A.11}$$

Rewriting the denominator in terms of the round-trip factor $r_1 r_2 e^{-j2\beta L}$, the transmitted field can be written in the compact form:

$$b_2 = \frac{t_1 t_2 e^{-j\beta L}}{1 - r_1 r_2 e^{-j2\beta L}} a_1, \tag{A.12}$$

The corresponding transmission coefficient becomes:

$$S_{21} = \frac{b_2}{a_1} = \frac{t_1 t_2 e^{-j\beta L}}{1 - r_1 r_2 e^{-j2\beta L}}. \tag{A.13}$$

Because the Fabry–Perot segment is reciprocal and lossless under the assumptions adopted here, the scattering matrix is symmetric, and therefore $S_{12} = S_{21}$. The remaining element S_{22}, which describes the complex reflection coefficient seen from the right side, can be obtained by repeating the above procedure for excitation from the right, or more simply by symmetry. The result is:

$$S_{22} = \frac{-r_2 + t_2^2 r_1 e^{-j2\beta L}}{1 - r_1 r_2 e^{-j2\beta L}}. \tag{A.14}$$

Equations (A.9)– (A.14) thus provide the complete set of scattering coefficients for the Fabry–Pérot resonator.

A.2 FWHM dependence with FSR and Finesse

Starting from the symmetric lossless cavity with $r = \sqrt{R}$, $t = \sqrt{1-R}$, the intensity transmission coefficient results:

$$T(\delta) = \left| \frac{t^2}{1 - r^2 e^{i\delta}} \right|^2 = \frac{t^4}{|1 - Re^{i\delta}|^2}. \tag{A.15}$$

Compute the denominator:

$$|1 - Re^{i\delta}|^2 = (1 - Re^{i\delta})(1 - Re^{-i\delta}) = 1 + R^2 - 2R\cos\delta. \tag{A.16}$$

Using $\cos\delta = 1 - 2\sin^2(\delta/2)$,

$$1 + R^2 - 2R\cos\delta = (1-R)^2 + 4R\sin^2(\delta/2). \tag{A.17}$$

Since $t^2 = 1 - R$, hence $t^4 = (1-R)^2$, Eq. (A.15) becomes:

$$T(\delta) = \frac{(1-R)^2}{(1-R)^2 + 4R\sin^2(\delta/2)} = \frac{1}{1 + \frac{4R}{(1-R)^2}\sin^2(\delta/2)}. \tag{A.18}$$

Therefore,

$$T(\delta) = \frac{1}{1 + F\sin^2(\delta/2)},\ \mathrm{F} = \frac{4R}{(1-R)^2}. \tag{A.19}$$

For $|\delta| \ll \pi$, $\sin(\delta/2) \approx \delta/2$, it follows:

$$T(\delta) \approx \frac{1}{1 + F(\delta/2)^2}. \tag{A.20}$$

At half maximum, $T = 1/2$, hence

$$1 + \mathcal{F}(\delta_{1-2}/2)^2 = 2 \Rightarrow \mathcal{F}\left(\frac{\delta_{1/2}}{2}\right)^2 = 1 \Rightarrow \delta_{1-2} = \frac{2}{\sqrt{\mathcal{F}}}. \tag{A.21}$$

Because the phase detuning is symmetric, the FWHM in phase results:

$$\Delta\delta = 2\delta_{1/2} = \frac{4}{\sqrt{\mathcal{F}}}. \tag{A.22}$$

Near resonance, the linewidth $\Delta\delta$ can be expressed in the frequency domain ν as:

$$\delta(\nu) = 2\pi\frac{\nu - \nu_m}{\mathrm{FSR}}, \Rightarrow \frac{d\delta}{d\nu} = \frac{2\pi}{\mathrm{FSR}}. \tag{A.23}$$

Thus,

$$\Delta\delta = \frac{2\pi}{\text{FSR}}\,\Delta\nu \Rightarrow \Delta\nu = \frac{\text{FSR}}{2\pi}\Delta\delta = \frac{\text{FSR}}{2\pi}\frac{4}{\sqrt{\mathcal{F}}} = \frac{2\,\text{FSR}}{\pi\sqrt{\mathcal{F}}}. \tag{A.24}$$

Hence the finesse results: $\mathcal{F} = \frac{\text{FSR}}{\Delta\nu} \approx \frac{\pi}{2}\sqrt{F}$.

Appendix B: Derivation of resonator dispersion terms

In this Appendix are derived the relations used in the main text to connect the discrete mode-index expansion of the resonance frequencies to the continuous propagation-constant dispersion of the guided mode, following references [2-4].

B.1 Resonance condition

A single spatial mode of a Fabry–Pérot or ring resonator of physical length L is considered. The longitudinal modes are characterized by an integer mode number m and resonate at angular frequencies ω_m such that the round-trip phase is an integer multiple of 2π:

$$\beta(\omega_m)\,L = 2\pi m, \tag{B.1}$$

where $\beta(\omega)$ is the propagation constant of the guided mode. The reference mode (m_0) has resonance frequency ω_0, and the relative mode index μ is defined as $\mu = m - m_0$, such that $\mu = 0$ corresponds to the reference frequency. Subtracting $\beta(\omega)$ evaluated at m_0 from (B.1) evaluated at m, gives:

$$[\beta(\omega_\mu) - \beta(\omega_0)]\,L = 2\pi\mu \tag{B.2}$$

B.2 Expansion of the modal spectrum in mode index

Because the resonances are nearly equally spaced, the modal frequencies $\omega_\mu$are smooth functions of μ. Therefore, the expansion of $\omega_\mu$in a Taylor series around $\mu = 0$, gives:

$$\omega_\mu = \omega_0 + D_{1,\omega}\mu + \frac{1}{2}D_{2,\omega}\mu^2 + \frac{1}{6}D_{3,\omega}\mu^3 + \cdots, \tag{B.3}$$

where $D_{n,\omega} = \frac{\partial^n\omega_\mu}{\partial\mu^n}\,|_{\mu=0}$ are the dispersion coefficient terms of order n. By using Eq. (B.3), the integrated dispersion defined in the main text results:

$$D_{\text{int},\omega}(\mu) = \omega_\mu - (\omega_0 + D_{1,\omega}\mu) \tag{B.4}$$

That takes the explicit form:

$$D_{\text{int},\omega}(\mu) = \frac{1}{2}D_{2,\omega}\mu^2 + \frac{1}{6}D_{3,\omega}\mu^3 + \cdots, \tag{B.5}$$

B.3 Expansion of the propagation constant

Expanding the propagation constant $\beta(\omega)$around ω_0 as:

$$\beta(\omega) = \beta_0 + \beta_{1,\omega}(\omega - \omega_0) + \frac{1}{2}\beta_{2,\omega}(\omega - \omega_0)^2 + \frac{1}{6}\beta_{3,\omega}(\omega - \omega_0)^3 + \cdots, \tag{B.6}$$

where $\beta_{1,\omega}$is the group delay per unit length, $\beta_{2,\omega}$is the group-velocity dispersion (GVD), and $\beta_{3,\omega}$is the third-order dispersion (TOD). Substituting (B.6) into the resonance condition (B.2), and considering $\Delta\omega_\mu = \omega_\mu - \omega_0$, can be obtained:

$$[\beta_{1,\omega}\Delta\omega_\mu + \frac{1}{2}\beta_{2,\omega}\Delta\omega_\mu^2 + \frac{1}{6}\beta_{3,\omega}\Delta\omega_\mu^3 + \cdots]L = 2\pi\mu, \tag{B.7}$$

B.4 Relation between $D_{1,\omega}$and $\beta_{1,\omega}$

Differentiating the resonance condition (B.2) with respect to μ, results:

$$\frac{\partial}{\partial\mu}[\beta(\omega_\mu) - \beta(\omega_0)]L = 2\pi. \tag{B.8}$$

The term $\beta(\omega_0)$is independent of μ, consequently it follows:

$$\frac{\partial\beta(\omega_\mu)}{\partial\mu}L = 2\pi. \tag{B.9}$$

Using the chain rule:

$$\frac{\partial\beta(\omega_\mu)}{\partial\mu} = \frac{\partial\beta}{\partial\omega}|_{\omega_\mu}\frac{\partial\omega_\mu}{\partial\mu} = \beta_{1,\omega}(\mu)\, D_{1,\omega}(\mu), \tag{B.10}$$

where it can be replaced $D_{1,\omega}(\mu) = \partial\omega_\mu/\,\partial\mu$. Eq. (B.9) reduces to:

$$\beta_{1,\omega}(\mu)\, D_{1,\omega}(\mu)\, L = 2\pi, \tag{B.11}$$

$$\beta_{1,\omega}(\mu) = \frac{2\pi}{L\, D_{1,\omega}(\mu)} \tag{B.12}$$

This is the expression used in the main text and in the analysis, where $\beta_{1,\omega}$.

B.5 Relation between $D_{2,\omega}$and $\beta_{2,\omega}$

By the differentiation of (B.12) with respect to μ. It yields to:

$$\frac{\partial\beta_{1,\omega}(\mu)}{\partial\mu} = \frac{2\pi}{L}(-1)D_{1,\omega}^{-2}(\mu)\frac{\partial D_{1,\omega}(\mu)}{\partial\mu} = -\frac{2\pi}{L}\frac{D_{2,\omega}(\mu)}{D_{1,\omega}^2(\mu)}, \tag{B.13}$$

where $\partial D_{1,\omega}(\mu)/\,\partial\mu = D_{2,\omega}(\mu)$. On the other hand, by the chain rule,

$$\frac{\partial\beta_{1,\omega}(\mu)}{\partial\mu} = \frac{\partial\beta_{1,\omega}(\mu)}{\partial\omega}\frac{\partial\omega}{\partial\mu} = \beta_{2,\omega}(\mu)\, D_{1,\omega}(\mu), \tag{B.14}$$

Equating (B.13) and (B.14), and re-calling Eq. (B.12), it results:

$$\beta_{2,\omega}(\mu)\, D_{1,\omega}(\mu) = -\beta_{1,\omega}(\mu) D_{1,\omega}(\mu) \frac{D_{2,\omega}(\mu)}{D_{1,\omega}(\mu)^2} = -\beta_{1,\omega}(\mu) \frac{D_{2,\omega}(\mu)}{D_{1,\omega}(\mu)}. \quad \text{(B.15)}$$

Solving for $\beta_{2,\omega}(\mu)$, yields:

$$\beta_{2,\omega}(\mu) = -\frac{D_{2,\omega}(\mu)\, \beta_{1,\omega}(\mu)}{D_{1,\omega}(\mu)^2}. \quad \text{(B.16)}$$

This expression has been reported in the main text.

B.6 Relation between $D_{3,\omega}$ and $\beta_{3,\omega}$

The final differentiation is applied on $\beta_{2,\omega}(\omega_\mu)$ with respect to μ and relate the result to $\beta_{3,\omega}(\omega_\mu)$. Starting from (B.16), introducing the shorthands $B_1(\mu) = \beta_{1,\omega}(\omega_\mu)$, and $B_2(\mu) = \beta_{2,\omega}(\omega_\mu)$,

$$B_2 = -\frac{D_{2,\omega} B_1}{D_{1,\omega}^2}. \quad \text{B.17)}$$

Differentiating with respect to μ gives:

$$\frac{\partial B_2}{\partial \mu} = -\frac{D_{3,\omega} B_1 + D_{2,\omega} \frac{\partial B_1}{\partial \mu}}{D_{1,\omega}^2} + 2\,\frac{D_{2,\omega}^2 B_1}{D_{1,\omega}^3}, \quad \text{(B.18)}$$

where it is used $\partial D_{2,\omega}/\,\partial\mu = D_{3,\omega}$ and $\partial D_{1,\omega}^{-2}/\,\partial\mu = -2D_{1,\omega}^{-3} D_{2,\omega}$. The derivative $\partial B_1/\,\partial\mu$ is computed using the chain rule:

$$\frac{\partial B_1}{\partial \mu} = \frac{\partial \beta_{1,\omega}}{\partial \omega}\frac{\partial \omega}{\partial \mu} = \beta_{2,\omega}(\mu)\, D_{1,\omega}(\mu) = B_2 D_{1,\omega} \quad \text{(B.19)}$$

Substituting (B.19) into (B.18), derives:

$$\frac{\partial B_2}{\partial \mu} = -\frac{D_{3,\omega} B_1 + D_{2,\omega} B_2 D_{1,\omega}}{D_{1,\omega}^2} + 2\,\frac{D_{2,\omega}^2 B_1}{D_{1,\omega}^3} \quad \text{(B.20)}$$

On the other hand, by definition,

$$\frac{\partial B_2}{\partial \mu} = \frac{\partial \beta_{2,\omega}}{\partial \omega}\frac{\partial \omega}{\partial \mu} = \beta_{3,\omega}(\mu)\, D_{1,\omega}(\mu) \quad \text{(B.21)}$$

Equating (B.20) and (B.21) and multiplying both sides by $D_{1,\omega}^3$, it results:

$$\beta_{3,\omega}(\omega_\mu)\, D_{1,\omega}^4 = -D_{3,\omega} B_1 D_{1,\omega} - D_{2,\omega} B_2 D_{1,\omega}^2 + 2D_{2,\omega}^2 B_1. \quad \text{(B.22)}$$

Using again the relation between B_2 and B_1 from (B.17), the term in the middle becomes:

$$-D_{2,\omega} B_2 D_{1,\omega}^2 = -D_{2,\omega}\left(\frac{D_{2,\omega} B_1}{D_{1,\omega}^2}\right) D_{1,\omega}^2 = D_{2,\omega}^2 B_1. \quad \text{(B.23)}$$

Hence the right-hand side simplifies to

$$-D_{3,\omega} B_1 D_{1,\omega} + D_{2,\omega}^2 B_1 + 2D_{2,\omega}^2 B_1 = -D_{3,\omega} B_1 D_{1,\omega} + 3D_{2,\omega}^2 B_1. \quad \text{(B.24)}$$

Then, Eq. (B.22) becomes:

$$\beta_{3,\omega}(\omega_\mu)\, D_{1,\omega}^4 = -D_{3,\omega}(\mu)\, \beta_{1,\omega}(\omega_\mu) D_{1,\omega}(\mu) + 3D_{2,\omega}(\mu)^2\, \beta_{1,\omega}(\omega_\mu). \tag{B.25}$$

Dividing by $D_{1,\omega}^3$, it yields:

$$\beta_{3,\omega}(\mu) = -\frac{1}{D_{1,\omega}(\mu)^3}\left[\beta_{1,\omega}(\mu) D_{3,\omega}(\mu) + 3\beta_{2,\omega}(\mu) D_{1,\omega}(\mu) D_{2,\omega}(\mu)\right], \tag{B.26}$$

which is the expression used in the main analysis for $\beta_{3,\omega}$.

B.7 Frequency-derivative representation

For completeness, are briefly summarized the relation between the dispersion coefficients defined with respect to angular frequency and those defined with respect to optical frequency. Defining $\beta_{1,f} = \frac{\partial\beta}{\partial f}, \beta_{2,f} = \frac{\partial^2\beta}{\partial f^2}, \beta_{3,f} = \frac{\partial^3\beta}{\partial f^3}$, and recalling that $\omega = 2\pi f$, it follows that:

$$\frac{\partial}{\partial f} = \frac{\partial\omega}{\partial f}\frac{\partial}{\partial\omega} = 2\pi\,\frac{\partial}{\partial\omega}. \tag{B.27}$$

Applying this repeatedly leads to:

$$\begin{cases} \beta_{1,f} = (2\pi)\, \beta_{1,\omega} \\ \beta_{2,f} = (2\pi)^2 \beta_{2,\omega} \\ \beta_{3,f} = (2\pi)^3 \beta_{3,\omega} \end{cases} \tag{B.28}$$

These relations are used whenever dispersion quantities are expressed in Hz instead of rad/s.

Appendix C: Laser cavity model

This section presents the mathematical derivation of the round-trip conditions for two-mirror and three-mirror lasers, combined with the related figure of merit, as well as the derivation of the dispersion coefficients and the TCMT model. All these are supported by references [1],[5],[6].

C.1 Two-mirror laser cavity round-trip condition

When is considered a Fabry–Pérot cavity consisting of an active section of length $L_g$with material gain $g$and internal loss $\alpha_{i,g}$, followed by a passive section of length $L_p$with loss $\alpha_{i,p}$, bounded by mirrors of amplitude reflectivities $r_1$and r_2, it can be defined single-pass gain/loss factor for the field propagation in the two sections.

For the active section of length L_a, the material provides a gain per unit length Γg and an internal loss per unit length $\alpha_{i,g}$. The net gain coefficient is therefore $\Gamma g - \alpha_{i,g}$, and the field after propagating through this section is multiplied by:

$$\exp\left[(\Gamma g - \alpha_{i,g}) L_g\right], \tag{C.1}$$

In the passive section of length $L_p$there is only loss $\alpha_{i,p}$, so propagation through this region contributes a factor:

$$\exp\left(-\alpha_{i,p}L_p\right). \tag{C.2}$$

The total propagation factor for one round trip (excluding the mirrors) is the product of these two exponentials. Including the reflections from the two mirrors, with amplitude reflectivities $r_1$and r_2, the overall round-trip amplitude factor becomes:

$$r_1 r_2 \exp\left[(\Gamma g - \alpha_{i,g})L_g - \alpha_{i,p}L_p\right], \tag{C.3}$$

which is the round-trip amplitude condition for a two-mirror cavity including gain and loss in both active and passive sections. At threshold, the field must reproduce after a round trip (neither grow nor decay in amplitude), so the round-trip factor must have magnitude 1. Neglecting the phase here, this gives the scalar condition:

$$r_1 r_2 \exp\left[(\Gamma g_{\text{th}} - \alpha_{i,g})L_g - \alpha_{i,p}L_p\right] = 1, \tag{C.4}$$

The round-trip amplitude condition is

$$r_1 r_2 \exp\left(\Gamma_{xy} g_{\text{th}} L_g - \alpha_{i,g}L_g\right) \exp\left(-\alpha_{i,p}L_p\right) = 1, \tag{C.5}$$

where $\Gamma_{xy}$is the transverse confinement factor. Taking the natural logarithm of both sides:

$$\Gamma_{xy} g L_a - \alpha_{i,g}L_g - \alpha_{i,p}L_p + \ln\left(r_1 r_2\right) = 0. \tag{C.6}$$

Defining the mean mirror intensity reflection $R_m = r_1 r_2$, and re-arranging Eq. (C.6).

$$\Gamma_{xy} g_{\text{th}} L_a = \alpha_{i,g}L_g + \alpha_{i,p}L_p + \ln\left(\frac{1}{R_m}\right) \tag{C.7}$$

To obtain a per-unit-length form, divide both sides of (C.7) by L that is the sum of the passive and active section lengths:

$$\Gamma_{xy} \frac{L_g}{L} g_{\text{th}} = \frac{\alpha_{i,g}L_g + \alpha_{i,p}L_p}{L} + \frac{1}{L}\ln\left(\frac{1}{R_m}\right). \tag{C.8}$$

Introducing the longitudinal confinement factor $\Gamma_z = \frac{L_g}{L}$, valid in the limit $L_g \gg \lambda$, and define the 3D confinement factor:

$$\Gamma = \Gamma_{xy}\,\Gamma_z \tag{C.9}$$

The length-weighted average internal loss is defined as:

$$\langle \alpha_i \rangle = \frac{\alpha_{i,a}L_a + \alpha_{i,p}L_p}{L}, \tag{C.10}$$

while the equivalent mirror loss:

$$\alpha_m = \frac{1}{L}\ln\left(\frac{1}{R_m}\right). \tag{C.11}$$

Substituting (C.9)– (C.11) into (C.8), yields:

$$\Gamma\, g_{\mathrm{th}} = \langle \alpha_i \rangle + \alpha_m, \tag{C.12}$$

which is Eq. (2.65) in the main text.

C.2 Three-mirror laser cavity figures of merits

This section derives additional figures of merit for the three-mirror external-cavity laser. Above threshold, the steady-state photon rate equation can be written in per-unit-length form as:

$$v_g\, \Gamma\, g(N)\, S = v_g(\langle \alpha_i \rangle + \alpha_m)S, \tag{C.13}$$

where α_i is the average internal loss per unit length and α_m is the distributed mirror loss defined in Eq. (2.67). A small increase in drive current I then induces a change in carrier density ΔN (and hence in gain Δg) such that the additional stimulated emission exactly compensates for the corresponding increase in total loss; in steady state this condition can be written as:

$$\frac{\mathrm{d}S}{\mathrm{d}I} = \frac{\eta_i}{qV_a}\, \frac{1}{\langle \alpha_i \rangle + \alpha_m}, \tag{C.14}$$

with η_i the internal quantum efficiency and V_a the active volume. The total photon flux leaving the cavity through all mirrors is $v_g \alpha_m S$; the incremental photon flux through the chosen output mirror is therefore $v_g \alpha_{m,1} S$. While the corresponding incremental optical power is:

$$\frac{\mathrm{d}P_{\mathrm{out}}}{\mathrm{d}I} = h\nu\, v_g \alpha_{m,1}\, \frac{\mathrm{d}S}{\mathrm{d}I} = \frac{h\nu}{q}\, \eta_i\, \frac{\alpha_{m,1}}{\langle \alpha_i \rangle + \alpha_m}, \tag{C.15}$$

The differential quantum efficiency $\eta_d$is defined as the ratio between the photon flux at the output facet and the injected electron flux above threshold:

$$\eta_d = \frac{q}{h\nu}\, \frac{\mathrm{d}P_{\mathrm{out}}}{\mathrm{d}I} = \eta_i\, \frac{\alpha_{m,1}}{\langle \alpha_i \rangle + \alpha_m}, \tag{C.16}$$

which is the compact form used in the main text (Eq. (2.69)). The ratio $\alpha_{m,\mathrm{ext}}/\alpha_m$expresses the fraction of the total mirror-related power loss that appears as useful output at the external reflector. When it is considered one round trip in the equivalent two-mirror cavity with amplitude reflectivities r_1(HR facet) and r_{eff} (effective external reflector), let the forward intracavity field at the external mirror be E. The power lost at the HR mirror in a single pass:

$$P_1^{(1)} = (1 - r_1^2)\ \mid E \mid^2. \tag{C.17}$$

Total power lost at the external mirror in a single pass:

$$P_{\mathrm{ext,total}}^{(1)} = (1 - r_{\mathrm{eff}}^2)\ \mid E \mid^2. \tag{C.18}$$

Only a fraction of $P_{\mathrm{ext,\,total}}^{(1)}$emerges as useful power into the bus waveguide. Denote by t_e^2 the intensity transmission of the external reflector into the bus waveguide; the corresponding useful output power per pass is:

$$P_{\text{out,ext}}^{(1)} = t_e^2 \ | E |^2. \tag{C.19}$$

Because the two mirrors form a Fabry–Pérot cavity, part of the field that is transmitted or lost at the external mirror is replenished by multiple reflections between the two mirrors. Summing the geometric series of forward and backward passes leads to an effective external-mirror loss per round trip of the form:

$$P_{\text{ext,eff}}^{(1)} = [(1 - r_{\text{eff}}^2) + r_1 r_{\text{eff}}\, t_e^2] \ | E |^2, \tag{C.20}$$

where the term proportional to $r_1 r_{\text{eff}} t_e^2$ accounts for power that reaches the external mirror after one or more reflections at the HR facet. The total mirror-related loss per round trip is then:

$$P_{\text{mirr,total}}^{(1)} = (1 - r_1^2) \ | E |^2 + [(1 - r_{\text{eff}}^2) + r_1 r_{\text{eff}} t_e^2] \ | E |^2. \tag{C.21}$$

F_1 expresses the fraction of the total mirror-related power loss that appears as useful output at the external reflector. By definition:

$$F_1 = \frac{\text{useful power from external mirror}}{\text{total mirror-related power loss}} = \frac{P_{\text{out,ext}}^{(1)}}{P_{\text{mirr,total}}^{(1)}}. \tag{C.22}$$

Using Eqs. (C.19) and (C.21) and cancelling $| E |^2$ gives:

$$F_1 = \frac{t_e^2}{(1 - r_1^2) + (1 - r_{\text{eff}}^2) + r_1 r_{\text{eff}} t_e^2}. \tag{C.23}$$

Regrouping the terms associated with each mirror yields the compact form:

$$F_1 = \frac{t_e^2}{(1 - r_{\text{eff}}^2) + \dfrac{r_1 r_{\text{eff}}\, t_e^2}{1 - r_1^2}} \tag{C.24}$$

This expression shows that F_1 decreases as r_{eff} increases: stronger external reflection assigns a larger share of the mirror loss to the external mirror, but only part of that loss (t_e^2) appears as useful transmitted power. The slope efficiency η_s(in W/A) is the differential output power with respect to current, that refers to:

$$\eta_s = \frac{\mathrm{d}P_{\text{out}}}{\mathrm{d}I} \tag{C.25}$$

Combining Eq. (C.25) with the definition of η_d in Eq. (C.16) gives:

$$\eta_s = \frac{h\nu}{q}\, \eta_d = \frac{h\nu}{q}\, \eta_i \, \frac{\alpha_{m,1}}{\langle \alpha_i \rangle + \alpha_m}. \tag{C.26}$$

When the useful output is taken at the lossy external mirror, it is convenient to factor out the facet fraction F_1 by writing:

$$\eta_d = F_1 \, \eta_i \, \frac{\alpha_m}{\langle \alpha_i \rangle + \alpha_m},. \tag{C.27}$$

so that

$$\eta_s = \frac{h\nu}{q}\, F_1\, \eta_i\, \frac{\alpha_m}{\langle \alpha_i \rangle + \alpha_m}. \tag{C.28}$$

Integrating this linear relationship with respect to current yields the standard expression for the output power above threshold,

$$P_{\text{out}}(I) = \eta_s\,(I - I_{\text{th}}) = \eta_d\, \frac{h\nu}{q}\,(I - I_{\text{th}}), \tag{C.29}$$

Finally, the output power at the external mirror can be written as:

$$P_{\text{out}} = \eta_s\, \frac{h\nu}{q}\,(I - I_{\text{th}}), \tag{C.30}$$

where h is Planck's constant, q is the elementary charge, $\nu$is the lasing frequency, $I$and I_{th} are the drive and threshold currents, and η_s is the slope efficiency of the laser. For a cavity with a lossy external mirror, the differential quantum efficiency at that mirror can be written as:

$$\eta_d = F_{\text{out}}\, \eta_i\, \frac{\alpha_m}{\langle \alpha_i \rangle + \alpha_m}, \tag{C.31}$$

with $\langle \alpha_i \rangle$ the average internal loss, $\alpha_m$the total mirror loss, and η_i the internal quantum efficiency. Here F_{out} is the fraction of total mirror-coupled power that emerges as useful output at the external reflector, rather than being dissipated inside the photonic crystal cavity or re-injected towards the HR mirror. The fraction F_{out} for the vertically coupled reflector is:

$$F_{\text{out}} = \frac{t_e^2}{(1 - r_{\text{eff}}^2) + \frac{r_1 r_{\text{eff}}\, t_e^2}{1 - r_1^2}}, \tag{C.32}$$

where t_e^2 is the intensity transmission of the external mirror into the bus waveguide, r_{eff} is the effective amplitude reflectivity at the gain–passive interface, and $r_1$is the HR-facet reflectivity. Substituting Eq. (C.32) into Eq. (C.31) gives the explicit expression for η_d,

$$\eta_d = \eta_i\, \frac{t_e^2}{(1 - r_{\text{eff}}^2) + \frac{r_1 r_{\text{eff}}\, t_e^2}{1 - r_1^2}} \times \frac{\alpha_m}{\langle \alpha_i \rangle + \alpha_m}, \tag{C.33}$$

Finally, combining $\eta_s = (h\nu/q)\,\eta_d$ with Eq. (C.33) yields:

$$\eta_s = \frac{h\nu}{q}\, \eta_i\, \frac{t_e^2}{(1 - r_{\text{eff}}^2) + \frac{r_1 r_{\text{eff}}\, t_e^2}{1 - r_1^2}} \times \frac{\alpha_m}{\langle \alpha_i \rangle + \alpha_m}, \tag{C.34}$$

C.3 Resonant reflector: TCMT model derivation

For a single resonance driven from one port the amplitude equation is:

$$\frac{da}{dt} = (j\omega_0 - \Gamma_0 - \Gamma_c)a + \kappa_c s_{+,in}(t), \tag{C.35}$$

where ω_0 is the cavity resonance, Γ_0 intrinsic loss, Γ_c coupling loss, and κ_c the coupling coefficient, as defined in Eq. (2.77). Assuming a monochromatic excitation input source at frequency ω:

$$\begin{cases} s_{+,in}(t) = s_+ e^{j\omega t} \\ a(t) = Ae^{j\omega t} \end{cases} \tag{C.36}$$

Eq. (C.35) becomes:

$$\frac{da}{dt} = j\omega A e^{j\omega t} \tag{C.37}$$

Substituting Eq. (C.37) into Eq. (C.35) and factoring out the term $e^{j\omega t}$ results:

$$j\omega A e^{j\omega t} = (j\omega_0 - \Gamma_0 - \Gamma_c)Ae^{j\omega t} + \kappa_c s_+ e^{j\omega t}. \tag{C.38}$$

With simple mathematical manipulations, it can be rearranged to:

$$[j\omega - (j\omega_0 - \Gamma_0 - \Gamma_c)]A = \kappa_c s_+. \tag{C.39}$$

Defining the detuning parameter as $\Delta\omega = \omega - \omega_0$, the steadystate cavity amplitude is:

$$A = \frac{\kappa_c s_+}{j\Delta\omega + \Gamma_0 + \Gamma_c}. \tag{C.40}$$

References

[1] Coldren, Larry A., Scott W. Corzine, and Milan L. Mashanovitch. *Diode lasers and photonic integrated circuits*. John Wiley & Sons, 2012.

[2] Karabchevsky, Alina, and Amol Choudhary, eds. On-Chip Photonics: Principles, Technology and Applications. Elsevier, 2024.

[3] Chembo, Yanne K. "Kerr optical frequency combs: theory, applications and perspectives." Nanophotonics 5.2 (2016): 214-230.

[4] Herr, Tobias, Michael L. Gorodetsky, and Tobias J. Kippenberg. "Dissipative Kerr solitons in optical microresonators." Nonlinear optical cavity dynamics: from microresonators to fiber lasers (2016): 129-162.

[5] Liles, Alexandros Athanasios. Hybrid photonic crystal cavity based lasers. Ph.D. Diss. University of St Andrews, 2017.

[6] Iadanza, Simone. MOS Compatible Deposited Materials for Optical Interconnects. Ph.D. Diss. Munster Technological University of Cork, 2022.